Revealing Plasmonic Effects of One-Dimensional Periodic Structures through Mueller Matrix Spectroscopic Ellipsometry

Von der Fakultät Mathematik und Physik der Universität Stuttgart
zur Erlangung der Würde eines Doktors der Naturwissenschaften
(Dr. rer. nat.) genehmigte Abhandlung

vorgelegt von
Meng Wang
aus Jiangsu (China)

Hauptberichter: Prof. Dr. Martin Dressel
Mitberichter: Apl.-Prof. Dr. Jürgen Weis

Tag der mündlichen Prüfung: 21.02.2018

1. Physikalisches Institut der Universität Stuttgart

2018

Contents

Zusammenfassung

Mikro- und Nanostrukturen stellen bis heute eine vielversprechende Technologie dar, weil sie Funktionalitäten erlauben, die entweder so in der Natur nicht existieren, oder weil sie es erlauben bestehende Anwendungen mit viel kleinerem Aufwand und höherer Effizient umzusetzen.

Die Wechselwirkung von komplexen plasmonischen Nanostrukturen, ob periodisch oder ungeordnet, mit polarisiertem Licht erzeugt interessante Physik, bei der Streuung, Beugung und Absorption verbunden werden, zu einer Vielzahl von dispersiven Moden und Kopplungseffekten. Jede dieser Anregungen hängt stark von der Polarisation, dem Einfallswinkel, der azimuthalen Orientierung der Probe und der Wellenlänge ab. Das alles führt zu einer vielfältigen Wechselwirkung mit polarisiertem Licht. Auf der einen Seite ist dieses Zusammenspiel der verschiedenen Wechselwirkungen nicht leicht zu verstehen, auf der anderen Seite eröffnet es die Möglichkeit gezielt optische Antworten maßzuschneidern.

Die komplette optische Antwort einer Probe lässt sich über Müller-Matrizen (MM), gemessen für verschiedene k-Vektoren und einen weiten Frequenzbereich, unabhängig von irgendwelchen Modellannahmen, bestimmen. Obwohl spektroskopische Müller-Matrix Ellipsometrie mittlerweile vielfältige Anwendungen in der Charakterisierung von komplexen Nanostrukturen gefunden hat, bleibt die zugrundeliegende Physik oft in den komplizierten Daten versteckt, was bei der physikalischen Interpretation der gemessenen MM immer noch zu Herausforderungen führt.

Das Ziel dieser Arbeit ist es, an zwei relativ einfachen plasmonischen Nanostrukturen zu zeigen, dass sich die optische Antwort dieser Proben vollständig im Rahmen der MM-Ellipsometrie verstehen lässt. In der Arbeit wird gezeigt, dass eine systematische Korrelation der in den MMs beobachteten Polarisationsmischung zu der ihr zugrundeliegenden Physik eine zuverlässige analytische Methode darstellt, die auf alle Proben angewandt werden kann, die sowohl anisotrop sind, als auch Dispersion zeigen. Außerdem kann die Methode auf einen weiten Bereich von Proben ausgedehnt werden, ob anisotrop oder nicht, ob sie lokalisierte oder propagierende Plasmonenmoden zeigt, oder ob die beobachtete Dispersion ihren Ursprung in Wellenleitermoden oder photonischen Moden hat, solange für die k-Abhängigkeit der Dispersion ein analytischer Ausdruck angeben werden kann. Am Beispiel von zwei relativ einfachen Proben wird die Mächtigkeit und Implementierung der Methoden gezeigt: an einem eindimensionalen plasmonischen Metallgitter und an einem metallischen Nanopartikel-Array. Diese beiden Beispiele werden im Rahmen der Arbeit komplett analysiert und gelöst und es wird gezeigt, dass die Ergebnisse im Prinzip für neue Anwendungen genutzt werden können.

Eindimensionale Au-Gitter und Au/Ni/Au-Gitter

Ergebnisse publiziert unter: M. Wang, A. Löhle, B. Gompf, M. Dressel, and A. Berrier,

“Physical interpretation of Mueller matrix spectra: a versatile method applied to gold gratings,” *Opt. Express*, vol. 25, no. 6, pp. 6983–6996, 2017.

Eindimensionale Metallgitter erlauben es durch ihre periodische Struktur die Dispersion von anregendem Licht und Plasmonen aufeinander abzustimmen und dadurch sehr effizient Oberflächenplasmonen (SPP) anzuregen. Es ist seit langem bekannt das Metallgitter abrupte Änderungen in ihrer optischen Antwort zeigen können, die als Rayleigh-Woods Anomalien (RWA) bezeichnet werden. RWA können zu sehr schmalen Plasmonenresonanzen in geordneten metallischen Anordnungen führen, durch die beugungsbedingte Kopplung von lokalisierten Plasmonen, oder sie können die Reflexion von nicht-plasmonischen metallischen Kreuzgittern beeinflussen. Obwohl SPPs in metallischen Gittern seit langer Zeit untersucht werden und RWAs seit Jahrzehnten bekannt sind, fehlt bis heute ein tieferes Verständnis wie sie die Polarisationsmischung in Metallgittern beeinflussen.

Der erste Teil der Arbeit behandelt die eindimensionalen plasmonischen Metallgitter, die durch Aufdampfen von dünnen Au- bzw. Au/Ni/Au-Filmen auf PDMS-Gittern hergestellt werden (siehe Abb.1). In einem ersten Schritt wird die Reflexion entlang der zwei optischen Achsen der Probe, also entlang der Rillen und senkrecht dazu, mit s- und p-polarisiertem Licht gemessen. Die so gemessene Reflexion wird dann mit einem einfachen anisotropen „effective medium“ Ansatz mit Drude-Lorentz Oszillatoren moduliert. Aus diesem einfachen Modell werden dann Intensitätsplots über den ganzen Wellenlängen- und Winkelbereich generiert. Ist die Übereinstimmung zwischen gemessenen und simulierten Intensitäten gut, können Mueller-Matrix Plots erstellt werden. Diesen Plots werden dann die, aus der bekannten Periodizität des Gitters erwarteten dispersiven SPP- und RWA-Moden überlagert. Der Vergleich der so simulierten MM mit den gemessenen MM erlaubt es dann, den Einfluss der Anisotropie, proparierender SPPs, der Beugung und der materialabhängigen Absorption durch ihre unterschiedliche Dispersion zu identifizieren und ihre Wechselwirkung und Kopplung hervorgehoben (Abb.2). Man sieht, dass SPPs sowohl durch p- als auch durch s-polarisiertes Licht angeregt werden können, wenn die Einfallebene senkrecht oder parallel zu den Gitterlinien verläuft. Beide Moden sind dispersiv und folgen den gleichen Phasenanpassungsbedingungen. Dadurch kommt es zur einer Polarisationsmischung, die s- in p-polarisiertes Licht durch die Anregung von SPPs verwandelt und umgekehrt. Diese Polarisationsmischung ist maximal, wenn die Einfallsebene unter 45° zu den Gitterlinien verläuft. Zusätzlich zu der Anregung von SPPs, werden die optischen Eigenschaften auch durch die geometrische Anisotropie, die RWAs, die direkt mit der Periodizität des Gitters zusammenhängen, und zu einem kleineren Teil, durch die Au Interbandübergänge beeinflusst. Die Anisotropie, die Interbandübergänge und nichtdispersive Näherung für die SPPs können ganz gut in Rahmen eines „effective medium“ Ansatzes beschrieben werden, der sich nur durch die Anpassung an die gemessenen Intensitäten ergibt. Die dispersiven SPP- und RWA-Moden müssen dann aber diesem einfachen Modell überlagert werden.

Danach werden die Au/Ni/Au-Gitter mit einem ähnlichen Ansatz analysiert. Auch hier lässt sich die Rolle der Anisotropie, propagierender SPPs und die materialabhängige Absorption in gleicher Weise identifizieren. Beugungseffekte haben bei den Au/Ni/Au-Gittern nur einen schwachen Einfluss, vermutlich wegen der hohen Absorption innerhalb des Ni-Films. Am Ende des Kapitels wird noch die Möglichkeit, die plasmonischen Eigenschaften durch Strecken einzustellen und die Reversibilität dieses Zugangs diskutiert.

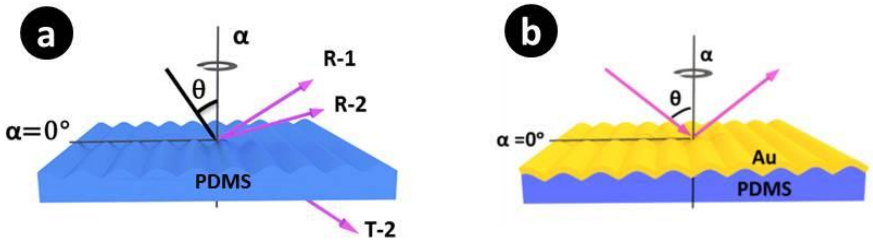

Abbildung 1: Schematische Darstellung des reinen PDMS-Gitters (a) und des Au-bedampften (b).

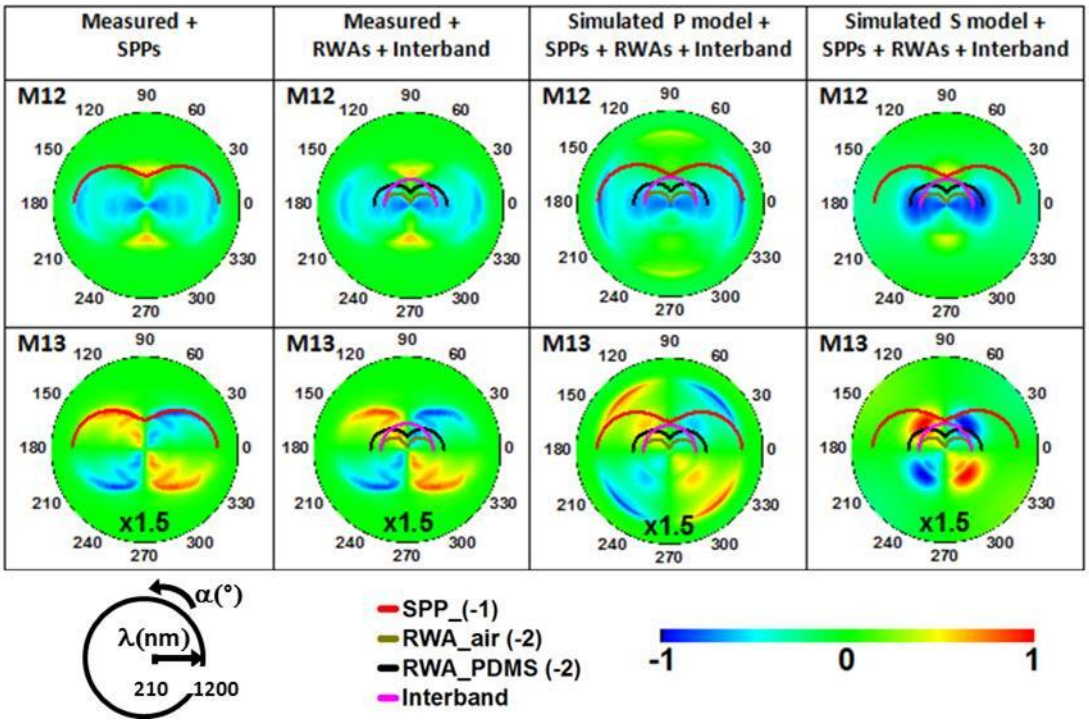

Abb. 2: Gemessene und simulierte Mueller-Matrix Elemente M12 und M13 zusammen mit den dispersiven SPPs und RWAs und den Interbandübergängen in der oberen Hälfte der Plots für einen Einfallswinkel von 45°.

Ag-Nanopartikel Arrays

Manuskript eingereicht: Meng Wang, Bruno Gompf, Martin Dressel, Nathalie Destouches, and Audrey Berrier, "Pure circular dichroism by curved rows of plasmonic nanoparticles." submitted to *Optical Materials Express*

Arrays aus metallischen Nanopartikeln wurden in den letzten Jahrzehnten intensiv untersucht. Ihre optische Antwort hängt nicht nur von der Größe und Form der einzelnen Partikel ab, sondern auch von ihrer spezifischen Anordnung. Das Wechselspiel zwischen den verschiedenen Beiträgen kann dann zu einer komplexen optischen Antwort führen, bei der der Einfluss der verschiedenen Beiträge nicht mehr leicht voneinander zu trennen ist. Auf der anderen Seite ist es

aber wichtig dieses Wechselspiel der Beiträge verstanden zu haben, wenn man gezielt optische Antworten für gewünschte Anwendungen entwickeln will. Es gibt zwar zahlreiche Arbeiten die das Wechselspiel in spezifischen Anordnungen von Nanopartikeln und ihre optische Antwort untersuchen, aber es gibt im Fall von komplexen Proben, wo unterschiedliche optische Eigenschaften, photonische und plasmonische, überlappen, keine eindeutigen Verfahren diese sauber zu trennen.

Der zweite Teil der Arbeit beschäftigt sich mit metallischen Nanopartikel-Arrays, die durch einen laser-induzierten Selbstorganisationsprozess hergestellt wurden (Abb. 3). Die Ag-Nanopartikel sind in einen TiO_2-Wellenleiter eingebettet und bilden dort eine periodische Anordnung entlang gekrümmter Linien. In diesem Teil wird gezeigt, wie die optische Antwort dieses komplexen Nanopartikel-Arrays in ihre Details zerlegt und damit verstanden werden kann. Bei dieser komplexen Probe tritt ein kompliziertes Wechselspiel von plasmonischen Resonanzen, durch Periodizität bedingter Moden, Wellenleitermoden, Interferenzeffekten und Kopplungseffekten zwischen nächsten Nachbarn auf. All diese Einflüsse lassen sich im Rahmen der Mueller-Matrix Ellipsometrie und mit Hilfe der anschließenden Matrixzerlegung, entflechten. Dadurch lassen sich die fundamentalen physikalischen Mechanismen der beobachteten optischen Signaturen identifizieren. Zuerst lässt sich aus der azimuthabhängigen Transmission auf die Anisotropie, und aus der Einfallswinkel-Abhängigkeit auf die Dispersion durch eine periodische Anordnung schließen, woraus sich dann ein erstes einfaches Modell entwickeln lässt. Danach werden dann die gemessenen MM mit denen aus dem einfachen Modell simulierten verglichen. Die Dekomposition der MM in ihre fundamentalen optischen Eigenschaften erlaubt es anschließend die beobachteten optischen Signaturen spezifischen Anregungen der Nanopartikel zuzuordnen: einfache lokalisierte Oberflächenplasmonen, Doppelbrechung durch eine anisotrope Anordnung in Linien, die Kopplung zwischen den Linien, Beugung in Wellenleitermoden oder eine gebrochene Symmetrie die zu echtem zirkularem Dichroismus führt (Abb.1.2 (b)). Vor allen der letzte Aspekt lässt sich nur durch eine vollständige Analyse der Mueller-Matrizen erreichen; nur die differenzielle Zerlegung der gemessenen Mueller-Matrizen in ihre fundamentalen optischen Eigenschaften erlaubt es zwischen einer Polarisationsdrehung hervorgerufen durch Doppelbrechung und echtem zirkularem Dichroismus zu unterscheiden.

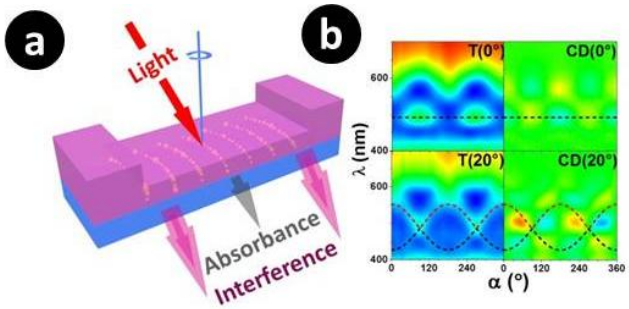

Abb. 3: (a) Schematische Darstellung des Ag-Nanopartikel-Arrays (b) Transmission und zirkularer Dichroismus über eine volle Rotation der Probe bei einem Einfallswinkel von 0° und 20°.

Abstract

Micro-and nanostructures are nowadays very important in science and technology as they allow for a whole range of functionalities that either does not exist in nature or reproduce existing effects with a much smaller footprint and higher efficiency.

The interaction of complex plasmonic nanostructures, periodic or random, with polarized light creates very rich physics where scattering, diffraction and absorbance are linked to a variety of dispersive modes and coupling effects. Each of these excitations depends strongly on polarization, angle of incidence, azimuthal orientation of the sample and wavelength. The presence of these modes and coupling effects results in manifold interaction with polarized light. On the one hand the interplay of these interactions cannot be easily understood and on the other hand it opens up the possibility to tailor the optical response.

The complete optical response of complex samples can be measured by Mueller matrices at various k-vectors over a broad frequency range independently from any model. Even though Mueller matrix spectroscopic ellipsometry (MMSE) is widely used in characterizing the optical properties of complex nanostructures, MMSE results in complex data hiding the underlying physics, making the physical interpretation of a measured Mueller matrix (MM) a big challenge.

The goal of this project is to demonstrate on the example of two simple plasmonic nanostructures, that the optical response of these samples can be fully understood in the framework of MM ellipsometry. It is demonstrated that a systematic correlation of the observed polarization mixing in MMs to their underlying physical origin is a versatile analytical method suitable to all samples exhibiting both anisotropy and dispersive modes. Further, the applicability can be extended to a wide variety of samples whether anisotropic or not, presenting localized or propagating plasmonic resonances, photonic modes -whether originating from waveguiding or scattering- or other dispersive modes at the only condition that an analytical expression for the dispersion of these modes exists. To demonstrate the power of this method and its implementation, we apply it to two very simple examples: the one-dimensional plasmonic metallic grating and metallic nanoparticle arrays. These two examples are completely analyzed and solved in the following topics and the results can in principle be used for new application.

Au gratings and Au/Ni/Au gratings

Manuscript published: M. Wang, A. Löhle, B. Gompf, M. Dressel, and A. Berrier, "Physical interpretation of Mueller matrix spectra: a versatile method applied to gold gratings," *Opt. Express*, vol. 25, no. 6, pp. 6983–6996, 2017.

One-dimensional gratings are very efficient tools to excite SPPs by matching their dispersion to that of light. When considering grating-based structures, it is well known that regular periodic nanostructures can show abrupt changes in the optical response, referred to as Rayleigh wood´s anomalies (RWAs) [11]. RWAs can result in very narrow plasmon resonances in regular plasmonic arrays of metallic nanoparticles, originating from the diffraction coupling of localized plasmons, or modify the reflectance of non-plasmonic metallic square arrays. Even though SPPs on metallic gratings have been studied for a long time and RWA effects have also been well

known for decades, a clear understanding of how SPPs and RWAs influence the polarization mixing of gratings is still lacking.

We focus on the one-dimensional plasmonic metallic grating which is fabricated by evaporating Au (Figure 1) or Au/Ni/Au thin film on PDMS grating.

First, for Au grating, we measure the reflectance along the two optic axes of the grating, along and perpendicular to the grooves under s- and p-polarization. The reflectance is then modelled by a simple anisotropic effective medium approach using Drude-Lorentz oscillators. From this anisotropic model, the intensity plots over the whole spectral and angular range are generated. Once the agreement between the generated and measured plots is insured, the Mueller-matrix plots can be calculated. On top of this calculated MME we superimpose the expected dispersive SPP and RWA modes, calculated from the known periodicity of the grating. Comparing this composed result with measured MMs gives a deep insight on how the different physical contributions originating from periodicity, anisotropy and material properties influence the complex polarization mixing (Figure 2). We have seen that SPPs can be excited by both p- or s-polarized light when the incident plane is perpendicular or parallel to the grating grooves. Both SPP modes are dispersive with the AOI and follow the same phase matching condition. P- or s-polarized light can be converted to s- or p- polarized light via SPP excitation, and maximum polarization conversion occurs when the angle between incident plane and grooves is 45°. Additionally to the excitation of SPPs, the optical properties are influenced by geometric anisotropy, the RWAs related to the periodic grating structure and, to a lesser extent, the Au interband transition. The anisotropy, the interband transition and the non-dispersive approximation of the SPPs are understood in terms of an effective medium approach, obtained from fitting the measured reflectance. However, the dispersion of the SPP modes and the RWAs effects should be added on top of this model.

Then we have demonstrated how the complex optical response of a simple Au/Ni/Au grating can be decomposed into its physical ingredients in the same approach with Au grating. The optical properties are influenced by the excitation of SPPs, geometric anisotropy and to a lesser extent, the Au/Ni/Au interband transition. Due to the high absorption of Ni, the influence of RWAs disappears and the plasmonic feature becomes broader as compared with Au grating. Finally, we introduced an active way for tuning SPP via mechanical stretching. By actively stretching the PDMS grating template, the periodicity of grating increases and SPP peak position red shifts. The releasing of a stretched metallic grating gives us a way for tuning the gap size between grating bulks with the shape of grating bulks unchanged.

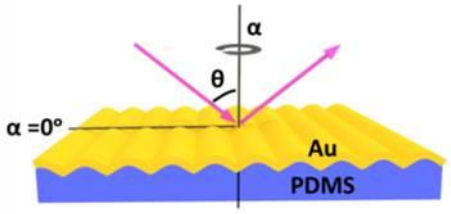

Figure 1: Schematic of Au gratings.

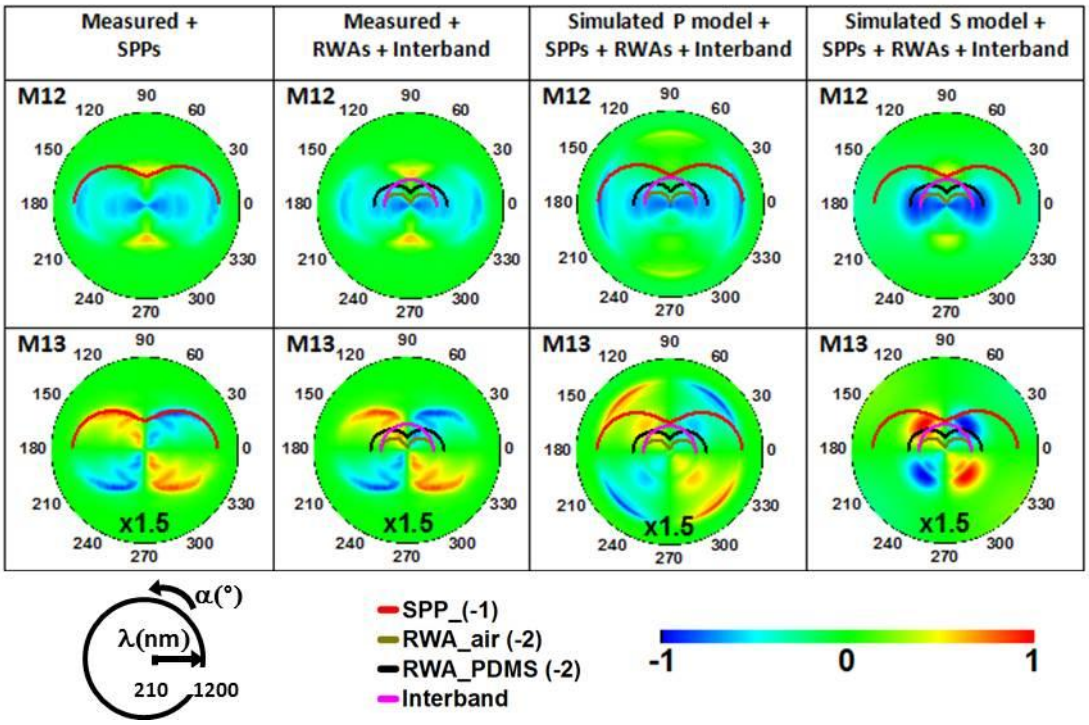

Figure. 2: Measured and simulated Mueller matrix elements M12, M13 together with the SPP, RWA and interband transitions draws in the upper half space at AOI 45°.

Ag nanoparticle arrays

Manuscript submitted: Meng Wang, Bruno Gompf, Martin Dressel, Nathalie Destouches, and Audrey Berrier, "Pure circular dichroism by curved rows of plasmonic nanoparticles." submitted to *Optical Materials Express*

Metallic nanoparticle arrays have been widely studied over the last decades. Their optical response depends not only on the individual particle, but also on their specific arrangement. The interplay of different contributions can lead to a complex optical response, where the influence of the different ingredients cannot be easily separated. On the other hand, however, this interplay has to be perfectly known, in order to tailor the optical response for any desired application. Numerous investigations describe the interplay between specific geometrical arrangements of nanoparticles and their optical response in different configurations where nanoparticles are ordered or randomly distributed, with different sizes and shapes. However, in the case of complex samples, where different optical – photonic or plasmonic – effects overlap and interact with each other, hitherto no clear procedure is readily available.

We have in full detail and completeness investigated the optical properties of a complex plasmonic sample where an interplay is found of the contributions from plasmonic resonances, periodicity, interference with waveguide modes and nearest-neighbor coupling between adjacent particles. To fully characterize this sample, we have used the powerful framework of Mueller matrices advanced by the differential decomposition formalism. We show that even in the presence of large complexity, the optical response can be easily disentangled by the presented method. The investigated sample is easily manufactured in a self-assembly process stirred by the

properties of the illuminating laser light during fabrication (Figure 3(a)). It consists of silver nanoparticles periodically arranged along curved lines, which are embedded in a TiO_2 waveguide. When light is impinging on the sample surface and reaches the nanoparticle layer, several phenomena occur. First the plasmonic resonance of the individual nanoparticles is excited, and part of the transmitted light is hence absorbed. The nanoparticles also serve as scattering elements for the incident light: part of the light is coupled to the waveguide modes via interaction with nanoparticles. On its turn, the waveguide modes are leaky modes and can be scattered by the presence of nanoparticles: this diffracted part of the leaky mode will interfere with the directly transmitted light. The result of this interference is the so-called "destructive interference mode". The destructive interference mode has a large influence on the optical response of the sample. Its signature is found both in intensity plots as well as in the phase, as attested by MM measurements. Moreover, it was discovered that such structures are characterized by a particular circular dichroism behavior (Figure 3(b)), which cannot be explained by the sole superposition of the linear optical properties. Whereas the linear circular dichroism is coming from the anisotropy of the sample, the true circular dichroism is due to the coupling between destructive interference mode and plasmonic modes as well as the nearest-neighbor coupling between plasmonic nanoparticles.

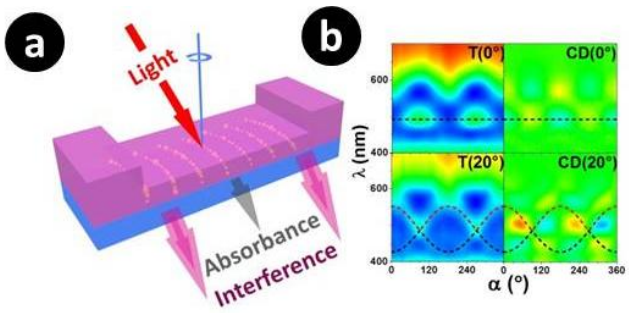

Figure 3: (a) Schematic of Ag nanoparticle array (b) Transmittance and circular dichroism at AOI 0° and 20° over the whole azimuthal angles from 0° to360°.

Chapter 1

Introduction

Micro-and nanostructures are nowadays very important in science and technology as they allow for a whole range of functionalities that either does not exist in nature or reproduce existing effects with a much smaller footprint and higher efficiency. Plasmonics which explores how electromagnetic fields can be confined to the order of micro-and nanometer is one way to use micro-and nanostructures in the field of photonics. Plasmonic modes can be propagating or localized. Surface plasmon polaritons (SPPs) are collective electron excitations coupled to the electromagnetic radiation propagating along metal-dielectric interfaces, evanescently confined in the perpendicular direction as shown in Figure 1. 1 [1]. Owing to their unique dispersion and strong field confinement, SPPs have attracted attention during the last decades and have promising applications in integrated optics [2], field enhancement [3], [4], sensing [5]–[7] and imaging [8]. Localized surface plasmons (LSPs) on the other hand are non-propagating excitations of the conduction electrons of metallic nanostructures coupled to the electromagnetic field (Figure 1. 1). It is well known that the LSPs depends on the size, shape, and material properties of the nanoparticle as well as of the surrounding medium [9].

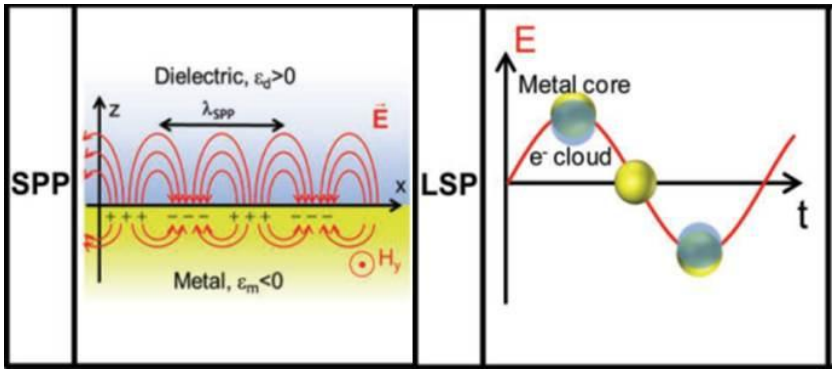

Figure 1. 1: (left) Sketch of charges oscillation and fields for a SPPs at a metal/dielectric interface; (right) Sketch of charges oscillation for a LSP in a metallic nanoparticle [10].

The interaction of complex plasmonic nanostructures, periodic or random, with polarized light creates very rich physics where scattering, diffraction and absorbance are linked to a variety of dispersive modes and coupling effects. Each of these excitations depends strongly on polarization, angle of incidence, azimuthal orientation of the sample and wavelength. The presence of these modes and coupling effects results in manifold interaction with polarized light. On the one hand the interplay of these interactions cannot be easily understood and on the other hand it opens up the possibility to tailor the optical response.

The complete optical response of complex samples can be measured by Mueller matrices at various k-vectors over a broad frequency range independently from any model. Mueller matrix spectroscopic ellipsometry (MMSE) is therefore a powerful and sensitive tool to fully

characterize complex plasmonic nanostructures. Even though MMSE is widely used in characterizing the optical properties of complex nanostructures, MMSE results in complex data hiding the underlying physics, making the physical interpretation of a measured Mueller matrix (MM) a big challenge. In principle it is of course possible to calculate the MMs for different angles of incidence, various azimuthal orientations and a broad range of frequencies by solving the Maxwell-equations under the specific boundary conditions. But this approach is on the one hand time-consuming and computer intensive and on the other hand it does not really promote the physical understanding of the origin of the observed optical behavior.

The goal of this project is to demonstrate on the example of two simple plasmonic nanostructures, that the optical response of these samples can be fully understood in the framework of MM ellipsometry. It is demonstrated that a systematic correlation of the observed polarization mixing in MMs to their underlying physical origin is a versatile analytical method suitable to all samples exhibiting both anisotropy and dispersive modes. Further, the applicability can be extended to a wide variety of samples whether anisotropic or not, presenting localized or propagating plasmonic resonances, photonic modes -whether originating from waveguiding or scattering- or other dispersive modes at the only condition that an analytical expression for the dispersion of these modes exists. To demonstrate the power of this method and its implementation, we apply it to two very simple examples: the one-dimensional plasmonic metallic grating and metallic nanoparticle arrays. These two examples are completely analyzed and solved and the results can in principle be used for new application.

One-dimensional gratings are very efficient tools to excite SPPs by matching their dispersion to that of light. When considering grating-based structures, it is well known that regular periodic nanostructures can show abrupt changes in the optical response, referred to as Rayleigh wood´s anomalies (RWAs) [11]. RWAs can result in very narrow plasmon resonances in regular plasmonic arrays of metallic nanoparticles, originating from the diffraction coupling of localized plasmons, or modify the reflectance of non-plasmonic metallic square arrays. Even though SPPs on metallic gratings have been studied for a long time and RWA effects have also been well known for decades, a clear understanding of how SPPs and RWAs influence the polarization mixing of gratings is still lacking.

Metallic nanoparticle arrays have been widely studied over the last decades. Their optical response depends not only on the individual particle, but also on their specific arrangement. The interplay of different contributions can lead to a complex optical response, where the influence of the different ingredients cannot be easily separated. On the other hand, however, this interplay has to be perfectly known, in order to tailor the optical response for any desired application. Numerous investigations describe the interplay between specific geometrical arrangements of nanoparticles and their optical response in different configurations where nanoparticles are ordered or randomly distributed, with different sizes and shapes. However, in the case of complex samples, where different optical – photonic or plasmonic – effects overlap and interact with each other, hitherto no clear procedure is readily available.

This work is organized as follows. For convenience of comparison, we first present a thorough characterization of one dimensional pure polydimethylsiloxane (PDMS) grating (Figure 1. 2(a)) via MMSE and atomic force microscopy. The comparison of the measured MM with calculations based on a Bruggeman biaxial layer model traces back the observed polarization mixing to pure anisotropy and RWAs.

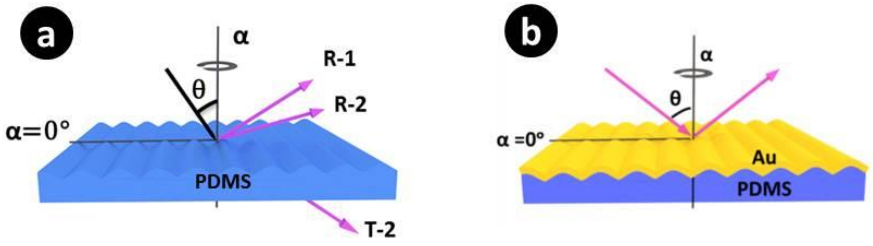

Figure 1. 2: Schematic of (a) pure PDMS grating and (b) Au gratings.

Subsequently, we focus on the one-dimensional plasmonic metallic grating which is fabricated by evaporating Au (Figure 1. 2(b)) or Au/Ni/Au thin film on PDMS grating. First of all, we compare both measured reflectance and full MM data obtained from a one-dimensional gold grating in a broad wavelength range, full azimuthal range and varied angles of incidence. The role of sample anisotropy, propagating SPPs, diffraction orders and material related absorbance is respectively identified by their different dispersion behavior and their interaction and coupling are highlighted. The comparison of the measured MM with calculations based on a simple biaxial layer traces back the observed polarization mixing to its physical origin. Second of all, we analyze the Au/Ni/Au grating in the similar approach with Au grating. The role of sample anisotropy, propagating SPPs and material related absorbance is respectively identified. Diffraction orders in Au/Ni/Au grating show very weak influence which is probably due to the big absorption inside the system by Ni. The ability of tuning plasmonic properties by mechanical stretching and the reversibility of this approach is discussed at the end of this section.

Finally, we focus on a metallic nanoparticle array (Figure 1. 3(a)) which is obtained by laser-induced self-assembly. We demonstrate how to decompose the optical response of a complex nanoparticle array in all details and full completeness. This enables us to identify the basic physical mechanisms for the different optical features observed. Starting with the azimuthal dependent transmitted intensity giving the anisotropic arrangement and the dependence on the angle of incidence (AOI) giving the dispersion due to a periodic arrangement of the nanoparticles a first simple model is developed. Comparing the measured Mueller-matrices with the simulated ones from the simple model and subsequently decomposing the Mueller-matrices into their basic optical properties allows us to explain the observed optical features to the specific excitations of the nanoparticles: simple localized surface plasmon resonances, birefringence due to anisotropic arrangement in lines, coupling between the lines, diffraction into waveguide modes or a broken symmetry leading to true circular dichroism (Figure 1. 3 (b)).

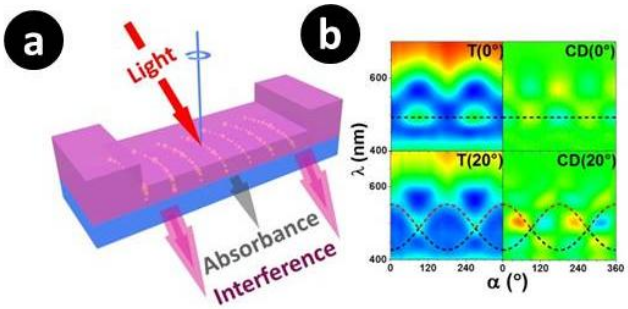

Figure 1. 3: (a) Schematic of Ag nanoparticle array (b) Transmittance and circular dichroism at AOI 0° and 20° over the whole azimuthal angles from 0° to360°.

Chapter 2

General Theory

2.1 Ellipsometry

2.1.1 Maxwell´s equation

Maxwell´s equations [12] are a set of differential equations that together with Lorentz force law are the foundation of classical electromagnetism, classical optics, and electric circuits. They describe how electric and magnetic fields are generated by charges, currents, and changes of each other, and how they are influenced by objects. The Maxwell´s equations in the free space in SI-units are:

Gauss´s law for electricity: $$\nabla \cdot \mathbf{D} = \rho \tag{2.1}$$

Gauss´s law for electricity: $$\nabla \cdot \mathbf{B} = 0 \tag{2.2}$$

Faraday´s law: $$\nabla \times \mathbf{E} = -\frac{\partial \mathbf{B}}{\partial t} \tag{2.3}$$

Ampere´s law: $$\nabla \times \mathbf{H} = \mathbf{J} + \frac{\partial \mathbf{D}}{\partial t} \tag{2.4}$$

where **E** and **H** are the electric and magnetic field respectively and **D** and **B** are the electric displacement field and the magnetic induction. The quantities ρ and **J** are the volume charge density and the electric current density.
The definitions of the auxiliary fields are:

$$\mathbf{D} = \varepsilon_0 \mathbf{E} + \mathbf{P} \tag{2.5}$$

$$\mathbf{H} = \frac{1}{\mu_0} \mathbf{B} - \mathbf{M} \tag{2.6}$$

where **P** is the polarization field and **M** is the magnetization field which are defined in terms of microscopic bound charges and bound currents respectively. ε_0 and μ_0 are the permittivity and permeability of free space. The equations specifying the dependence of the polarization **P** and the magnetization **M** on the applied electric and magnetic field are called constitutive relations. More generally, for linear materials the constitutive relations are:

$$\mathbf{D} = \varepsilon \varepsilon_0 \mathbf{E} \tag{2.7}$$

$$\mathbf{H}=\frac{1}{\mu\mu_0}\mathbf{B} \tag{2.8}$$

In a homogeneous isotropic medium, ε and μ known as relative permittivity and permeability of the material are related to the electric and magnetic polarization properties of the medium by the electric and magnetic susceptibilities χ_e and χ_m as follows:

$$\varepsilon=1+\chi_e \tag{2.9}$$

$$\mu=1+\chi_m \tag{2.10}$$

The relative permittivity is a complex value described as:

$$\varepsilon(\omega)=\boldsymbol{\varepsilon_1}(\omega)+i\boldsymbol{\varepsilon_2}(\omega) \tag{2.11}$$

where ω shows frequency dependence of the permittivity.

2.1.2 Polarization states

Maxwell's equations for a no charges and no currents region appear as follows:

$$\nabla\cdot\vec{\mathbf{E}}=0 \tag{2.12}$$

$$\nabla\cdot\vec{\mathbf{B}}=0 \tag{2.13}$$

$$\nabla\times\vec{\mathbf{E}}+\frac{\partial\vec{\mathbf{B}}}{\partial t}=0 \tag{2.14}$$

$$\nabla\times\vec{\mathbf{B}}-\frac{\varepsilon}{\boldsymbol{c^2}}\frac{\partial\vec{\mathbf{E}}}{\partial t}=0 \tag{2.15}$$

We can obtain the wave equation for the electric field by taking the curl of the curl equations, and using the curl of the curl identity $\nabla\times(\nabla\times\mathbf{X})=\nabla(\nabla\cdot\mathbf{X})-\nabla^2\mathbf{X}$

$$\nabla^2\vec{\mathbf{E}}-\frac{\varepsilon}{c^2}\frac{\partial^2\vec{\mathbf{E}}}{\partial^2 t}=0 \tag{2.16}$$

Electromagnetic plane wave is one of the solutions of the electric field wave equation:

$$\mathbf{E}=\mathbf{E_0}\exp\left[i(\omega t-kz+\delta)\right] \tag{2.17}$$

where $\mathbf{E_0}$ is a complex vector indicating the amplitude and polarization state of the wave. ω is the angular frequency, k is wave number and δ is the initial phase.

Polarization states are usually only defined in terms of the direction and phase of the vector of electric filed. We can describe the polarization state of light traveling along z direction by vector sum of electric field components along two orthogonal axes x and y:

$$\mathbf{E}(z,t)=\mathbf{E_x}(z,t)+\mathbf{E_y}(z,t)=\{E_{x0}\exp[i(\omega t-k_z+\delta_x)]\}\mathbf{x}+\{E_{y0}\exp[i(\omega t-k_z+\delta_y)]\}\mathbf{y} \quad (2.18)$$

where x and y are unit vectors along x and y directions.

The polarization state of a light beam refers to the path of electric field traces at a fixed position as the light propagates. In the description of the polarization states, only the relative phase difference δ_y-δ_x is important and taken into account. Polarization states are classified as three types in Figure 2. 1: linear, circular and elliptical states. Linear polarization is defined when two component waves in x and y directions are in phase (δ_y-δ_x=0). Circular polarization is defined when E_{x0} and E_{y0} are equal in magnitude but are 90° out of phase (δ_y-δ_x=±90°). In general cases, the polarization states are elliptical polarizations.

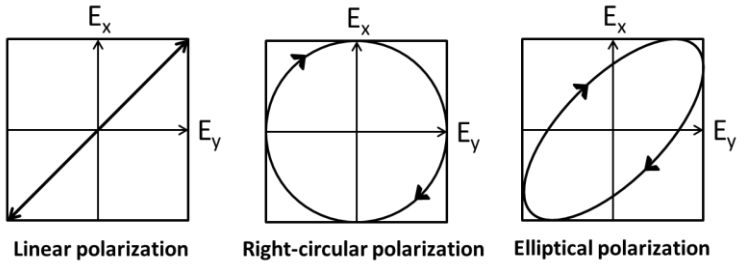

Figure 2. 1: Representation of linear, right-circular and elliptical polarizations.

2.1.3 Jones vector

The Jones vector is defined by superimposing the two electric field vectors in the x and y directions. Jones vector can describe all totally polarized states including linear and elliptical polarizations. Therefore, the Jones matrix is used to mathematically describe ellipsometry measurement. If we use Eq. (2.18), the Jones vector is given by

$$\mathbf{E}(z,t)=\begin{bmatrix}E_{x0}\exp\{i(\omega t-Kz+\delta_x)\}\\ E_{y0}\exp\{i(\omega t-Kz+\delta_y)\}\end{bmatrix}=\exp\{i(\omega t-Kz)\}\begin{bmatrix}E_{x0}\exp(i\delta_x)\\ E_{y0}\exp(i\delta_y)\end{bmatrix} \quad (2.19)$$

By omitting the term $\exp\{i(\omega t-kz)\}$ and using the phase difference (δ_x-δ_y), we can simplify the equation to

$$\mathbf{E}(z,t)=\begin{bmatrix}E_x\\ E_y\end{bmatrix}=\begin{bmatrix}|E_x|\exp[i(\delta_x-\delta_y)]\\ |E_y|\end{bmatrix} \quad (2.20)$$

In ellipsometry measurement, only relative changes in amplitude and phase are taken into account. So, we express the Jones vector by the normalized light intensity (I=1). The linearly polarized light parallel to the x and y directions are expressed by

$$\mathbf{E}_{\text{linear,x}}=\begin{bmatrix}1\\0\end{bmatrix} \qquad \mathbf{E}_{\text{linear,y}}=\begin{bmatrix}0\\1\end{bmatrix} \tag{2.21}$$

The right-circular polarized light and left-circular polarized light are described by

$$\mathbf{E}_{\text{R}}=\frac{1}{\sqrt{2}}\begin{bmatrix}1\\\text{i}\end{bmatrix} \qquad \mathbf{E}_{\text{L}}=\frac{1}{\sqrt{2}}\begin{bmatrix}1\\\text{-i}\end{bmatrix} \tag{2.22}$$

Optical elements along the light path in the ellipsometry measurement can be described by Jones matrix to analyze the transformation of polarization states. The Jones matrices for a polarizer (**P**) and an analyzer (**A**) in the case when the transmission axis is parallel to the x axis are expressed by

$$\mathbf{P}=\mathbf{A}=\begin{bmatrix}1 & 0\\0 & 0\end{bmatrix} \tag{2.23}$$

The Jones matrix for a compensator when the fast axis is parallel to the x axis is expressed by

$$\mathbf{C}=\begin{bmatrix}1 & 0\\0 & \exp(\text{-i}\delta)\end{bmatrix} \tag{2.24}$$

In general cases, a polarizer or compensator is not installed with axes along x or y axis. However, we can simplify the equations by rotating the coordinate systems. The rotation matrices are:

$$\mathbf{R}(\alpha)=\begin{bmatrix}\cos(\alpha) & \sin(\alpha)\\\text{-}\sin(\alpha) & \cos(\alpha)\end{bmatrix} \qquad \mathbf{R}(\text{-}\alpha)=\begin{bmatrix}\cos(\alpha) & \text{-}\sin(\alpha)\\\sin(\alpha) & \cos(\alpha)\end{bmatrix} \tag{2.25}$$

The above R(-α) and R(α) correspond to the matrices when the coordinate system is rotated clockwise and anti-clockwise, respectively.

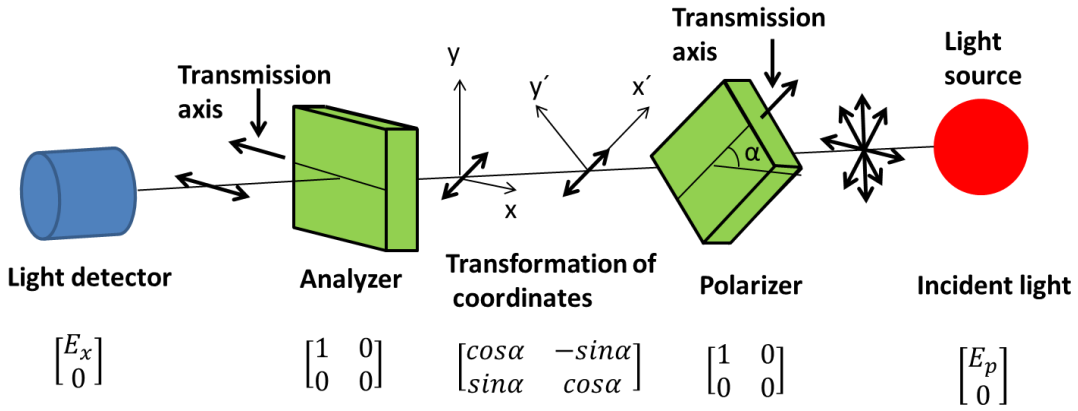

Figure 2. 2: Representation of an optical instrument by Jones matrices [13].

Figure 2. 2 shows a simple example of using Jones matrices to describe an optical instrument. The measured intensity can be easily obtained by multiplying the Jones matrices of every element consequently along light path.

$$\begin{bmatrix} E_x \\ E_y \end{bmatrix} = \begin{bmatrix} 1 & 0 \\ 0 & 0 \end{bmatrix} \begin{bmatrix} \cos\alpha & -\sin\alpha \\ \sin\alpha & \cos\alpha \end{bmatrix} \begin{bmatrix} 1 & 0 \\ 0 & 0 \end{bmatrix} \begin{bmatrix} E_p \\ 0 \end{bmatrix} = \begin{bmatrix} E_p \cos\alpha \\ 0 \end{bmatrix} \tag{2.26}$$

So we obtain the measured light intensity:

$$I = |E_x|^2 = |E_p|^2 \cos^2\alpha \tag{2.27}$$

This above result is known as Malus´s law.
Jones matrix can also be used to describe a sample (**S**). If a sample is isotropic and not too rough, then off-diagonal elements in the sample Jones matrix are zero:

$$\boldsymbol{S} = \begin{bmatrix} \vec{r}_p & 0 \\ 0 & \vec{r}_s \end{bmatrix} \tag{2.28}$$

where $\vec{r}_p$ and $\vec{r}_s$ are the complex Fresnel reflection coefficients for the p- and s-polarized light, respectively. If a sample is anisotropic, then the sample Jones matrix will probably have off-diagonal elements:

$$\boldsymbol{S} = \begin{bmatrix} \vec{r}_{pp} & \vec{r}_{ps} \\ \vec{r}_{sp} & \vec{r}_{ss} \end{bmatrix} \tag{2.29}$$

2.1.4 Reflectance and Transmittance

Figure 2. 3 shows light reflection and transmission of p- and s- polarized light on an interface between two media. The plane of incidence is defined as the plane which contains the surface normal and the wave vector of the incoming radiation. The oscillatory direction of electric field of p-polarized light is in the plane of incidence, while the oscillatory direction of electric field of s-polarized light is perpendicular to the plane of incidence. p- and s-polarized lights can interact quite differently with the sample. The reflectance is defined as the ratio of reflected light intensity I_r to incident light intensity I_i. The reflectance for p- and s-polarized light is expressed by

$$R_p = \frac{I_{rp}}{I_{ip}} = \left|\frac{E_{rp}}{E_{ip}}\right|^2 = |r_p|^2 \qquad R_s = \frac{I_{rs}}{I_{is}} = \left|\frac{E_{rs}}{E_{is}}\right|^2 = |r_s|^2 . \tag{2.30}$$

The transmittances for p- and s-polarized light are given by the following equations:

$$T_p = \left(\frac{N_2 \cos\theta_2}{N_1 \cos\theta_1}\right) |t_p|^2 \qquad T_s = \left(\frac{N_2 \cos\theta_2}{N_1 \cos\theta_1}\right) |t_s|^2 . \tag{2.32}$$

where N_1 and N_2 are the complex refractive indexes of the upper and lower medium respectively and θ_1 and θ_2 are AOI and angle of transmission. r_p,r_s, t_p and t_s are Fresnel coefficients and obtained by solving Maxwell´s equations under interface boundary conditions. The equations for r_p, r_s, t_p and t_s are known as Fresnel equations:

$$r_p = \frac{N_2\cos\theta_1 - N_1\cos\theta_1}{N_2\cos\theta_1 + N_1\cos\theta_2} \qquad r_s = \frac{N_1\cos\theta_1 - N_2\cos\theta_2}{N_1\cos\theta_1 + N_2\cos\theta_2}. \tag{2.31}$$

$$t_p = \frac{E_{tp}}{E_{ip}} = \frac{2N_1\cos\theta_1}{N_2\cos\theta_1 + N_1\cos\theta_2} \qquad t_s = \frac{E_{ts}}{E_{is}} = \frac{2N_1\cos\theta_1}{N_1\cos\theta_1 + N_2\cos\theta_2}. \tag{2.33}$$

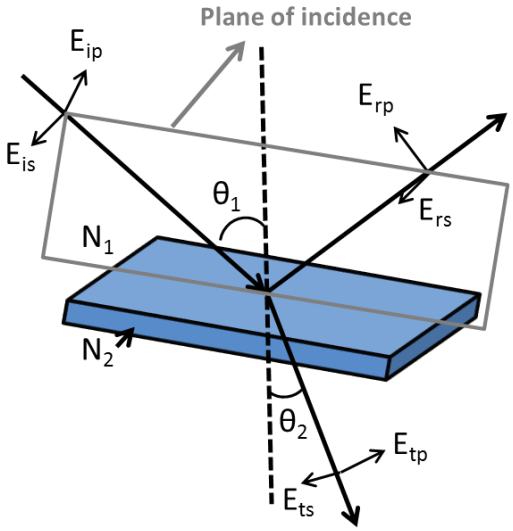

Figure 2. 3: Electric field E for p- and s-polarization reflected and transmitted by an interface between two media with refractive indexes N_1 and N_2. The AOI and angle of transmission are θ_1 and θ_2 [14].

2.1.5 Ellipsometry

The amplitude reflection coefficients for p- and s-polarizations differ significantly due to the difference in electric dipole radiation. Therefore, after interaction with the sample, the incoming linearly polarized light often becomes elliptically polarized light as shown in Figure 2. 4. Ellipsometry measures the change in polarization state of light reflected from (or transmitted through) the surface of a sample. The change in polarization state is commonly characterized by the two ellipsometric angles Ψ and Δ as Eq (2.34).

$$\rho = \tan\Psi \exp(i\Delta) = \frac{r_p}{r_s} \tag{2.34}$$

where r_p and r_s are the Fresnel reflection coefficients for p- and s-polarized light, respectively. $\tan\Psi$ is the magnitude of the reflectivity ratio, and Δ is the phase difference. Ellipsometric

measurement has advantages over simple intensity-based reflection or transmission measurements in terms of the high accuracy, precision, and sensitivity, making it highly suited for applications in thin film metrology [15].

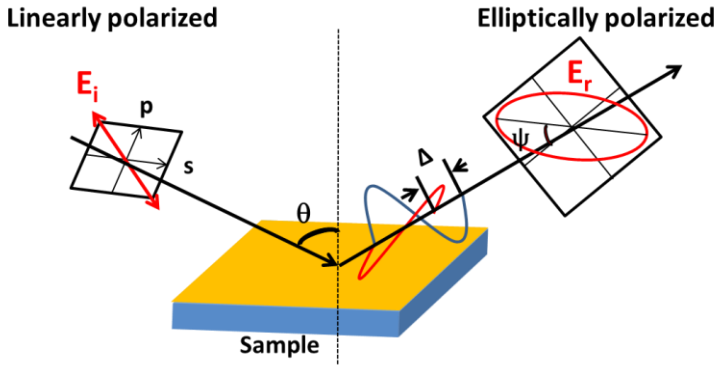

Figure 2. 4: Measurement principle of spectroscopic ellipsometry.

The measured quantities (Ψ, Δ) are not directly measured parameters of interest (thicknesses, optical constants, etc.) rather they are a function of them. It is then necessary to solve the inverse problem by modeling. This model should contain both known parameters and unknown physical parameters. We can vary the unknown physical parameters in the model, and generate data until a set of optimized parameters are found and can yield calculated data that closely match the measured optical data. The Levenberg-Marquardt multivariate regression algorithm is employed for the fitting process. Overall, the four steps of the whole optical experiment procedure are illustrated in Figure 2. 5 below [16].

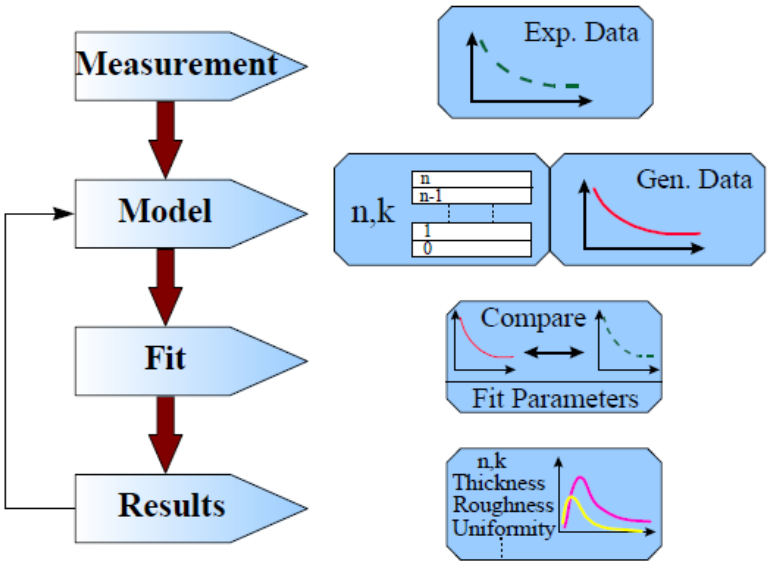

Figure 2. 5: General procedure used in ellipsometry measurements to determine material properties [16].

2.1.6 Dielectric function Models

There are many dielectric function models available for us to select in the data analysis of spectroscopic ellipsometry. The appropriate dielectric function models are chosen according to the optical properties of the sample.

The Lorentz Oscillator Model

The Lorentz oscillator model is a classical physical model used to describe the dielectric function in the visible/UV region arise from the response of bound charges to the applied electric fields. The electron and atomic nucleus are bound similar to a mass-spring system and follows Hooke´s law. The applied electric field causes the motion of the electrons as oscillating in a viscous fluid. According to Newton's second law, the equation of motion can be expressed as [13]:

$$m\frac{\mathrm{d}^2\vec{r}}{\mathrm{d}t^2}+m\Gamma_0\frac{\mathrm{d}\vec{r}}{\mathrm{d}t}+m\omega_0^2\vec{r}=-e\vec{E}_0\exp(\mathrm{i}\omega t) \tag{2.35}$$

where m and e are the mass and the charge of the free electron and $\vec{\mathrm{r}}$ is the displacement, $\vec{\mathrm{E}}_0\exp(\mathrm{i}\omega\mathrm{t})$ is the applied electric field, md^2r/dt^2 is the acceleration force, $m\omega_0^2\boldsymbol{r}$ is the Hooke´s force, where ω_0 is the resonant frequency of the oscillator. $m\Gamma_0\frac{\boldsymbol{dr}}{\boldsymbol{dt}}$ is the viscous force. $\Gamma_0=1/\tau$ is the damping factor which describes the damping due to scattering, where τ is the mean time an electron travels between two collisions. The electron oscillates at the same frequency as the applied electric field (i.e.$\exp(i\omega t)$). Thus, if we assume the solution can be described by the form $\mathrm{x(t)}=a\exp(i\omega t)$, we can get the description of a as follows:

$$a=-\frac{eE_0}{m}\frac{1}{(\omega_0^2-\omega^2)+\mathrm{i}\Gamma\omega} \tag{2.36}$$

The dielectric polarization is expressed as $P=-eN_ex(t)$, where N_e is the number of electrons per unit volume. So we obtain the dielectric function ε as follows:

$$\varepsilon=1+\frac{e^2N_\mathrm{e}}{\varepsilon_0 m}\frac{1}{(\omega_0^2-\omega^2)+\mathrm{i}\Gamma\omega} \tag{2.37}$$

This dielectric function is the Lorentz oscillator model. We can obtain the real and imaginary part of this complex dielectric function as:

$$\varepsilon_1=1+\frac{e^2N_\mathrm{e}}{\varepsilon_0 m}\frac{(\omega_0^2-\omega^2)}{(\omega_0^2-\omega^2)^2+\Gamma^2\omega^2} \tag{2.38}$$

$$\varepsilon_2=\frac{e^2N_\mathrm{e}}{\varepsilon_0 m}\frac{\Gamma\omega}{(\omega_0^2-\omega^2)^2+\Gamma^2\omega^2} \tag{2.39}$$

In actual ellipsometry data analysis, Lorentz model is expressed using photon energy as follows [16]:

$$\varepsilon(E)=\varepsilon_1+\mathrm{i}\varepsilon_2=1+\sum_{\mathrm{k}}\frac{A_{\mathrm{k}}}{E_{\mathrm{k}}^2-E^2-\mathrm{i}B_{\mathrm{k}}E} \tag{2.40}$$

where A_{k} is the amplitude, E_{k} is the center energy, and B_{k} is the broadening of the k^{th} oscillator, E is the photon energy in eV.

The Drude Oscillator Model

The Drude oscillator model [17] is based on the kinetic theory of electrons in a metal which assumes that the material has a mass of motionless positively charged ions detached from an electron gas with neglecting electron-electron interaction. It was constructed in order to explain the transport behavior of free electrons in metals and free carriers in semiconductors. Drude oscillator is a special case of the Lorentz oscillator model having no restoring force and resonance frequency. The motion equation is:

$$m\frac{\mathrm{d}^2\vec{r}}{\mathrm{d}t^2}+m\Gamma_0\frac{\mathrm{d}\vec{r}}{\mathrm{d}t}=-e\vec{E}_0\exp(\mathrm{i}\omega t) \tag{2.41}$$

By solving the motion equation, we obtain ε as:

$$\varepsilon=1-\frac{e^2N_{\mathrm{e}}}{\varepsilon_0 m}\frac{1}{\omega^2-\mathrm{i}\Gamma\omega}=1-\frac{\omega_{\mathrm{p}}^2}{\omega^2-\mathrm{i}\Gamma\omega} \tag{2.42}$$

where $\omega_{\mathrm{p}}=(\frac{e^2N_{\mathrm{e}}}{\varepsilon_0\varepsilon_\infty m^*})^{1/2}$ is the plasma frequency of the material. In the case of semiconductors, ω_{p} is located in the infrared region, while ω_{p} is in the visible/UV region in metals. The real part and imaginary part of dielectric function are:

$$\varepsilon_1=1-\frac{\omega_{\mathrm{p}}^2}{\omega^2+\Gamma^2} \tag{2.43}$$

$$\varepsilon_2=\frac{\omega_{\mathrm{p}}^2\Gamma}{\omega(\omega^2+\Gamma^2)} \tag{2.44}$$

The Cauchy Oscillator Model

The Cauchy model [18] corresponds to the spectral region where $k\sim0$ in the Lorentz model. By assuming $\Gamma\to0$ at $\omega\ll\omega_0$ and using $\omega/c=2\pi/\lambda$, we obtain

$$\varepsilon=\varepsilon_1=1+\frac{e^2N_{\mathrm{e}}}{\varepsilon_0 m(2\pi c)^2}\frac{\lambda_0^2\lambda^2}{\lambda^2-\lambda_0^2} \tag{2.45}$$

Cauchy oscillator model is then obtained from the series expansion of equation 2.45 and given by:

$$n = A + \frac{B}{\lambda^2} + \frac{C}{\lambda^4} + \cdots \qquad K = 0 \tag{2.46}$$

Cauchy oscillator model works best when materials are transparent and it may be regarded as an approximation of the low-energy tail of oscillators in the UV far away from the energy range of the instrument. Different from Lorentz and Drude oscillator models, the relation between n and k are not Kramers-Kronig consistent.

2.2 Mueller Matrix

Although the Jones vector describes polarized light and Jones matrix provides an elegant method to describe the interaction between optical elements and polarized light, unpolarized or partially polarized light cannot be expressed by Jones vector. Therefore, Stokes vectors are used in order to describe all types of polarized light. The Stokes parameters are defined as [13]:

$$S_0 = I_x + I_y \tag{2.47a}$$

$$S_1 = I_x - I_y \tag{2.47b}$$

$$S_2 = I_{+45^\circ} - I_{-45^\circ} \tag{2.47c}$$

$$S_3 = I_R - I_L \tag{2.47d}$$

Here S_0 is the total intensity of light, S_1 shows the light intensity determined by subtracting the light intensity of linear polarization in the y direction from that in x direction, S_2 shows the light intensity obtained by subtracting the light intensity of linear polarization at -45° from that at +45°, S_3 represents the light intensity of left-circular polarized light subtracted from that of right-circular polarized light. Conventionally the x- and y-directions correspond to the directions of s- and p- polarized light. In other words parameters $S_{1\text{-}3}$ represent relative intensity difference of each state of polarization which can be described by four Stokes parameters or a Stokes vector: $\boldsymbol{S} = [S_0, S_1, S_2, S_3]$.

The Stokes parameters are real quantities and can be measured experimentally. Once light is reflected or transmitted by a sample it can generally change its initial polarization state from $\mathbf{S}_{in}$ to $\mathbf{S}_{out}$. The transformation of the Stokes vector is described by a 4x4 matrix called Mueller matrix M:

$$\mathbf{S}_{out} = \mathbf{M} \cdot \mathbf{S}_{in} = \begin{bmatrix} M11 & M12 & M13 & M14 \\ M21 & M22 & M23 & M24 \\ M31 & M32 & M33 & M34 \\ M41 & M42 & M43 & M44 \end{bmatrix} \cdot \mathbf{S}_{in} \tag{2.48}$$

Although the Stokes vector are traditionally numbered from 0 to 3, for sake of convenience, the MM elements are numbered from 1 to 4.

For a non-depolarizing sample, MM is also called Mueller-Jones matrix. In this case, the MM elements can be derived from complex 2x2 Jones matrix as follows [19]:

$$M11=\frac{1}{2}\left(|r_{pp}|^2+|r_{sp}|^2+|r_{ps}|^2+|r_{ss}|^2\right) \quad (2.49a)$$

$$M12=\frac{1}{2}\left(|r_{pp}|^2+|r_{sp}|^2-|r_{ps}|^2-|r_{ss}|^2\right) \quad (2.49b)$$

$$M13=\mathrm{Re}\left(r_{pp}r_{ps}^*+r_{sp}r_{ss}^*\right) \quad (2.49c)$$

$$M14=\mathrm{Im}\left(r_{pp}r_{ps}^*+r_{sp}r_{ss}^*\right) \quad (2.49d)$$

$$M21=\frac{1}{2}\left(|r_{pp}|^2-|r_{sp}|^2+|r_{ps}|^2-|r_{ss}|^2\right) \quad (2.49e)$$

$$M22=\frac{1}{2}\left(|r_{pp}|^2-|r_{sp}|^2-|r_{ps}|^2+|r_{ss}|^2\right) \quad (2.49f)$$

$$M23=\mathrm{Re}\left(r_{pp}r_{ps}^*-r_{sp}r_{ss}^*\right) \quad (2.49g)$$

$$M24=\mathrm{Im}\left(r_{pp}r_{ps}^*-r_{sp}r_{ss}^*\right) \quad (2.49h)$$

$$M31=\mathrm{Re}\left(r_{pp}r_{sp}^*+r_{ps}r_{ss}^*\right) \quad (2.49i)$$

$$M32=\mathrm{Re}\left(r_{pp}r_{sp}^*-r_{ps}r_{ss}^*\right) \quad (2.49j)$$

$$M33=\mathrm{Re}\left(r_{pp}r_{ss}^*+r_{ps}r_{sp}^*\right) \quad (2.49k)$$

$$M34=\mathrm{Im}\left(r_{pp}r_{ss}^*-r_{ps}r_{sp}^*\right) \quad (2.49l)$$

$$M41=-\mathrm{Im}\left(r_{pp}r_{sp}^*+r_{ps}r_{ss}^*\right) \quad (2.49m)$$

$$M42=-\mathrm{Im}\left(r_{pp}r_{sp}^*-r_{ps}r_{ss}^*\right) \quad (2.49n)$$

$$M43=-\mathrm{Im}\left(r_{pp}r_{ss}^*+r_{ps}r_{sp}^*\right) \quad (2.49o)$$

$$M44=\mathrm{Re}\left(r_{pp}r_{ss}^*-r_{ps}r_{sp}^*\right) \quad (2.49p)$$

All MM elements are conventionally normalized to the *M*11 element which represents total reflected/transmitted intensity. The off-block-diagonal sub-matrices $\begin{bmatrix} M13 & M14 \\ M23 & M24 \end{bmatrix}$ and $\begin{bmatrix} M31 & M32 \\ M41 & M42 \end{bmatrix}$ represent polarization conversion effects. MM of a sample gives complete information about polarization properties of a sample under study therefore MM is a powerful and sensitive tool to fully characterize anisotropy and depolarization of samples, which cannot be achieved by simple intensity measurements. Mueller matrix spectroscopic ellipsometry (MMSE) has been applied in different fields for example, depolarization [20], [21], metrology [22], [23], plasmonic nanomaterials [24]–[29] as well as magnetic or biological materials [30], [31]. In

particular it is a powerful method to characterize optical nanostructures, such as for instance plasmonic meanders for polarization control and depolarizers [27], [29], and reveal their optical properties.

2.3 Mueller Matrix decomposition

Even though MM is a powerful tool to fully characterization, the interpretation of the hidden physical effects in MM is a challenge. MM is normally reduced to Jones Matrix in order to obtain the physical interpretation of the measured MM in terms of optical anisotropy [32]. However, not all MM can be deduced to Jones matrix due to depolarization effects. Therefore, various decomposition methods are built and used to determine the physics behind the depolarizing MM.

2.3.1 Product decomposition

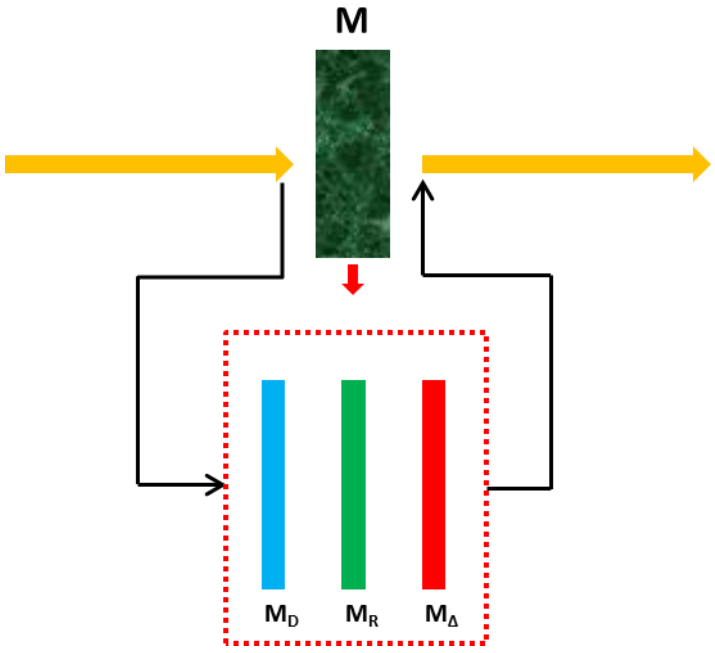

Figure 2. 6: Schematic of product decomposition.

As shown in Figure 2. 6, an arbitrary depolarizing MM M can be decomposed into the product of a diattenuator $\mathbf{M}_D$, a retarder $\mathbf{M}_R$ and a depolarizer $\mathbf{M}_\Delta$ in sequence as [33]

$$\mathbf{M}=\mathbf{M}_\Delta\mathbf{M}_R\mathbf{M}_D \tag{2.50}$$

Diattenuator is the optical component only changes the amplitude of the incoming electric field, while retarder is the optical component only changes the phase. Polarizer and wave plate are simple examples of diattenuator and retarder. The diattenuator MM $\mathbf{M}_D$ is completely constructed from the first row of M as

$$\mathbf{M}_{\mathrm{D}} = T_u \begin{bmatrix} 1 & \boldsymbol{D}^T \\ \boldsymbol{D} & \mathbf{m}_D \end{bmatrix}, \tag{2.51}$$

$$\mathbf{m}_{\mathrm{D}} = \sqrt{1-D^2}\,\mathbf{I} + \left(1-\sqrt{1-D^2}\right)\frac{\boldsymbol{D}}{|\boldsymbol{D}|}\left(\frac{\boldsymbol{D}}{|\boldsymbol{D}|}\right)^T, \tag{2.52}$$

$$\boldsymbol{D} = \frac{1}{m_{00}}\begin{pmatrix} m_{01} \\ m_{02} \\ m_{03} \end{pmatrix},\ T_u = m_{00} \tag{2.53}$$

where $\boldsymbol{D}$ is the diattenuation vector, $\mathbf{I}$ is the 3x3 identity matrix and T_u is the transmittance for unpolarized light.
The depolarizer is defined as

$$\mathbf{M}_{\Delta} = \begin{bmatrix} 1 & \mathbf{0}^T \\ \boldsymbol{P}_{\Delta} & \mathbf{m}_{\Delta} \end{bmatrix}, \tag{2.54}$$

with $\boldsymbol{P}_{\Delta}$ and $\mathbf{m}_{\boldsymbol{\Delta}}$ given by

$$\boldsymbol{P}_{\Delta} = \frac{\boldsymbol{P} - m\boldsymbol{D}}{1-D^2},\ \boldsymbol{P} = \frac{1}{m_{00}}\begin{pmatrix} m_{10} \\ m_{20} \\ m_{30} \end{pmatrix} \tag{2.55}$$

$$\mathbf{m}_{\Delta} = \pm\left[\mathbf{m}'(\mathbf{m}')^{\mathrm{T}} + \left(\sqrt{\lambda_1\lambda_2} + \sqrt{\lambda_2\lambda_3} + \sqrt{\lambda_3\lambda_1}\right)\mathbf{I}\right]^{-1} \times \left[\left(\sqrt{\lambda_1} + \sqrt{\lambda_2} + \sqrt{\lambda_3}\right)\mathbf{m}'\left(\mathbf{m}'\right)^{\mathrm{T}} + \sqrt{\lambda_1\lambda_2\lambda_3}\,\mathbf{I}\right]. \tag{2.56}$$

where $\boldsymbol{P}$ is the polarizance vector, $\mathbf{m}'$ is the 3x3 sub-matrix of the matrix $\mathbf{M}' = \mathbf{M}\mathbf{M}_{\mathrm{D}}^{-1}$ and $\lambda_1, \lambda_2, \lambda_3$ are the eigenvalues of $\mathbf{m}'$.Then, finally $\mathbf{M}_{\mathbf{R}}$ is calculated as

$$\mathbf{M}_{\mathrm{R}} = \mathbf{M}_{\Delta}^{-1}\mathbf{M}\mathbf{M}_{\mathrm{D}}^{-1} \tag{2.57}$$

2.3.2 Cloude decomposition

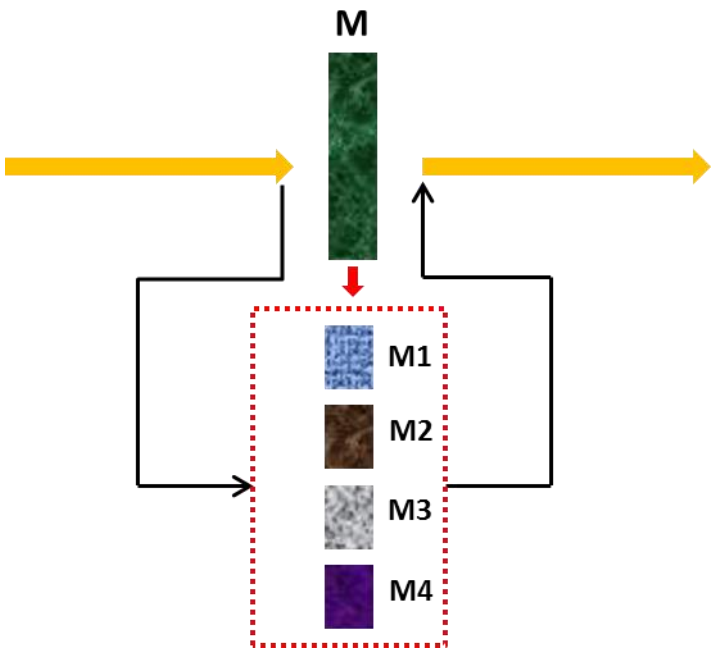

Figure 2. 7: Schematic of Cloude decomposition.

Cloude pointed out that any depolarizing MM can be represented by a linear combination of up to four non-depolarizing matrices [34]

$$\mathbf{M}=\lambda_1\mathbf{M}_1+\lambda_2\mathbf{M}_2+\lambda_3\mathbf{M}_3+\lambda_4\mathbf{M}_4, \qquad \sum_{i=1}^{4}\lambda_i=1, \quad \lambda_i\geq 0. \tag{2.58}$$

The coefficients λ_i are the four real eigenvalues of the so called 4 x 4 Hermitian covariance matrix **C** of **M**. From convention, these are sorted according to the order $\lambda_1>\lambda_2>\lambda_3>\lambda_4$. The physical image for the Cloude decomposition is that the medium is not homogeneous in the direction perpendicular to the light propagation. The sample can be regarded as separated areas with different **M** which are pure Mueller-Jones matrices [35]. Various partial beams of the incident light thus have different interactions. This incoherent manner results in depolarized **M**. This is shown schematically in Figure 2. 7.

The Hermitian covariance matrix **C** is constructed from **M** by the following linear operation

$$\mathbf{C}=\sum_{i,j}\mathrm{M}_{ij}\left(\sigma_i\otimes\sigma_j^{*}\right) \tag{2.59}$$

where the $\boldsymbol{\sigma_i}$ are Pauli spin matrices given by

$$\sigma_1=\begin{bmatrix}1 & 0\\ 0 & 1\end{bmatrix}\ \sigma_2=\begin{bmatrix}1 & 0\\ 0 & -1\end{bmatrix}\ \sigma_3=\begin{bmatrix}0 & 1\\ 1 & 0\end{bmatrix}\ \sigma_4=\begin{bmatrix}0 & i\\ -i & 0\end{bmatrix} \tag{2.60}$$

Let λ_i and $\mathbf{e}_i$ be the eigenvalues and normalized eigenvectors of $\mathbf{C}$, respectively. The covariance matrices $\mathbf{C}_i$ of the non-depolarizing component $\mathbf{M}_i$ are then found from

$$\mathbf{C}_i=\mathbf{e}_i\mathbf{e}_i^{\dagger} \qquad i=(1, 2, 3, 4) \tag{2.61}$$

where † stands for the Hermitian conjugate. Once $\mathbf{C}_i$ in Eq. (2.61) is found, $\mathbf{M}_i$ are finally obtained by inverting Eq. (2.59).

2.3.3 Differential decomposition

With a given light path in an optical system, there are eight effects namely, mean absorption k, mean refraction η, linear birefringence LB and LB´ (along x-y and ±45° axes, respectively), linear dichroism LD and LD´(along x-y and ±45° axes, respectively), circular birefringence CB and circular dichroism CD, can be measured. The definition of these effects are presented in Table 2.1 [36], where n is refractive index; κ is extinction coefficient; l is the path length through the medium; λ_0 is vacuum wavelength of light; the polarization of light is specified with subscripts x, y, 45° and 135° for linear polarized light and +,- for right circular and left circular polarized light. By using differential decomposition formalism as follows, LB and LB´, LD and LD´, CB and CD can be retrieved.

Table 2.1: Definition of symbols [36]

Effect	Symbol	Definition
Isotropic phase retardation	η	$2\pi nl/\lambda_0$
Isotropic amplitude absorption	k	$2\pi\kappa l/\lambda_0$
(x-y) linear dichroism	LD	$2\pi(\kappa_x-\kappa_y)l/\lambda_0$
(x-y) linear birefringence	LB	$2\pi(n_x-n_y)l/\lambda_0$
45° linear dichroism	LD´	$2\pi(\kappa_{45}-\kappa_{135})l/\lambda_0$
45° linear birefringence	LB´	$2\pi(n_{45}-n_{135})l/\lambda_0$
Circular dichroism	CD	$2\pi(\kappa_--\kappa_+)l/\lambda_0$
Circular birefringence	CB	$2\pi(n_--n_+)l/\lambda_0$

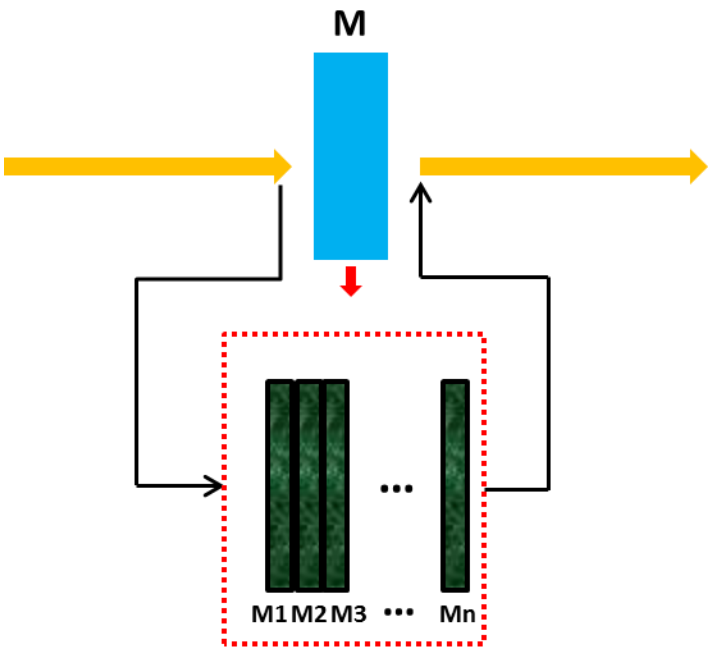

Figure 2. 8: Schematic of differential decomposition.

Figure 2. 8 shows the schematic of differential decomposition. The differential MM, **m**, relates to the MM, **M**, as the following propagation equation [37]–[39]:

$$\frac{d\mathbf{M}}{dz} = \mathbf{mM} \tag{2.62}$$

where **M** and **m** are the MM and differential MM of the medium at the position z. If m does not depend on z, i.e., the sample is uniform in the direction of light propagation, then the solution of this differential equation is obtained by taking the logarithm of **M**. If **L**=ln **M**, then **L** is the accumulated differential matrix: **L**=**m***l*, where *l* is the sample thickness.
The matrix **L** can further decomposed as $\mathbf{L}=\mathbf{L_m}+\mathbf{L_u}$. $\mathbf{L_m}$ and $\mathbf{L_u}$ can be written as:

$$\mathbf{L_m} = \frac{1}{2}(\mathbf{L} - \mathbf{GL^TG}) = \begin{bmatrix} 0 & \mathrm{LD} & \mathrm{LD}' & \mathrm{CD} \\ \mathrm{LD} & 0 & \mathrm{CB} & -\mathrm{LB}' \\ \mathrm{LD}' & -\mathrm{CB} & 0 & \mathrm{LB} \\ \mathrm{CD} & \mathrm{LB}' & -\mathrm{LB} & 0 \end{bmatrix} \tag{2.63}$$

$$\mathbf{L_u} = \frac{1}{2}(\mathbf{L} + \mathbf{GL^TG}) = \begin{bmatrix} \mathrm{A} & \Delta p_1 & \Delta p_2 & \Delta p_3 \\ -\Delta p_1 & \mathrm{A}-\mathrm{LDP} & \Delta p_4 & \Delta p_5 \\ -\Delta p_2 & \Delta p_4 & \mathrm{A}-\mathrm{LDP}' & \Delta p_6 \\ -\Delta p_3 & \Delta p_5 & \Delta p_6 & \mathrm{A}-\mathrm{CDP} \end{bmatrix} \tag{2.64}$$

G is the Minkowski metric and expressed as **G**=diag(1,-1,-1,-1). $\mathbf{L_m}$ corresponds to a nondepolarizing MM. LDP, LDP' and CDP in $\mathbf{L_u}$ describe the selective depolarization of linear horizontal, linear 45°, and circular polarized light respectively. These three parameters vanish for

a non-depolarizing MM. The inhomogeneity of the sample or time-irreversal events would result in the nondiagonal terms Δp_{i} [37].

The optical response of anisotropic materials which show circular effects cannot be simulated through ellipsometric modeling. Because ellipsometric modeling is based on Fresnel's equations by a three-dimensional dielectric tensor in cartesian coordinates. Even though the Euler angle can always specify an arbitrarily oriented optical axis for orthorhombic crystals, the ellipsometric modeling can only generate the linear effects (birefringence and linear dichroism) rather than circular effects (circular birefringence and circular dichroism).

2.4 Circular dichroism and birefringence

Circular Birefringence (CB) is the difference in refraction of left and right circularly polarized light. CB effect can be observed in liquids and solutions and reflects the dissymmetry of the liquid molecules or dissolved chromophores with lack of mirror symmetry. The polarization plane of linearly polarized light rotates after traversing a CB medium. The rotation angle is given by

$$\varphi = \frac{\pi(n_{-}\text{-}n_{+})l}{\lambda} \tag{2.65}$$

where n_{-} and n_{+} are the refraction index of the medium for left- and right- circularly polarized light. λ is the vacuum wavelength of light and l is the optical path length of the medium. Circular Dichroism (CD) is the difference in the absorption of left and right circularly polarized light. Like CB, the CD effect can be observed in liquids and solutions in which the chromophores are randomly oriented in space and reflects the dissymmetry of the liquid molecules or dissolved chromophores. CB and CD stem from the same quantum mechanical phenomena and are connected with each other by Kramer-Krönig (KK) relation.

Nowadays CD spectroscopy is a technique used in chemistry and biotechnology for the conformational analysis of chiral molecules of all types and sizes. Commercial CD instruments measures the difference of transmittance or absorbance of the sample for left- and right-circularly polarized light. However, one cannot say a medium is optical active just by sensing the differential absorption of circularly polarized light. The propagation of light in a material is a continuous process. The polarization of the initial wave progressively changes due to effects such as linear effects (retardation, diattenuation or depolarization). Therefore, only in the case of an isotropic optically active media, the circular polarization is preserved everywhere in the path length and only in this case, commercial CD instrument measures CD [40]. In all other cases, MM differential decomposition is advised to determine the CD [41]. In transmission geometry, the general MM for a homogeneous non-depolarizing optical media can be written in the following matrix [42]:

$$M = \begin{pmatrix} 1+\frac{1}{2}(\mathrm{LD}'^2+\mathrm{LD}^2) & -\mathrm{LD} & -\mathrm{LD}' & \mathrm{CD}+\frac{1}{2}(\mathrm{LBLD}'-\mathrm{LB}'\mathrm{LD}) \\ -\mathrm{LD} & 1+\frac{1}{2}(\mathrm{LD}^2-\mathrm{LB}'^2) & \mathrm{CB}+\frac{1}{2}(\mathrm{LBLB}'+\mathrm{LDLD}') & \mathrm{LB}' \\ -\mathrm{LD}' & -\mathrm{CB}+\frac{1}{2}(\mathrm{LBLB}'+\mathrm{LDLD}') & 1+\frac{1}{2}(\mathrm{LD}'^2-\mathrm{LB}^2) & -\mathrm{LB} \\ \mathrm{CD}-\frac{1}{2}(\mathrm{LBLD}'-\mathrm{LB}'\mathrm{LD}) & -\mathrm{LB}' & \mathrm{LB} & 1+\frac{1}{2}(\mathrm{LB}^2+\mathrm{LB}'^2) \end{pmatrix} \tag{2.66}$$

where CD is the true CD corresponding to the intrinsic CD ($\mathrm{CD_{int}}$), and CB is the true CB corresponding to the intrinsic CB ($\mathrm{CB_{int}}$). This MM representation illustrates clearly that each MME can be described by combinations of the 6 basic optical properties. In particular, it is worth to mention that $\mathrm{M14} = \mathrm{CD_{int}} + \frac{1}{2}(\mathrm{LBLD'} - \mathrm{LB'LD}) = \mathrm{CD_{app}}$ is the apparent CD with $\frac{1}{2}(\mathrm{LBLD'} - \mathrm{LB'LD}) = \mathrm{CD_{lin}}$ the linear part of the CD originating from the combination of the linear optical properties. Similarly, $\mathrm{M23} = \mathrm{CB_{app}}$ and $\frac{1}{2}(\mathrm{LBLB'} - \mathrm{LDLD'}) = \mathrm{CB_{lin}}$. Moreover, we can see, if $\mathrm{CB_{int}} << \mathrm{CB_{lin}}$ and $\mathrm{CD_{int}} << \mathrm{CD_{lin}}$, then $\mathrm{M14} \approx -\mathrm{M41}$ and $\mathrm{M23} \approx \mathrm{M32}$. Commercial CD instruments measure M14 as the CD. However, we can see M14 is CD only when M14 has no contribution from linear effects. In these cases, MM differential decomposition is required to obtain the intrinsic CD.

2.5 Plasmonics

2.5.1 Surface plasmon polaritons

Surface plasmon polaritons (SPPs) are electromagnetic excitations propagating at the interface between a dielectric and a conductor, evanescently confined in the perpendicular direction. As already known from previous section, in the absence of external charge and current densities and neglect the variation of the dielectric function over distances on the order of one optical wavelength, we obtain the central equation of electromagnetic wave theory [43]:

$$\nabla^2\mathbf{E} - \frac{\varepsilon}{c^2}\frac{\partial^2\mathbf{E}}{\partial^2 t} = 0 \cdot \tag{2.67}$$

First, we assume a harmonic time dependent electric field $\mathbf{E}(\mathbf{r},t)=\mathbf{E}(\mathbf{r})e^{-i\omega t}$. Then the known Helmholz equation can be obtained:

$$\nabla^2\mathbf{E} + k_0^2\varepsilon\mathbf{E} = 0 \tag{2.68}$$

Next, we define the wave propagates along x direction and shows no spatial variation in the perpendicular, in plane y direction. We can obtain two sets of self-consistent solutions with TM modes (p polarization) and TE modes (s polarization) of the propagating waves.
For TM modes, the governing equations of the system describes as:

$$E_x = -i\frac{1}{\omega\varepsilon_0\varepsilon}\frac{\partial H_y}{\partial z} \tag{2.69}$$

$$E_z = -\frac{\beta}{\omega\varepsilon_0\varepsilon}H_y, \tag{2.70}$$

and the wave equation for TM mode is

$$\frac{\partial^2 H_y}{\partial z^2} + (k_0^2\varepsilon - \beta^2)H_y = 0 \tag{2.71}$$

For TE modes, the governing equations are:

$$H_x = i\frac{1}{\omega\mu_0}\frac{\partial E_y}{\partial z} \tag{2.72}$$

$$H_z = \frac{\beta}{\omega\mu_0}E_y, \tag{2.73}$$

and the wave equation for TE mode is

$$\frac{\partial^2 E_y}{\partial z^2} + (k_0^2\varepsilon - \beta^2)E_y = 0, \tag{2.74}$$

where $\beta = K_x$ is called the propagating constant [43].

In the last step, we consider SPPs propagates along a single, flat interface between a dielectric (z>0) and conductor (z<0). Then, the equations (2.71 and 2.74) have to be solved separately in both regions and the resulted solutions have to be matched using appropriate boundary conditions. For instance, if we consider p polarization, then the continuity of H_y and $\varepsilon_i E_z$ at the interface should be fulfilled. By applying the boundary condition to the above equations for TM mode, the dispersion relation of SPPs propagating along the interface can be obtained [43].

$$k_{\mathrm{x}} = \frac{\omega}{c}\sqrt{\frac{\varepsilon_{\mathrm{m}}\varepsilon_{\mathrm{d}}}{\varepsilon_{\mathrm{m}}+\varepsilon_{\mathrm{d}}}}, \tag{2.75}$$

where ε_m and ε_d are the dielectric functions of metal and dielectic.

For TE polarization, the continuity of E_y and H_x at the interface induces no possibility of the existence of SPPs. So SPPs only exists for TM polarization.

If we assume that $\varepsilon_m'' < |\varepsilon_m'|$, then k_x is a complex value expressed as [44]

$$k_x = k_x' + ik_x'' = \frac{\omega}{c}\left(\frac{\varepsilon_m'\varepsilon_{\mathrm{d}}}{\varepsilon_m'+\varepsilon_{\mathrm{d}}}\right)^{1/2} + \frac{\omega}{c}\left(\frac{\varepsilon_m'\varepsilon_{\mathrm{d}}}{\varepsilon_m'+\varepsilon_{\mathrm{d}}}\right)^{3/2}\frac{\varepsilon_m''}{2(\varepsilon_m')^2}\,i \tag{2.76}$$

In order to have real k_x', $\varepsilon_m' < 0$ and $|\varepsilon_m'| > \varepsilon_{\mathrm{d}}$ which can be fulfilled in a metal or doped semiconductor materials. The intensity of SPPs propagating along the interface decreases as $e^{-2k_x''x}$, where k_x'' determines the internal absorption. Therefore, the propagation length of the SPPs can be defined as:

$$L_{sp} = (2k_x'')^{-1} \tag{2.77}$$

Since $k_z = k_0^2\varepsilon - \beta^2$ and relations $\omega/c < k_x$ and $\varepsilon_m' < 0$, wave vectors k_{zm} and k_{zd} are imaginary, so the field amplitude of SPPs decreases exponentially as exp(-$|k_{z1}||z|$), normal to the surface. The skin depth is defined as the length where the field amplitude decreases to 1/e, so the skin depths in metal and dielectric are [44]:

$$z'_m = \frac{1}{|k_{zm}|} = \frac{\lambda}{2\pi}\left(\frac{\varepsilon'_m+\varepsilon_d}{\varepsilon'^2_m}\right)^{1/2} \quad (2.78)$$

$$z'_d = \frac{1}{|k_{zd}|} = \frac{\lambda}{2\pi}\left(\frac{\varepsilon'_m+\varepsilon_d}{\varepsilon_d^2}\right)^{1/2} \quad (2.79)$$

Figure 2. 9(a) shows the charge oscillation and fields for SPPs in the interface between metal and dielectric. We can see from Figure 2. 9(b) that the projection of the momentum $k_x = ksin\theta$ along the interface on the dielectric side is always smaller than the propagation constant of SPPs, therefore SPPs cannot be excited directly by light beam.

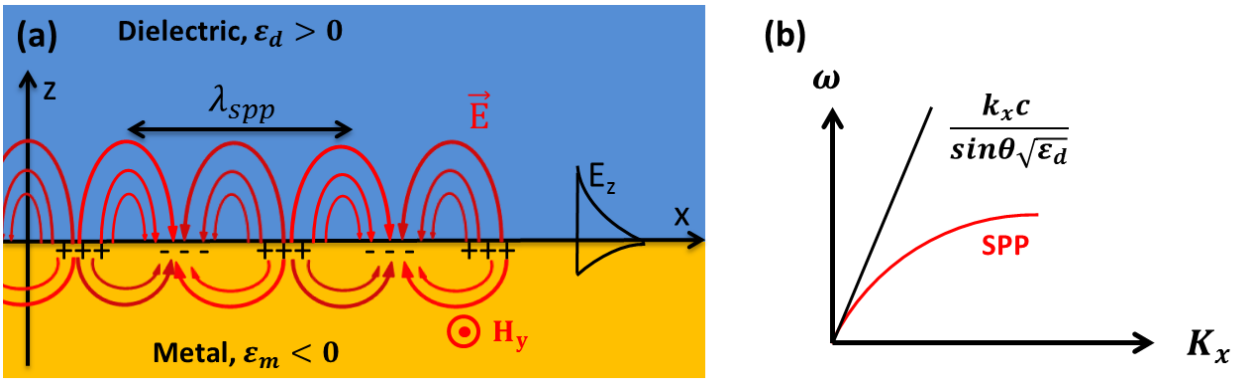

Figure 2. 9: (a) Sketch of charges oscillation and fields for a SPPs in a metal/dielectric interface; (b) Dispersion relation of SPPs(red line) and light line in dielectric (black line) at AOI θ [10].

In order to excite SPPs, special phase matching techniques are used. Andreas Otto was the first to propose a configuration for optically exciting nonradiative SPPs [45]. In Otto configuration (Figure 2. 10(b)), the beam of light is incident upon the prism with high refractive index and refracted towards its bottom surface. The prism is spaced by air gap with a small distance from the surface of the metal. The light in the prism would undergo total internal reflection and an evanescent field would exist within the air gap if the AOI upon the bottom surface of the prism is high enough. The tunneling of the evanescent field to the metal/air interface can excite the SP if the energy and momentum conservation laws are satisfied. The reflectivity drops, sometimes nearly to zero, and thus this coupling scheme is also known as attenuated total reflection. Another prism-based configuration which has become the most popular configuration for SPPs excitation was proposed by Kretschmann and Raether [46]. In Kretschmann configuration (Figure 2. 10(c)), a thin metal film is evaporated on top of a glass prism. Similar to Otto configuration, the light beam impinging from the glass side at an AOI greater than the critical angle of total internal reflection. The tunneled field into the metal film excites SPPs at the metal/air interface. In both Otto and Kretschmann configurations, the incident beam must have a component of p polarization to couple to this surface charge oscillation. s polarization cannot excite SP because the electric field lies in the direction orthogonal to the surface charge oscillation. Besides, the thickness of the metal film in Kretschmann configuration and thickness of air gap in Otto configuration are critical for SPPs coupling efficiency [43], [47].

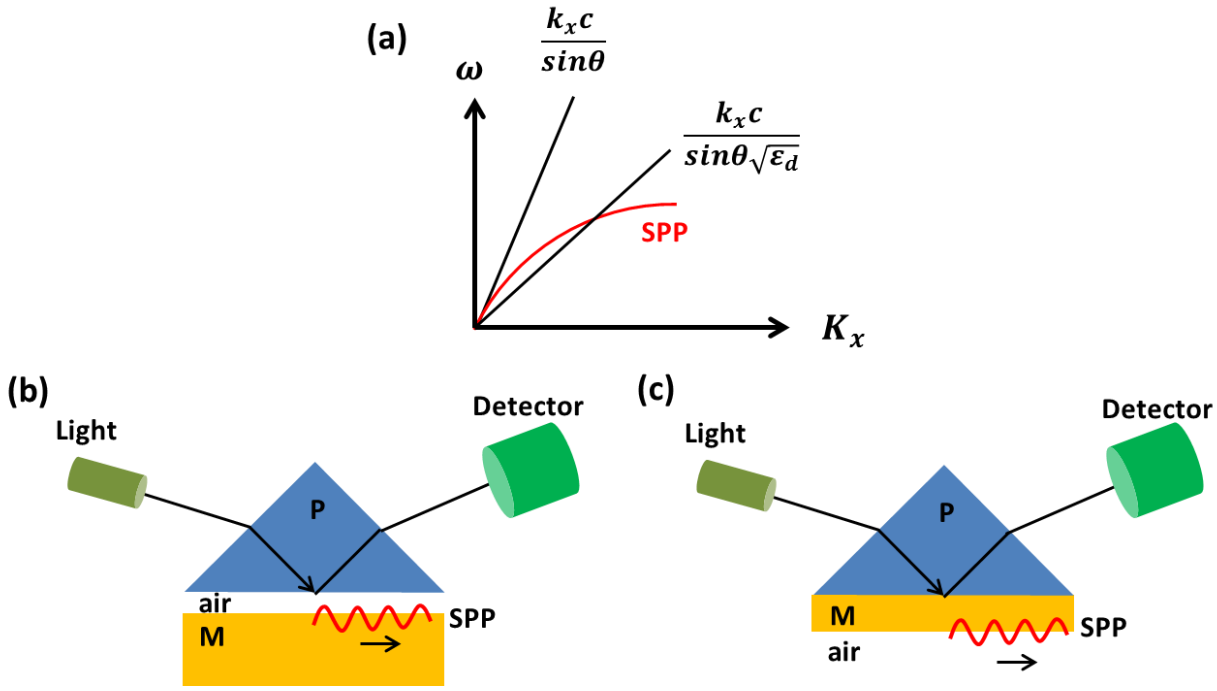

Figure 2. 10: (a) The dispersion relation of the free-space light line and the tilted light line in prism. (b) Otto configuration. (c) Kretschmann configuration. The metal layer and prism are indicated as M and P, respectively [47].

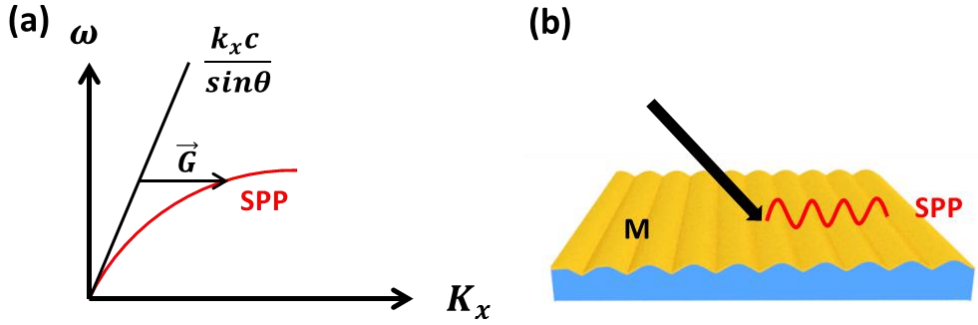

Figure 2. 11: (a) k matching of light to excite SPPs using grating. (b) Schematic of SPPs excitation by grating.

The wave vector mismatch between the in-plane momentum of the incoming photons and that of the SPPs k_{sp} can also be overcome by a grating structure with periodicity P as shown in Figure 2. 11. Then the conservation of momentum is obtained by setting k_{sp} equals to the sum of the projected wave vector of the incident light on the sample surface with an integer multiple of the grating vector [1]:

$$\boldsymbol{k_{sp}} = \boldsymbol{k_i} + m\boldsymbol{G} = k_0\,[(\sin\theta\,\sin\alpha)\boldsymbol{x} + (\sin\theta\,\cos\alpha)\boldsymbol{y}] + \frac{2\pi m}{P}\boldsymbol{y} \qquad (2.80)$$

where $\boldsymbol{k_i}$ is the in plane momentum of the incoming photons, P is the period of the grating, **G** is the grating vector equal to $2\pi/P$, **x** and **y** are unit length vectors in x and y directions, m is an arbitrary integer, θ is the incident angle, and α is the azimuthal angle.
Replacing $\boldsymbol{k_{sp}}$ by equation (2.75), we can obtain the relation:

$$k_0\sqrt{\frac{\varepsilon_1\varepsilon_2}{\varepsilon_1+\varepsilon_2}} = k_0\,[(\sin\theta\,\sin\alpha)\boldsymbol{x} + (\sin\theta\,\cos\alpha)\boldsymbol{y}] + \frac{2\pi m}{P}\boldsymbol{y} \qquad (2.81)$$

Then the condition for SPPs excitation is obtained by taking the square value of both sides of equation (2.81):

$$(\sin\theta)^2 + \frac{2\pi\lambda}{P}\sin\theta\cos\alpha + (\frac{m\lambda}{P})^2 = \frac{\varepsilon_1\varepsilon_2}{\varepsilon_1+\varepsilon_2} \qquad (2.82)$$

The above relation for SPPs excitation is not related to the incident polarization, which means that mixed s- and p -modes can be used to excite SPPs obeying equation (2.82). However, by tuning the incident polarization value, optimal coupling with SPPs can be obtained at a given incident angle [48]. The optimal coupling condition is given by:

$$\tan\varphi = \cos\theta\,\tan\alpha \qquad (2.83)$$

where φ is the polarization angle (from -90° to 90°, φ =0° and φ=±90° correspond respectively to p-polarization and s-polarization), θ is the AOI and α is the azimuthal angle (α=0° corresponds to grating ridges perpendicular to the plane of incidence).

2.5.2 Metallic nanoparticles: Particle Plasmon Resonance

If the particle size d is much smaller than the wavelength of light in the surrounding medium, the interaction of particle with the electromagnetic field can be analyzed using the quasi-static approximation. We start with a simple geometry: an isotropic spherical particle with radius a is located in an isotropic and non-absorbing medium with dielectric function ε_m. The dielectric response of the sphere to the applied static electric field $\mathrm{E} = \mathrm{E}_0\vec{\mathrm{z}}$ is described by the dielectric function ε. Due to the azimuthal symmetry in this condition, the solution for the potential of the Laplace equation $\nabla^2\Phi = 0$ is as follow [43]:

$$\Phi(r,\theta) = \sum_{l=0}^{\infty}\left[A_l r^l + B_l r^{-(l+1)}\right] P_l(\cos\theta), \qquad (2.84)$$

where $P_l(\cos\theta)$ are the Legendre Polynomials of order l, and θ the angle between the position vector $\boldsymbol{r}$ at point P and the z-axis. By applying the boundary conditions of equality of the tangential components of the electric field and the equality of the normal components of the displacement field and fulfilling requirement that the potentials remain finite at the origin, the inside and outside potentials are evaluate to

$$\Phi_{\text{in}}=-\frac{3\varepsilon_m}{\varepsilon+2\varepsilon_m}E_0 r\cos\theta, \tag{2.85}$$

$$\Phi_{\text{out}}=-E_0 r\cos\theta+\frac{\varepsilon-\varepsilon_m}{\varepsilon+2\varepsilon_m}E_0 a^3\frac{\cos\theta}{r^2}, \tag{2.86}$$

If we introduce the dipole moment $\mathbf{p}$, Φ_{out} can be expressed as

$$\Phi_{\text{out}}=-E_0 r\cos\theta+\frac{\mathbf{p}\cdot\mathbf{r}}{4\pi\varepsilon_0\varepsilon_m r^3} \tag{2.87}$$

$$\mathbf{p}=4\pi\varepsilon_0\varepsilon_m a^3\frac{\varepsilon-\varepsilon_m}{\varepsilon+2\varepsilon_m}\boldsymbol{E}_0. \tag{2.88}$$

So, we can see that Φ_{out} describes the potential superposition of the applied field and that from a dipole located at the particle center. If we introduce the polarizability α, defined via $\mathbf{p}=\varepsilon_0\varepsilon_m\alpha\mathbf{E}_0$, we arrive at

$$\alpha=4\pi a^3\frac{\varepsilon-\varepsilon_m}{\varepsilon+2\varepsilon_m}. \tag{2.89}$$

$\varepsilon_m(\omega)=\varepsilon_m'+i\varepsilon_m''$ is the dielectric function of the metal sphere. A resonant enhancement of polarizability occurs when the condition that $|\varepsilon+2\varepsilon_m|$ is a minimum is fulfilled. So the resonance condition is as

$$\text{Re}[\varepsilon(\omega)]=-2\varepsilon_m. \tag{2.90}$$

This is known as the Fröhlich condition [49]. For a Drude metal with a dielectric function given in equations (2.43, 2.44), the particle plasmonic resonance frequency becomes

$$\omega_{\text{pp}}^2=\frac{\omega_{\text{p}}^2}{\varepsilon_\infty+2\varepsilon}-\Gamma^2 \tag{2.91}$$

where Γ is the damping constant. For example, a Drude metal with $\varepsilon_\infty=1$ and $\Gamma<<\omega_{\text{p}}$ in air, the resonance frequency becomes $\omega_{\text{pp}}=\omega_{\text{p}}/\sqrt{3}$ [49].

Figure 2. 12 shows the spectral plane-wave extinction cross-sections of silver particles of 20, 60 and 100 nm diameter in glass, calculated using the MiePlot software [50]. We can see quasistatic approximation is valid for the 20 nm particle since only one dipolar mode is observed. However, at larger diameters, the dipolar mode is redshifted due to retardation and higher multi-

polar modes start to appear, so quasistatic approximation is not valid any more. Therefore, for spheres at higher dimension, a more general theory (Mie theory [51]) is needed.

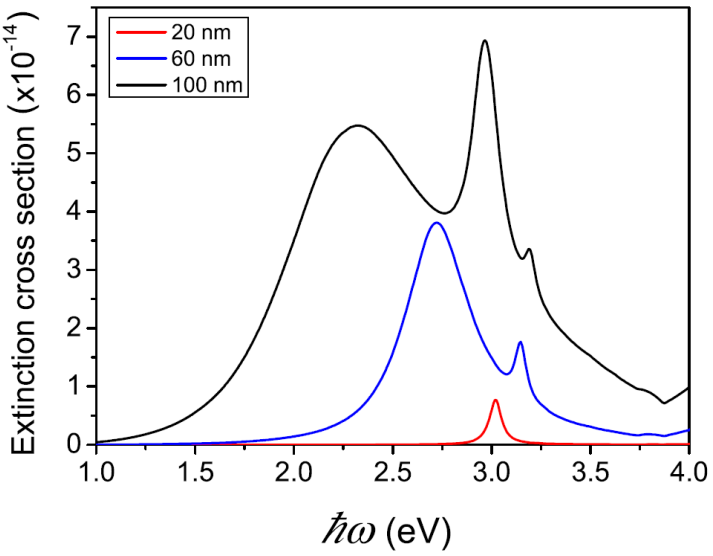

Figure 2. 12: Calculated extinction cross section for single silver spheres using the Mie theory [52].

The nanoparticles are strongly influenced by the presence of other particles in the near-neighbor range and the interaction of the neighboring nanoparticles result in a shift in the position of the plasmonic resonance compared to the case of an isolated particle. The influence of nearby particles can be understood by using the simple approximation of an array of interacting point dipoles under in-phase illumination. Transverse mode (longitudinal mode) is defined when polarization direction of the exciting light is perpendicular (parallel) to the nanoparticle chain. As sketched in Figure 2. 13, the restoring force acting on the oscillating electrons of each particle in the chain is either increased or decreased by influenced of neighboring particles, resulting in blue-shift for transverse modes, and a red-shift for longitudinal modes [43].

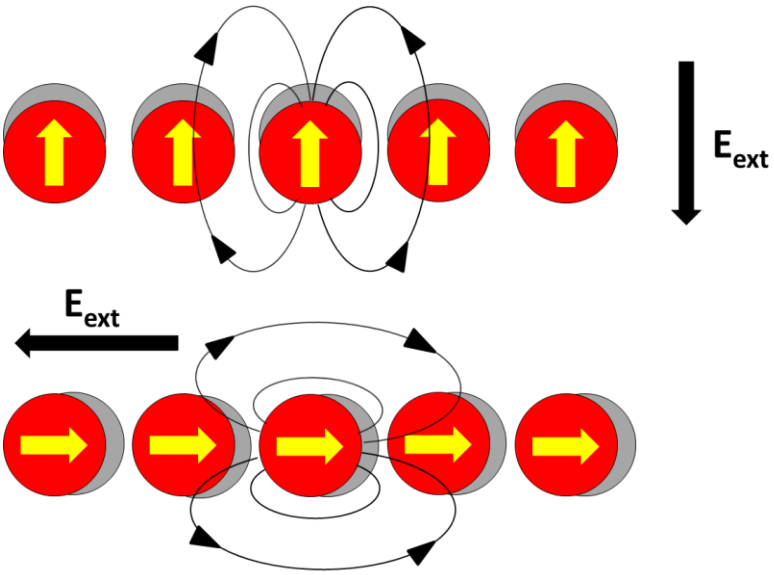

Figure 2. 13: Schematic of near-field dipole coupling between metallic nanoparticles for the two different polarizations [52].

2.6 Rayleigh-Wood anomalies

Grating anomalies were first discovered dates back to 1902 by Robert Wood [53]. He studied the spectra of ruled metallic diffraction gratings with p-polarized incident radiation and viewed abrupt changes in the reflectivity spectrum at certain condition. Few years later in 1907, Lord Rayleigh [11] correctly predicted the positions of the anomalies in the TM spectra as part of his dynamical theory of gratings. As shown in Figure 2. 14, Rayleigh explained these anomalies as a disappearance of the diffracted beam either in reflection or transmission when it crosses the boundary between ambient medium and substrate. So, the condition for RWAs is given by

$$\boldsymbol{K}_{//} + m\boldsymbol{G} = n\boldsymbol{K}_0 \tag{2.92}$$

Here, $\boldsymbol{K}_{//} = K_0 sin\,\theta$ is the component of the incident wave vector parallel to the sample surface, m is an integer indicating the order of the RWA, and n is the refractive index of the medium. Solving this equation (2.92) gives the final condition for RWAs

$$\lambda_m = -\frac{P}{m}\left(n_1 sin\,\theta\,|cos\,\alpha| \pm \sqrt{n_2^2 - n_1^2\,(sin\,\theta)^2\,(sin\,\alpha)^2}\right) \tag{2.93}$$

where λ_m is the wavelength for RWAs at m^{th} order, and n_2 is the refractive index of medium where the diffraction light propagates. The positive sign of the term in brackets corresponds to negative diffraction orders, whereas the negative sign corresponds to positive orders.

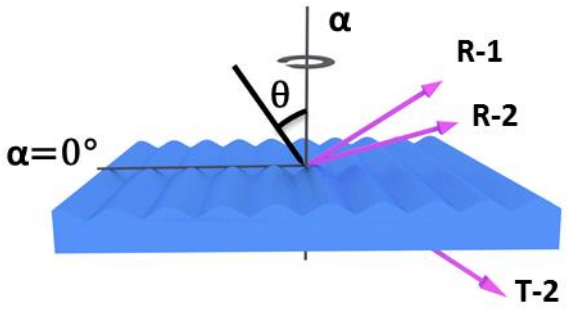

Figure 2. 14: Schematic shows diffraction orders of PDMS grating both in reflection and transmission regions.

2.7 Waveguide mode

Dielectric slab of high refractive index can support confined electromagnetic propagation. The modes of propagation are the so-called guided modes and the structures that support guided waves are called waveguides. Optical modes are presented as the solution of the eigenvalue equation, which is derived from Maxwell´s equations subject to the boundary conditions imposed by waveguide geometry. TE or TM mode can be excited and propagated along the waveguide if the conditions are fulfilled.

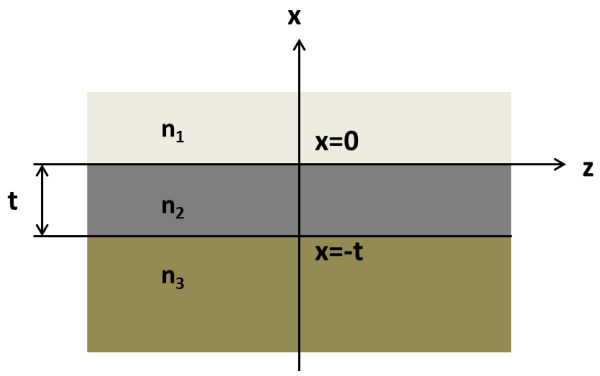

Figure 2. 15: Schematic drawing of an asymmetric slab waveguide [54].

TE mode condition can be expressed as:

$$h\sin(ht)-q\cos(ht)=p\,(\cos(ht)+\frac{q}{h}\sin(ht)) \tag{2.94}$$

or

$$\tan(ht)=\frac{p+q}{h(1-pq/h^2)} \tag{2.95}$$

where t is the thickness of the waveguide layer and h, q, and p are given by

$$h=[(\frac{n_2\omega}{c})^2-\beta^2]^{1/2},\ q=[\beta^2-(\frac{n_1\omega}{c})^2]^{1/2},\ p=[\beta^2-(\frac{n_3\omega}{c})^2]^{1/2} \tag{2.96}$$

For TM mode, the condition can be expressed as:

$$\tan(ht)=\frac{h(\bar{p}+\bar{q})}{(h^2-\bar{p}\bar{q})} \tag{2.97}$$

where t is the thickness of the waveguide layer, h is given in Eq (2.96) and $\bar{p}$ and $\bar{q}$ are expressed:

$$\bar{p}=\left(\frac{n_2^2}{n_3^2}\right)p,\ \bar{q}=\left(\frac{n_2^2}{n_1^2}\right)q \tag{2.98}$$

The propagation constant β must satisfy the condition for TE and TM. Equations in general yield a finite number of solutions for β provided the thickness t is large enough. Figure 2. 16 shows the dependence of propagation constants β on the waveguide thickness for an asymmetric waveguide. We can see the mode becomes confined above a certain cutoff value, while there is no cutoff value in the case of symmetric slab waveguide ($n_1 = n_3$). Besides, the number of modes which can be supported by waveguide can be tuned by varing the ratio of thickness and wavelength.

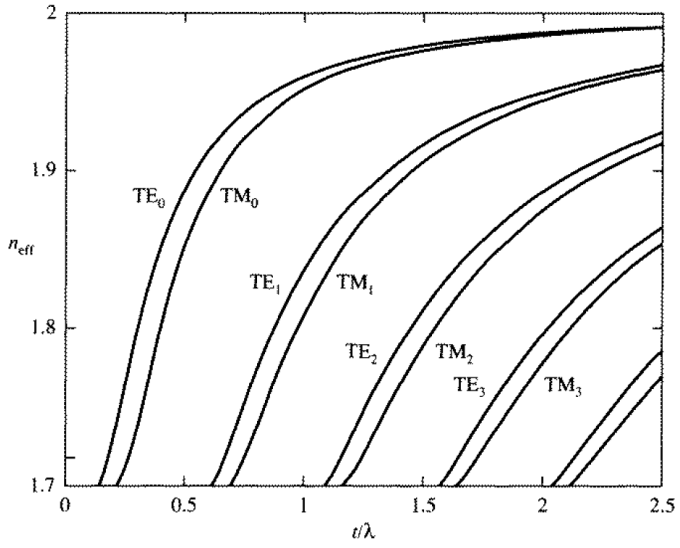

Figure 2. 16: Effective index versus thickness/wavelength for the confined modes of an asymmetric waveguide with n_1=1.0, n_2=2.0, and n_3=1.7 [54].

The modes for TE and TM not only can be solved by the wave equation but also can be derived by using geometric optics. The wave propagating in the waveguide experiences total internal reflection at both interfaces. However, not all trapped rays by internal reflection

constitute a mode, only when the extra transverse phase shift is an integral multiple of 2π. For asymmetric waveguide, the condition can be written as:

$$\Delta\varphi=2k_2h-2\varphi_1-2\varphi_2=2f\pi, \qquad f=0,\pm1\cdots \tag{2.99}$$

where f indicates the number of the modes which can propagate in the waveguide layer.
The phases induced at the two interfaces for TE are expressed as [55], [56]:

$$2\varphi_1=2\tan^{-1}\left\{\frac{\left(n_2^2\sin^2\theta_d-n_1^2\right)^{\frac{1}{2}}}{n_2\cos\theta_d}\right\} \tag{2.100a}$$

$$2\varphi_2=2\tan^{-1}\left\{\frac{\left(n_2^2\sin^2\theta_d-n_3^2\right)^{\frac{1}{2}}}{n_2\cos\theta_d}\right\} \tag{2.100b}$$

For TM polarization (p-polarization), the phases induced by the total internal reflection are:

$$2\varphi_1=2\tan^{-1}\left\{\frac{n_2^2}{n_1^2}\frac{\left(n_2^2\sin^2\theta_d-n_1^2\right)^{\frac{1}{2}}}{n_2\cos\theta_d}\right\} \tag{2.101a}$$

$$2\varphi_2=2\tan^{-1}\left\{\frac{n_2^2}{n_3^2}\frac{\left(n_2^2\sin^2\theta_d-n_3^2\right)^{\frac{1}{2}}}{n_2\cos\theta_d}\right\} \tag{2.101b}$$

where θ_d is the angle of reflection respective to the direction of x axis.

2.8 Destructive interference mode (DIM)

After discussing the waveguide eigenmode in section 2.7, now in this section, we will show how the waveguide can be excited by the presence of a grating embedded in waveguide layer and how DIM is defined and excited when Ag nanoparticle grating is embedded. Figure 2. 17 shows a cross section of the system, where we can see a grating with grating vector along x axis is embedded in the waveguide layer. The grating diffracts the incident light into various diffraction orders (violet open arrows in Figure 2. 17).

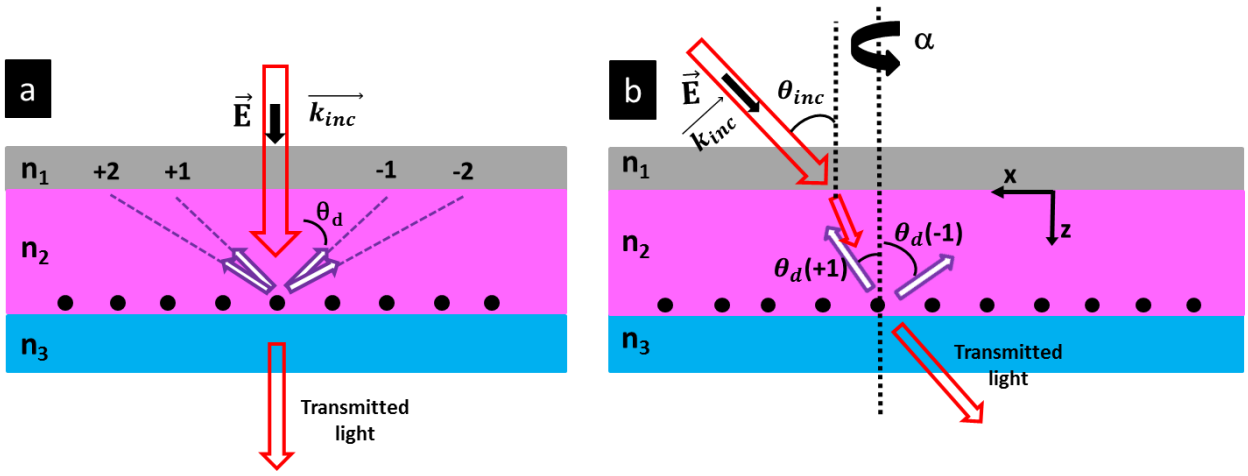

Figure 2. 17: Schematic of various diffraction orders in reflection in waveguide layer at (a) normal incidence and (b) oblique incidence in the case the incident plane is parallel to the grating vector at α=0°.

In the case $\alpha = 0°$ (Figure 2. 17a), the diffracted angle θ_d can be calculated from the grating equation along x axis as:

$$\sin\theta_{inc} \pm n_2 \sin\theta_d = m\frac{\lambda_0}{P},\ m = \pm 1, \pm 2 \cdots \tag{2.102}$$

where θ_{inc} is the angle of incidence, n_2 is the refractive index of the waveguide layer, P is the grating periodicity and m is diffraction orders.

In the case $\alpha \neq 0°$(Figure 2. 17b), the projection of the wave vector along the y-axis also plays a role. So the grating equation is written along x and y directions as follows:

X axis: $$\sin\theta_{inc}\cos\alpha \pm n_2 \sin\theta_d \cos\alpha_d = m\frac{\lambda_0}{P},\ m = \pm 1, \pm 2 \cdots \tag{2.103a}$$

Y axis: $$n_2 \sin\theta_d \sin\alpha_d = \sin\theta_{inc}\sin\alpha \tag{2.103b}$$

where α is the azimuthal angle of the sample, θ_{inc} is the angle of incidence, $\alpha_d$is the azimuthal angle of diffracted light, P is the grating periodicity. Then we can reach Eq.2.104 by combining Eqs 2.103(a) and (b) as follows:

$$\sin\theta_{inc}\cos\alpha \pm n_2 \sin\theta_d \sqrt{1 - \left(\frac{\sin\theta_{inc}\sin\alpha}{n_2\sin\theta_d}\right)^2} = m\frac{\lambda_0}{P},\ m = \pm 1, \pm 2 \cdots \tag{2.104}$$

If the Ag nanoparticle grating is immersed in a homogeneous environment, when the diffracted light propagates along the x-y plane, this situation results in an energy redistribution observed in reflectance or transmittance, the Rayleigh-Wood anomaly. However, the situation is different when waveguide system is formed. As shown in the schematic in Figure 2. 17a, when one of these diffracted light fulfills the condition of waveguide mode excitation in Eq. 2.99, the

waveguide mode will be excited. In other words, the waveguide mode equation in Eq. 2.99 and the grating equation in Eq. 2.104 should be combined to determine the conditions of excitations of the waveguide mode.

In addition to the part of light which is diffracted to various diffraction orders, the other part of the incident light directly transmits through the waveguide. This part of light is absorbed and reradiated by Ag nanoparticles resulting in the characteristic presence of the localized surface plasmon (LSP) resonance spectrum. The plasmonic resonance shape depends on the individual particle shape and size distributions, as well as on nanoparticle interactions along the lines or between lines.

As shown in the schematic in Figure 2. 18, the waveguide mode is leaky and the leaky part of the wave can interfere either constructively or destructively with the transmitted, non-diffracted, part from the incident light that is characterized by the plasmonic absorbance.

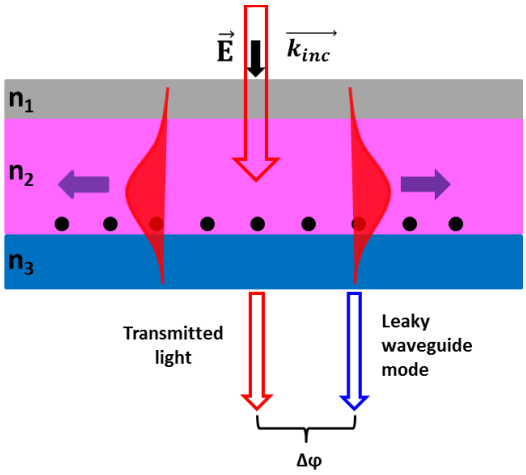

Figure 2. 18: Schematic of leaky waveguide mode.

From the schematic in Figure 2. 19 which shows ray optics approximation of the light beam in the waveguide, the phase difference between transmitted beam and leaky waveguide mode can be expressed as $2k_2h$-$(2\varphi_1+2\varphi_2)$, where $2k_2h = 2n_2\frac{2\pi}{\lambda}h\cos\theta_d$ approximates the phase of the waveguide mode, k_2 is the wave vector along z direction, h is the thickness of waveguide and $2\varphi_1$ and $2\varphi_2$ are the two polarization-dependent phase shifts introduced at the two interfaces (Goos-Hänchen shifts). In case of DIM, the phase difference $\Delta\varphi$ between the leaky waveguide mode and the transmitted incident light beam should be equal to a multiple of π, which is expressed by the following equation:

$$\Delta\varphi=2k_2h-(2\varphi_1+2\varphi_2)=(2f+1)\pi, \qquad f=0,\pm1\cdots \tag{2.105}$$

$2\varphi_1$ and $2\varphi_2$ for TE polarization are expressed as:[55], [56]

$$2\varphi_1=2\tan^{-1}\left\{\frac{\left(n_2^2\sin^2\theta_d-n_1^2\right)^{\frac{1}{2}}}{n_2\cos\theta_d}\right\},\ 2\varphi_2=2\tan^{-1}\left\{\frac{\left(n_2^2\sin^2\theta_d-n_3^2\right)^{\frac{1}{2}}}{n_2\cos\theta_d}\right\} \tag{2.106}$$

For TM polarization (p-polarization), the phases induced by the total internal reflection are:

$$2\varphi_1=2\tan^{-1}\left\{\frac{n_2^2}{n_1^2}\frac{\left(n_2^2\sin^2\theta_d-n_1^2\right)^{\frac{1}{2}}}{n_2\cos\theta_d}\right\},\ 2\varphi_2=2\tan^{-1}\left\{\frac{n_2^2}{n_3^2}\frac{\left(n_2^2\sin^2\theta_d-n_3^2\right)^{\frac{1}{2}}}{n_2\cos\theta_d}\right\} \qquad (2.107)$$

Therefore, in order to calculate the DIM between transmitted light and leaky waveguide mode, the equations 2.104 and 2.105 should be combined.

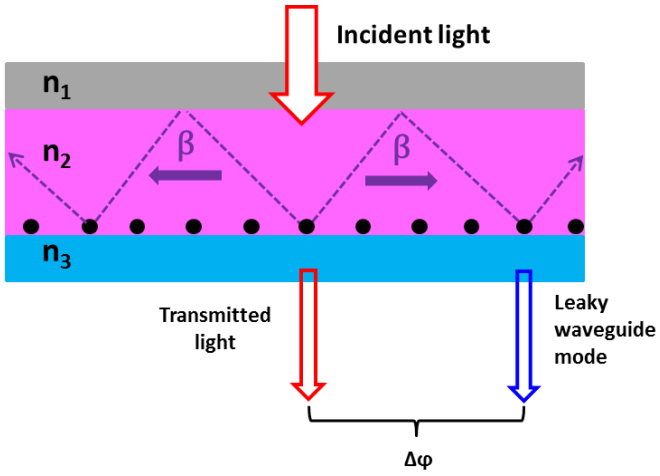

Figure 2. 19: Schematic of the waveguide mode in ray optics approximation at normal incidence.

Chapter 3

Experimental Techniques

3.1 Atomic force microscopy

Atomic-force microscopy (AFM) is a very-high-resolution type of scanning probe microscopy to examine surface structures at the nanometer-scale which is more than 1000 times better than the optical diffraction limit. It was developed in the 1980s by Gerd Binning, Calvin F. Quate and Henrich Rohrer [57]. An AFM is a mechanical imaging instrument that measures the three dimensional image based on the force interaction between a sharpened tip and the sample surface. The tip is mounted on a reflective cantilever. The deflection of the tip both laterally and vertically according to the surface morphology is caused by attracted and repulsive forces on the surface of the sample. The movements of the cantilever are measured by a laser, reflected off the cantilever onto a position sensitive four-quadrant photodiode [58]. Then the deflection of cantilever is fed back into the feedback controller (PID) which moves the probe over the sample to return the deflection of the cantilever to its original value. The AFM can be operated in a number of modes, such as contact modes and a variety of non-contact modes where the cantilever is vibrated. The AFM images in our project were measured in air by means of TT-AFM system (Figure 3. 1) working in vibrating mode using probes purchased from Schaffer technology GmbH. The images are analyzed by open-source software called Gwyddion [59].

Figure 3. 1: TT-AFM system [60].

3.2 Mueller Matrix ellipsometer

It is possible to measure MM experimentally by means of a MM ellipsometer which generally consists of a light source, a polarizer on the incident side and analyzer and the detector on the reflection/transmission side. Recently, MM ellipsometers of various types have been developed. Figure 3. 2 shows 4 types of rotating-element MM ellipsometers. Figure 3. 2(a) illustrates the simplest ellipsometer which is called the rotating-analyzer ellipsometry (RAE). Other ellipsometers shown in Figure 3. 2(b)-(d) are just built with compensators introduced in the RAE configuration. Only when the ellipsometer additionally contains two rotating compensators (one before and one after the sample) with different rotating frequencies can enable us to measure all sixteen MM elements.

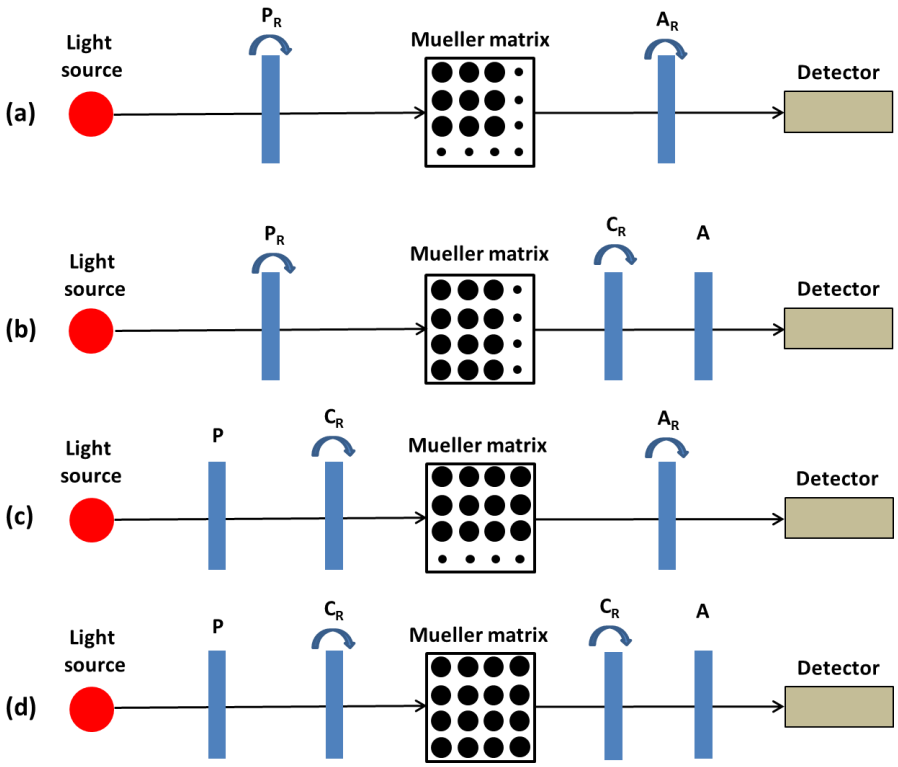

Figure 3. 2: Optical configurations for MM ellipsometry. P_R, A_R and C_R are rotating polarizer, rotating analyzer and rotating compensator [13].

3.2.1 RAE with compensator

RAE with compensator is popular in recent years because all the Stokes parameters S_0 to S_3 can be measured.

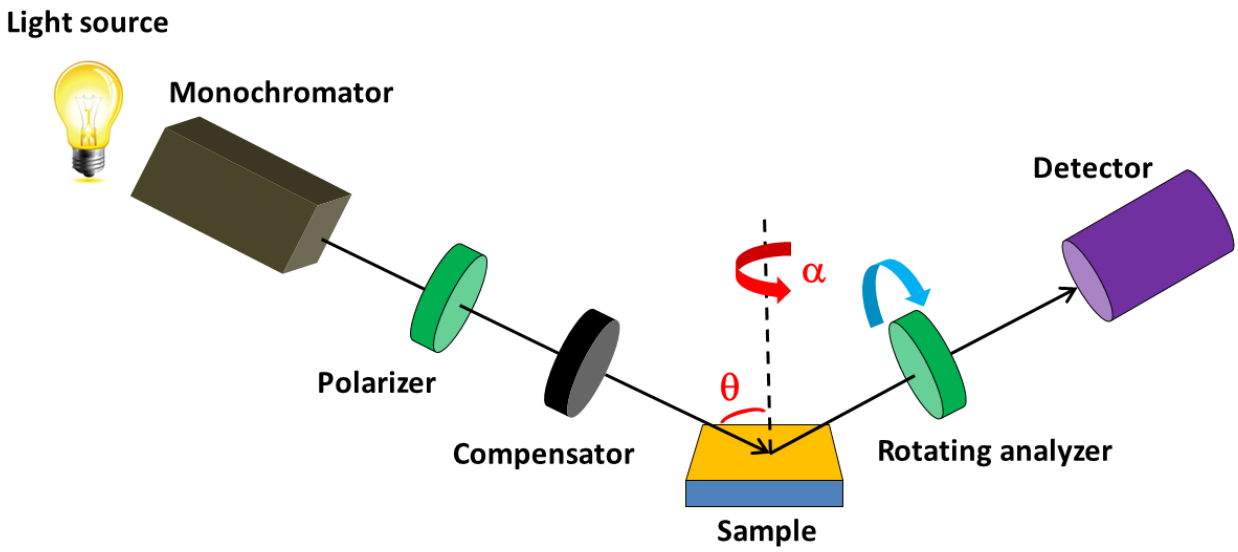

Figure 3. 3: Schematic of a RAE with compensator [61].

The configuration of a RAE with compensator is shown in Figure 3. 3. It can be described as:

$$L_{out} = \boldsymbol{A}R(A)\boldsymbol{S}\boldsymbol{C}R(-P)\boldsymbol{P}L_{in} \tag{3.1}$$

where L_{out} represents the Jones vector of the light detected by the detector, L_{in} shows the normalized Jones vector of incident light. $\boldsymbol{A}$, $\boldsymbol{S}$, $\boldsymbol{C}$ and $\boldsymbol{P}$ represents the Jones matrix of analyzer, sample, compensator and polarizer, respectively. A is the rotation angle of analyzer and P is the rotation angle of polarizer. When the fast axis of the compensator is in the direction of s-polarization, the Jones matix of compensator $\boldsymbol{C}$ is expressed by:

$$\boldsymbol{C} = \begin{bmatrix} \exp(-i\delta) & 0 \\ 0 & 1 \end{bmatrix} \tag{3.2}$$

When the fast axis of the compensator is not in the direction of p- or s-polarization, the compensator is expressed as R(-C)$\boldsymbol{C}$R(C), where C is the rotation angle of the compensator. Jones matrix for sample $\boldsymbol{S}$ is expressed by:

$$\boldsymbol{S} = \begin{bmatrix} sin\psi\exp(i\Delta) & 0 \\ 0 & cos\psi \end{bmatrix} \tag{3.3}$$

where ψ and Δ are the two ellipsometric angles measured in spectroscopic ellipsometry as shown in section 2.1.5. So the matrix representation of above equation is described as [13]:

$$\begin{bmatrix} E_A \\ 0 \end{bmatrix} = \begin{bmatrix} 1 & 0 \\ 0 & 0 \end{bmatrix} \begin{bmatrix} cosA & sinA \\ -sinA & cosA \end{bmatrix} \begin{bmatrix} sin\psi \exp(i\Delta) & 0 \\ 0 & cos\psi \end{bmatrix}$$
$$\times \begin{bmatrix} \exp(-i\delta) & 0 \\ 0 & 1 \end{bmatrix} \begin{bmatrix} cosP & -sinP \\ sinP & cosP \end{bmatrix} \begin{bmatrix} 1 & 0 \\ 0 & 0 \end{bmatrix} \begin{bmatrix} 1 \\ 0 \end{bmatrix}$$
$$= \begin{bmatrix} 1 & 0 \\ 0 & 0 \end{bmatrix} \begin{bmatrix} cosA & sinA \\ -sinA & cosA \end{bmatrix} \begin{bmatrix} cosPsin\psi \exp[i(\Delta - \delta)] \\ sinPcos\psi \end{bmatrix} \quad (3.4)$$

The measured light intensity for an arbitrary angle of the polarizer and analyzer by the detector is obtained as:

$$I = |E_A|^2 = I_0\{(1 - cos2P\ cos2\psi) + (cos2P - cos2\psi)cos2A + [(sin2P\ sin2\psi \cos(\Delta - \delta)sin2A]\} \quad (3.5)$$

By normalizing the term $(1 - cos2P\ cos2\psi)$, we can describe the intensity as:

$$I = |E_A|^2 = I_0\left\{1 + \frac{cos2P - cos2\psi}{1 - cos2Pcos2\psi}\cos(2A) + \frac{sin2Psin2\psi\cos(\Delta - \delta)}{1 - cos2Pcos2\psi}\sin(2A)\right\} \quad (3.6)$$

$$\alpha = \frac{cos2P - cos2\psi}{1 - cos2Pcos2\psi} = \frac{tan^2\psi - tan^2P}{tan^2\psi + tan^2P} \quad (3.7)$$

$$\beta = \frac{sin2Psin2\psi cos(\Delta - \delta)}{1 - cos2Pcos2\psi} = \frac{2tan\psi cos(\Delta - \delta)tanP}{tan^2\psi + tan^2P} \quad (3.8)$$

where (α, β) are referred to as normalized Fourier coefficients. We can rewrite the measured light intensity as:

$$I = I_0(1 + \alpha\ cos2A + \beta\ sin2A) \quad (3.9)$$

Then, the equations for describing (ψ, Δ) are obtained by solving the equations:

$$tan\psi = \sqrt{\frac{1+\alpha}{1-\alpha}}\ |tanP| \qquad cos(\Delta - \delta) = \frac{\beta}{\sqrt{1-\alpha^2}} \quad (3.10)$$

When P=45°, the detected intensity is expressed:

$$I = |E_A|^2 = I_0\{1 - cos2\psi \cos 2A + sin2\psi cos(\Delta - \delta) \sin 2A\}$$
$$= I_0\{1 - cos2\psi \cos 2A + (sin2\psi cos\Delta\cos\delta + sin2\psi sin\Delta\sin\delta) \sin 2A\}$$
$$= I_0\{1 + S_1 \cos 2A + (S_2\cos\delta - S_3\sin\delta)\sin 2A\} \quad (3.11)$$

We can see from the above equation, S_1 and $S_2\cos\delta - S_3\sin\delta$ are measured as Fourier coefficients. However, in order to obtain S_2 and S_3 separately, at least two measurements with different δ should be performed.

Figure 3. 4 shows the VASE from J. A. Woollam company. VASE uses the RAE combined with patented AutoRetarder configuration. A xenon lamp light in the wavelength range 230 nm-

2.3 μm is used as light source. Then the light passes through a scanning monochromator with a fiber and separated into individual wavelengths. The scanning monochromator is designed specifically for spectroscopic ellipsometry which automatically controls the selection of wavelengths and spectral resolution. After reflection or transmission on the sample, light passes through a rotating analyzer, which operates at a frequency between 10 Hz and 100 Hz. Finally, the intensity of the light is converted into voltage signal. The VASE has two detectors, one of the two detectors is made of silicon with a spectral range between 185 nm and 1100 nm and the other is made of InGaAs with a spectral range between 800 nm to 1700 nm.

Broad range of wavelength and AOI (15°-90°) allow a large variety if measurement geometries including: reflection, transmission and scattering. Ellipsometry in reflection and transmission, reflectance and transmittance intensity, cross-polarized reflectance and transmittance, depolarization, scatterometry and MM can be measured [16]. However, for the MM measurement, VASE ellipsometer can only measure the first 3 rows of whole 4x4 MM elements because only one compensator is included in the configuration.

Figure 3. 4: VASE ellipsometer from J.A. Woollam [62].

3.2.2 RAE with dual rotating compensators

In order to measure all sixteen MM elements, two rotating compensators (one before and one after the sample) are introduced in RAE as shown in Figure 3. 5.

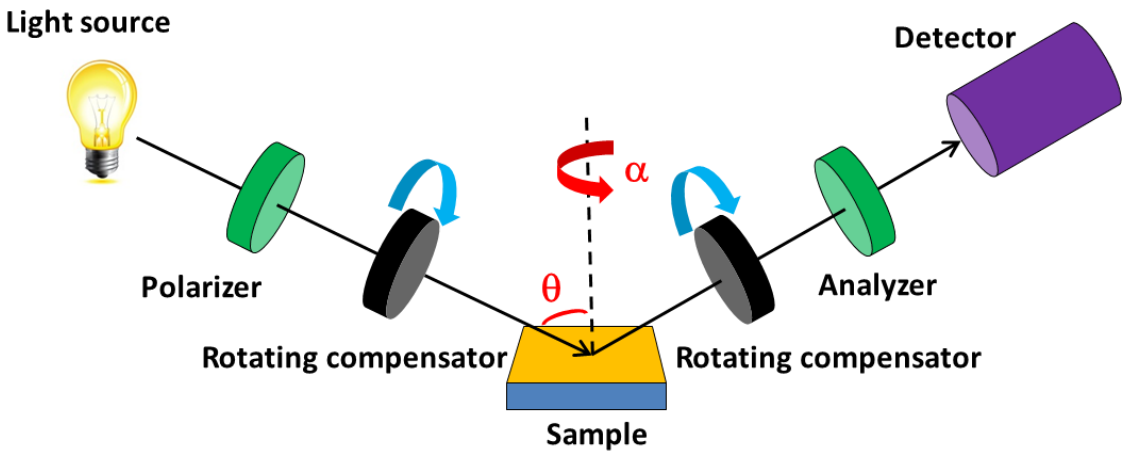

Figure 3. 5: Schematic of ellipsometer combined with dual rotating compensators.

The determination of the MM by an ellipsometer with two rotating compensators is roughly explained below. The Stokes vector S_{out} of the light after passing through the analyzer can be expressed as the MM product [63]:

$$S_{out} = \boldsymbol{M}_A R(A') R(-C_2') \boldsymbol{M}_{C2}(\delta_2) R(C_2') \times \boldsymbol{M}_S R(-C_1') \boldsymbol{M}_{C1}(\delta_1) R(C_1') R(-P') \boldsymbol{M}_P R(P') S_{in} \quad (3.12)$$

where $\boldsymbol{M}_A$, $\boldsymbol{M}_P$ and $\boldsymbol{M}_S$ represent the MM of analyzer, polarizer and sample respectively. A', P', C_1', C_2' are the rotation angles of analyzer, polarizer and compensator before and after the sample. δ_1 and δ_2 are the phase introduced by the compensator before and after the sample. The Mueller matrices of all these components are expressed as:

$$\boldsymbol{M}_A = \boldsymbol{M}_P = \begin{bmatrix} 1 & 1 & 0 & 0 \\ 1 & 1 & 0 & 0 \\ 0 & 0 & 0 & 0 \\ 0 & 0 & 0 & 0 \end{bmatrix}, \quad \boldsymbol{M}_S = \begin{bmatrix} M11 & M12 & M13 & M14 \\ M21 & M22 & M23 & M24 \\ M31 & M32 & M33 & M34 \\ M41 & M42 & M43 & M44 \end{bmatrix} \quad (\mathbf{3.13})$$

$$\boldsymbol{M}_{c1} = \begin{bmatrix} 1 & 0 & 0 & 0 \\ 0 & 1 & 0 & 0 \\ 0 & 0 & \cos\delta_1 & \sin\delta_1 \\ 0 & 0 & -\sin\delta_1 & \cos\delta_1 \end{bmatrix}, \quad \boldsymbol{M}_{c2} = \begin{bmatrix} 1 & 0 & 0 & 0 \\ 0 & 1 & 0 & 0 \\ 0 & 0 & \cos\delta_2 & \sin\delta_2 \\ 0 & 0 & -\sin\delta_2 & \cos\delta_2 \end{bmatrix} \quad (\mathbf{3.14})$$

Multiplication of the matrices leads to the expression of the first Stokes parameter:

$$I = I_0\{K_1 + [c_2 cos2A' + s_2 \cos(4C_2' - 2A')]K_2 + [c_2 sin2A' + s_2 \sin(4C_2' - 2A')]K_3 - [\sin\delta_2 \sin(2C_2' - 2A')]K_4\} \quad (3.15)$$

where

$$K_j = M_{j1} + [c_1 cos2P' + s_1 \cos(4C_1' - 2P')]M_{j2} + [c_1 sin2P' + s_1 \sin(4C_1' - 2P')]M_{j3} + [\sin\delta_1 \sin(2C_1' - 2P')]M_{j4} \quad (3.16)$$

and $$c_j = \cos^2(\delta_j/2)$$

$$S_j = \sin^2(\delta_j/2)$$

The two compensators have the rotation frequencies $n\omega$, with numbers n still to be determined. Their phase difference C_{S1}-C_{S2} must be determined by calibration. Together with the sample in the middle, the structure corresponds to the four indicated Müller matrices. After selecting an exact ratio between the rotational frequencies of the compensators, for example of 3: 5, and substituting of $C_1^{'}=5\left(C\text{-}C_{S1}\right)$ and $C_2^{'}=3\left(C\text{-}C_{S2}\right)$ into above equation, we obtain:

$$\mathrm{I(t)}=\mathrm{I_0}\left\{1+\sum_{n=1}^{16}[\alpha_{2\mathrm{n}}\cos(2nC\text{-}\phi_{2n})+\beta_{2n}\sin(2nC\text{-}\phi_{2n})]\right\} \qquad (3.17)$$

where ϕ_{2n} depends on the phases C_{si}. The intensity signal is thus modulated in time by the rotation of the compensators. The equations (3.15-3.17) show that the Muller matrix elements m_{ij} are explicitly contained in the coefficients (α_{2n}, β_{2n}) of the sine and cosine terms. They can therefore be obtained by Fourier transformation of the signal from the Fourier coefficients. The detailed procedure for inverting the obtained coefficients is described, for example, in [63].

Figure 3. 6 shows variable angle dual rotating compensator spectroscopic ellipsometer (RC2) from J. A. Woollam company. Synchronous rotation of two compensators provides high accuracy, high speed, and complete Mueller-matrix measurements. RC2 is a CCD-based ellipsometry, therefore it is fast and allows advanced measurement capabilities with the best accuracy. RC2 collects wavelengths from 210 nm to 1690 nm simultaneously.

Figure 3. 6: RC2 ellipsometer from J.A. Woollam [64].

Chapter 4

Results and Discussion

4.1 Pure PDMS gratings

We start the results and discussion chapter with pure PDMS gratings. In this section, I will first introduce the fabrication method for PDMS gratings. Then I will show some MM measurements and how we decompose MM into physical effects by anisotropic modeling. The pure gratings are not interesting themselves, but this section lays a foundation for the analysis of metallic gratings in the following sections 4.2 and 4.3.

4.1.1 Sample fabrication method

The pure PDMS grating is fabricated in the following two steps: PDMS fabrication and PDMS grating fabrication.

PDMS fabrication

PDMS is a silicon- based polymer consisting of repeating $[Si(CH_3)_2O]$ units and is the simplest silicone oil among the siloxanes. PDMS has high hydrophobicity, contamination resistance, and long-term endurance, making it a very useful polymer for insulation, anticorrosion, and antifouling coatings [65]. PDMS are fabricated from Sylgard 184, which consists two commercially available components (silicone elastomer base and curing agent in Figure 4. 1) manufactured by Dow Corning [66].

The PDMS can be fabricated by the following procedure [61]:

1. Mix Silicone elastomer base and curing agent inside a beaker in a mass ratio of 10: 1 with the help of a conventional digital scale (Silicone elastomer base and curing agent are taken out and poured inside the beaker with plastic syringe)
2. Stir the mixture immediately after the components are mixed in a beaker with a glass pipette
3. Place the beaker in an ultrasonic bath for 10 minutes to remove unwanted air bubbles brought in the PDMS after stirring (It is important to ensure that the water is in the same level as the PDMS, so that all air bubbles are eliminated)
4. Place the beaker in a desiccator for a total of 15 minutes to continue eliminate the bubbles by means of a vacuum
5. Pour the liquid PDMS mixture in the prepared petri dish (procedure for preparation is shown below) slowly and try to make the layer have homogeneous thickness
6. Place the petri dish in an oven at 100 °C for 60 minutes

The petri dish should be prepared before the above procedure in order to remove the cured PDMS from petri dish freely. The procedure for preparation of petri dish:

1. Clean the petri dish with acetone to remove all the oily and water residuals on the surface and let it dry in the air
2. Mix 20 mL acetone with 0.4 mL 3-Aminopropyltriethoxysilan and then give the solution for around 3 minutes in the petri dish
3. Remove the solution and clean the petri dish three times with distilled water
4. Remove the last water inside the petri dish by evaporating in the oven at 120℃

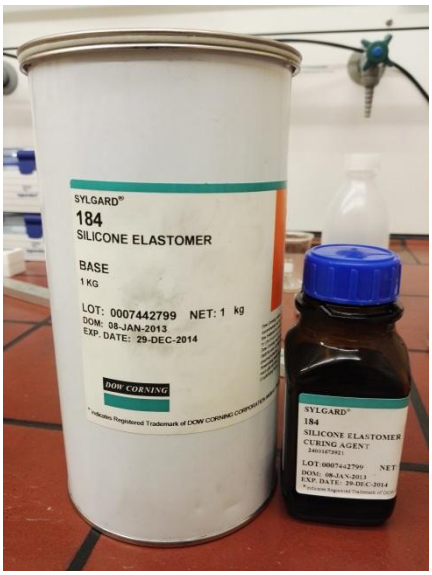

Figure 4. 1: Two components of PDMS (Sylgard 184). On the left is the silicone elastomer and on the right is the curing agent.

PDMS grating fabrication

The surface property of fabricated PDMS can be changed from strong hydrophobicity to hydrophilicity by oxygen plasma treatment. Plasma etching equipment includes a reaction chamber, a power supply, and a vacuum part. The plasma etching process is actually a reactive plasma process [67]. The stretched PDMS slab is fed into the reaction chamber evacuated by the vacuum pump. The oxygen plasma initiates the oxidization at the surface of PDMS and generates a thin surface film of silica-like material. Then, by slowly releasing the pre-strain on the PDMS, thin silica-like film supported by PDMS substrates spontaneously buckles and sinusoidal grating is obtained. The physical mechanism is that the stiff silica-like film tends to buckle to release the total energy of the whole system by introducing the bending energy due to the out-of-plane deformation of the thin films [68]–[70]. We used this physical principle to produce our grating sample. The fabrication procedure of pure PDMS grating can be detailed in Figure 4. 2 and described here:

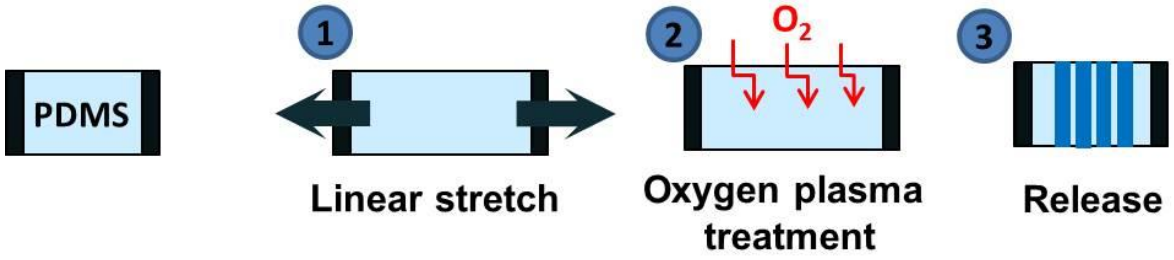

Figure 4. 2: The fabrication process of pure PDMS grating.

1. The PDMS slab with size 1 mm thick, 13 mm wide and 27 mm long was glued (Figure 4. 3(a)) on a home-made stretching stage (Figure 4. 3(b)) with the un-glued area 1 mm thick, 13 mm wide and 8 mm long.
2. PDMS slab was put in the oven with 85°C for 1h.

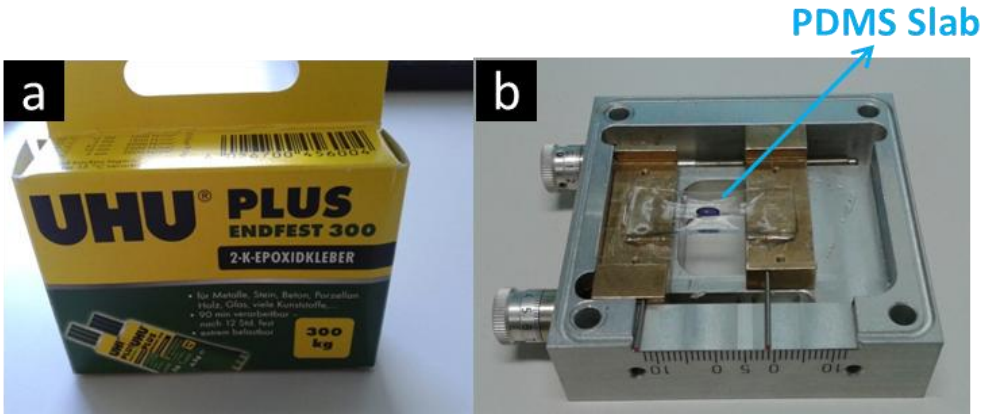

Figure 4. 3: (a) Glue and (b) home-made stretching stage.

3. PDMS slab was linearly stretched up to a percentage X less than 60%.
4. The stretched PDMS slab was treated by an O_2 plasma (90 W) for Y min inside a plasma etcher chamber at a pressure of 1.4 mbar in order to modify the nature of the surface of the elastomer.
5. One dimensional periodic grating was formed by slowly releasing the pre-strain.

During the fabrication process, only the parameters X and Y were changed to tune the periodicity and amplitude of the grating. A repetitive experiment was performed in order to investigate the dependence of stretching percentage on the stretching length. A drop of black ink was put on the center of the PDMS slab surface and formed a circular shape. The lengths of the elongated ellipse along the stretching direction were measured as shown in Figure 4. 4(a) and (b). The percentage of stretching was then calculated as $(L\text{-}L_0)\times 100\% / L_0$, where L_0 is the diameter of the circular drop without stretching and L is the length after stretching. Figure 4. 4(c) shows the relation between stretching percentage and stretching length. We can see the stretching percentage is linearly dependent on the stretching length when stretching length is less than 3 mm, while non-linear behavior appears at stretching length more than 3 mm.

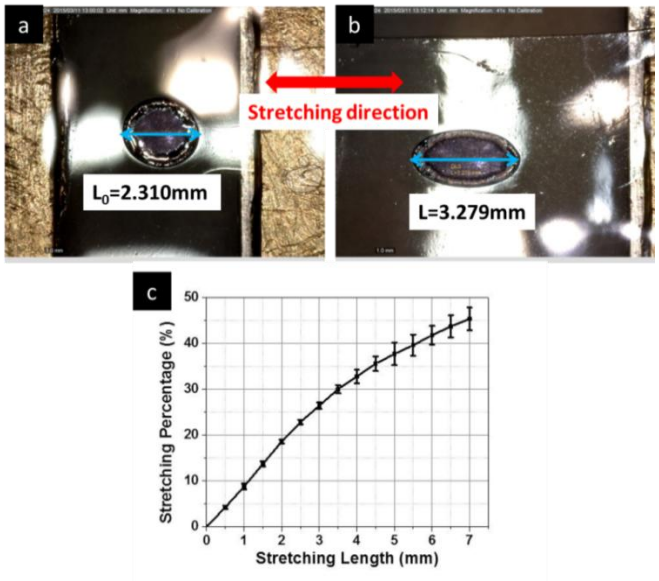

Figure 4. 4: Images of PDMS slab under the condition (a) without stretching and (b) after stretching with 7 mm. (c) The relation between stretching percentage and stretching length.

Figure 4. 5 shows the plasma system used in our method. It is a Pico low-pressure plasma system from Diener electronic company. The detailed procedure for oxygen plasma treatment in the 4th step of the fabrication process is as follows:

1. Main power on, ventilation on and open the chamber
2. Put the sample in a glass petri dish and place the petri dish below the black rod in the chamber. In order to get reproducible results, the sample should be always placed at same position.
3. Close the chamber, ventilation off and pump on
4. Adjust the generator power button to wanted power 4.3 (equals 90 W)
5. Set timer and wait pressure 0.1<P<0.2
6. Press GAS 1 to use oxygen gas. Adjust the oxygen valve just a little smaller than 1.4 mbar.
7. When the pressure is OK, press generator to start the plasma. When time is over, plasma switches off automatically.
8. Oxygen valve off and GAS 1 off
9. Pump off and ventilation on.
10. Remove the sample from the chamber, close the chamber
11. Ventilation off and Pump on.
12. Pump off when pressure below 0.6 mbar
13. Main power off

For the whole oxygen plasma treatment procedure above, only the value of timer Y is varied to investigate the dependence of stretching percentage on the stretching length.

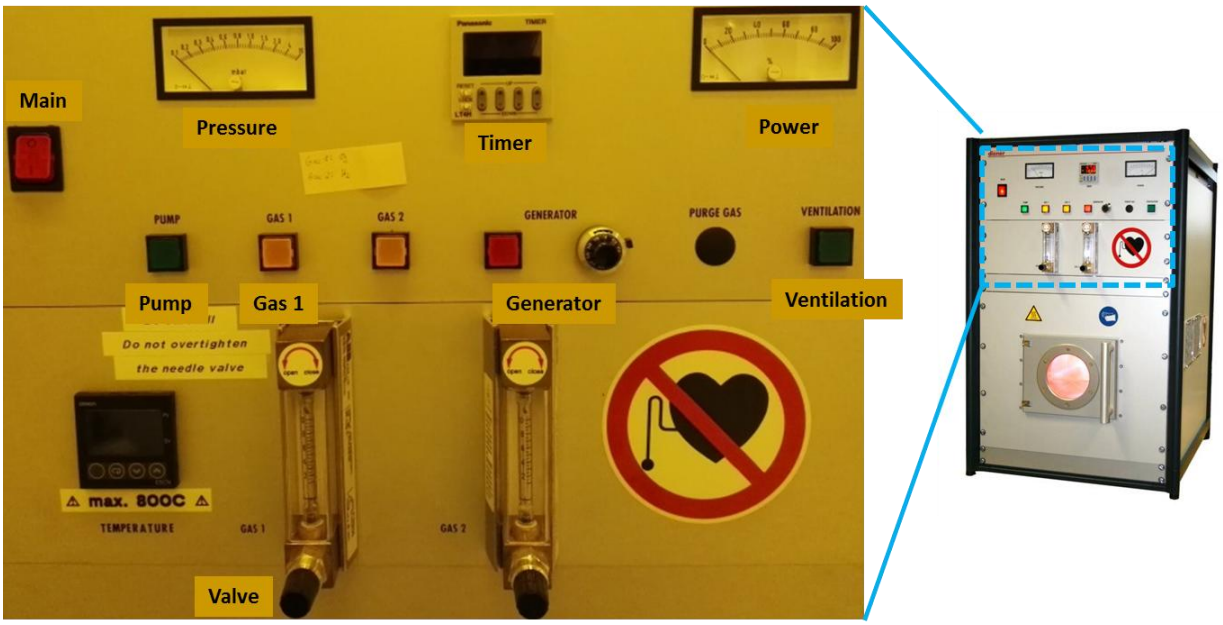

Figure 4. 5: Pico low-pressure plasma system from Diener electronic company.

The periodicity and amplitude of fabricated grating only depend on the percentage of prestrain X and O_2 plasma treatment time Y if the rest parameters are fixed. All the grating samples (not only pure PDMS grating in this section, but also Au, Au/Ni/Au grating in the next sections) in the thesis were fabricated with different X and Y values by keeping other parameters unchanged. The dependence on O_2 plasma time (keeping the prestrain constant at 30%) is shown in Figure 4. 6. We can see, both period and amplitude increase as the treatment time. By treating the PDMS surface with different time less than 9 min, we can have big tuning range of the period (300 nm-550 nm) and amplitude (40 nm-140 nm).

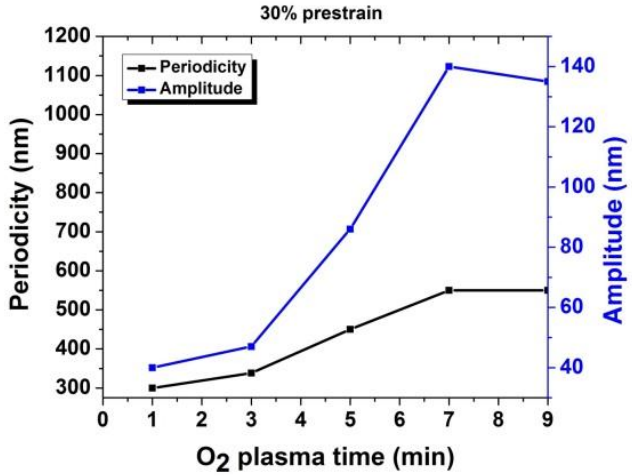

Figure 4. 6: Dependence of grating periodicity and amplitude on O_2 plasma treated time with fixed prestrain at 30%

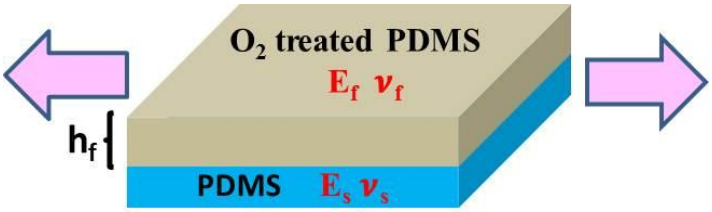

Figure 4. 7: Schematic shows the parameters of the system after O_2 plasma treatment before releasing the pre-strain.

Mechanics models have been developed to calculate the periodicity *P* and amplitude *A* of PDMS grating based on energy method [69]:

$$P = \frac{2\pi h_f}{(1+\varepsilon_{pre})(1+\xi)^{\frac{1}{3}}}\left[\frac{E_f(1-\nu_s^2)}{3E_s(1-\nu_f^2)}\right]^{\frac{1}{3}} \tag{4.1}$$

$$A = \frac{h_f}{\sqrt{1+\varepsilon_{pre}}(1+\xi)^{\frac{1}{3}}}\sqrt{\frac{\varepsilon_{pre}}{\varepsilon_c}-1} \tag{4.2}$$

where as shown in Figure 4. 7, E_f and $E_s$are the Young's modulus of treated stiff thin film and PDMS substrate; ν_f and ν_s are the corresponding Poisson's ratio. h_f is the thickness of the stiff thin film. $\xi = \frac{5}{32}\varepsilon_{pre}(1+\varepsilon_{pre})$ represents the large deformation and geometrical nonlinearity in the substrate under prestrain, ε_{pre} and $\varepsilon_c = \frac{1}{4}\left[\frac{3E_s(1-\nu_f^2)}{E_f(1-\nu_s^2)}\right]^{\frac{2}{3}}$ denote the pre-strain and minimum strain needed to achieve buckling, respectively. The thickness of stiff thin film increases as increasing the oxygen plasma treatment time. So both periodicity and amplitude increase as we can see from Equations (4.1) and (4.2). Besides, the prestrain X also influences the period and amplitude. Amplitude increases and periodicity decreases with the increase of the prestrain [54**,** 56]. Therefore, by tuning both X and Y, we have a big freedom to tune the periodicity and amplitude of gratings. One of our pure PDMS grating samples is fabricated with 25% prestrain and 8 min O_2 plasma treatment. Figure 4. 8 shows three photographs taken at different angles from a fixed light source. The homogeneous colors of the patterned areas (8x13 mm) indicate the high quality and excellent homogeneity of the grating made by our method.

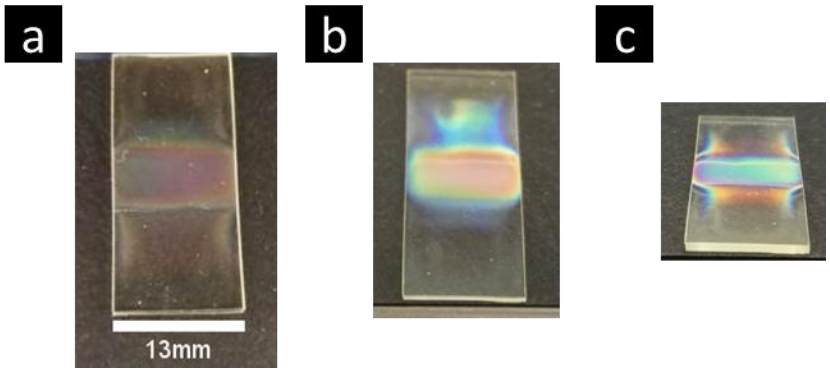

Figure 4. 8: Three photographs taken from different reflection angles with sunlight coming from the incident side with fixed incident angle.

In order to obtain the precise periodicity and amplitude of fabricated grating, AFM was measured. Figure 4. 9 (a) and (b) show the top view and 3 dimensional view of measured AFM image over an area of 5 µmx5 µm, respectively. The fabricated grating had a sinusoidal shape and is quite homogeneous. The periodicity and amplitude of this grating were analyzed from the Gwyddion software to be 670 nm and 140 nm.

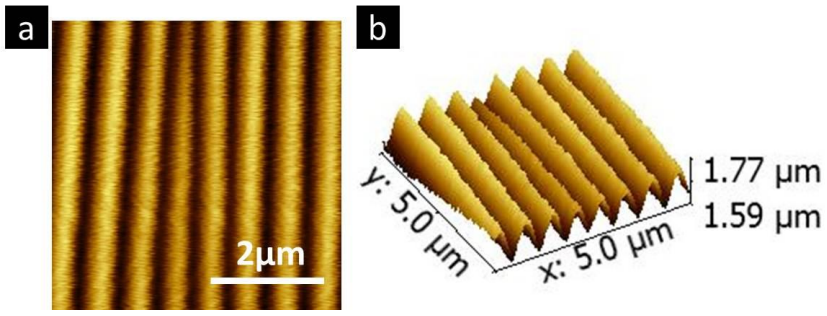

Figure 4. 9: AFM image over an area of 5 µmx5 µm of the grating fabricated with 25% prestrain and 8 min O_2 plasma treatment in (a) top view and (b) 3D view.

4.1.2 Ellipsometry of pure PDMS

Spectroscopic ellipsometric measurements were performed on flat PDMS at AOI35° and 65° over the spectral range from 210 nm to 1690 nm. The complex refractive index of PDMS was extracted from a general oscillator layer model with 1mm thickness. We can see from Figure 4. 10(c) that refractive index *n* increases towards the ultraviolet region and keeps constant at 1.4 in the visible and infrared range. The extinction coefficient *k* is zero over the spectral range from 210 nm to 1690 nm which means our PDMS sample is a very good transparent material without absorption.

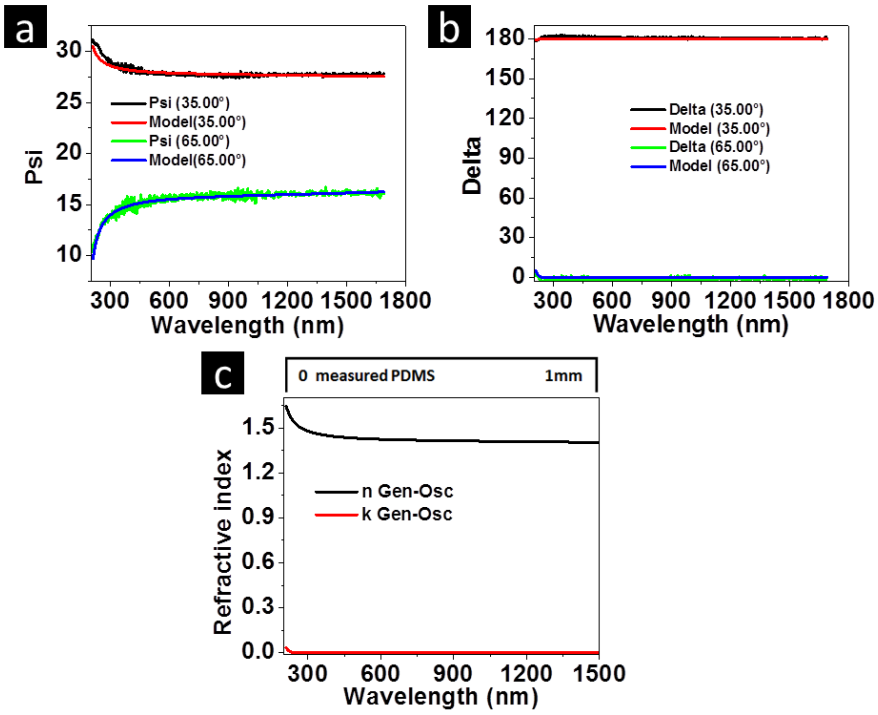

Figure 4. 10: Ellipsometric angles (a) ψ and (b) Δ measured at two different angles of incidence 35° and 65° fitted with a general oscillator model. (c) Refractive index n and k of PDMS extracted from this model.

4.1.3 Mueller Matrix in reflection

To get an insight in the influence of different physical origins on the optical behavior of the PDMS grating, MME measurements were carried out in reflection in the spectral range between 400 nm and 1500 nm at AOI30° and 60° over a complete azimuthal rotation (Figure 4. 11). All the MM elements were normalized to M11 element which represents the total reflectance of the sample. To visualize the huge amount of data accumulated in this kind of measurement, the elements of the MM are presented at a given incident angle as polar contour plots, where the azimuthal angle α is the polar angle and the radial axis represents the wavelength. In general, as we can see from Figure 4. 11, all 16 elements exhibit complex patterns and depend on the azimuthal angle and the wavelength. In reflection, the MMEs show the expected symmetry with identical element pairs M12/M21, M14/M41, M24/M42 and opposite element pairs M13/M31, M23/M32 and M34/M43. All the patterns reflect the symmetry of the grating with optical axes along α=0° and 90°. From the off-block-diagonal elements which are the upper right and the lower left 2x2 sub-matrices and represent the anisotropy and cross-polarization information of the sample, one can see that our simple PDMS grating is strongly anisotropic and therefore mixes polarization states.

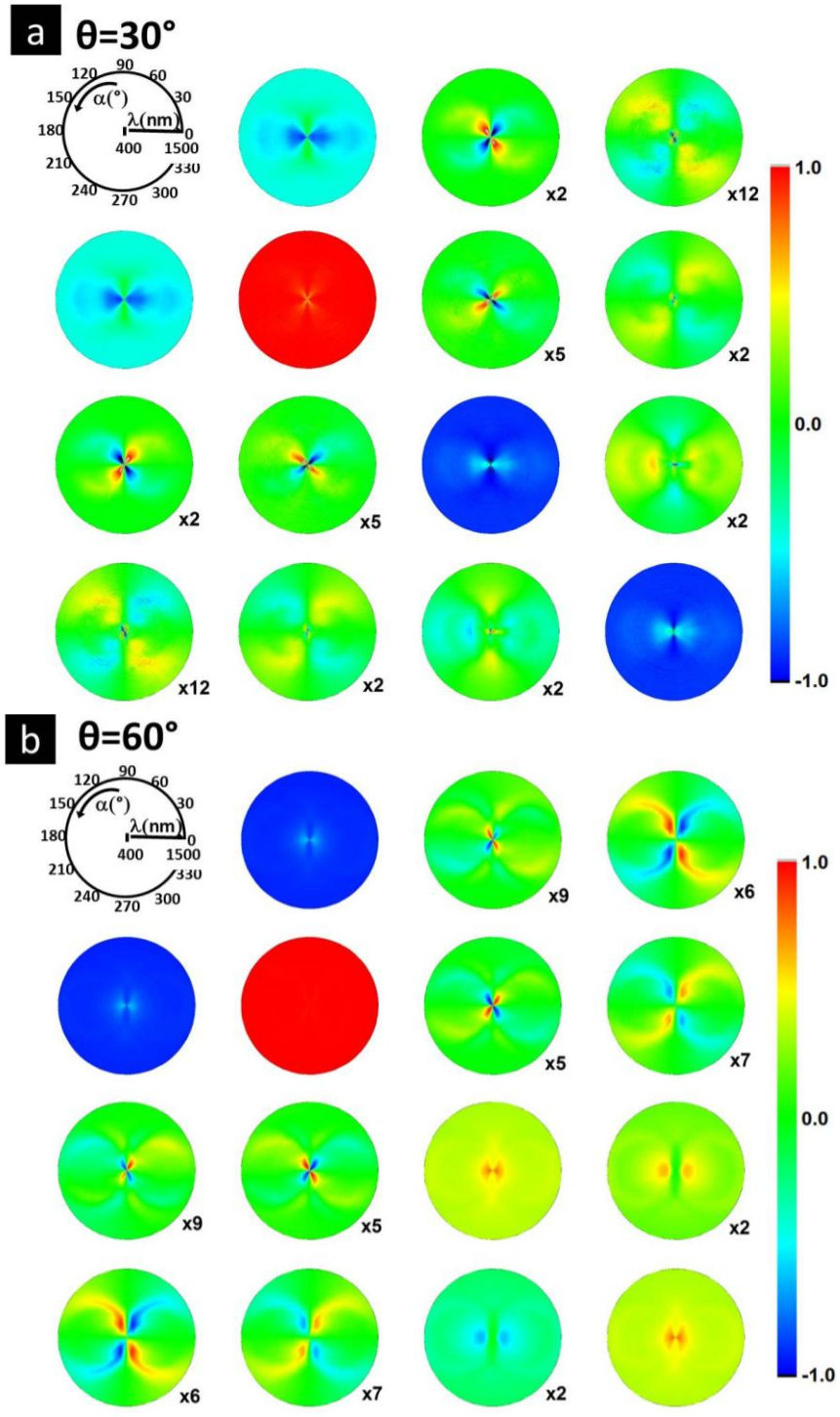

Figure 4. 11: MM measured in reflection at AOI (a) 30° and (b) 60° in the spectral range between 400 nm and 1500 nm as a function of whole azimuthal rotation.

4.1.4 Modelling and interpretation

After viewing the measured MM, we discuss in this section how we decompose the MM into different physical origins via an effective model. From the schematic of diffraction orders in reflection and transmission shown in Figure 2. 14, it is intuitive to see only the negative diffraction orders in reflection and transmission can fulfill the condition of RWAs. $RWAs\_{air(-1)}$ and $RWAs\_{PDMS(-1)}$ which were calculated with Equation 2.93 represent the first negative order RWA in reflection and transmission, respectively. As shown in Figure 4. 12, RWAs_air(-1) and $RWAs\_{PDMS_{(-1)}}$ were superimposed in the MM elements. Along the 180°-0° azimuthal line, we can see from Figure 4. 12(a) that the anisotropy lobe in M12, M33 and M44 is modulated by the presence of the RWAs_air(-1). For other MM elements, we can see lobes at higher wavelength follow RWAs lines. So we can attribute these lobes to the influence of the presence of $RWAs\_{air(-1)}$ and $RWAs\_{PDMS(-1)}$. It is interesting to see all MM at AOI30° and 60° show anisotropy at wavelength near 400 nm. The second order RWAs (not shown) which are supposed to appear at lower wavelength show no clear effect on the MM.

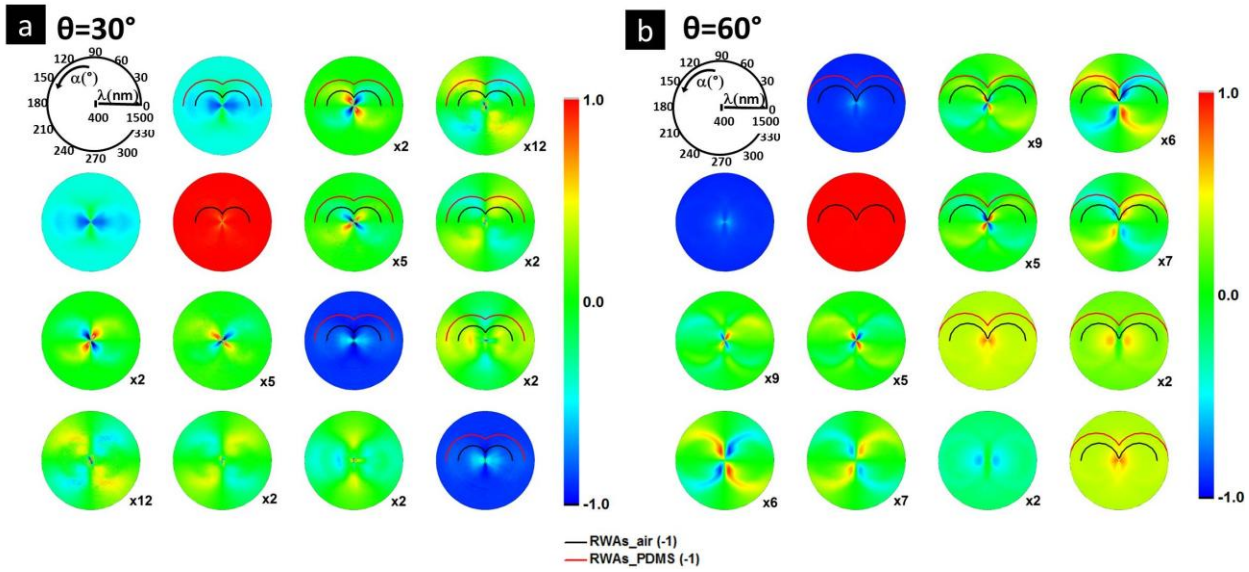

Figure 4. 12: MM measured in reflection at AOI (a) 30° and (b) 60° in the spectral range between 400 nm and 1500 nm as a function of whole azimuthal rotation together with RWAs lines.

In order to understand the hidden physical effects of the anisotropic lobe at lower wavelength, modeling was made. In the first step, we generated the MM of pure flat PDMS layer at AOI 60° in the wavelength range 400 nm to 1500 nm. PDMS layer with optical constants from ellipsometry library was used. The thickness of PDMS layer was defined to be 1mm. As expected from an isotropic material, the values of off-block-diagonal elements are all zero as shown in Figure 4. 13. In addition, the lobes in M12, M21, M33 and M44 are isotropic.

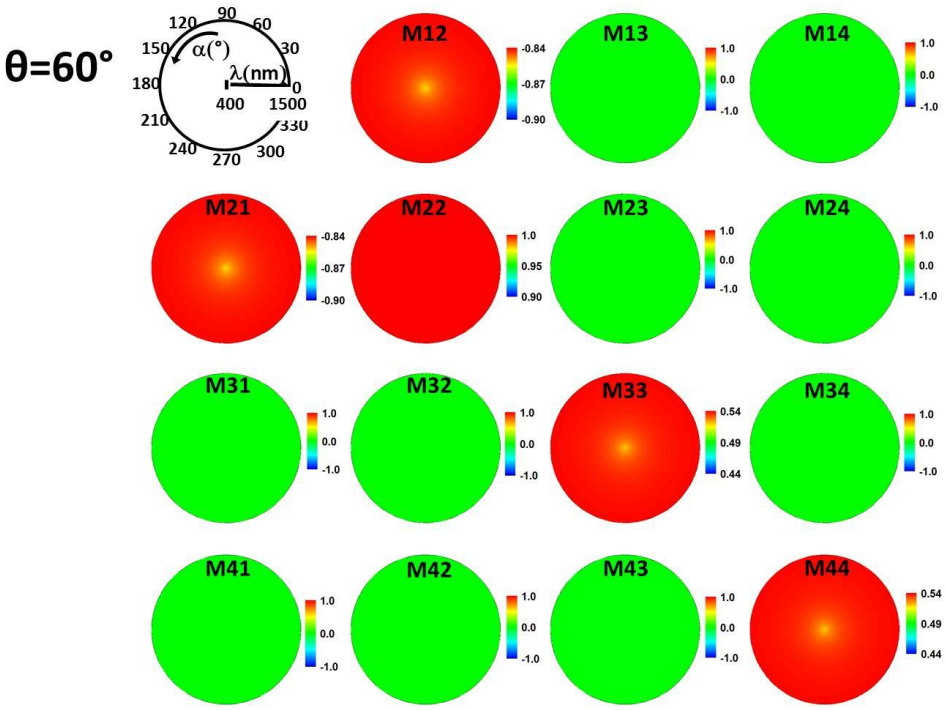

Figure 4. 13: MM generated from ellipsometric model with flat PDMS layer in reflection at AOI 60° in the spectral range 400 nm to 1500 nm as a function of whole azimuthal rotation.

In the second step, according to the geometry of the grating structure, we built an anisotropic model to see the influence of the anisotropy from geometry on the MM elements. As shown in Figure 4. 14, we simulated the grating sample as a biaxial Bruggeman effective medium approximation layer with thickness 110 nm on top of 1 mm substrate of PDMS. The Bruggemann effective medium approximation (BEMA) is a homogeneous system composed by two materials. The equation describes the BEMA is as follows [71]:

$$f_m \frac{\varepsilon_m - \varepsilon_{eff}}{\varepsilon_{eff} + L(\varepsilon_m - \varepsilon_{eff})} + (1 - f_m) \frac{\varepsilon_d - \varepsilon_{eff}}{\varepsilon_{eff} - L(\varepsilon_d - \varepsilon_{eff})} = 0 \tag{4.3}$$

Where ε_m and $f_m$are the dielectric constant and filling fraction for one material, ε_d and $f_d = 1 - f_m$ are the dielectric constant and filling fraction for the other material. L is the depolarization factor and has values in the range (0:1). L is a descriptor of the extent to which the inclusion polarization is diminished according to the particle's shape and orientation with respect to the applied electrical field [72]. In our model, we used a biaxial BEMA layer model, where 3-dimensional shape of the inclusions is defined by L in x, y and z directions (L_x, L_y and L_z). We considered PDMS as the inclusions inside the air environment.

Now I will introduce how we define the parameters in this Biaxial Bruggeman layer. First of all, due to the symmetric geometry of sinusoidal structure, the filling fraction of PDMS f is 50%. From the results of AFM, the periodicity of the grating is about 5 times bigger than the amplitude. So, we defined PDMS inclusions as elliptical shape with long axis along x direction

as shown in the cross-section in Figure 4. 14. In the 3-dimensional space, the inclusions are cylinders with infinite length along y direction. So, we defined depolarization factors in x, y and z directions as L_x=0.25, L_y=0 and L_z=0.75.

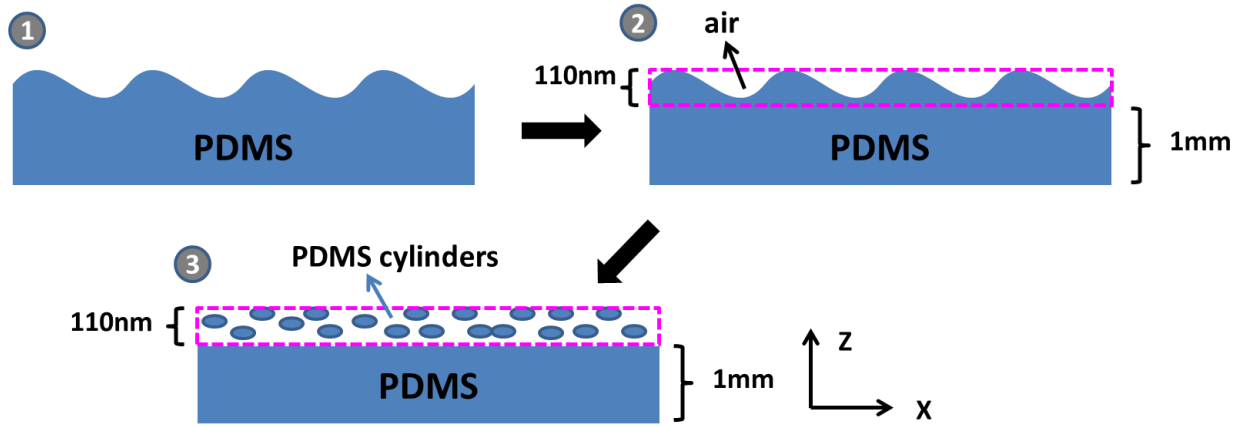

Figure 4. 14: Biaxial Bruggeman effective medium approximation model for PDMS grating.

Then, MM in reflection at AOI 30° and 60° were calculated from this effective model. Figure 4. 15 shows the measured and simulated MM at AOI 30° in the spectral range from 400 nm to 1500 nm as a function of whole azimuthal rotation. Figure 4. 16 shows the measured and simulated MM at AOI 60°. In order to obtain a better visualization due to weak values in some MM elements, we scale some elements with multiplication factors. For convenience of comparison, measured and simulated MM have same multiplication factors. We can see all the MM element at AOI 30° and 60° reproduce the anisotropy at wavelength close to 400 nm, while the lobes at higher wavelength cannot be reproduced. Our effective model only considers the geometry of the grating which is described by the depolarisation factor (L_x, L_y, L_z) of PDMS inclusions but neglects the effects from periodicity. Therefore we can say the anisotropic lobe at wavelength near 400 nm is coming from the pure geometry of the grating. Since the periodicity is neglected in the model, our RWAs effects cannot be generated. However, by adding the lobes manually which following the RWAs lines on the simulated MM elements, we can reproduce the measured MM.

To conclude, the physical origin shown by measured MM can be decomposed into two parts, one at lower wavelength coming from the pure anisotropy from geometry and the other one at higher wavelength from RWAs.

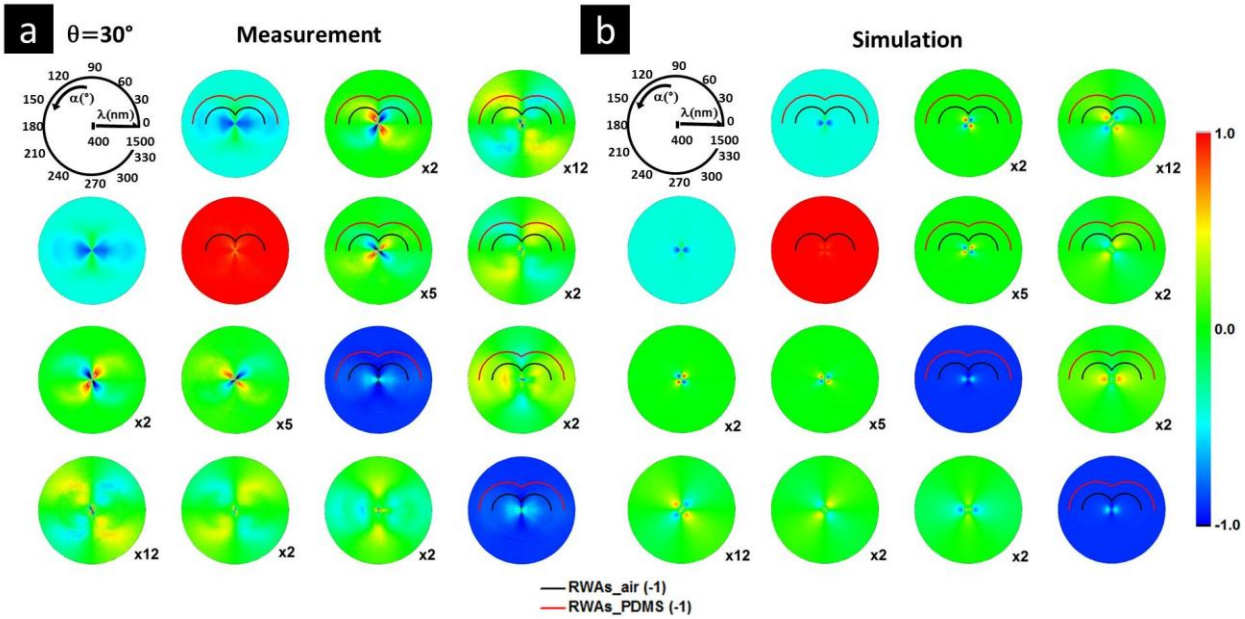

Figure 4. 15: MM measured and simulated in reflection at AOI 30° as a function of whole azimuthal rotation together with RWAs lines.

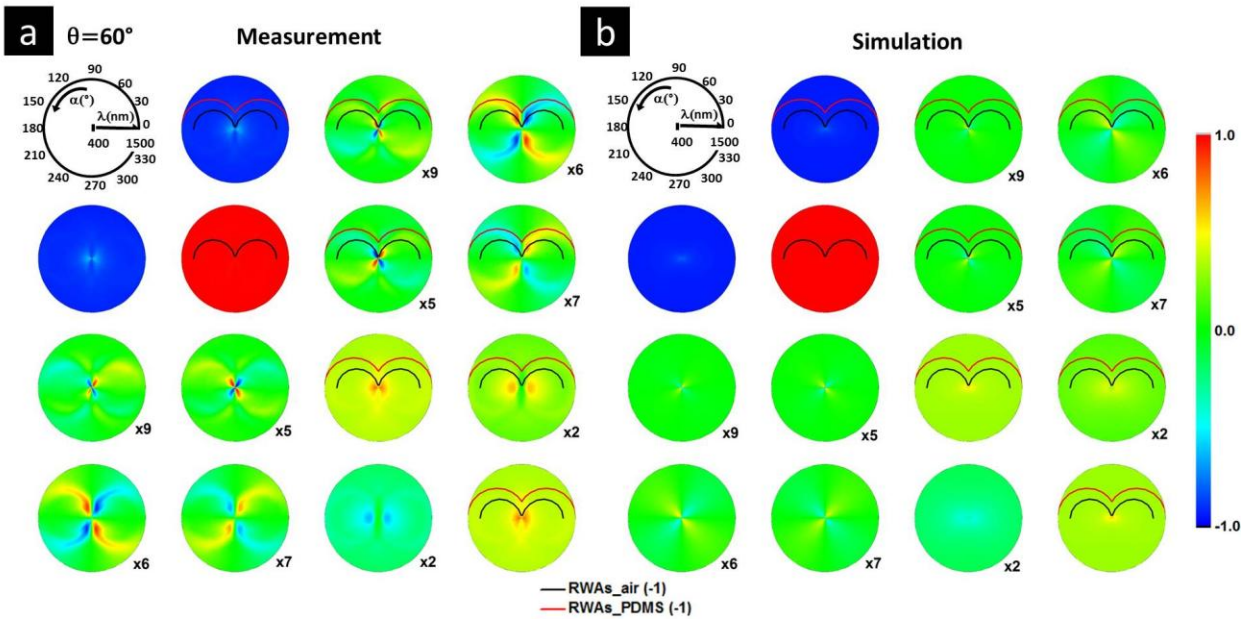

Figure 4. 16: MM measured and simulated in reflection at AOI 60° as a function of whole azimuthal rotation together with RWAs lines.

4.1.5 Conclusion

In summary, we have demonstrated how the complex optical response of a simple sinusoidal PDMS grating can be decomposed into its physical ingredients. First, we measured the MM in refection at different AOI over a complete azimuthal rotation. The MM was then modelled by a simple anisotropic effective medium approach called Biaxial Bruggeman effective approximation. From this simple anisotropic model, the MM plots over the whole spectral and angular range were generated. On top of this calculated MME we superimposed the expected dispersive RWA modes, calculated from the known periodicity of the grating. Comparing this composed result with measured MMs gives a deep insight on how the different physical contributions originating from periodicity and geometry influence the complex polarization mixing.

4.2 Au gratings

After showing PDMS gratings in the previous section, we turn out attention to metallic gratings formed by evaporating a thin Au layer on top of PDMS gratings. The presence of propagating surface plasmon modes makes the optical response more complex than the PDMS gratings. Mode coupling or hybridization can take place and results in complex interactions with polarized light which is very interesting to be unraveled by MM characterization. Similar to PDMS gratings, our goal is to correlate the observed polarization mixing in MMs to their underlying physical origins via effective media approximation model.

4.2.1 Introduction

One-dimensional metallic gratings are very efficient tools to excite SPPs by matching their dispersion to that of light. Figure 4. 17 shows the measurement configurations. α=0° is defined as the classical mounting which means that the grating ridges are perpendicular to the plane of incidence of the incoming light, while $\alpha\neq$0° is defined as conical mounting. The excitation of SPPs in one-dimensional gratings follows either the classical mounting or the conical mounting.

For classical mounting, where α=0° as shown in Figure 4. 17 (a), p-polarized light instead of s-polarized light is used to excite the SPPs. In this configuration, the propagation direction of SPPs is along the grating vector. Contrary to the case α=0°, as shown in Figure 4. 17(c), s-polarized light rather than p-polarized light can excite the SPPs at α=90°. In this case, in plane wave vector of incident light K_x, grating vector G and wave vector of SPP K_{spp} form a right triangular relation. For all other azimuthal rotations, the symmetry is broken and both p- and s-polarized light can be used to excite SPPs [73], [74] as shown in Figure 4. 17(b). The propagating direction of SPPs can be determined from the triangle relation between K_x, G and K_{spp} regardless of any azimuthal rotations.

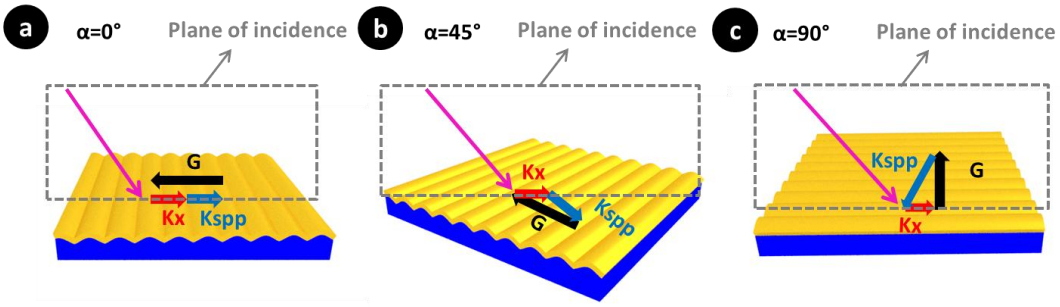

Figure 4. 17: Schematic drawing of the measurement configuration at (a) α=0° (b) α=45° and (c) α=90°. α is the azimuthal angle with α=0° for classical mounting and $\alpha\neq$0° for conical mounting.

Similar to PDMS gratings, RWAs is expected to induce abrupt changes in the optical response of Au gratings. RWAs can result in very narrow plasmon resonances in regular plasmonic arrays of metallic nanoparticles, originating from the diffraction coupling of localized plasmons [75]–[79], or modify the reflectance of non-plasmonic metallic square arrays [80].

Even though SPPs have been studied for a long time and RWA effects have also been well known for decades [48], [81]–[84], a clear understanding of how SPPs and RWAs influence the polarization mixing of gratings is still lacking. Moreover, so far, only few reports discuss the

azimuthal angle dependence of the optical response of gratings in terms of MMs or the influence of diffraction orders in MM elements (MMEs) [28], [85].

Here we present a simple but versatile method to identify the physical properties present in the Mueller matrices. We present a very general procedure to analyze the MM data of a one-dimensional gold grating using simple analytical tools. The calculated MM contour plots obtained from an effective anisotropic layer model which is different from the effective anisotropic model in section 4.1 are completed by the presence of plasmonic modes, Rayleigh-Woods anomalies and the interband transition absorbance. A comparison of the so-constructed contour plots with the measured ones satisfactorily connects the optical properties of the grating to their physical origin.

4.2.2 Sample Fabrication

For our study we use Au gratings produced by the same self-assembly technique as described in section 4.1. First of all, the PDMS grating template was fabricated with 30% prestrain and 10 min O_2 plasma treatment. Then, the PDMS grating template was treated again by O_2 plasma for 1 minute to increase the surface hydrophilicity and enable the deposition of a homogeneous metallic thin film. A 35 nm thin gold film was finally evaporated (Univex 300) on the sample surface while keeping the time after plasma treatment as short as possible to avoid degradation of the surface treatment (less than 1 h). An AFM image over an area of 5 µmx5 µm is shown in Figure 4. 18(b). The AFM analysis reveals that the fabricated gratings have a regular grating period equal to p=570 nm. The depth of the grating is estimated to H=100 nm. Figure 4. 18(c) shows five photographs taken at different angles from a fixed light source. The homogeneous colors of the patterned areas change from blue to red with increasing viewing angle indicating the high quality and excellent homogeneity of the grating.

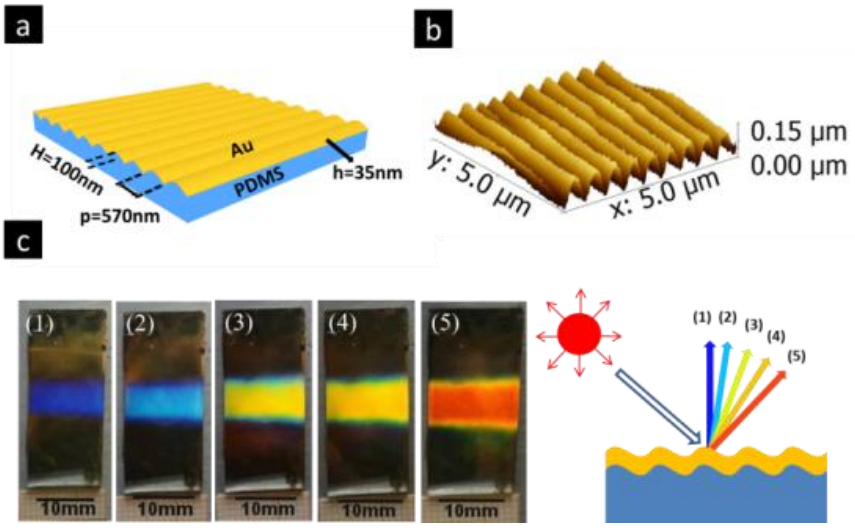

Figure 4. 18: (a) Schematic drawing and (b) 3D AFM image of the sinusoidal Au grating with period p=570 nm, amplitude H=100 nm and Au thickness h = 35 nm. (c) Five photographs taken from different reflection angles with sunlight coming from the incident side with fixed incident angle. The numbers of the photographs are related to the angles in the schematics in the right inset.

4.2.3 Reflectance dispersion

In order to visualize the dispersion of the excited modes, the measured reflectance for p and s-polarized light at AOI from 25° to 65° are shown together with the expected positions (dashed lines) of the SPPs and RWAs in Figure 4. 19(a) and (b). Figure 4. 19(a) shows the reflectance measured with p-polarized light at an azimuthal angle α=0°. The dispersion from 822 nm at AOI 25° to 1052 nm at AOI 65° indicates the excitation of SPPs propagation along the sample surface. The line cut on the left side represents the values at AOI 45° along the vertical dotted lines. SPP dispersion relation is calculated and shown by a black dashed line and it follows the measured SPPs mode dispersion. The air (-1 order) RWA indicated by the red dashed curve is slightly shifted to lower wavelength from SPPs positions. Figure 4. 19(b) shows the reflectance measured with s-polarized light at α=90°. Interestingly, s-polarization also excites a surface plasmon resonance at α=90° indicated by an resonance around 570 nm for AOI 25° and around 515 nm for AOI 65° and it also fits quite well with the calculated SPP line. The reflectance at AOI 45° with SPP excited around 540 nm is shown in the line cut. However, instead of the large red shift as for p-polarization, the SPP excited by s-polarization blue shifts slightly with increasing AOI. Besides, the RWAs_air(-1) at α=90° does not follow the SPP anymore and strongly influences reflectance away from the SPP resonance.

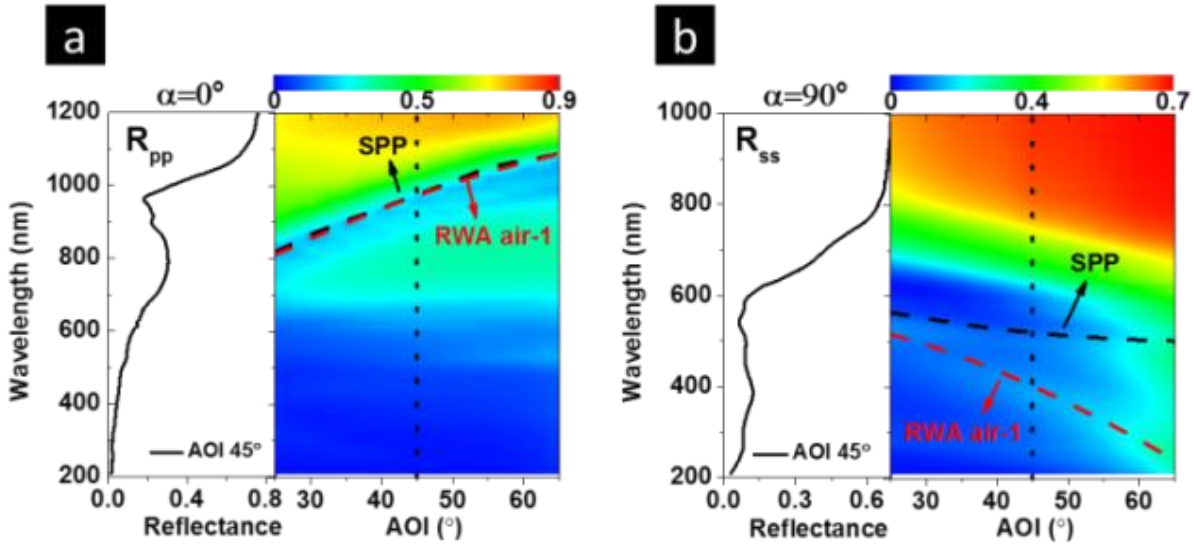

Figure 4. 19: (a) Contour plot of the reflectance with p-polarized light between AOI 25° and 65° in steps of 5° at α=0° in the spectral range between 210 and 1200 nm. (b) Contour plot of the reflectance with s-polarized light between AOI 25° and 65° in steps of 5° at α=90° in the spectral range between 210 and 1000 nm. The dashed lines in the contour plots correspond to SPPs and RWAs. The line cuts in the left side of (a) and (b) are reflectance measured at AOI 45°, along the dotted lines, with p-polarized light at α=0° and with s-polarized light at α=90°, respectively.

4.2.4 Reflectance angular dependence

In order to visualize the azimuthal dependence of the excited modes, the measured reflectance for p and s-polarized light at AOI from 25° to 65° by 10° over a complete azimuthal rotation in

steps of 5° in the spectral range between 210 nm and 1200 nm together with SPPs is shown in Figure 4. 20. To illustrate the influence of RWAs at higher angle of incidence, the expected position of RWAs_air(-1) is only superimposed in R_{ss} at AOI 65°. As expected, the reflectance shows a simple C2-symmetric behavior due to the symmetry of the grating. According to Equation (2.83), the optimal azimuthal angles for SPP excitation with p- and s- polarized light is at α=0° and α=90°, respectively. The positions of the excited resonances (i.e., reflectance dips) in Figure 4. 20 follow the calculated SPPs lines very well confirming their plasmonic origin. We can see that the SPP mode excited by s-polarized light becomes weaker, while the influence from RWAs_air(-1) becomes stronger with increasing the AOI. This is in accordance with the dispersion plot shown in Figure 4. 19(b).

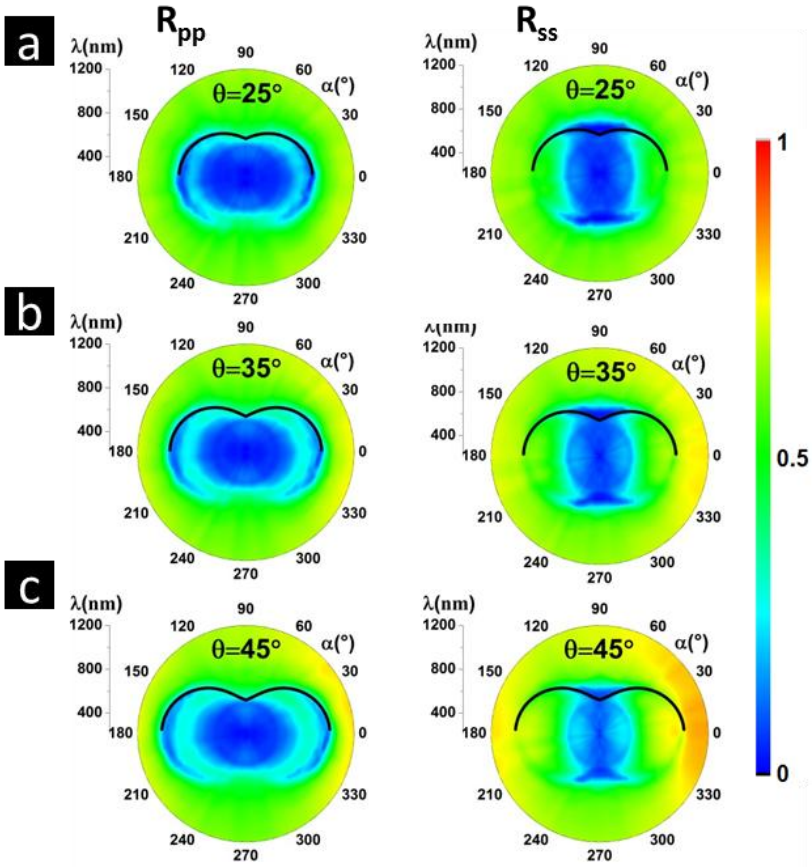

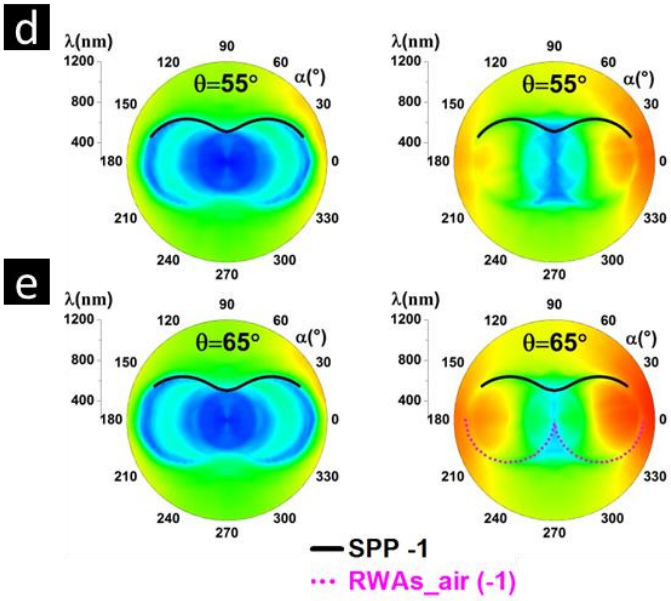

Figure 4. 20: Measured R_{pp} and R_{ss} at θ from 25º to 65º by 10º are plotted with full azimuthal rotation in the spectral range from 210 nm to 1200 nm. The black and magenta lines indicate the calculated position of the SPP mode and $RWAs_{air(-1)}$, respectively.

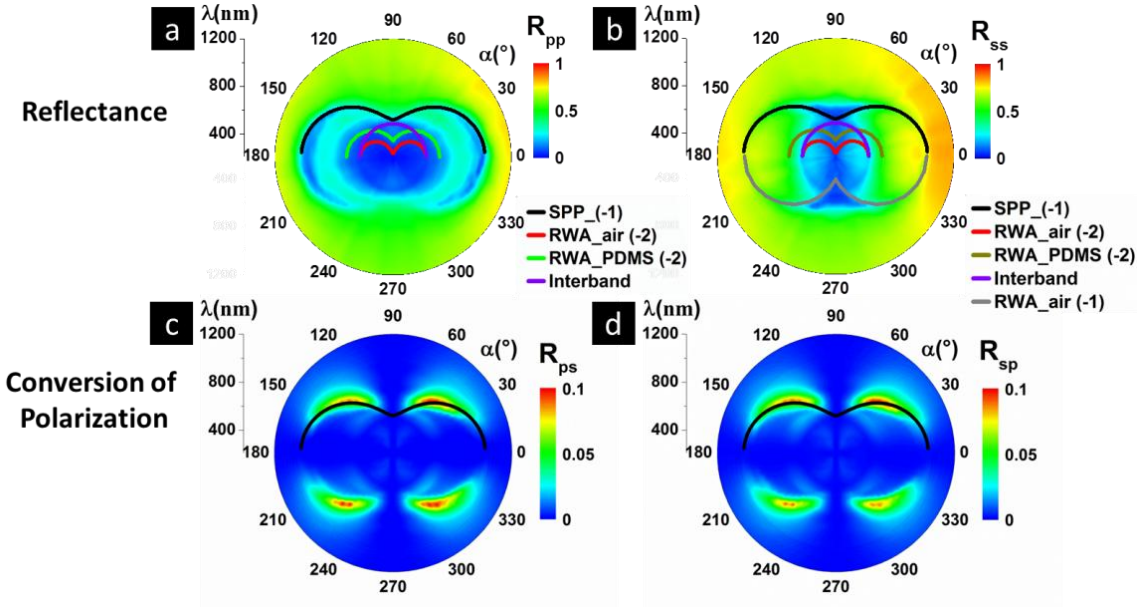

Figure 4. 21: Contour plots of experimental reflectance with p-polarized (a) and s-polarized light (b) together with the SPPs, different order RWAs and the interband transition lines. The excitations are only plotted in the upper half-space to avoid masking of the raw data in the other half space. (c), (d) experimental polarization conversion R_{ps} and R_{sp} with SPP lines. All the contour plots are at AOI 45° over a complete azimuthal rotation in step of 5° in the spectral range between 210 nm and 1200 nm. The polar axis represents the wavelength λ and the polar angle represents the azimuthal angle α.

Figure 4. 21(a) and (b) show the measured reflectance for p- and s-polarized light at AOI 45° together with SPPs, RWAs and interband transition lines. The interband transition of Au at 480 nm [86] exhibits no dispersion and therefore corresponds to a circle in the polar plot, while the azimuthal dependent RWAs form arched curves. In Figure 4. 21(a) and (b) the influence of the RWAs is in general rather weak. In Figure 4. 21(c) and (d), the polarization conversion R_{ps} (incoming p-into reflected s-polarized light) and R_{sp} (vice versa) are shown. As expected for a C2-anisotropic sample R_{ps} and R_{sp} are identical with maximum values at α=45° and two optical axes at α=0° and 90°. The polarization conversions R_{ps} and R_{sp} basically trace the calculated SPPs curve, indicating that polarization conversion is mainly caused by surface plasmons and that the contribution of the RWAs is small. The isotropic interband transition exhibits no polarization conversion.

In the previous section, we already know the wavelength position of SPPs. From phase matching relation described by Equation (2.80), we can also obtain the propagating direction of SPPs. In Equation (2.80), the wave vector of SPPs can be described as the sum of the in-plane incident wave vector K_x and an integer multiple of the grating vector G. Experimental reflectance in Figure 4. 21(a) and (b) are expressed in contour plot with Cartesian coordinate system in Figure 4. 22(a) and (b). The insets show the phase matching relations at different azimuthal angles. We can see from Figure 4. 22(a), by using p-polarized light, SPPs propagates perpendicular to the grating grooves only when the in-plane component of incident wave vector is perpendicular to the grating grooves. At α=90°, SPPs cannot be excited with p-polarized light. However, we can see from Figure 4. 22(b), s-polarized light can excite SPPs at α=90°. Besides, K_x, G and K_{spp} form a right angular relation at α=90°.

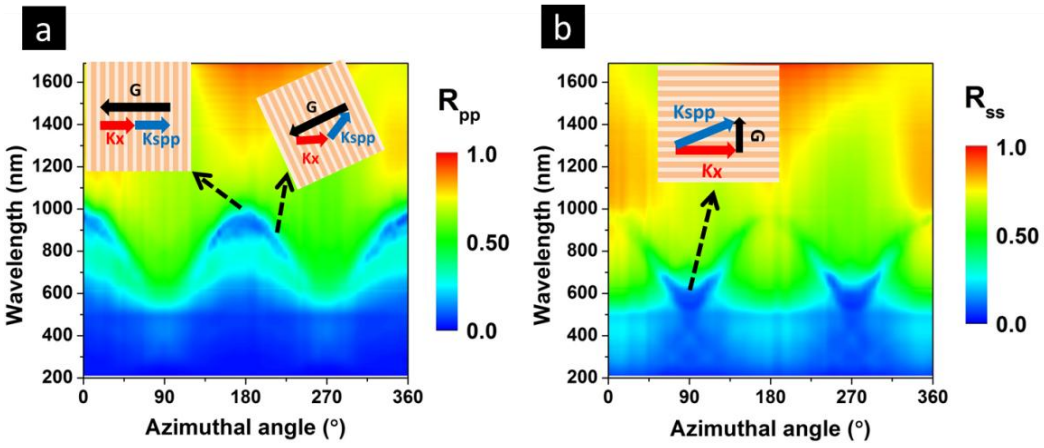

Figure 4. 22: Contour plots of experimental reflectance with (a) p-polarized and (b) s-polarized light over a complete azimuthal rotation in Cartesian coordinate together with phase matching relation in the insets.

4.2.5 Mueller matrix in reflection

To get a deeper insight in the influence of SPPs and RWAs on the complex optical behavior of the Au grating, MME measurements were carried out in reflection geometry in the spectral range between 210 nm and 1200 nm at AOI from 25° to 65° by 10° over a complete azimuthal rotation (Figure 4. 23). All the MM elements are normalized to M11 element which represents the total

reflectance of the sample. MM are presented at a given AOI as polar contour plots, same as MM plotted for PDMS gratings in section 4.1. Also, some elements are scaled with multiplication factors to improve visualization. In general, we can see all 16 MM elements exhibit complex patterns and show the expected symmetry in reflection. All the patterns reflect the symmetry of the grating with optical axes at α=0° and 90°. From the off-block-diagonal elements, one can see that the Au grating is strongly anisotropic and therefore mixes polarization states. Moreover, the off-block-diagonal elements show curved lobes with maxima around α=45° and 135° at the excitation wavelengths of the dispersive SPP and RWA modes. The element M12 represents linear dichroism and reflects R_{ps} and R_{sp}, which are equal. The diagonal elements resemble the reflectance plots of Figure 4. 20. We can see the anisotropy at lower wavelength becomes weaker at higher angle of incidence. The lobes near azimuthal angle 90° in M12, M33 and M43 become weaker as increasing AOI. These lobes come from the SPPs excited by s-polarized light. SPPs become weaker as increasing AOI which are shown in the reflectance plots (Figure 4. 19(b)). Moreover, we can see the lobes near azimuthal angle 90° which follow the SPP lines in M23 at AOI 35° disappear at AOI 55°. By multiplying the MM by an input Stokes vector corresponding to p-polarized light S_{in}=(1 1 0 0) or s-polarized light S_{in}=(1 -1 0 0) we obtain a contour plot equal to measured R_{pp} or R_{ss} (not shown).

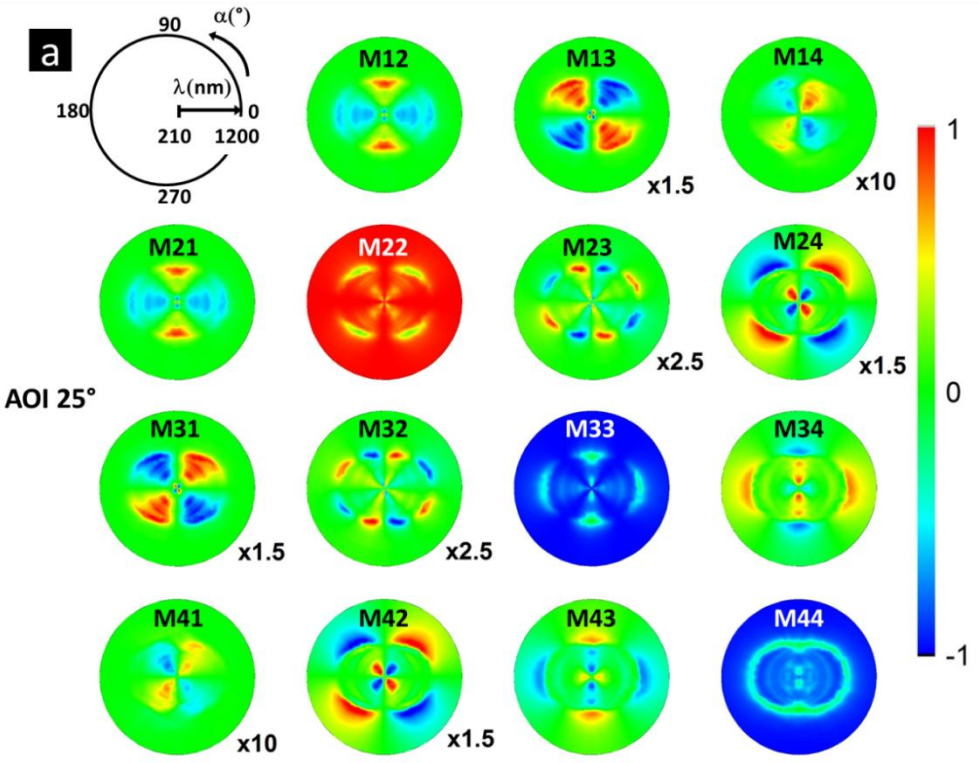

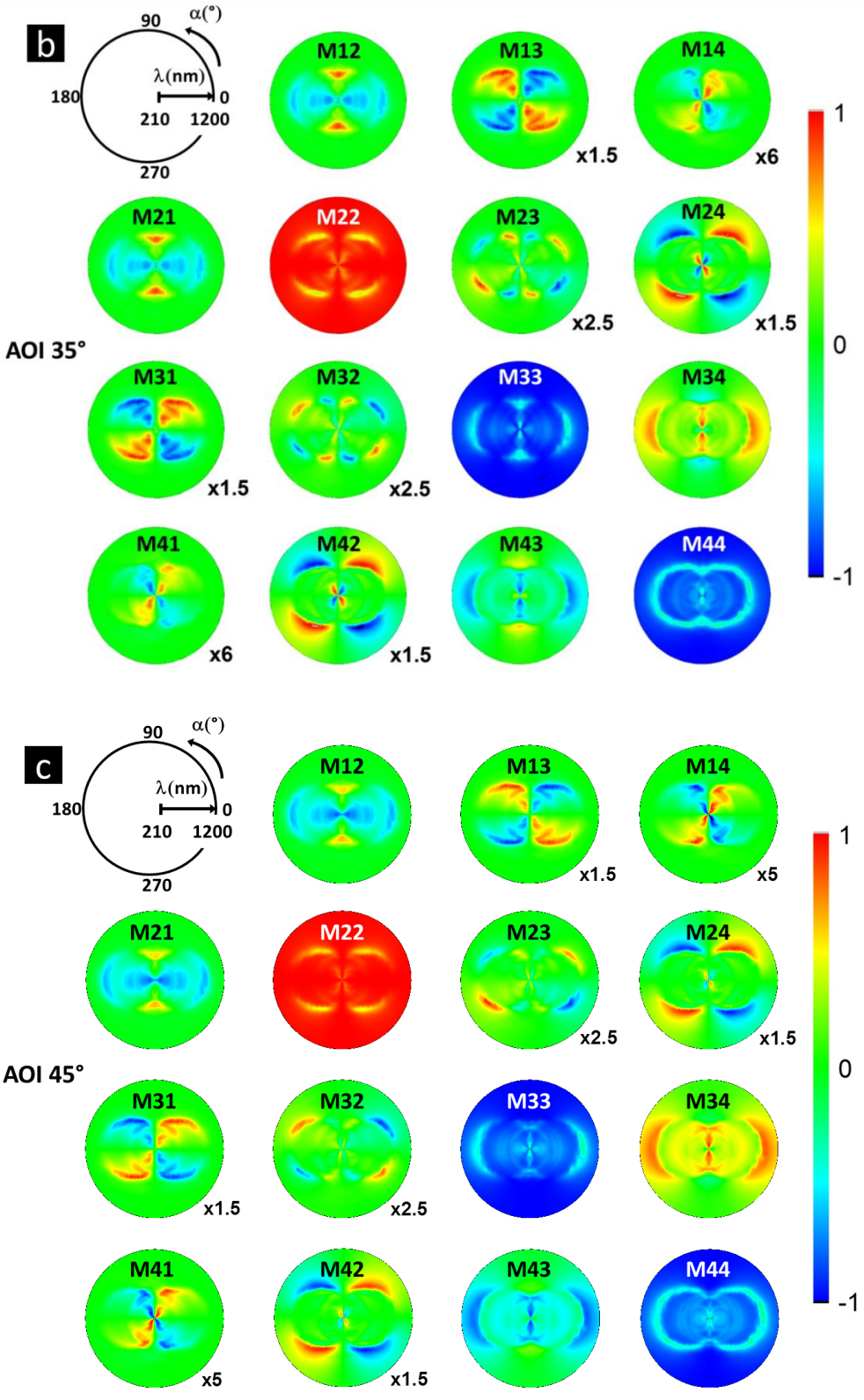
b
90
α(°)
λ(nm)
180
0
210
1200
270
M12
M13
x1.5
M14
x6
M21
M22
M23
x2.5
M24
x1.5
AOI 35°
M31
x1.5
M32
x2.5
M33
M34
M41
x6
M42
x1.5
M43
M44
1
0
-1
c
90
α(°)
λ(nm)
180
0
210
1200
270
M12
M13
x1.5
M14
x5
M21
M22
M23
x2.5
M24
x1.5
AOI 45°
M31
x1.5
M32
x2.5
M33
M34
M41
x5
M42
x1.5
M43
M44
1
0
-1

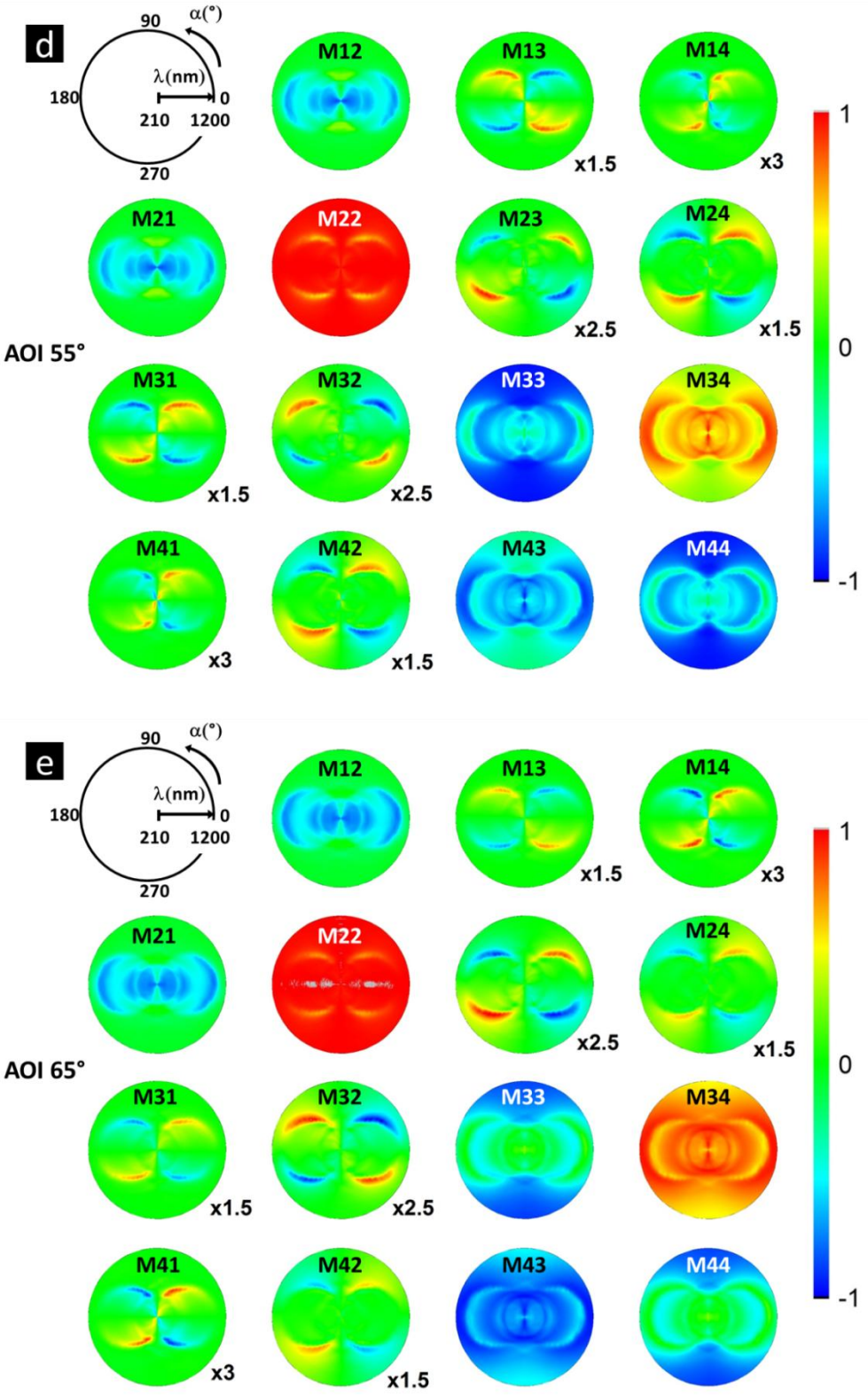

Figure 4. 23: MMEs measured in reflection at AOI from 25° to 65° by 10° over the complete azimuthal rotation in the spectral range between 210 nm and 1200 nm. All MMEs are normalized to M11.

4.2.6 Biaxial Model

In principle it is of course possible to calculate the MMs for different angles of incidence, various azimuthal orientations and a broad range of frequencies by solving the Maxwell-equations under the boundary conditions given by the 3-dimensional geometry of the grating. But this approach is on the one hand time-consuming and computer intensive and on the other hand it does not really promote the physical understanding of the origin of the observed optical behavior. In order to correlate the observed MM pattern to the known properties of the grating, i.e., its periodicity, the material parameters and the SPP and RWA modes, we present here a much simpler 2-dimensional approach based on a cumulative method, starting with a simple anisotropic effective medium model based on the Fresnel equations to which we add the dispersive modes described above. To begin with a simple anisotropic effective medium model, the dielectric function of PDMS and 35 nm Au is required.

Dielectric function of Au layer

In order to obtain the dielectric function of the Au layer, spectroscopic ellipsometry measurement was performed on a 35 nm thin gold film which is evaporated on an O_2 plasma treated flat PDMS slab under the same evaporation conditions as the Au grating sample at AOI from 20° to 60°. Then an Au_nk1 layer with 35 nm from the CompleteEase software was used. Figure 4. 24 show the measured and modeled ellipsometric angles ψ and Δ as a function of broad range of wavelength from 210 nm to 1690 nm. Both measured ψ and Δ fit the modeled ones. So, we can say 35 nm Au thin layer is already a flat film and has the similar dielectric function with Au_nk1. In the next sections, dielectric function of Au_nk1 as shown in Figure 4. 25 is used in simulations to represent the dielectric function of the 35 nm Au.

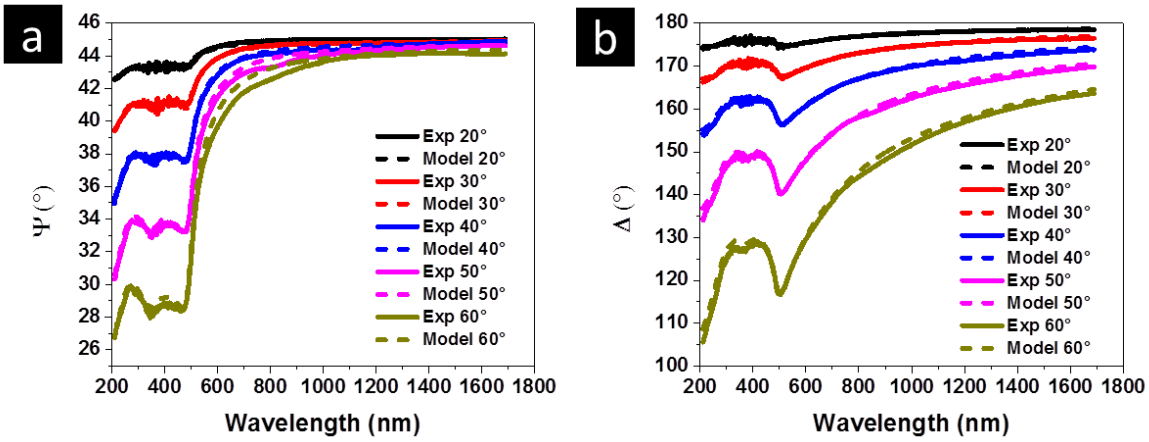

Figure 4. 24: Spectroscopic ellipsometric angles ψ and Δ at AOI from 20° to 60° in the spectral range from 210 nm to 1690 nm.

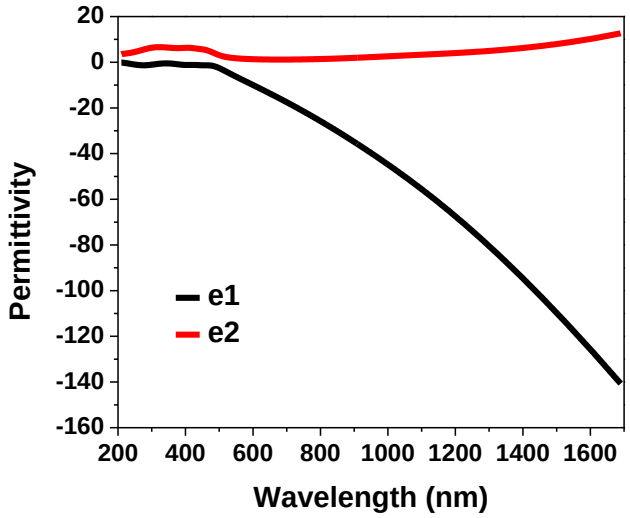

Figure 4. 25: Dielectric function of 35 nm Au.

After obtaining the dielectric function of PDMS and Au layer, we start to prepare an optical model able to reproduce the measured intensity taking into account the anisotropy of the sample. According to the symmetry of the grating, the sample has two optical axes along X and Y. Therefore, we model the reflectance along α=0° and α=90° using Gaussian oscillators with the ellipsometry software [18]. The extracted permittivity of PDMS with 1 mm thickness is used as substrate of for all models. A 35 nm thick biaxial layer is placed on top of the substrate. Along Z direction normal to the layer interface, a Cauchy oscillator is used, while in X and Y directions we use general oscillator models. The parameters of the oscillators in X and Y direction are obtained by fitting the measured reflectance R_{pp} and R_{ss}, along the azimuthal angles 0° and 90°. The model generated by fitting the measured R_{pp} (R_{ss}) along its optical axis is called in this work "p-model" and "s-model" respectively.

P-model

In a first step, R_{pp} at α=0° is modeled with a 35 nm general oscillator layer (genoscx) on measured PDMS layer using nine Gaussian oscillators. Then R_{pp} at α=90° is modeled with 35 nm general oscillator layer (genoscy) on measured PDMS layer using seven Gaussian oscillators and one Drude oscillator. A perfect fit was obtained in both directions as shown in Figure 4. 26(a) and (b). Then, as shown in Figure 4. 26(c), a biaxial model is built with a Cauchy oscillator along Z direction and genoscx and genoscy in X and Y directions, respectively. The thickness of the biaxial layer is also 35 nm and the measured PDMS is used as substrate of thickness 1mm.

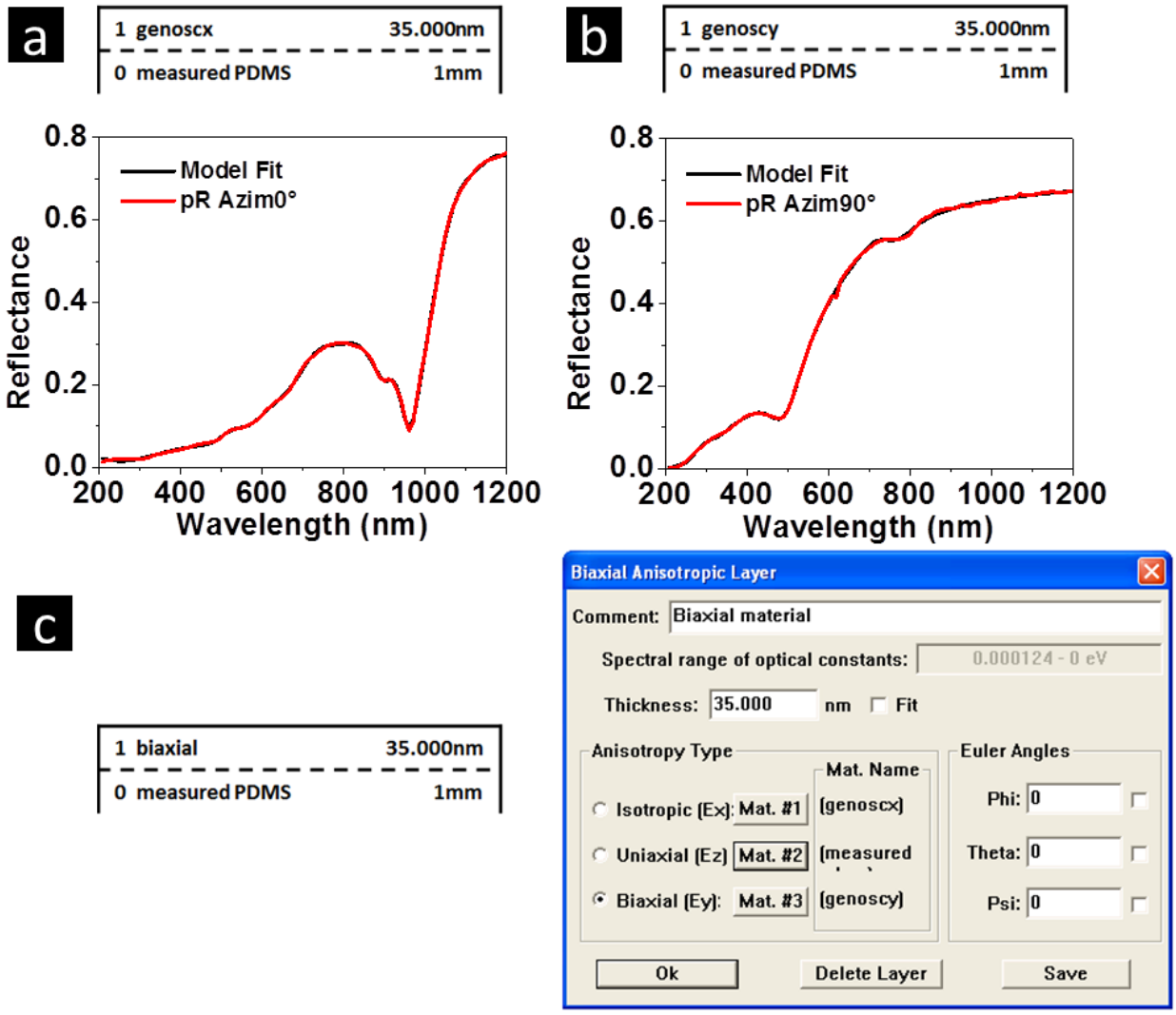

Figure 4. 26: (a) Genoscx and (b) Genoscy layer model with the R_{pp} fit at α=0° and 90° respectively. (c) Biaxial layer model.

S-model

The reflectance R_{ss} at both angles α=0° and α=90° were fitted in the S-model. R_{ss} at α=90° is modeled with a 35 nm general oscillator layer (genoscx) on the measured PDMS layer by eight Gaussian oscillators. R_{ss} at α=0° is modeled with 35 nm general oscillator layer (genoscy) on the measured PDMS layer by twelve Gaussian oscillators and one Drude oscillator. A perfect fit was obtained by genoscy layer model at α=0° shown in Figure 4. 27(b), the fit at α=90° (Figure 4. 27(a)) is not perfect but still works well. Then as shown in Figure 4. 27(c), a biaxial model is used with a Cauchy oscillator along Z direction and genoscx and genoscy in X and Y directions, respectively. Similarly to the p-model, the biaxial layer is 35 nm thick and again PDMS is used as a substrate.

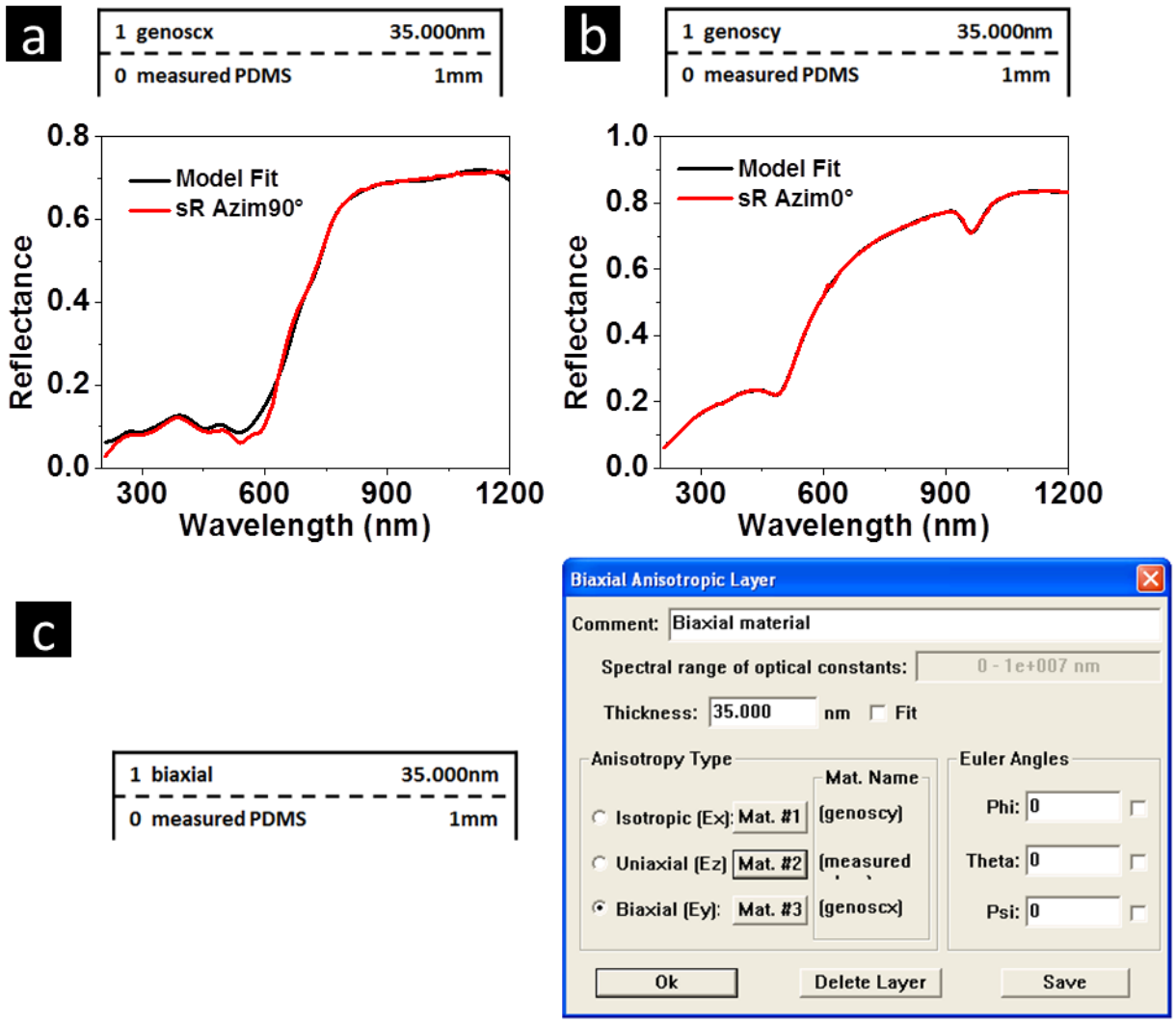

Figure 4. 27: (a) Genoscx and (b) Genoscy layer model with R_{ss} fit at α=90°and 0° respectively. (c) Biaxial layer model.

4.2.7 Modelling results and interpretation

Modelled reflectance

Using P- and S- models, we start by calculating both the p- and s-reflectance at AOI 45° over the whole azimuthal range and compare the result with the experimentally obtained reflectance plots in Figure 4. 28. The expected anisotropy of the reflectance is visible in both, the experimental and the modelled plots. The calculated and measured R_{pp} and R_{ss} are very similar.

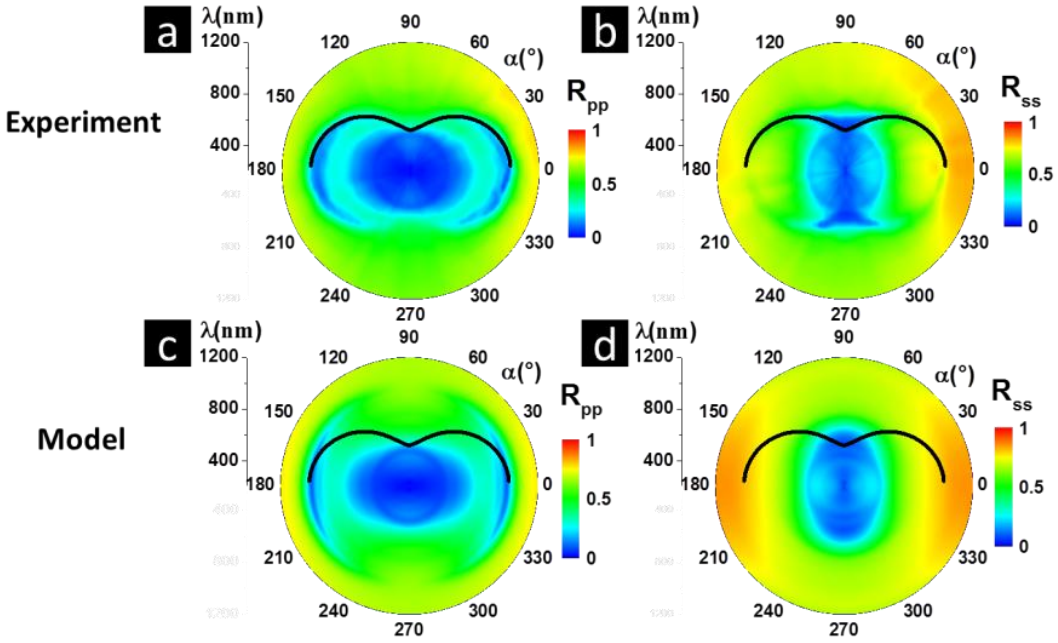

Figure 4. 28: R_{pp} (a) and R_{ss} (b) measured at AOI 45° over a complete azimuthal rotation in the spectral range between 210 nm and 1200 nm. R_{pp} (c) and R_{ss} (d) generated from the p- and s-biaxial models, respectively. All the plots are shown together with the calculated SPP lines in the top half space.

The second step of the method is to add the analytically calculated positions of the excited SPPs from Equation (2.82), which is also shown in all graphs of Figure 4. 28. Since no dispersion effects are included in our biaxial models, the dispersive SPP modes are not accurately reproduced. In particular, in our simple model the plasmonic resonances are independent of the azimuthal orientation and therefore appear as part of a circle due to the simplification of the model. This is visible when one compares Figure 4. 28(c) with (a). However, this method allows us to determine what comes from the plasmonic mode from what is due to anisotropy. The outer feature of the measured reflectance is attributed to the plasmonic resonance, which follows very well the analytical curve in Figure 4. 28(a). The signal at lower wavelengths is mostly determined by anisotropy and non-dispersive effects, therefore both modelled and measured graphs are very similar in this wavelength range. We now turn our attention to R_{ss} (Figure 4. 28(b) and (d)). Similarly to R_{pp}, the polar plots of R_{ss} are reproduced by the biaxial model at shorter wavelengths while deviations are observed at the SPP wavelength. In particular the "V-shape" of the SPP around α=90° is not reproduced by the pure biaxial model and can be identified only when the analytical mode dispersions are superimposed.

Modelled MM

Once the models obtained for p- and s-polarized light reproduce reasonably well the intensity data, we use them to calculate the MMs at AOI 45° as shown in Figure 4. 29(a) and (b), respectively. In general, we can see that both p and s-models can reproduce the measured signal in the shorter wavelength region (210-690 nm). However, in the longer wavelength region (890-990 nm), which is mainly influenced by SPPs, the generated MME show deviations to the measurements. Here also the effects of dispersion are not included and all the features at longer

wavelengths corresponding to SPPs follow circles instead of arcs. For example, the measured M12 shows SPP curved features near α=0° and another SPP feature at lower wavelength near α=90°. This can be understood by recalling that the p-model (s-model) considers as a simplification only the p-polarization (s-polarization respectively). However, the measured MME exhibit the full optical response and there s-polarization also plays an important role. Therefore, Figure 4. 29(a) and (b) need to be combined to explain the full measurements. We can see that the features near α=90° are reproducing the measured features, which also prove that the SPPs near α=90° are excited by s-polarization. However, the calculated M24, M23 and M34 at higher wavelength have opposite phase compared to the measurements, a feature obviously not captured by the simplifying model. From this preliminary result we can see that we obviously need both the pure anisotropy modelled by an effective medium approach for both s- and p-excitation, including the plasmonic effects, and the dispersion originating from the periodicity of the sample. In the next section, we will give more details on the physical interpretation of all the features as well as their interplay.

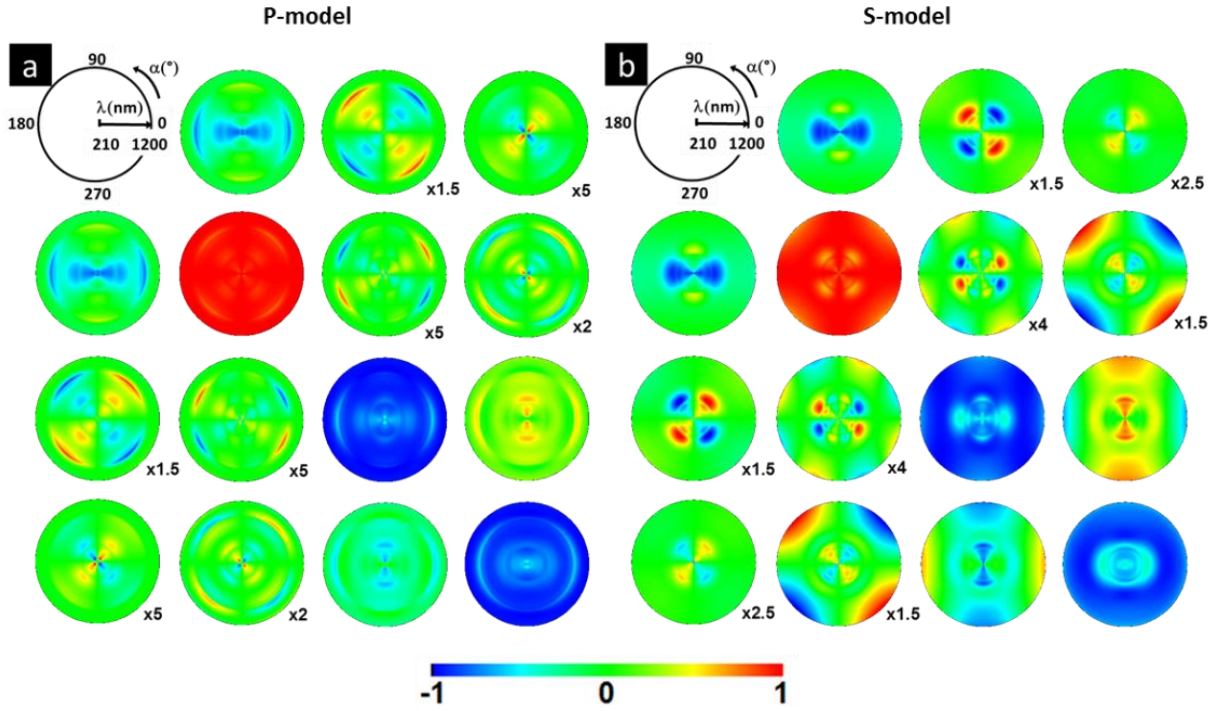

Figure 4. 29: Simulated MM at AOI 45° in the spectral range between 210 nm and 1200 nm with full azimuthal rotation generated from P biaxial model (a) and S biaxial model (b). Multiplication factors are used to scale the data to [-1;1].

Identification of the optical features

For sake of simplicity, we now choose only the four MME (M12, M13, M24 and M34) for a more detailed analysis shown in Figure 4. 30. Our aim here is to illustrate the method of superposition of the separated physical effects through their respective analytical models. This superposition, taking into account the assumptions of each model, is helpful in comparison with the measured data in order to reveal the origin of the optical properties. The detailed comparison of all the elements of this figure gives us a complete description and interpretation of the

complex pattern of the measured MM. Each row of Figure 4. 30 corresponds to one of the four chosen MME, all measured or generated at AOI 45°. The first column displays the measured data superposed with the analytical dispersion of the SPP modes. The second column compares the measured data with the expected positions of some RWA lines as well as the interband transition of gold. The last two columns illustrate the MME calculated by the anisotropic p- (resp. s-) models, together with the analytical positions of the SPPs, RWAs and the interband transition of gold.

The first column, comparing the measured data with the expected position of the propagating SPP mode, reveals that the outer feature of the MMEs is strongly influenced by the plasmonic mode. However we can see that the measured signal follows the SPP lines only over a certain azimuthal angle range. Indeed, the excitation angle range is determined by the sample anisotropy and can be calculated by our anisotropic layer model (last two columns): the simulated MMEs, dependent on anisotropy, indicate the azimuthal range where the excitation of the features is allowed and its respective strength. Moreover the comparison of the p-model and s-model allows us to determine which measured feature is linked with which polarization. However, since the anisotropic layer model does not take dispersion into account, it is expected that the curvature of the SPP mode is not reproduced. As a result of a dispersionless model, the simulated elements M12 and M13 predict the SPP mode position correctly only at α=0° (for p-model) and α=90° (for s-model). For all azimuthal angles in between these values, the spectral position of the SPP modes deviates following the SPP analytical line. In other words, intentionally curving the simulated features with respect to the azimuthal angle following the SPP mode dispersion leads to similar patterns as those measured. Therefore the interpretation of the comparison shown in Figure 4. 30 is as follows: the simulated MMEs – last two columns – display the range of azimuthal angles α where spectral features due to anisotropy appear (in the respective MMEs), while the position of the dispersive modes interact with the anisotropy related features by either curving the branches or modifying their shape and width.

When we turn our attention to the features at the center (shorter wavelengths between 210 nm and 690 nm), we can see that the superposition works similarly to the case of the SPP modes. In this spectral region, the optical properties are influenced by anisotropy, diffraction orders (RWAs) and interband transitions. In particular, the direct visual comparison between the anisotropy related lobes, the position of the RWAs and the measured MMEs indicate clearly that the shape of the MMEs is produced by a modification of the anisotropic signal by all the physical phenomena present in this spectral range. If we first consider M12, along the 180°-0° azimuthal line, we can clearly see that the anisotropy lobe is modulated by the presence of the RWA AIR (-2) (green) and RWA PDMS (-2) (black) orders. The same is valid for M13 along the 235°-45° line, and for M34 at most azimuthal angles. The latter is, in addition to the influence of the RWAs, also influenced by the Au interband transition. Quite interestingly, if we compare M13 with Figure 4. 21, we can see that M13 is really similar to the cross-polarized reflectance R_{ps} or R_{sp} over the whole measurement range, because M13 reflects the anisotropy effect of the sample, which strongly influences the polarization conversion.

The method presented here is based on the direct comparison of simple analytical models, each describing one distinct physical aspect: in our particular case, these are linked to anisotropy, SPP, dispersion, diffraction and interband transition. The influence of these four main aspects is easily identified. The interplay between modes can be found at the intersection between their expected positions.

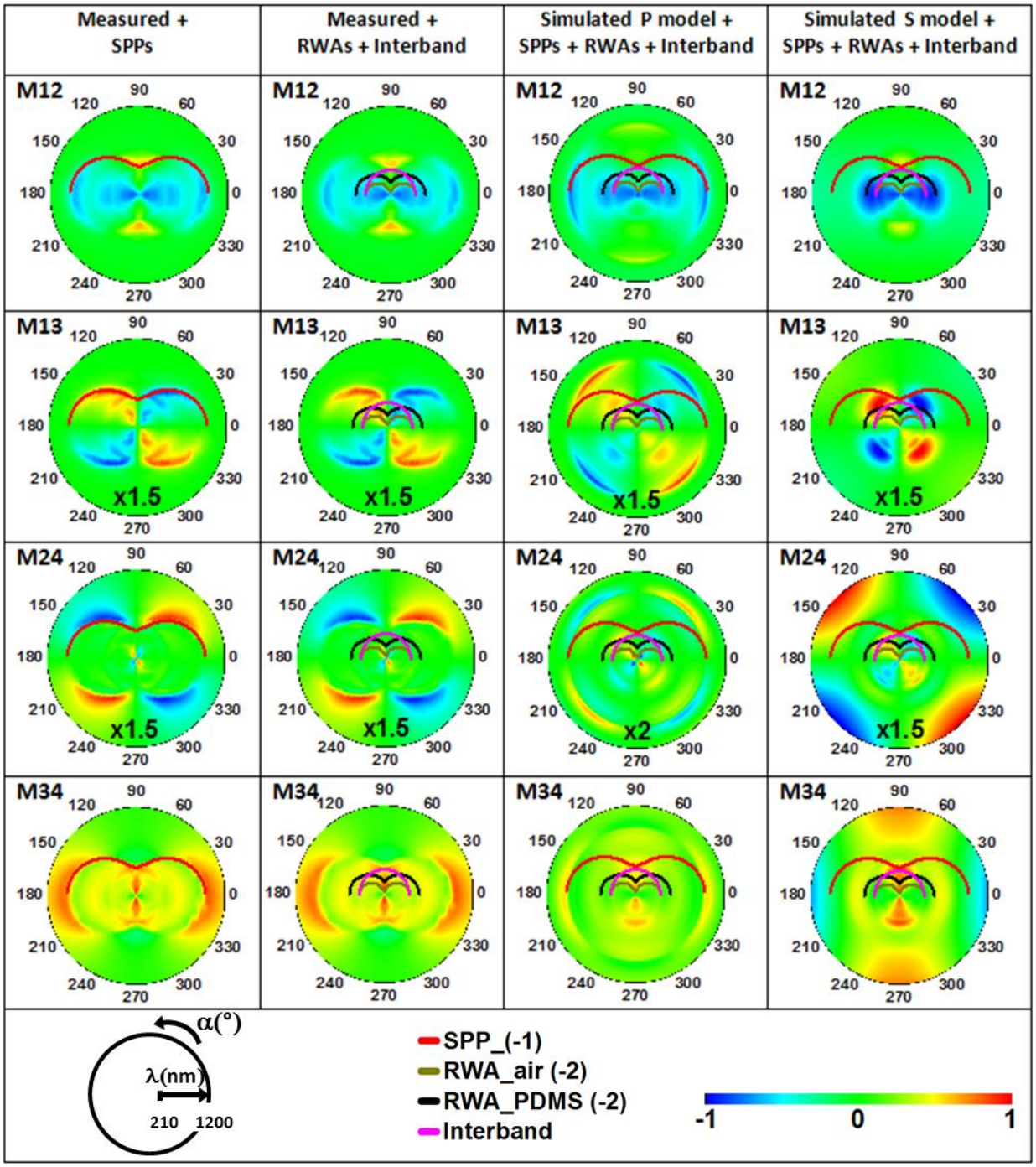

Figure 4. 30: Measured and simulated MM elements M12, M13, M24 and M34 together with the SPP, RWA and interband transitions draws in the upper half space at AOI 45°. Simulated p- and s-model means, that the Mueller matrices are calculated only from the anisotropic effective medium approach obtained from the s- and p-reflectance measurements. The multiplication factors give the enhancement factor in respect to the scale bar.

4.2.8 Conclusion

In summary, we have demonstrated how the complex optical response of a simple Au grating can be decomposed into its physical ingredients. First, we measure the reflectance along the two optic axes of the grating, along and perpendicular to the grooves under s- and p-polarization. The reflectance is then modelled by a simple anisotropic effective medium approach using Drude-Lorentz oscillators. From this anisotropic model, the intensity plots (reflectance in our case) over the whole spectral and angular range are generated. Once the agreement between the generated and measured plots is insured, the Mueller-matrix plots can be calculated. On top of this calculated MME we superimpose the expected dispersive SPP and RWA modes, calculated from the known periodicity of the grating. Comparing this composed result with measured MMs gives a deep insight on how the different physical contributions originating from periodicity, anisotropy and material properties influence the complex polarization mixing. We have seen that SPPs can be excited by both p- or s-polarized light when the incident plane is perpendicular or parallel to the grating grooves. Both SPP modes are dispersive with the AOI and follow the same phase matching condition. P- or s-polarized light can be converted to s- or p- polarized light via SPP excitation, and maximum polarization conversion occurs when the angle between incident plane and grooves is 45°. Additionally to the excitation of SPPs, the optical properties are influenced by geometric anisotropy, the RWAs related to the periodic grating structure and, to a lesser extent, the Au interband transition. The anisotropy, the interband transition and the non-dispersive approximation of the SPPs are understood in terms of an effective medium approach, obtained from fitting the measured reflectance. However, the dispersion of the SPP modes and the RWAs effects should be added (directly from their analytical expressions) on top of this model.

4.3 Au/Ni/Au gratings

After demonstrating how the complex optical response of a simple Au grating can be decomposed into its physical ingredients in section 4.2, we now turn out attention to another metallic gratings formed by evaporating a thin Au/Ni/Au multiple layers on top of PDMS grating. In this section, first of all, we apply the same analytical method used for Au grating in section 4.2 to decompose the complex optical response into its physical ingredients. Second of all, we compare the results of Au/Ni/Au grating with Au grating to see the influence of Ni layer on the optical response. Finally, we discuss the ability to tune SPP by mechanical stretching.

4.3.1 Sample Fabrication

Au/Ni/Au grating was produced by the same self-assembly technique as Au gratings. The PDMS grating was fabricated under the condition 40% prestrain and 10 min O_2 plasma treatment. Then 15 nm Au, 10 nm Ni and 10 nm Au layers were evaporated on top of the PDMS grating after a second time O_2 plasma treatment for 1min. The sample is shown in Figure 4. 31(a). The patterned grating structure is in the center with size 8 mmx13 mm. Figure 4. 31(b) and (c) respectively show the top view image over an area of 20 μmx20 μm and 3D view image over an area of 5 μmx5 μm measured by AFM. The AFM analysis reveals that the Au/Ni/Au grating has a period *p* equals to 530 nm and depth *H* equals to 95 nm.

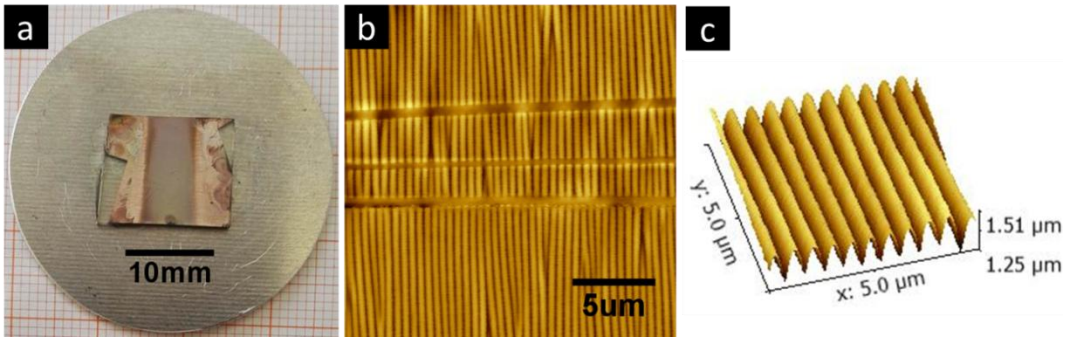

Figure 4. 31: (a) A photograph of the sample glued on an aluminum plate. (b) Top view of AFM image over an area of 20 μmx20 μm and (c) 3D view of AFM image over an area of 5 μmx5 μm.

4.3.2 Dielectric function of Au/Ni/Au

In order to get the dielectric function of the multiple Au/Ni/Au layers on the PDMS grating, spectroscopic ellipsometry measurement was performed on a sample with 15 nm Au/10 nm Ni/10 nm Au layers on a flat PDMS at AOI from 40° to 60° by 10°. The 15 nm Au/10 nm Ni/10 nm Au films were evaporated (Univex 300) on an O_2 plasma treated flat PDMS slab under the same evaporation conditions as the Au/Ni/Au grating sample. Then the General oscillator layer with 35 nm from the WVASE software was used. Figure 4. 32 shows the measured and modeled ellipsometric angles ψ and Δ in the spectral range from 300 nm to 1800 nm. Both measured ψ and Δ fit very well the modeled ones except deviations in the range near ultraviolet range. The real part ε_m' and imaginary part ε_m'' of effective dielectric constant of the multiple Au/Ni/Au layers

was then extracted and showed by the blue lines in Figure 4. 33. This dielectric constant was then used in the next sections to calculate the SPP dispersion lines.

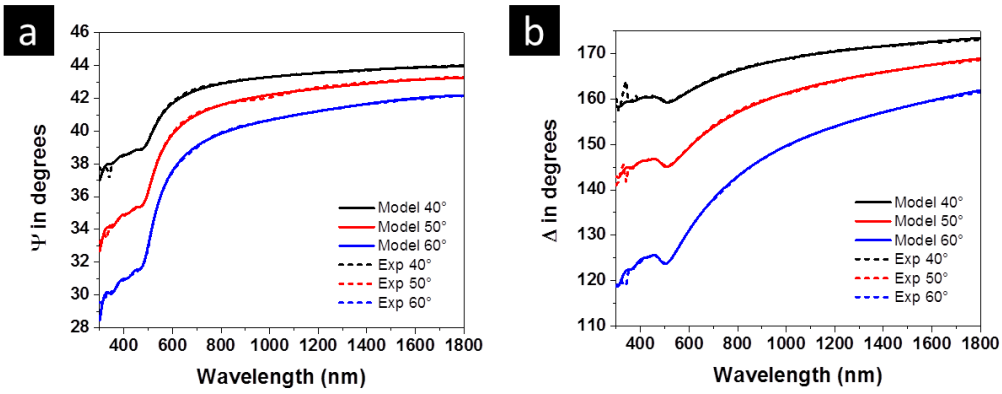

Figure 4. 32: Spectroscopic ellipsometric angles ψ and Δ at AOI from 40° to 60° by 10° in the spectral range from 300 nm to 1800 nm.

Figure 4. 33 also shows the dielectric constants of Ni (from Palik [86]) and Au (from Johnson and Christy [87]). As we expected, both the real and imaginary parts of the dielectric constants of Au/Ni/Au locate in between that of Ni and Au.

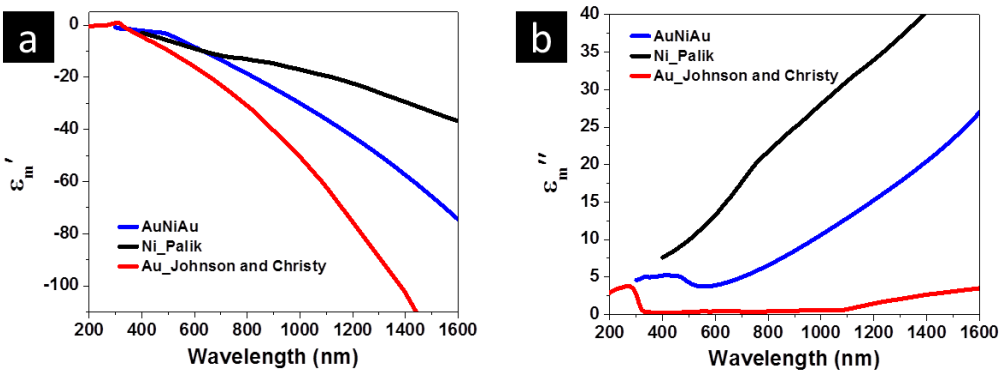

Figure 4. 33: (a) Real part ε_m' and (b) imaginary part ε_m'' of dielectric constants of Au/Ni/Au, Au and Ni.

4.3.3 Reflectance dispersion

Figure 4. 34(a) and (c) respectively show the reflectance dispersion plots measured with p-polarized light at α=0° and with s-polarized light at α=90° at AOI from 20° to 60° in a broad spectral range 200 nm-1600 nm together with calculated SPP line. Figure 4. 34(b) and (d) respectively show the reflectance at θ=20°, 30° and 40° in accordance to the left contour plots. We can see both p and s polarized light excite SPPs, which is the same with Au gratings. Besides, both SPP excited by p- and s- polarized light are dispersive modes. For p-polarization, the SPP resonance shifts to higher wavelength from 740 nm at θ=20° to 990 nm at θ=60°, while for s-polarization, the SPP resonance slightly shifts to lower wavelength from 550 nm at θ=20°

to 470 nm at θ=60°. We can see from Figure 4. 34(c) that the influence of RWAs_air(-1) on the reflectance is very weak, while for Au grating as shown in Figure 4. 19(b), RWAs_air(-1) shows strong influence.

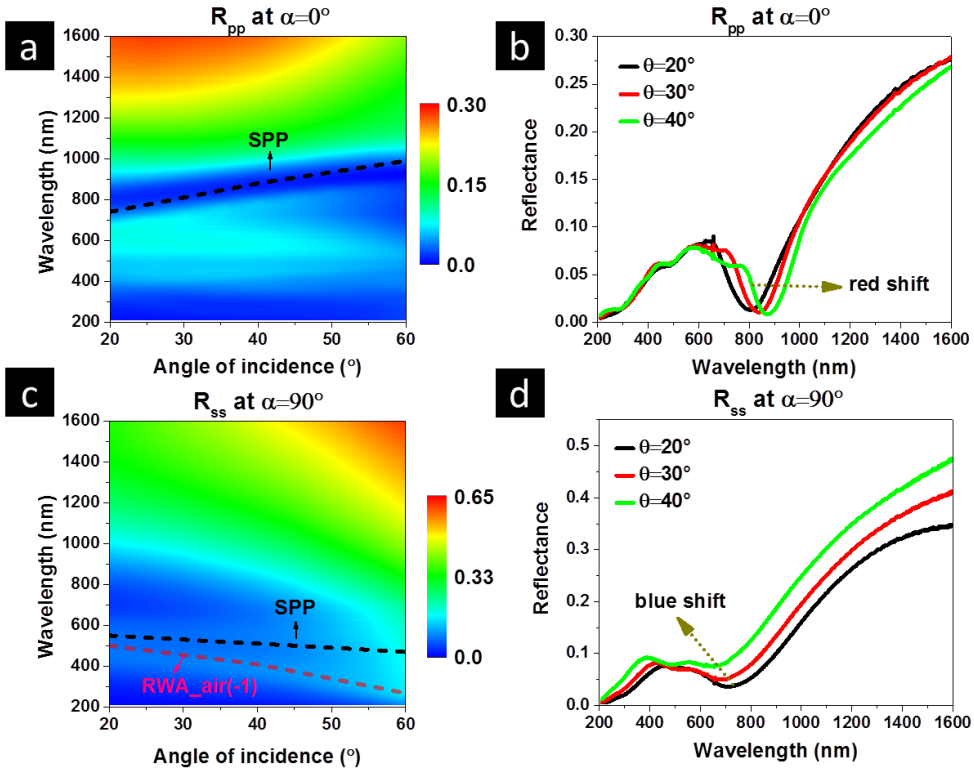

Figure 4. 34: Reflectance dispersion plots measured with (a) p-polarized light at α=0° and (c) s-polarized light at α=90° at AOI from 20° to 60° in spectral range from 200 nm to 1600 nm. (b) and (d) respectively show the reflectance at θ=20°, 30° and 40° in accordance to the (a) and (c) contour plots, respectively.

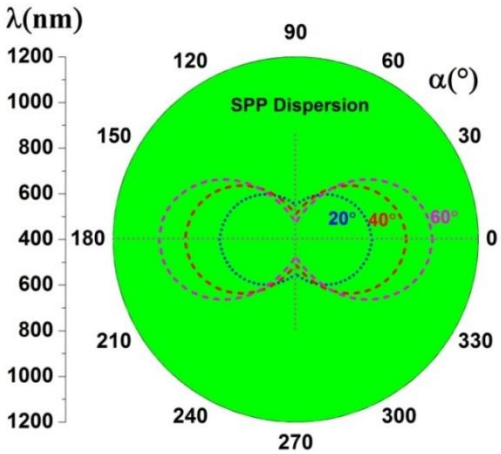

Figure 4. 35: SPP dispersion lines as a function of whole azimuthal angles and wavelength range (400-1200 nm) at AOI 20°, 40° and 60°.

We already know the condition for SPP excitation in Equation 2.82. By obeying equation 2.82, mixed s- and p- polarization can be used to excite SPPs. Therefore, we calculate the SPP lines from Equation 2.82 as a function of α (complete azimuth angles) and λ (400-1200 nm) at θ=20°, 40° and 60° in Figure 4. 35. We can see SPP lines appear as constricted circles and show strong dispersion as both AOI and azimuthal rotation. For instance, we can see the SPP position red shift along α=0° and blue shift along α=90° as AOI. The redshift and blueshift features shown in Figure 4. 34 (b) and (d) confirm the SPP origin.

Figure 4. 36 shows the comparison of reflectance of Au/Ni/Au grating and Au grating measured with p-and s-polarized light at AOI 30° and 40° in spectral range from 200 nm to 1600 nm. The total thickness of Au/Ni/Au layer is 35 nm which is the same with Au layer of Au grating. Besides, Au/Ni/Au and Au grating were fabricated with same method and have similar periodicity and amplitude. So even though SPPs for Au grating and Au/Ni/Au grating are excited at different wavelengths, we can still compare these two grating samples. We can see in general that reflectance for Au grating is higher than Au/Ni/Au grating. This is because Au has smaller extinction coefficient than Au/Ni/Au, resulting in small absorption. Besides, due to the large absorption of Ni, as expected from Equation (2.76), the full width at half maximum of the plasmonic peak for Au/Ni/Au grating is much broader than Au grating.

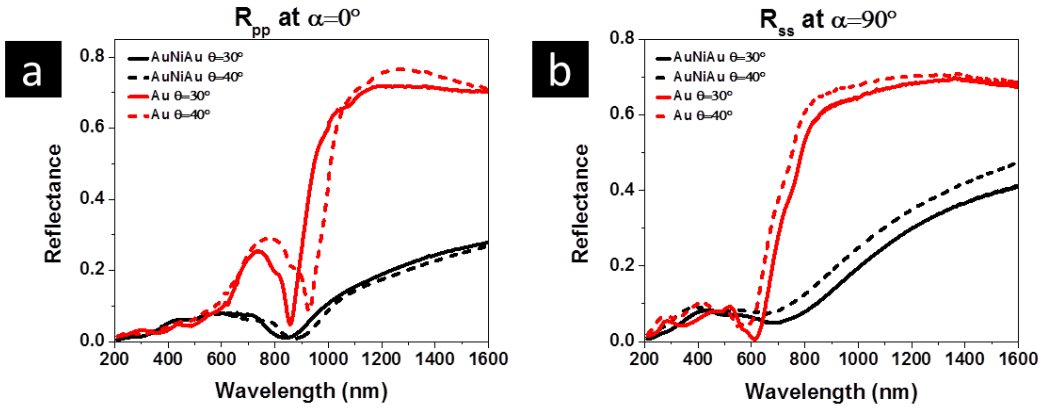

Figure 4. 36: Reflectance measured with (a) p-polarized light along α=0° and (c) s-polarized light along α=90° at AOI 30° and 40° in spectral range from 200 nm to1600 nm for Au grating and Au/Ni/Au grating.

4.3.4 Reflectance angular dependence

In order to visualize the azimuthal dependence of the excited modes, measured reflectance for p and s-polarized light at AOI from 20° to 60° by 20° over a complete azimuthal rotation in steps of 5° in the spectral range between 200 nm and 1600 nm together with calculated SPP, RWAs and interband transition lines is shown in Figure 4. 37. In general, same with Au grating, the reflectance shows a simple C2-symmetry. The positions of the excited resonances in Figure 4. 37 follow the calculated SPPs lines very well confirming their plasmonic origin. It is necessary for the incident light to have a component of polarization that is perpendicular to the grooves [1]. Therefore, only p-polarized light can excite SPP at α=0° and only s-polarized light can excite the SPP the positions at α=90°. Besides, we can see, the positions of the excited SPP resonances is in

the azimuthal range α=-45° to 45° for p-polarized light and is in the azimuthal range α=45° to 135° for s-polarized light.

If we compare the reflectance with Au grating, we can see the resonances are much more blurred and broader than that of Au gratings shown in Figure 4. 20. Also, the "V" shape lobe in R_{ss} due to SPP at around α=90° are broader than Au grating. The broad resonance at lower wavelength range 200 nm-700 nm is coming from the anisotropy and non-dispersive effects. Similar to the Au interband transition feature which is clearly visible and represented as a circle at 480 nm in Figure 4. 20, the reflectance for Au/Ni/Au grating also shows a weak circular intensity drop at around 510 nm as indicated with red dotted line which can be explained by the effective interband transition of the whole Au/Ni/Au layers. Moreover, same with Au grating, the influence of RWAs is rather weak as shown in these angular dependent reflectance plots.

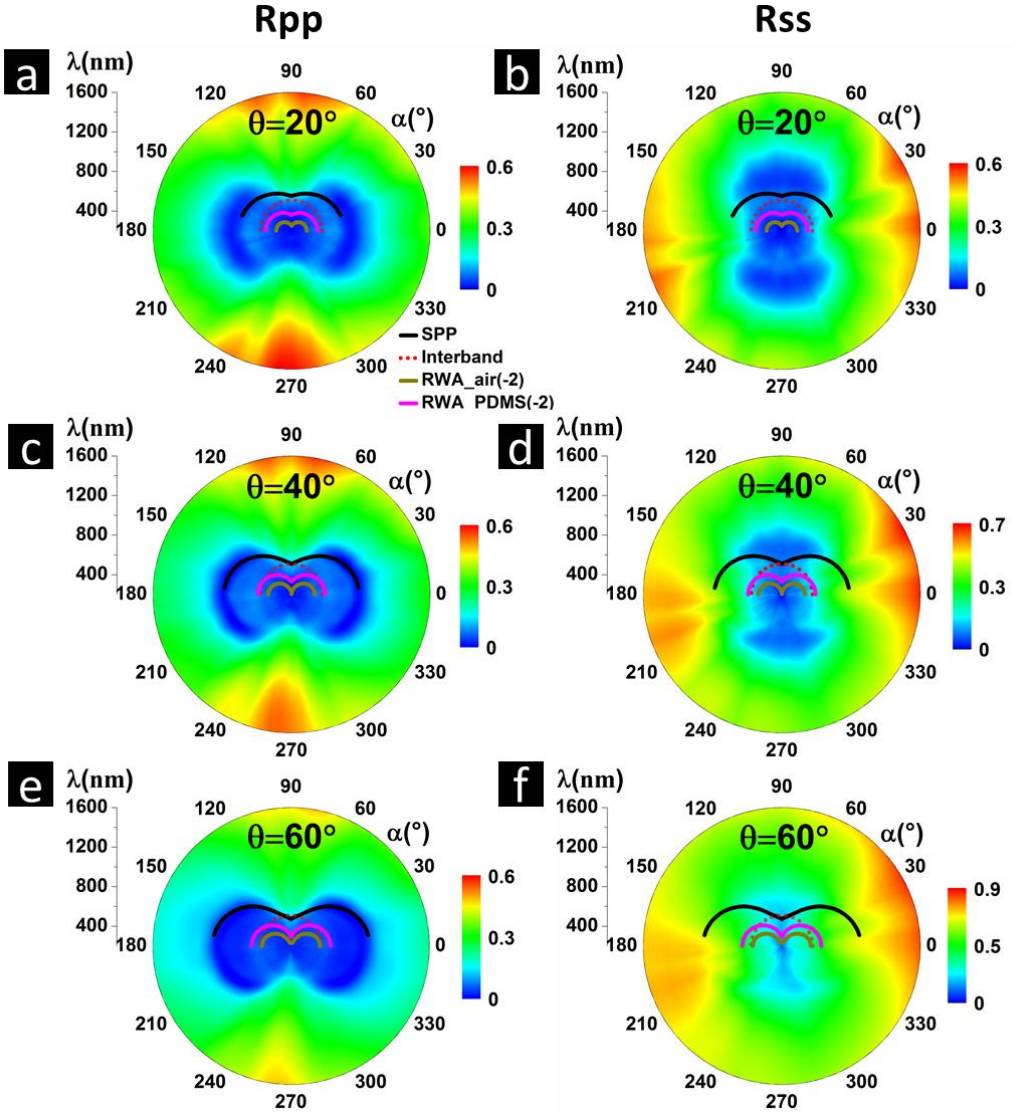

Figure 4. 37: Measured R_{pp} and R_{ss} at θ=20º, 40º and 60º are plotted with full azimuthal rotation in the spectral range from 200 nm to 1600 nm. The black and dotted red lines indicate the calculated position of the SPP mode and interband transition, respectively.

4.3.5 Mueller Matrix in reflection

To get a deeper insight in the influence of SPPs, interband transition and probably RWAs on the complex optical behavior of the Au/Ni/Au grating, MME measurements were carried out in reflection in the spectral range between 200 nm and 1600 nm at θ=20º, 40º and 60º over azimuthal rotation (0-180°). In order to display the completeness of whole azimuthal rotation, we duplicate the data in the range 180-360º based on the data in the range (0-180°) due to the symmetry of the grating (Figure 4. 38). All the MM elements are normalized to M11 element and some elements were scaled with multiplication factors in order to obtain a better visualization. In general, we can see all the lobes in MM elements can be explained by SPP line. The broad anisotropy lobe at lower wavelength range as shown in reflectance plots has no contribution to the MM patterns, therefore RWA_air(2), RWA_PDMS(2) and interband transition lines which locate at this lower wavelength range as shown in Figure 4. 39 also have no contribution to the MM lobes. Same with MM measured for Au grating, the MMEs for Au/Ni/Au grating show the expected symmetry and the off-block-diagonal elements present the strong anisotropy. In detail, the off-block-diagonal elements show curved lobes with maxima around α=45° and 135° at the excitation wavelengths of the dispersive SPP modes. The lobes near azimuthal angle 90° in M12, M33 and M43 become weaker as increasing AOI. These lobes come from the SPPs excited by s-polarized light. Moreover, we can see the lobes near azimuthal angle 70° in M23 which follow the SPP lines at AOI 20° and AOI 40° disappears at AOI 60° due to the dispersion of SPP excited by s polarized light.

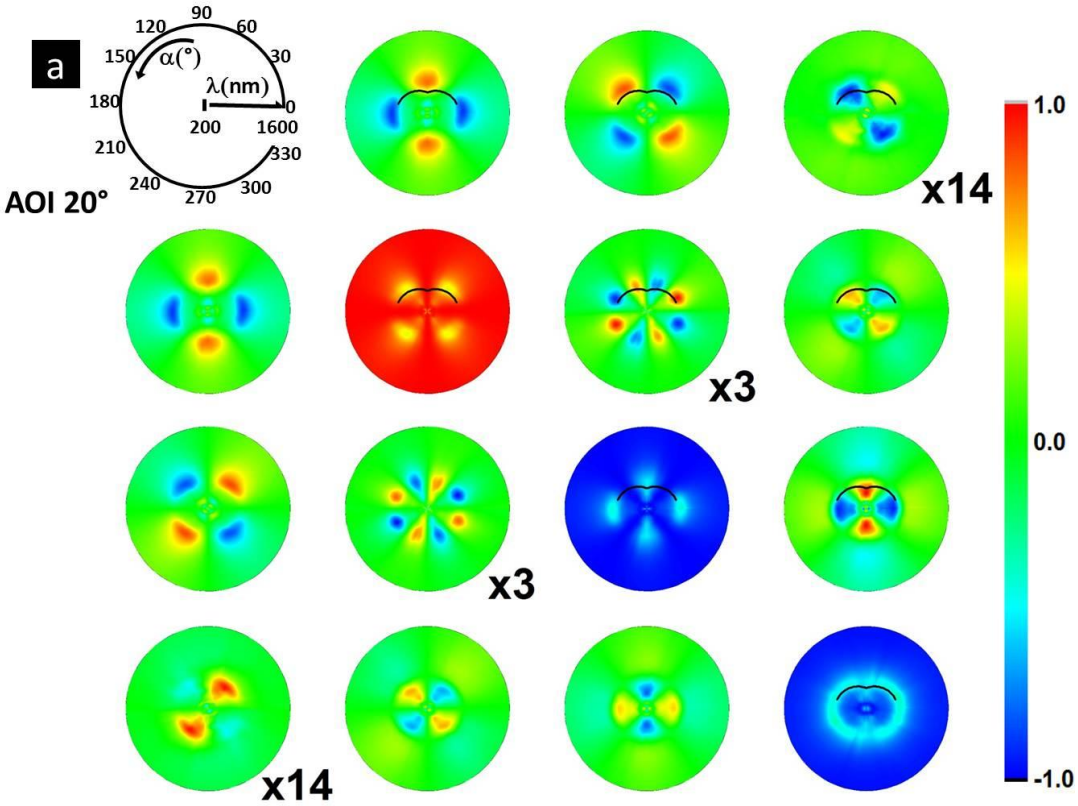

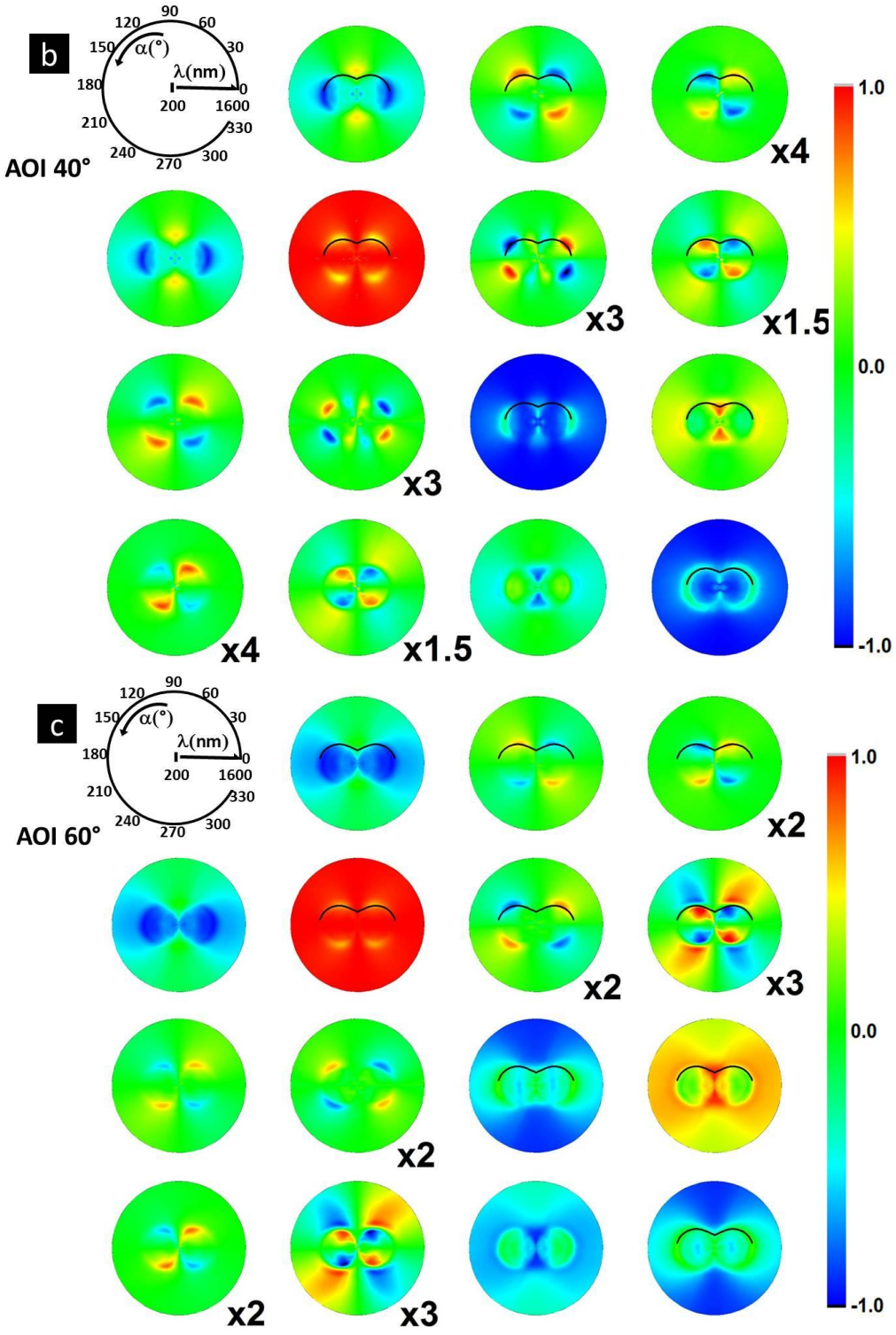

Figure 4. 38: MMEs measured in reflection at (a) θ=20º, (b) θ=40º and (c) θ=60º over the azimuthal rotation (0-180°) in the spectral range between 200 nm and 1600 nm. The data in the range (180-360°) are duplicated from measured data in the range (0-180°). All MMEs are normalized to M11.

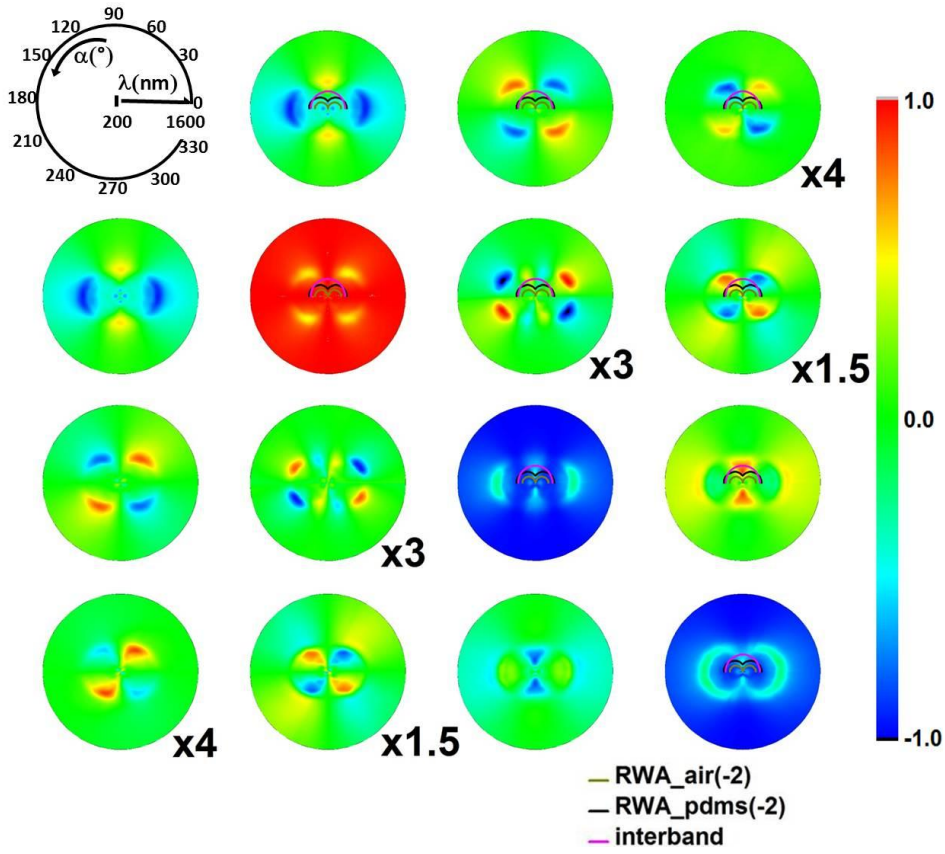

Figure 4. 39: MMEs measured in reflection at θ=40º over the azimuthal rotation (0-180°) in the spectral range between 200 nm and 1600 nm together with RWA_air(2), RWA_PDMS(2) and interband transition. The data in the range (180-360°) are duplicated from measured data in the range (0-180°). All MMEs are normalized to M11.

In general, we can see different from Au grating (Figure 4. 23) where SPP, interband transition and RWAs play important roles in the MM, here in Au/Ni/Au grating, only SPP line could explain all the lobes in MM elements. For a more detailed analysis, we compare MM12, MM13 between Au/Ni/Au grating at θ=40º and Au grating at θ=45º together with RWAs, SPP and interband transition as shown in Figure 4. 40. It reveals that the feature at longer wavelength in the MMEs is strongly influenced by the plasmonic mode. Different from M12 for Au grating, where along the 180°-0° azimuthal line, the anisotropy lobe is modulated by the presence of the RWA_air(-2), RWA_PDMS(-2) orders and interband transition, M12 for Au/Ni/Au grating shows no modulations from RWAs. It is the same for M13 along the 235°-45° line where Au/Ni/Au grating show only the lobe coming from SPP, while Au grating shows clear modulations from RWA_air(-2), RWA_PDMS(-2) and interband transition.

RWA_air(-2) appears in the interface between air and metallic layer (Au or Au/Ni/Au). Since Ni layer introduce more absorption of the incident light than Au layer, the reflected light has less intensity than Au grating which is as also confirmed from reflectance measurement in Figure 4. 36. Therefore, the less reflectance leads to the non-contribution of RWA_air(-2). Similarly, due to the large absorption, the incident light will not pass through the Au/Ni/Au layer as easy as passing through Au layer. So RWA_PDMD(-2) which appears in the interface between PDMS and Au/Ni/Au layer also has no contributions to the optical response.

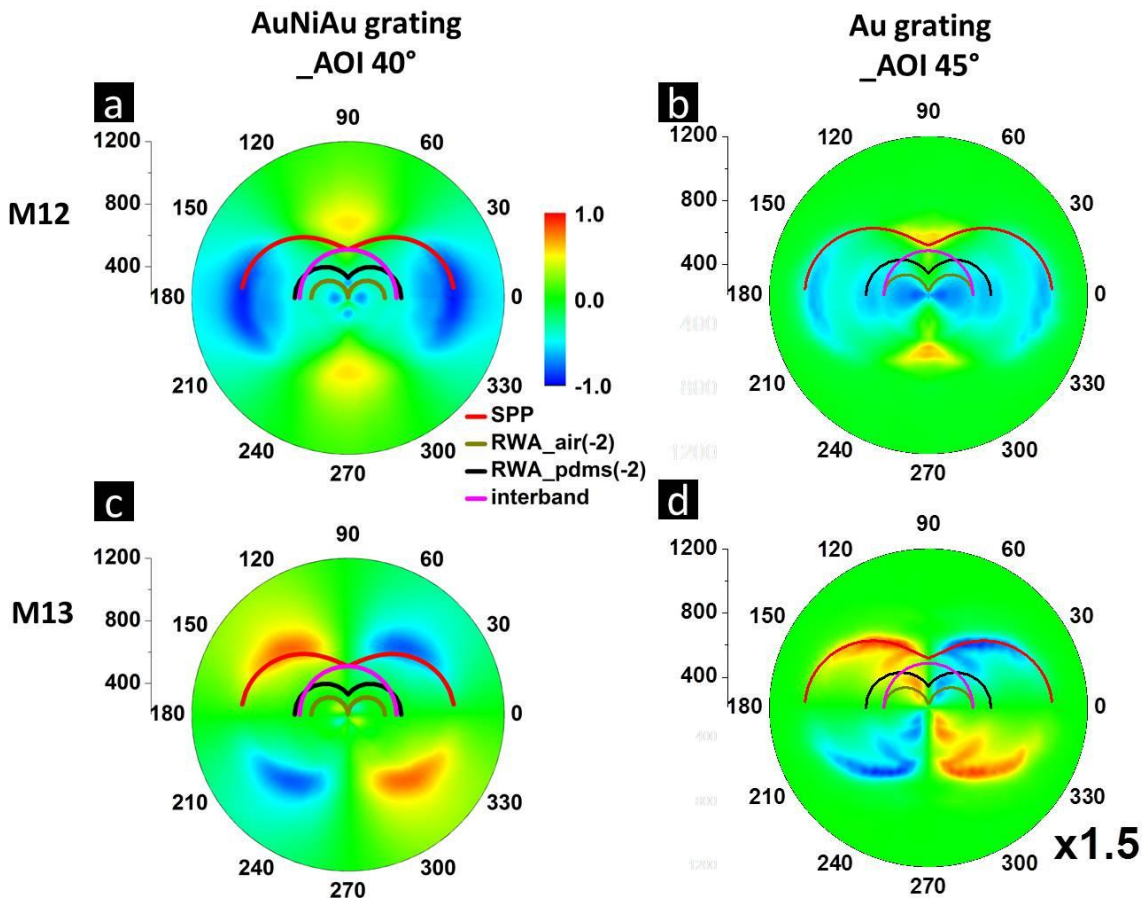

Figure 4. 40: (a) M12 and (c) M13 for Au/Ni/Au grating measured in reflection at θ=40º over the azimuthal rotation (0-180°) in the spectral range between 200 nm and 1200 nm. The data in the range (180-360°) are duplicated. (b) M12 and (d) M13 for Au grating measured in reflection at θ=45º over the complete azimuthal rotation in the spectral range between 200 nm and 1200 nm.

4.3.6 Modelling results and interpretation

In order to correlate the observed MM pattern to the polarization, we present here a similar P and S-modes as Au grating.

P-model

In a first step, R_{pp} at α=0° and 90° were respectively modeled with 35 nm general oscillator layers (genoscx layer and genoscy layer) on PDMS layer with a thickness of 1mm. In order to obtain a good fit as shown in Figure 4. 41(a) and (b), six Gaussian oscillators and one Drude oscillator were used in both directions. Then, as shown in Figure 4. 41(c), a biaxial model was built with a Cauchy oscillator along Z direction and genoscx and genoscy in X and Y directions. The thickness of the biaxial layer is 35 nm and the PDMS was used as substrate of thickness 1mm.

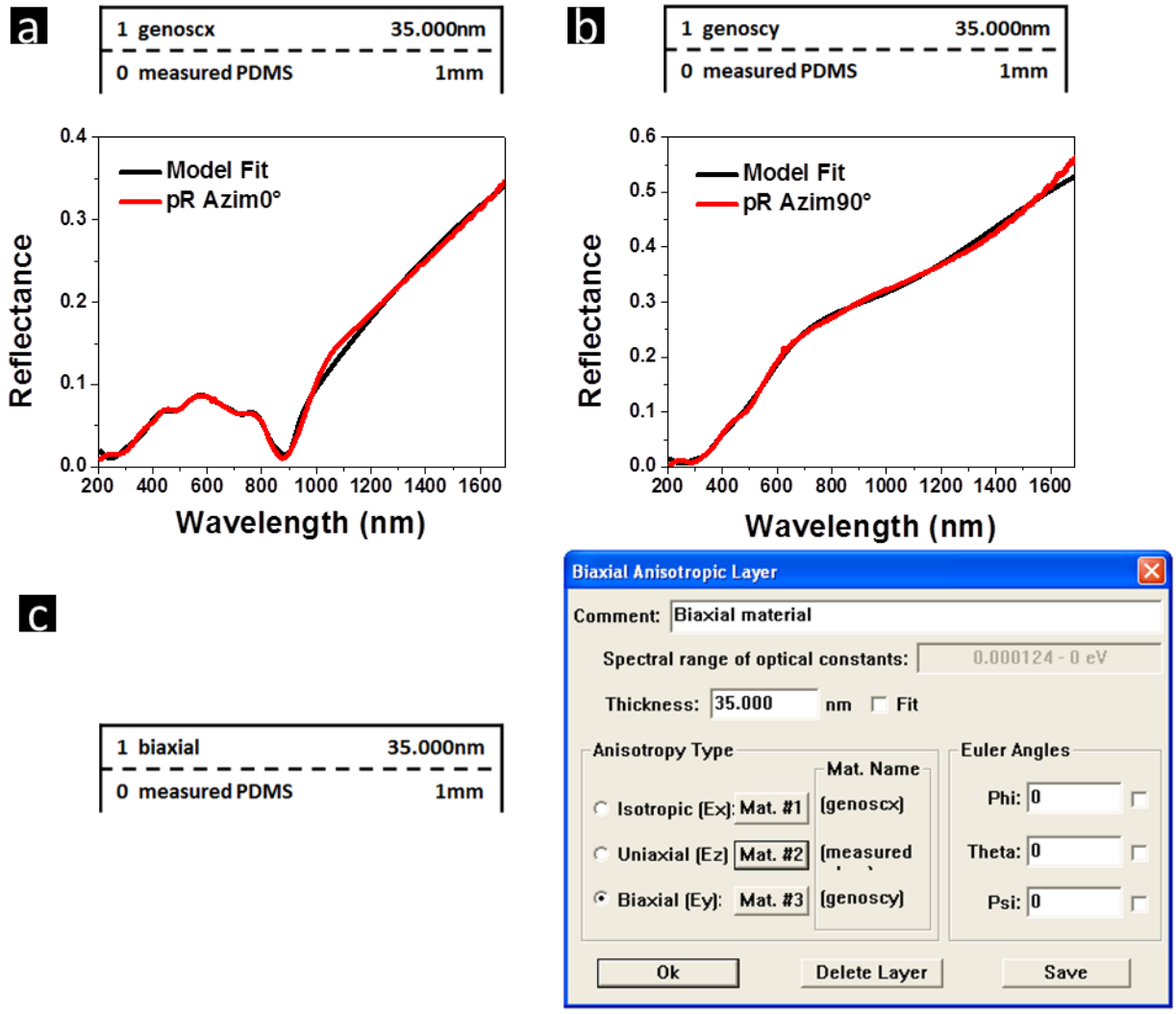

Figure 4. 41: (a) Genoscx and (b) Genoscy layer model with the R_{pp} fit at α=0° and 90° respectively. (c) Biaxial layer model.

S-model

Similar to P-model, the reflectance R_{ss} at angles α=0° and α=90° were fitted in the S-model. R_{ss} at α=90° was modeled with a 35nm general oscillator layer (genoscx) on the PDMS layer by three Gaussian oscillators and one Drude oscillator. R_{ss} at α=0° was modeled with 35nm general oscillator layer (genoscy) on the PDMS layer by five Gaussian oscillators and one Drude oscillator. A nice fit was obtained in the range 300 nm-1600 nm for R_{ss} at angle α=90° and 200 nm-1600 nm for R_{ss} at angle α=0° as shown in Figure 4. 42(a) and (b). Then a biaxial model (Figure 4. 42(c)) was used with a Cauchy oscillator along Z direction and genoscx and genoscy in X and Y directions. Same with p-model, the biaxial layer is 35 nm thick and again PDMS is used as a substrate.

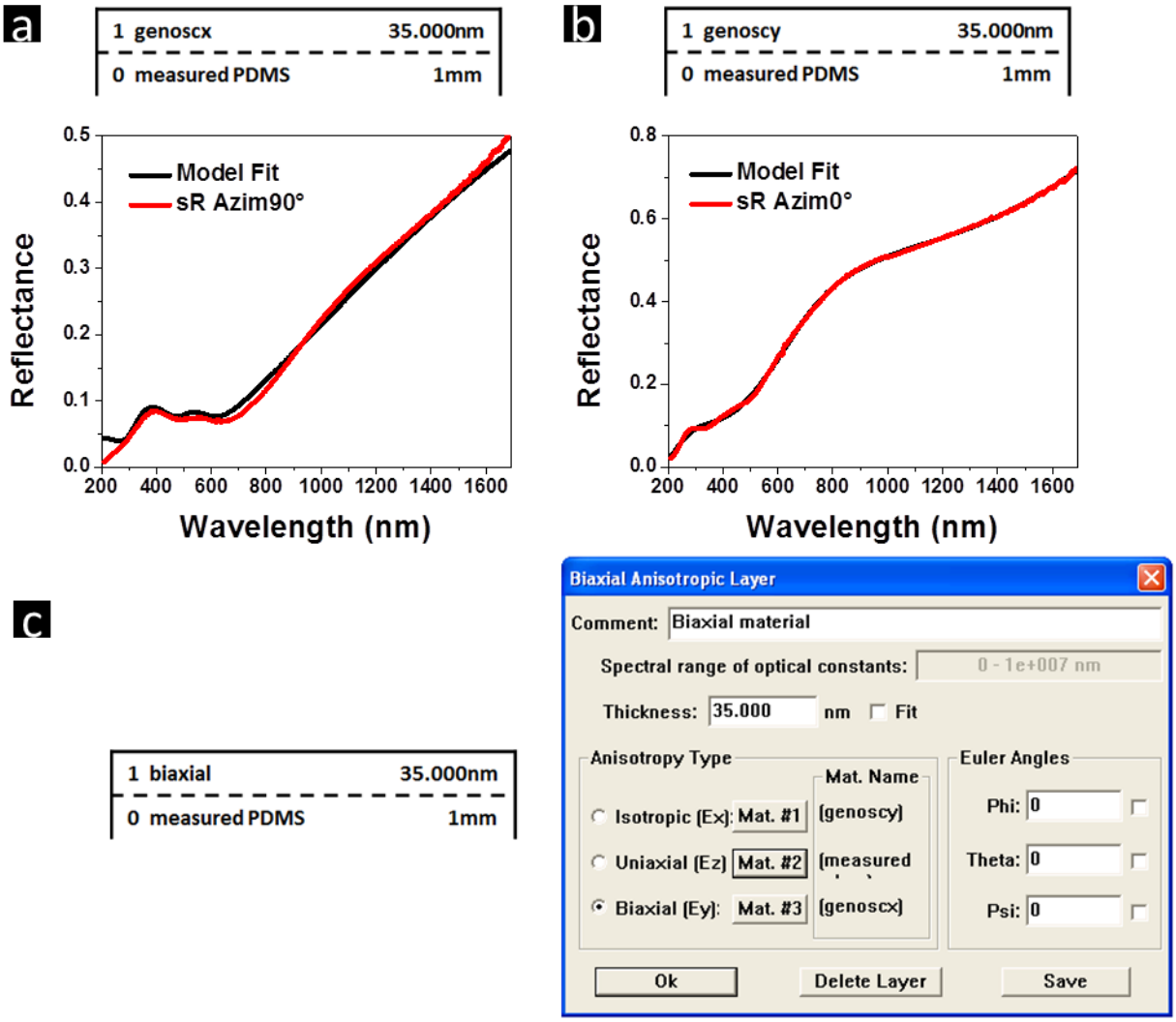

Figure 4. 42: (a) Genoscx and (b) Genoscy layer model with R_{ss} fit at α=90°and 0° respectively. (c) Biaxial layer model.

Modelled reflectance

Using P- and S- models, we start by calculating both the p- and s-reflectance at AOI 40° over the whole azimuthal range and compare the result with the experimentally obtained reflectance plots in Figure 4. 43. The expected anisotropy of the reflectance is visible in both, the experimental and the modelled plots. Then, the analytically calculated positions of the excited SPPs are added in all graphs of Figure 4. 43. As already discussed in section 4.2, no dispersion effects are included in our biaxial models, so the dispersive SPP modes are not accurately reproduced. This is visible when one compares Figure 4. 43(c) with (a). However, this method allows us to determine the feature at higher wavelength of the measured reflectance is attributed to the plasmonic resonance, which follows very well the analytical curve in Figure 4. 43(a) and the signal at lower wavelengths is mostly determined by anisotropy and non-dispersive effects. Both modelled and measured graphs are very similar in this lower wavelength range. We now turn our attention to R_{ss} (Figure 4. 43(b) and d). Similarly to Au grating, the polar plots of R_{ss} are

reproduced by the biaxial model at shorter wavelengths while deviations are observed at the SPP wavelength range. In particular the broad "V" shape of the SPP around α=90° is not reproduced by the pure biaxial model.

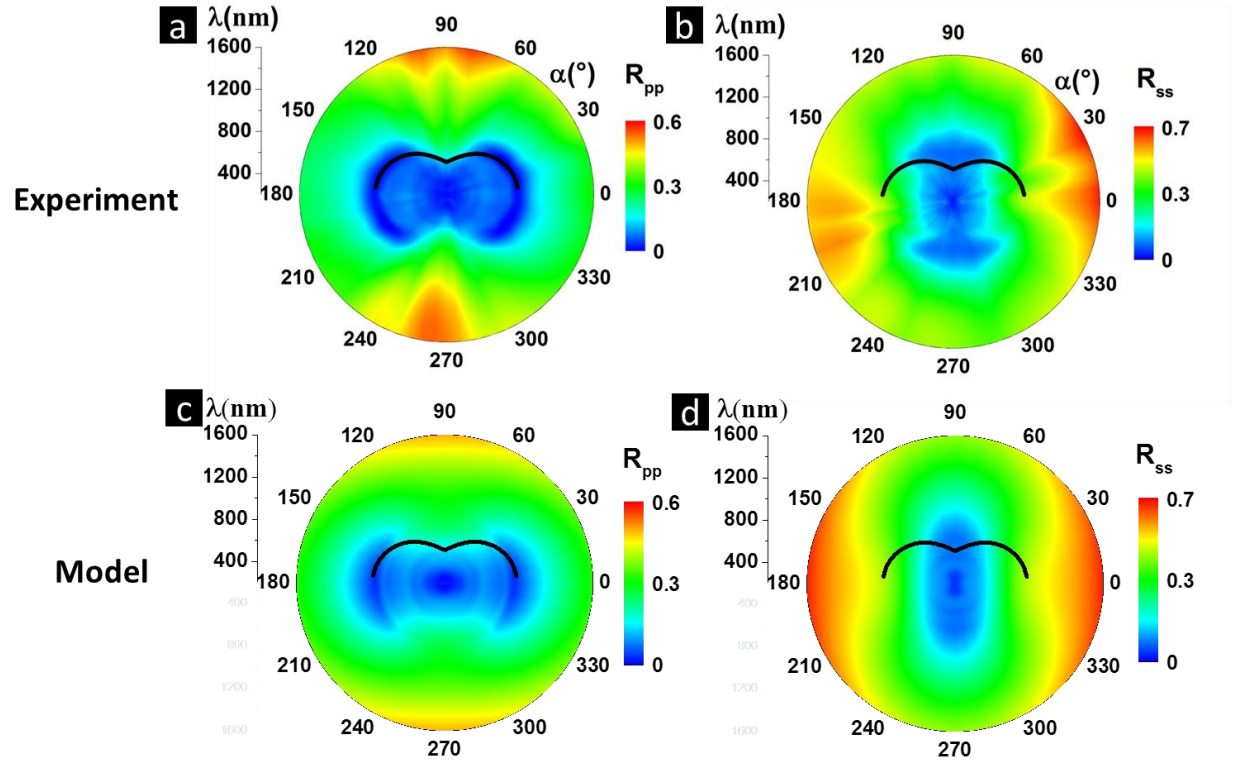

Figure 4. 43: R_{pp} (a) and R_{ss} (b) measured at AOI 40° over a complete azimuthal rotation in the spectral range between 200 nm and 1600 nm. R_{pp} (c) and R_{ss} (d) generated from the p- and s-biaxial models, respectively. All the plots are shown together with the calculated SPP lines in the top half space.

Modelled MM

Once the models obtained for p- and s-polarized light reproduce reasonably well the intensity data, we use them to calculate the MMs at AOI 40° as shown in Figure 4. 44(a) and (b) respectively. In general, we can see that both p and s-models can reproduce the correct symmetry as measured MM. However, in the longer wavelength region (750-1050 nm), which is mainly influenced by SPPs, the generated MME show deviations to the measurements. Here also the effects of dispersion are not included and all the features at longer wavelengths corresponding to SPPs follow circles. For example, the measured M12, M34 shows SPP curved features near α=0° (Figure 4. 44(a)) and another SPP feature at lower wavelength near α=90° (Figure 4. 44(b)). So we obviously need both s- and p-excitation, including the plasmonic effects to understand the whole optical response of Au/Ni/Au grating.

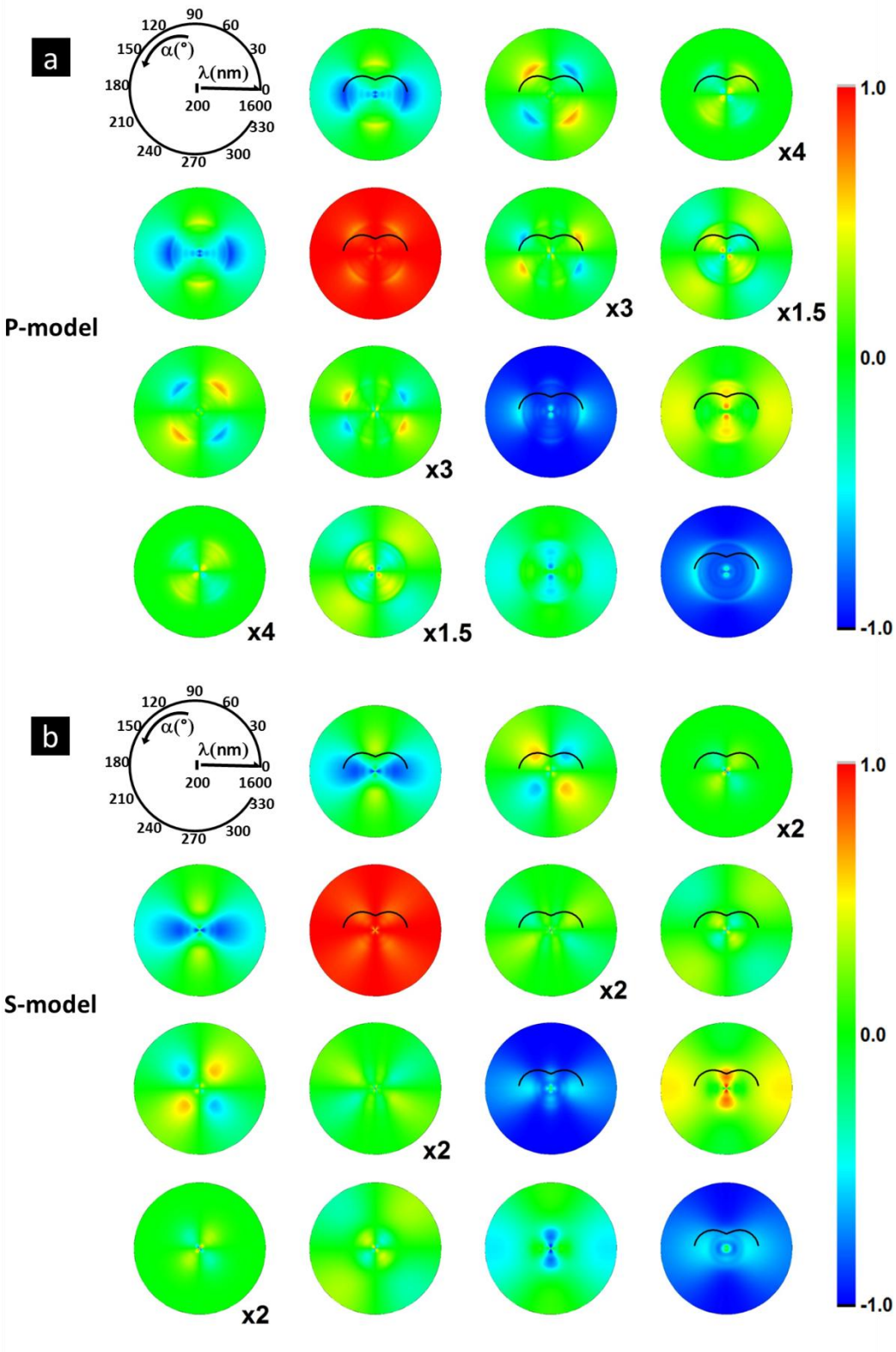

Figure 4. 44: Simulated MM at AOI 40° in the spectral range between 200 nm and 1600 nm with full azimuthal rotation generated from (a) P biaxial model and (b) S biaxial model. Multiplication factors are used to scale the data to [-1; 1].

4.3.7 Active tuning of surface plasmon polaritons

It is a dream of optics and material science to actively control the optical properties of materials. Currently, the booming field of plasmonics opens for the control of light-matter interactions in real time. This understanding of the behaviour of these novel materials is also crucial for the development of novel technologies and emerging applications. As we can see from the relation equation for SPP excitation by grating technique in Equation (2.82), SPP excitation dependent on AOI θ, azimuthal rotation α and grating periodicity P. As confirmed from Figure 4. 35, the dispersion line of SPP forms constricted circles and strongly dependent on θ and α. Besides, even though the grating amplitude A does not contribute to relation equation, it has influence on the intensity of resonance peak of SPP [84]. So, SPP can be tuned with these parameters (θ, α, P, A). On the other hand, recently nanosystems with combined magnetic and plasmonic functionalities become an active topic of research. The magnetic functionality permits the control of the SPP properties by an external magnetic field, which allows the development of active plasmonic devices [10]. In this section, I introduce an approach for SPP tuning by mechanically controlling the periodicity and amplitude of grating.

A 15 nm Au/10 nm Ni/10 nm Au layer was evaporated on one minute O_2 plasma treated PDMS grating fabricated with 20% prestrain and 10 min O_2 plasma treatment. Then, the fabricated Au/Ni/Au grating was glued on a home-made linear stretching stage (Figure 4. 45(a)) and put inside an oven with 85℃ for 1h to accelerate the curing process. After the glue is cured, the linear stretching stage together with Au/Ni/Au grating was mounted on the VASE ellipsometer (Figure 4. 45(b)). The sample was mounted in the condition the grating grooves are perpendicular to the plane of incidence where p-polarized light has maximum efficiency to excite SPP.

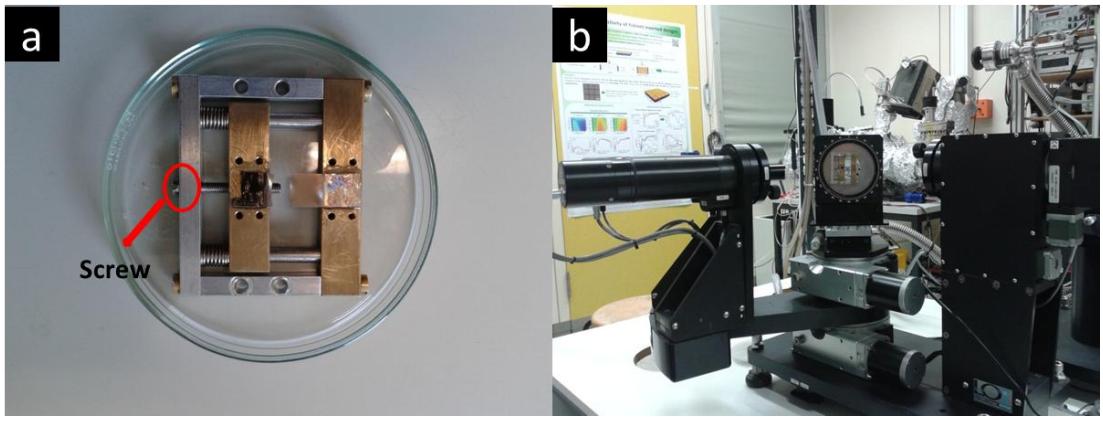

Figure 4. 45: (a) Home-made linear stretching stage. (b) Sample is mounted on the VASE ellipsometer in the condition the grating grooves are perpendicular to the plane of incidence.

R_{pp} was measured at AOI 30°. Every rotated circle of the screw shown in Figure 4. 45(a) makes 0.5 mm stretching of the sample. The sample broke after stretching length of 4 mm (8 turns). Figure 4. 46 shows the measured p-reflectance as a function of stretching turns. The SPP resonance position without stretching is at 1170 nm with full width at half maximum (FWHM) about 89 nm. After one turn stretching, the SPP resonance shifts to higher wavelength at 1250 nm and becomes broader with FWHM about 98nm. After the first turn stretching, the resonance

continuously becomes broader with FWHM increasing from 109 nm at 2 turns to 132 nm at 4 turns. Even though the resonance becomes broader, we can see the resonance position stays at around 1250 nm. In order to explain the feature shown in measured p-reflectance, microscopic images were taken at each stretching step (Figure 4. 47). By calculating the periodicity from the microscopic images, we obtain the periodicity without stretching is 735 nm and the periodicities after stretching with 1, 2, 3, 4 and 8 turns have similar value about 833 nm. The similar periodicity after 1 turn stretching is the reason why they have the similar resonance position of SPP. According to the relation between stretching percentage and stretching length shown in Figure 4. 4, we know that one turn rotation of the screw brings 4.2% stretching. So the periodicity can be predicted and calculated as P=735*(1+4.2%)=766 nm. In reality, the bigger period (833 nm>766 nm) measured from microscopic image after one turn stretching is because Au layer on PDMS grating template has much bigger Poisson ratio and leads to bigger stretching percentage than pure PDMS grating. Instead of periodicity, we can see few cracks occur in the sample after the first turn of stretching. Afterwards, more and more cracks appear as increasing the stretching turns, resulting in shorter and shorter distance between the cracks.

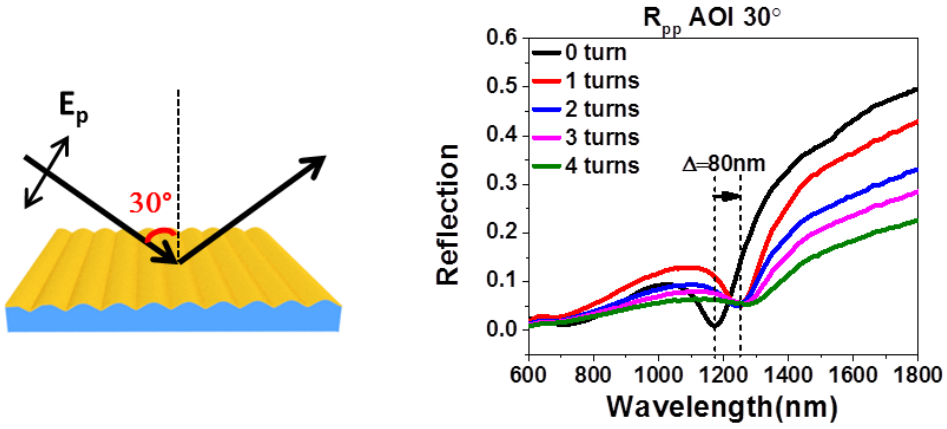

Figure 4. 46: Reflectance measured with p-polarized light at AOI 30° as a function of stretching turns.

The length of the SPPs propagating along the interface of air and Au/Ni/Au layer can be defined as:

$$L_{sp} = (2k_x'')^{-1} \tag{4.4}$$

$$k_x = k_x' + ik_x'' = \frac{\omega}{c}\left(\frac{\varepsilon_m'\varepsilon_d}{\varepsilon_m'+\varepsilon_d}\right)^{1/2} + \frac{\omega}{c}\left(\frac{\varepsilon_m'\varepsilon_d}{\varepsilon_m'+\varepsilon_d}\right)^{3/2}\frac{\varepsilon_m''}{2(\varepsilon_m')^2}\, i \tag{4.5}$$

The real and imaginary value of dielectric function at incident wavelength 1170 nm are obtained from Figure 4. 33 to be $\varepsilon_m' = -40.7$ and ε_m''= 14.5; ε_d is the permittivity of air which is 1. Then, the propagating length of SPP without stretching can be calculated to be L_{sp}=20.5 μm. We can see from Figure 4. 47(c) that the distance between the cracks in the case with 2 turns stretching is already smaller than 20.5 μm. Therefore the shorter distance between the cracks decreases the propagating length of SPP, leading to the broadening of the resonance.

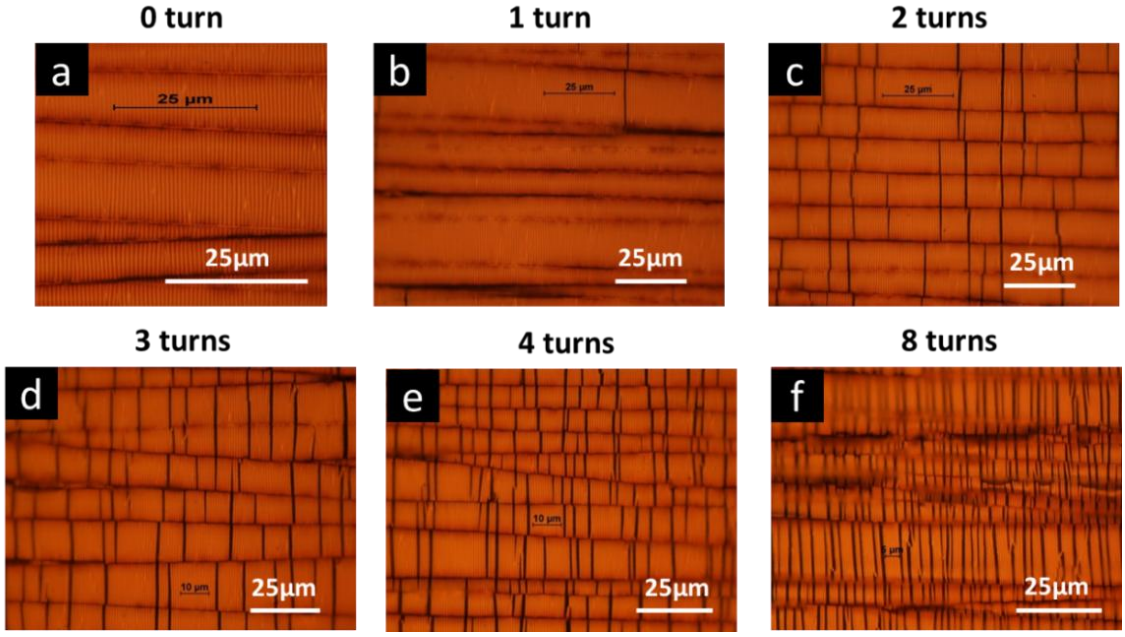

Figure 4. 47: Microscopic images at different stretching step for Au/Ni/Au grating sample fabricated with 20% prestrain and 10 min O_2 plasma treatment.

After analyzing the tuning ability of SPP via mechanical stretching, we are interested in the reversibility of this approach. However, since the sample broke after 8 turns stretching, a new 15 nm Au/10 nm Ni/10 nm Au grating sample was fabricated with 20% prestrain and 12.5 min O_2 plasma treatment. The sample was stretched until 4 turns and then was slowly released to the beginning stage without prestrain. After the sample was stretched or released at each step, R_{pp} at AOI 30° (Figure 4. 48) and microscopic images were measured (Figure 4. 49).

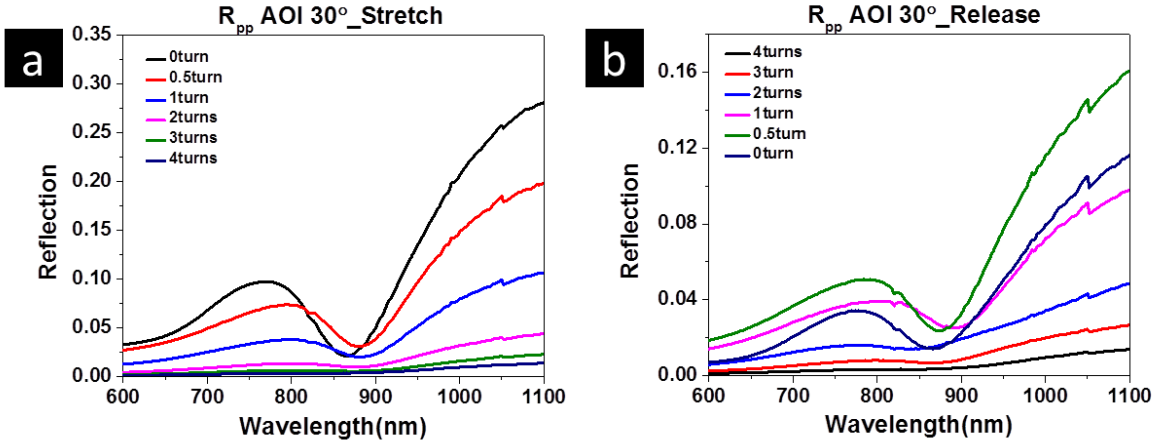

Figure 4. 48: Reflectance measured with p-polarized light at AOI 30° as a function of stretching turns during (a) stretching and (b) releasing process.

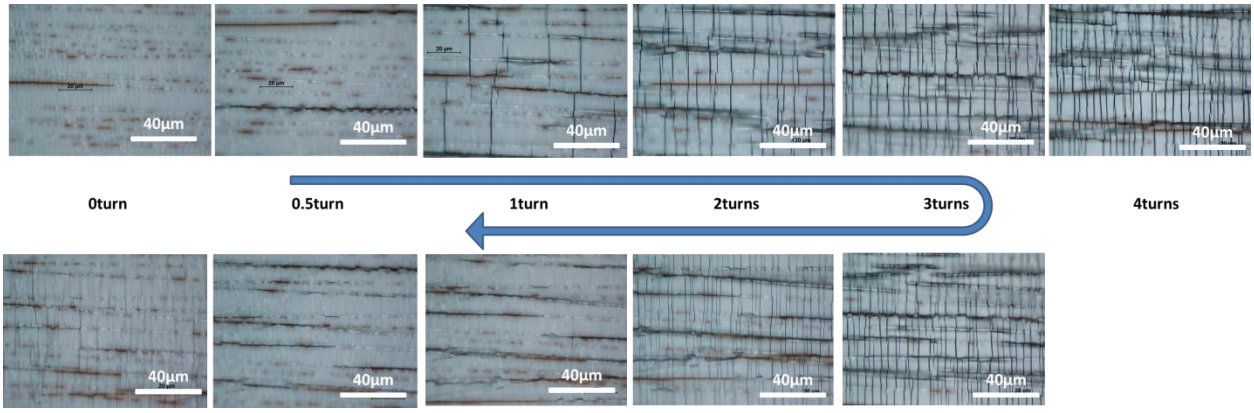

Figure 4. 49: Microscopic images at different stretching step for Au/Ni/Au grating sample fabricated with 20% prestrain and 12.5 min O_2 plasma treatment.

Same with the sample fabricated with 20% prestrain and 10 min O_2 plasma treatment, more and more cracks appear as increasing the stretching turns, resulting in shorter and shorter distance between the cracks. Figure 4. 48 (a) shows the peak position red shift as increasing the stretching. When the grating is released until only one turn prestrain is retained, the grating bulks between the cracks keep the shape and only the size of the cracks decrease. The microscopic images in Figure 4. 49 show the size of the cracks decrease to zero and the grating become continuous again when there is still 1 turn prestrain remained. Figure 4. 48 (b) shows the plasmonic peak become prominent when releasing back to the stage with 1 turn prestrain, confirming the continuous grating seen in Figure 4. 49. It is very interesting to see from Figure 4. 48 the position of plasmonic peak reverse exactly to the original stage without any stretching at 867 nm, indicating our approach for tuning SPPs is reversible.

4.3.8 Conclusion

In summary, first of all, following the approach with Au grating in Section 4.2, we have demonstrated how the complex optical response of a simple Au/Ni/Au grating can be decomposed into its physical ingredients. The optical properties are influenced by the excitation of SPPs, geometric anisotropy and to a lesser extent, the Au/Ni/Au interband transition. There is no influence of RWAs which comes from periodicity. The anisotropy, the interband transition and the non-dispersive approximation of the SPPs are understood in terms of an effective medium approach, obtained from fitting the measured reflectance. However, the dispersion of the SPP modes effects should be added on top of this model. Second of all, we compared the optical response of Au/Ni/Au grating and Au grating. Due to the absorption of Ni layer, plasmonic feature becomes broader and the influence of RWAs is disappears. Finally, we introduced an active way for tuning SPP via mechanical stretching. By actively stretching the PDMS grating template, the periodicity of grating increases and SPP peak position red shifts. The releasing of a stretched metallic grating gives us a way for tuning the crack size between grating bulks with the shape of grating bulks unchanged.

The cracks between the grating bulks can become hot spots with very high field enhancement. It will be very interesting to investigate the influence of the crack size on the polarization mixing by MM method.

4.4 Ag nanoparticle arrays

After discussing the PDMS based metallic gratings in section 4.2 and 4.3, we now turn our attention to another periodic plasmonic nanostructure which is metallic nanoparticle arrays. LSP instead of SPP plays a role in the optical response and inter-particle coupling introduce new excitations. Besides, the RWAs and waveguide excitation in the sample make the optical response even more complex. So it is very interesting for us to separate the influence of individual ingredient by using the similar approach in the previous sections.

4.4.1 Introduction

Metallic nanoparticle arrays have been widely studied over the last decades [75], [76], [88]–[93]. The optical response of nanoparticle array depends not only on the shape and environment of the individual particle [9], [94], but also on their specific arrangement, which not only modify their excitation but also can create new excitations via inter-particle coupling [95]–[97]. All these excitations depend on the wavelength, the polarization, the azimuthal orientation of the sample in case of an anisotropic arrangement and on the angle of incidence, when dispersion coming from periodicities or coupling to the neighbors is important. The interplay of all these different contributions can lead to a complex optical response, where the influence of the different ingredients cannot be easily separated.

In this section, we demonstrate how the intricate optical response of an elaborate nanoparticle array can systematically be disentangled by spectroscopic MM ellipsometry. The investigated nanoparticle array is produced by a self-organized growth process of Ag nanoparticles in a TiO_2 thin film loaded with metallic precursors by continuous laser light excitation. This type of sample is known to produce bright and robust colors [98]–[100]. The optical characterization starts with the AOI dependent transmission measurements revealing the dispersion coming from waveguide excitations due to the periodic arrangement of the Ag nanoparticles embedded into the thin TiO_2-film as well as the azimuthal dependent transmission showing the anisotropy of the sample. From these intensity measurements, a first simple effective medium model is developed. Comparing the full MM measurements with the simulated MMs calculated form this simple model and subsequently decomposing the obtained MMs allows us to decouple the different contributions to the optical response and learn about the special properties of this sample design.

4.4.2 Experimental

We consider an Ag nanoparticle ensemble embedded in a TiO_2 film produced by a single homogeneous continuous-wave laser beam according to a reported procedure [98], [99]: A mesoporous film of amorphous Titania loaded with silver salt and small silver nanoparticles was deposited on a glass substrate. The laser beam was slightly focused on the sample by a 10x microscope objective (Olympus MPlan N, N.A. 0.25) under normal incidence, the diameter of the circular spot in the focal plane can be varied by changing the focus. The incident power on the sample is 300 mW at laser wavelength 488 nm. During exposure, the samples are translated at a constant speed of 0.6 mm/s to draw 4 mm long lines with the laser beam. Under such illumination conditions, silver nanoparticles spontaneously grow along periodically spaced chains parallel to the laser polarization that form periodic Ag nanoparticle ensemble with

periodicity 270 nm measured from diffraction measurements in a back-scattering configuration [98]. Here the laser polarization is set perpendicularly to the laser path.

Spectroscopic ellipsometry was performed on the mesoporosity non-illuminated TiO_2 area in order to investigate the thickness and permittivity of TiO_2 film. Ellipsometric angles ψ and Δ were measured in the spectral range between 370 nm and 1690 nm at AOI from 35° to 65° by 10°. Then a general oscillator layer on glass substrate was used to fit the measured ellipsometric angles. In the general oscillator layer, 5 Gaussian and 2 Lorentz oscillators were used. By fitting both the thickness and all oscillators, a nice fit with mean-squared error (MSE) less than 1 was obtained (Figure 4. 50(a) and (b)). So the thickness of TiO_2 is 160 nm and the refractive index n is around 1.9 with little dispersion in the spectral range between 370 nm and 700 nm as shown in Figure 4. 50(c).

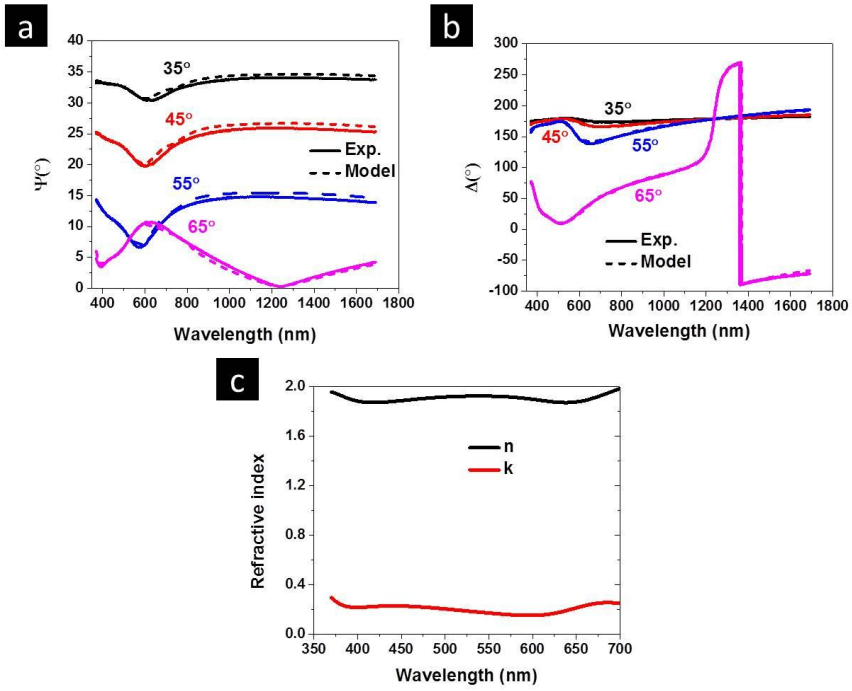

Figure 4. 50: Ellispsometric angles (a) ψ and (b) Δ measured and modeled in the spectral range between 370 nm and 1690 nm. (c) obtained dielectric constant of TiO_2 layer.

Figure 4. 51(a) displays a schematic of the fabricated sample. The nanoparticles are located at the TiO_2/glass interface. The size of silver nanoparticles ranges from 20 to 100 nm and the interparticle distance along a chain varies. The sample topography was measured with profilometer (Dektak). It is found that the thickness of the laser exposed area is 85 ± 35 nm thinner (the surface roughness induces the error bar) than the non-illuminated TiO_2 area, which is expected due to the collapse of the mesoporosity of the initial TiO_2 layer during the laser-induced heating. The thickness of the non-illuminated TiO_2 area is 160 nm as determined by ellipsometry measurement. Figure 4. 51(b) shows a SEM image of the Ag nanoparticle region of the sample. We can see that the Ag nanoparticle chains are not straight but arc-shaped lines that mainly follow the shape of the laser spot in the front edge of the translating elliptical beam. The radius of curvature of the nanoparticle lines is around 15 μm by analyzing the arc in SEM images. This value is confirmed by the optical microscopy pictures shown in Figure 4. 51(c) that shows

the starting area of the laser beam exposure. Figure 4. 51(d) illustrates the sample geometry. The angle α=0° is defined when the plane of incidence is perpendicular to the particle lines.

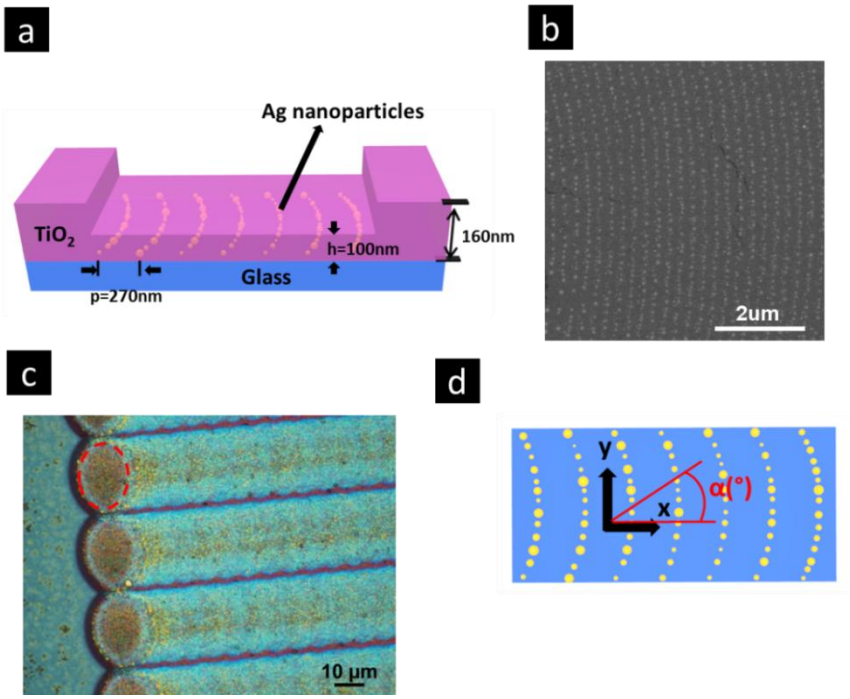

Figure 4. 51: (a) Schematic of the fabricated sample. The period between the NP chains is 270 nm. The thicknesses of the initial TiO_2 area and laser-processed area are estimated at 160 nm and 100 nm respectively. (b) SEM image of the Ag nanoparticle region. (c) Optical microscope image with magnification x100 of the starting area of laser beam exposure. The red dashed circle indicates the size of the focal spot of the laser beam. (d) Definition of azimuthal angle α as well as orientations x and y with respect to the NP lines.

4.4.3 Physical description of the sample

Before presenting the experimental data, we describe the behavior of the sample in transmission configuration emphasizing the possible excited modes. Similar samples have been produced and described in previous work [98]. Figure 4. 52(a) illustrates schematically the possible interactions inside the sample, while Figure 4. 52(b) presents a schematic of the cross-section of the processed part of the TiO_2 layer only. The incident light beam on its way through the sample interacts with the embedded Ag nanoparticles and it is be partly diffracted by the presence of the Ag nanoparticle grating (violet open arrows in Figure 4. 52(b) and (c). The directly transmitted light is be absorbed and reradiated by Ag nanoparticles resulting in the characteristic presence of the localized surface plasmon (LSP) resonance spectrum. The plasmonic resonance shape depends on the individual particle shape and size distributions, as well as on nanoparticle interactions along the lines or between lines. In the inset of Figure 4. 52(a), the electric field lines drawn between adjacent particles along a line evoke the possibility of a near field coupling between particles along a line. This kind of coupling, which differs depending on the incident polarization may change the overall behavior of individual particles. In the framework of the

dipolar approximation, we could say that for a polarization perpendicular to the lines Coulomb forces add up and strengthen the internal field. This leads to increase the resonance frequency and therefore a blue-shift of the resonance. For a polarization parallel to the lines, Coulomb forces subtract, the internal field decreases and leads to a red shift of the resonance. This can explain the broadening of the overall resonance observed when the polarization is parallel to the grating lines. On the other hand, the excitation of the guided mode (through the first diffraction order) leads to a far field coupling between the different nanoparticle lines. The diffracted light can in turn be coupled to the waveguide eigenmodes supported by the TiO_2 layer and propagate either to the right or to the left.[100] The waveguide mode is a leaky mode and part of the coupled light will be secondarily diffracted by the particle grating following the position of the Rayleigh-Woods anomalies (RWA). The diffracted part of the leaky waveguide mode interferes with the directly transmitted light and gives rise to a splitting of the LSP resonance. This splitting, or modulation of the transmittance minima, is due to the strong interaction of two absorbance modes: the plasmonic modes and the destructive interference mode. We name the result of the interference of the diffracted waveguide mode "destructive interference mode", or DIM, in the following. Details about the analytical analysis and the expressions for the DIM are to be found in the section 2.8. The effect of these physical phenomena will be investigated in terms of intensity signatures, dispersions and more importantly, using MM measurements, modelling and appropriate decomposition methods, the disentanglement of all the effects will be possible.

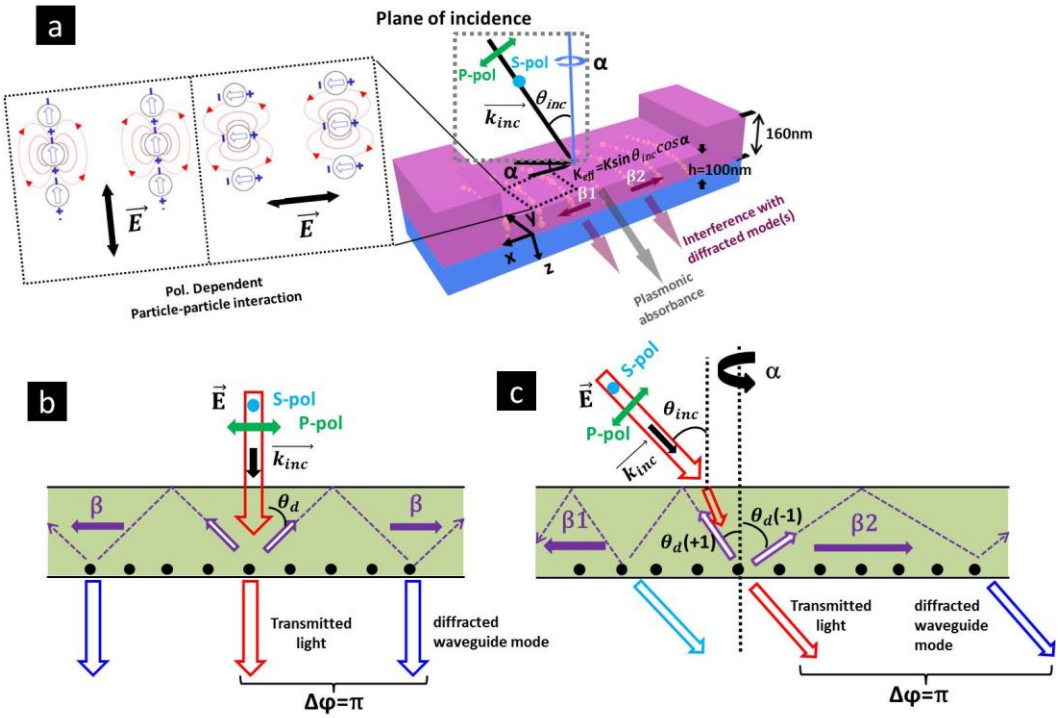

Figure 4. 52: (a) Schematic of the structure showing the principle of the DIM at $\alpha \neq 0°$ for oblique incidence, illustrating the different excitations in the sample. (b) Schematic of the structure showing the principle of the DIM at $\alpha = 0°$ at normal incidence, inspired from Ref. [98] and (c) oblique incidence.

4.4.4 Procedure to calculate DIM

After describing the possible physical effects of our sample, the next step is to obtain the parameters for the calculations. n_{air}=1 and n_{glass}=1.52 are known parameters. In this section, we first show how we obtain the thickness and refractive index of the waveguide TiO_2 layer in steps 1-3 and then we show how we calculate the dispersion of the DIM in step 4.

Step 1: The refractive index and thickness of pure mesoporous TiO_2 film on the edge

Due to the presence of the Ag nanoparticles, the permittivity of the TiO_2 matrix in the Ag nanoparticles region cannot be directly measured, so we measured the pure mesoporous TiO_2 film on the side with ellipsometer instead. The measured ellipsometric angles ψ and Δ were fitted very well with a General oscillator model with MSE<1. Finally the refractive index and thickness of mesoporous TiO_2 film can be precisely extracted from this model. The thickness of the TiO_2 outside the Ag nanoparticle region is 160 nm and the refractive index n is about 1.9 in the measurement range (370-700 nm) as shown in Figure 4. 53(b).

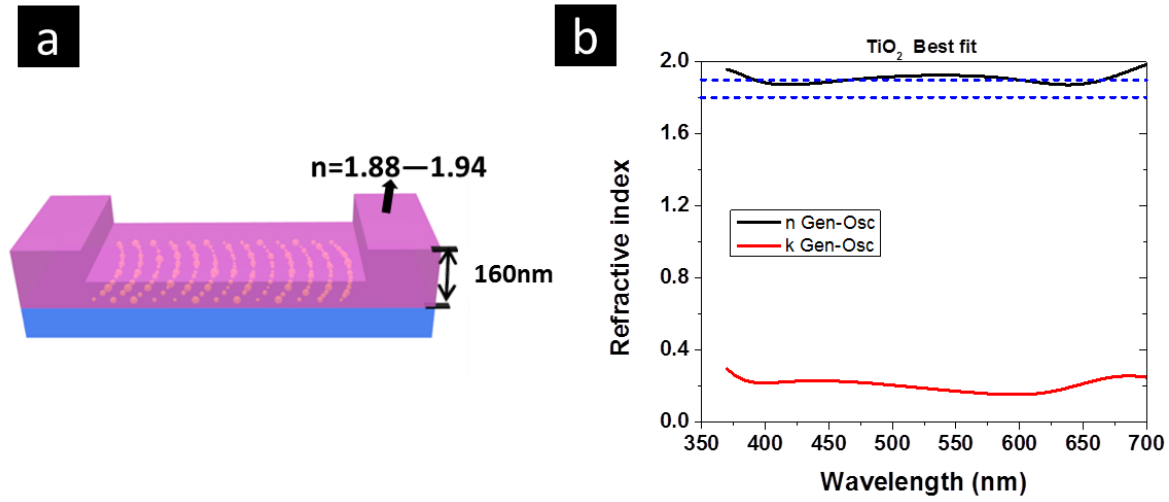

Figure 4. 53: (a) Schematic of the fabricated sample. (b) Refractive index of the initial TiO_2 area. The thicknesses and refractive index of the initial TiO_2 area are precisely extracted from ellipsometric modeling.

Step 2: Evaluation of the refractive index and the thickness of TiO_2 waveguide layer

The refractive index of bulk TiO_2 can be found in our ellipsometry library and shown in Figure 4. 54. Irrespective of the type of TiO_2, the refractive index is always higher than 2.33 over the whole interesting spectral range. Due to the collapse of the mesoporous TiO_2 after laser exposure, we expect that the refractive index of TiO_2 waveguide layer should be higher than that of the pure mesoporous TiO_2 film on the edge and smaller than the dense TiO_2 bulk from ellipsometry library. Therefore we consider that the refractive index of the TiO_2 matrix should be comprised in the range [1.9:2.33].

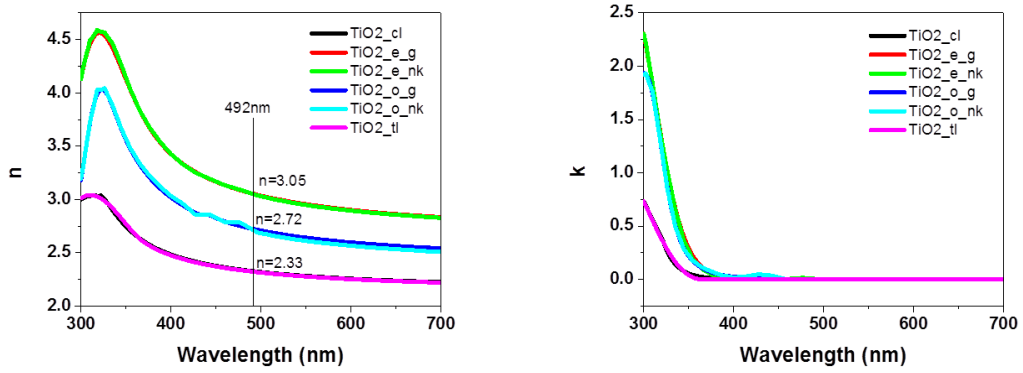

Figure 4. 54: The refractive index of bulk TiO_2 as found in our ellipsometry library.

The step height between initial and illuminated areas was measured by profilometer scan to be around 75-100 nm in average. The surface roughness induces an error bar in the range (+/-20 nm). From this, we estimate that the thickness of waveguide is in the range 40-105 nm.

Step 3: The effective values for the refractive index and the thickness of TiO_2 waveguide layer (h=100 nm, n_{TiO2}=2.21) are obtained based on the measured wavelength λ=492 nm of the DIM mode at θ=0°, α=0°.

In this step, we reduce the uncertainty on the values of refractive index n_{TiO2} of the TiO_2 matrix and thickness h of the TiO_2 waveguide comprising the Ag nanoparticles. As we can see from Figure 4. 55, experimentally the position of the DIM at θ=0°, α=0° is found to be λ=492 nm Then for each a given value of h, we can obtain a specific value for n_{TiO2} fulfilling this condition. We can obtain various pairs of h and n_{TiO2}. For instance we obtain the possible pairs of values:

- h =71 nm, n_{TiO2}=2.53
- h =100 nm, n_{TiO2}=2.21
- h =158 nm, n_{TiO2}=1.99

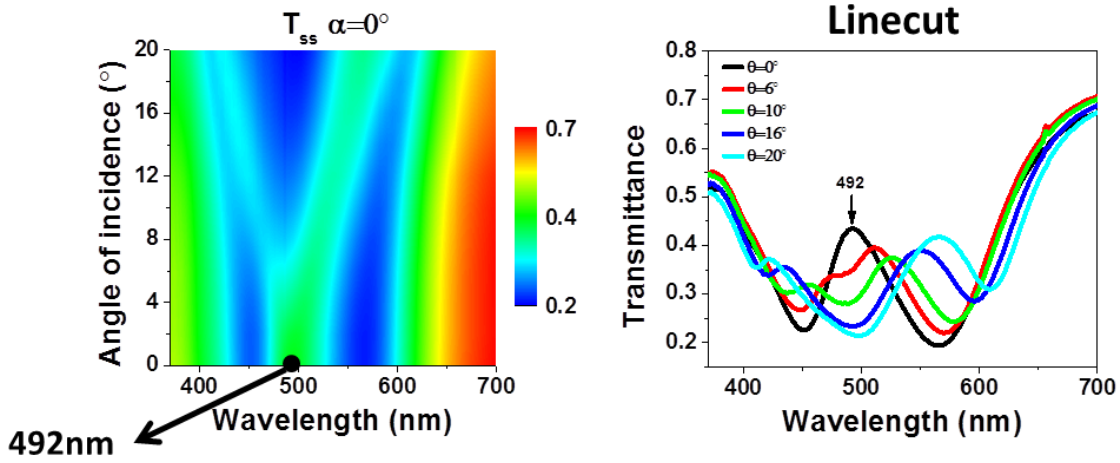

Figure 4. 55: (a) contour plot and (b) line cuts of measured T_{ss} as a function of angle of incidence.

For simplicity, we obtain the following equations by only considering the case f =0 in Equation (2.105) and first order of diffraction in Equation (2.104):

$$sin\theta_{inc}cos\alpha \pm n_{TiO_2}sin\theta_d\sqrt{1-\left(\frac{sin\theta_{inc}sin\alpha}{n_{TiO_2}sin\theta_d}\right)^2} = \pm\frac{\lambda_0}{P} \tag{4.6}$$

$$\Delta\varphi = 2k_{TiO_2}h - 2\varphi_1 - 2\varphi_2 = \pi \tag{4.7}$$

where the positive sign corresponds to +1 order and the negative sign corresponds to -1 order.

By using the conditioned values for the pairs of parameters with Equations 4.6 and 4.7, we can obtain the dispersion lines as a function of θ at α=0°. We now compare the slopes of the dispersion lines with the experimental slopes on both sides of the plasmonic resonance. The pair of values providing the best fitting slopes (i.e., fitting all the experimental dispersions) will be chosen. As we can see from Figure 4. 56, the slope of the dispersion line for the pair (h =100 nm, n_{TiO2}=2.21) fits the measured intensity modulation the best. Besides, h =100 nm, n_{TiO2}=2.21 are both inside the range deduced in step 2. Therefore we fixed the values h =100 nm, n_{TiO2}=2.21 to calculate the DIM lines.

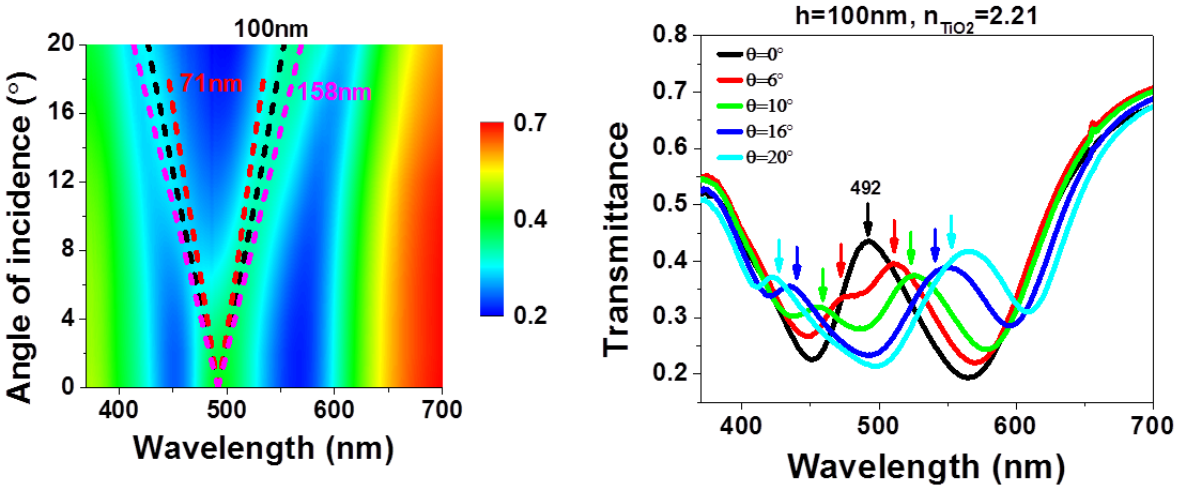

Figure 4. 56: (a) Contour plot of measured T_{ss} as a function of AOI together with calculated DIM lines in three different cases. (b) measured T_{ss} together with calculated position of DIM at θ=0°, 6°, 10°, 16° and 20° in the case h =100 nm, n_{TiO2}=2.21.

Step 4: Using h=100 nm, n_{TiO2}=2.21 to calculate the DIM lines as a function of θ and α.

At given values of the incidence angle θ_{inc} and of the azimuthal orientation α, Equation 4.6 only has two related and unknown parameters the diffraction angle θ_d and the excitation wavelength λ_0. By applying Equation 4.6, we sweep the value of θ_d from 0-90° by steps of 0.1° and we obtain the corresponding λ_0 for each value of θ_d. Subsequently, we plug each (θ_d , λ_0) pairs in Equation 4.7 to calculate which pair fulfills Equation 4.7. As a consequence, the obtained value of λ_0 which fulfills Equation 4.7 is the incident wavelength to excite DIM at this given

measurement geometry (θ_{inc} and α). Finally, sweeping for θ_{inc} from 0-20° by steps of 2° and α from 0-90° by steps 10° we obtain all the data points for DIM positions.

4.4.5 Dispersion and angular dependence of the transmittance

The transmittance spectra depend strongly on the polarization of the incident light, its AOI and on the orientation of the sample. Figure 4. 57(a) and (b) display the transmittance spectra for p- and s-polarization, for two perpendicular sample orientations, at normal incidence. For both polarizations, the spectra are influenced by the absorbance due to the plasmonic modes as well as a modulation of the transmittance within the absorption band. The sharp increase in transmittance inside the plasmonic absorption band originates from the destructive interference between the transmitted beam and the diffracted quasi-guided mode and is linked to the RWA position. It can be experimentally observed in the transmission spectra displayed on Figure 4. 57. These transmittance spectra are similar to earlier publications [98]. We note the important difference between light purely diffracted by a simple one-dimensional surface metallic grating for which the RWAs appear when surface plasmon polaritons are excited for a TM polarization, i.e., a polarization vector perpendicular to the grating lines [101], and the present case where the RWAs are indirectly excited via the propagating waveguide modes. The latter case results in an effective coupling polarization parallel to the grating lines. Therefore in the present case, the DIM, linked but not exactly equal to the RWAs, will be active for the s-polarized light when the sample is oriented at α=0° and for p-polarized light at α=90°, which corresponds to the inverted situation compared to the case of direct interaction with a simple grating. Let us now turn our attention to the dispersion and angular dependence of the transmittance.

Figure 4. 57 shows the transmittance measured with s- and p- polarized light at α=0° and 90°. Figure 4. 57(c), (d) and (e), (f) show the dispersion plots of T_{ss} (incoming s- into transmitted s-polarized light) and T_{pp} respectively. T_{ss} and T_{pp} at α=0° for θ =[0°,6°,10°,16°,20°] are shown in the insets of the respective plots, the colored arrows representing the calculated position of the DIM. The dispersion color plots underline the complexity of the optical response. The calculated dispersion of the DIM mode is added to the contour plots as dotted lines. For both polarizations and samples orientations, the position of the DIM explains the modulation of the transmittance of the sample very well. It is to be noted that the arc shape of the grating lines gives rise to an apparent widening of the position of the DIM line as well as some uncertainties at larger angles of incidence. Therefore the apparent difference between the DIM line and the experimental plots in Figure 4. 57 (e) is to be interpreted in this sense. The Ag nanoparticle ensemble gives rise to a broad plasmonic mode of about 130 nm FWHM, modified by the presence of the DIM. The large distribution of the size of nanoparticles as well as the radiative losses contributes to the resonance width.

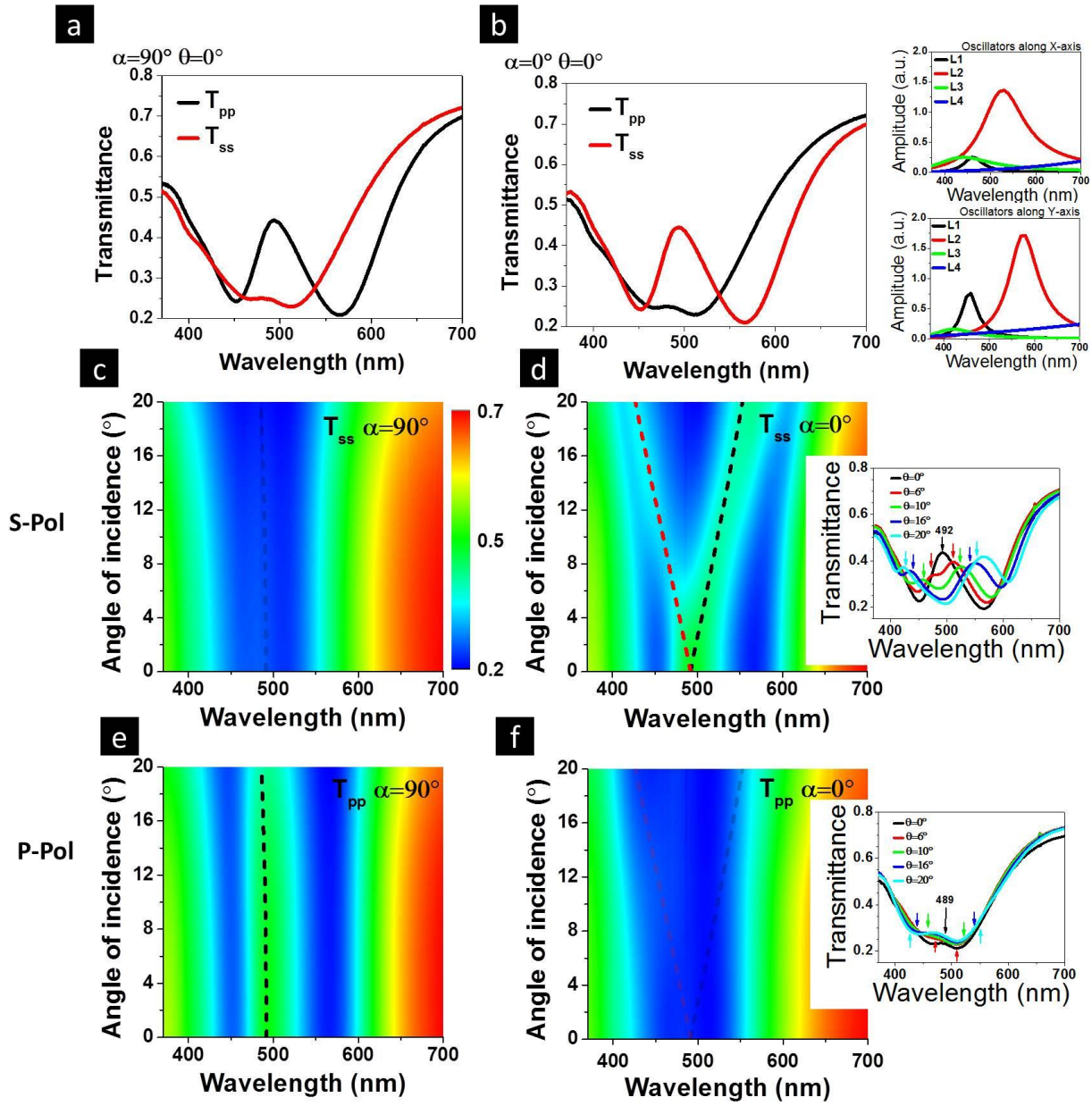

Figure 4. 57: Measured transmittance T_{ss} and T_{pp} (a) α=90° θ=0°and (b) α=0° θ=0°. The Lorentz oscillators used in general oscillator model for fitting the transmittance are found in inset; (c) Dispersion plots of the measured transmittance between θ=0° and 20° in steps of 2° in the spectral range between 370 and 700 nm with s-polarized light at α=90° and (d) at α=0°, (e) with p-polarized light at α=90° and (f) α=0°. All contour plots are shown together with dashed lines indicating DIM (±1). The insets represent T_{ss} and T_{pp} at α=0° at selected angles of incidence, the arrows indicating the calculated positions of DIM (±1).

Further, the azimuthal dependence of the transmittance allows us to discuss the induced anisotropy and the polarization mixing of the sample. Figure 4. 58 shows the measured transmittance for p-polarized light T_{pp}, for s-polarized light T_{ss} as well as the polarization conversion T_{ps} (incoming p- into transmitted s-polarized light) at angles of incidence 0°, 10° and

20° over the complete azimuthal rotation of the sample in steps of 5° over the spectral range 400 nm-700 nm together with the predicted position of the DIM (±1) lines in the top half-space as black (DIM-1) or red (DIM+1) lines. The azimuthal transmittance plots are characterized by a strong anisotropy between the directions along α=0° and 90°.This anisotropy is strongly linked to the sample geometry, and in particular to that of the nanoparticle grating. Similarly to the dispersion plots from Figure 4. 57, the locus of the DIM fits with the observed intensity modulations seen in the experiment. However the coupling strength of the DIM is anisotropic and depends on the light polarization. At normal incident s-polarized light, the interaction of the DIM mode is stronger at azimuthal orientation 0°. Indeed, in this case, the light coupled to the waveguide mode "sees" the particle grating at most. Correspondingly, in the case of p-polarization the larger split is along 90°. More interesting is the case at larger angles of incidence 10° and 20°. The complex intensity pattern for both p- and s-polarized light can be fully understood by the position of the DIM lines. At angles of incidence away from the normal, the modes DIM (+1) and DIM (-1) are non-degenerate and contribute both to the modification of the transmitted intensity.

The conversion of polarization T_{ps} in Figure 4. 58(i) to (k) show maximum values at azimuthal angle 45° as expected for a sample with two optical axes, similarly to the case of a simple quarter wave plate [102], which in our case are the axes perpendicular to the grating lines (X-axis) and along the lines (Y-axis). The areas of maximum polarization conversion follow the position of the DIM (+1) line, as a function of the incident angle. Indeed it is interesting to note that as the incident angle increases, these areas are stretched correspondingly to the elongation of the DIM (+1) lines.

Not only does the DIM influence the plasmonic resonance, the coupling between adjacent Ag nanoparticles will also play a role [103]. In order to make clear the physical origins of the resonance seen in the transmittance, we present here a simple anisotropic layer model based on Fresnel's equations. This model allows us to further understand the anisotropy and other underlying physical features of the observed optical behavior at normal incidence. A 100 nm thick biaxial layer, representing effectively the active TiO_2 layer with the embedded Ag NPs, is modelled on top of a glass substrate named bk7_g in ellipsometric software. The biaxial layer is defined by the oscillators along the three directions X, Y and Z. In the Z direction, which is normal to the layer interface, a Cauchy oscillator representing the TiO_2 matrix is used. We find the parameters of the oscillators along the two main optical axes in the X-direction (perpendicular to the grating lines) and Y-direction (parallel to the grating lines) by fitting the experimental transmittance measured at normal incidence along X and Y using two different general oscillator (Genosc) layer models as shown in Figure 4. 59(a) and (b) [18]. We note here that the created model is a purely biaxial model only valid at normal incidence since it is not able to reproduce dispersion as described extensively in a previous work [101]. Four Lorentz oscillators are used in both X and Y directions in order to obtain a perfect fit of the transmittance spectra and are represented in the inset of Figure 4. 57(b). The three Lorentz oscillators, L1 to L3, fully located inside the measured range 400-700 nm correspond to plasmonic excitations within the sample.

The nanoparticles are very close to spheres and the small deviation due to the arrangement of the NP into lines cannot explain the split of the resonances. Due to the size variation of the NP, the resulting plasmonic resonance is inhomogeneously broadened. When the incident polarization is along X the particles do not couple strongly in the near-field. However, then the incident polarization is exciting the resonances along the grating lines, the near-field coupling

between particles along the line is stronger and broadens the overall plasmonic resonance of the particle ensemble. The presence of the DIM mode induces a split into the plasmonic resonance by inducing an extra absorption feature inside the plasmonic absorbance. Therefore this results in an enhanced transmittance at the position of the DIM mode. Since our model does not take the destructive interference mode into account, the coupling strength between the DIM mode and the plasmonic absorbance results in the two modelled resonances L1 and L2, which do not represent independent resonances within the sample. In the case of Figure 4. 57(a), the E-field from the waveguide mode cannot excite the 1D grating and instead excites the particles along the lines. A slight sensing of the presence of the gratings is felt owing to the curvature of the particle lines. When the field from the waveguide mode is perpendicular to the grating lines, the influence of the grating, hence of the DIM, is much greater, as seen in the T_{ss} case at α=0°. There we can see that the diffraction mode, which lies at 492 nm at normal incidence, splits the broader plasmonic resonance into two well separated L1 and L2. Even though strictly speaking L1 and L2 are only defined at normal incidence in our model, we could imagine creating a similar model at $\theta \neq 0°$. In this case, when the AOI increases, the DIM lines split (dashed lines) and their relative position with respect to the plasmonic resonances change: L2 is still strongly red-shifted while L1, after being blue-shifted at low angles of incidence, becomes also red-shifted for $\theta > 12°$ and results in the strong transmittance dip in between the two DIM lines (Figure 4. 57(d)). The origin of the third resonance, L3, is not completely clear. When the direction of polarization rotates, the contribution of L3, strong along the particle line, is decreasing when the excitation is mostly perpendicular to the lines. One hypothesis is to speculate that it could correspond to the coupled particle resonance of a part of the nanoparticle ensemble strongly affected by the nearest-neighbor interaction between adjacent particles. Therefore the amplitude of L3 is lower in Figure 4. 57(b) than in Figure 4. 57(a). In order to lift this ambiguity, the investigation of samples with different geometrical parameters would be necessary. Finally, L4 is located outside the measured range, contributing only by a tail, and originates from the TiO_2 matrix. By using this model, both the T_{ss} and T_{pp} over the whole azimuthal range at θ=0° can be calculated (Figure 4. 58(d) and (h)) and reproduce well the measured transmittance shown in Figure 4. 57(a) and (b).

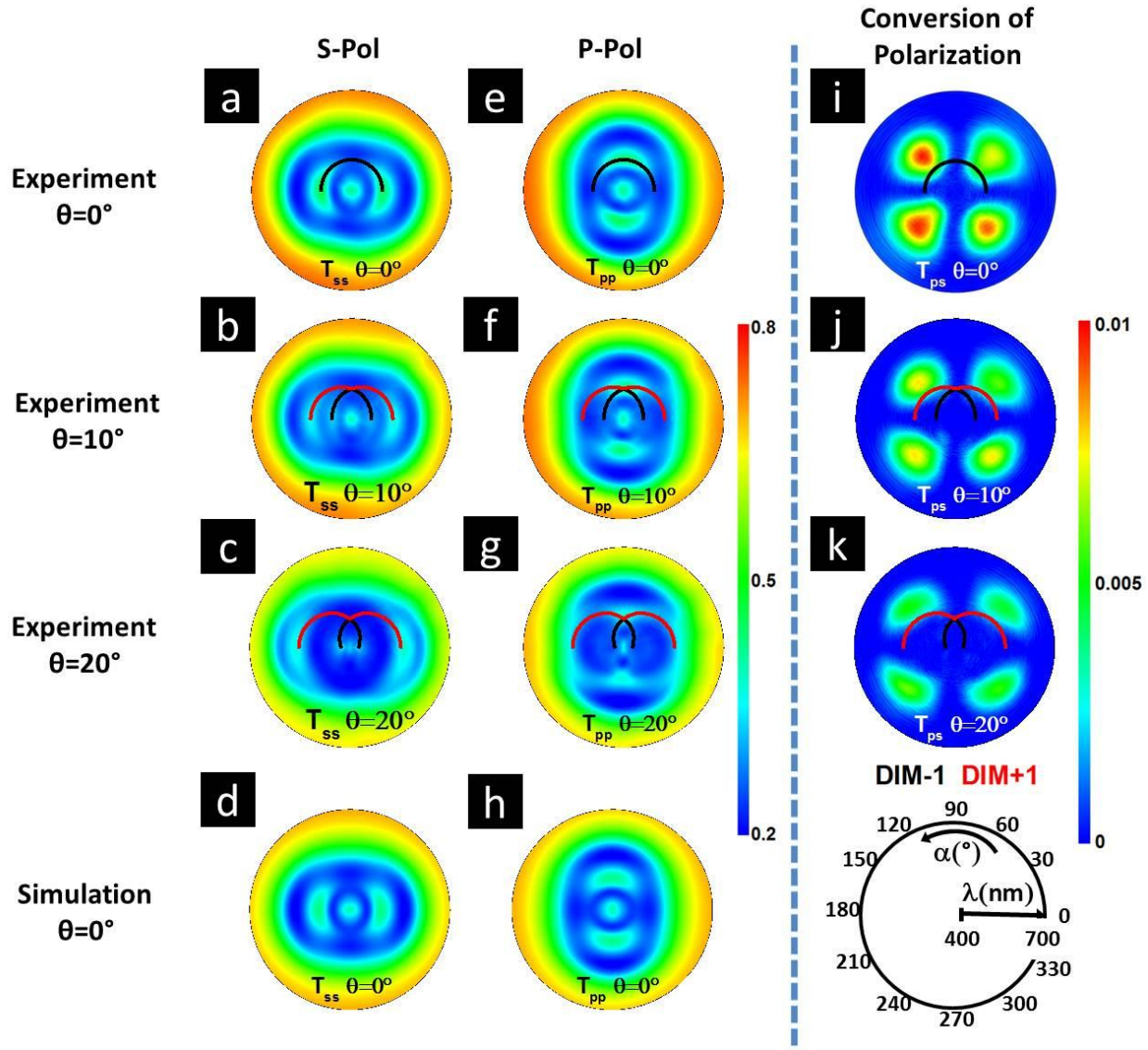

Figure 4. 58: Measured transmission at full azimuthal rotation in steps of 5° in the spectral range between 400 nm and 700 nm with s-polarized light at θ equals (a) 0°, (b) 10° and (c) 20° and with p-polarized light at θ equals (e) 0°, (f) 10° and (g) 20°. Experimental polarization conversion T_{ps} at θ=0°, 10° and 20° are shown in (i), (j) and (k) respectively. DIM(+1) and DIM(-1) are identical at θ =0°. At other θ, red and black lines represent DIM (+1) and DIM (-1) respectively. DIM (±1) lines are shown only in the half space not to mask the raw data in the other half space. (d) and (h) show simulated T_{ss} and T_{pp} at normal incidence. The polar axis is wavelength and the polar angle is the azimuthal angle.

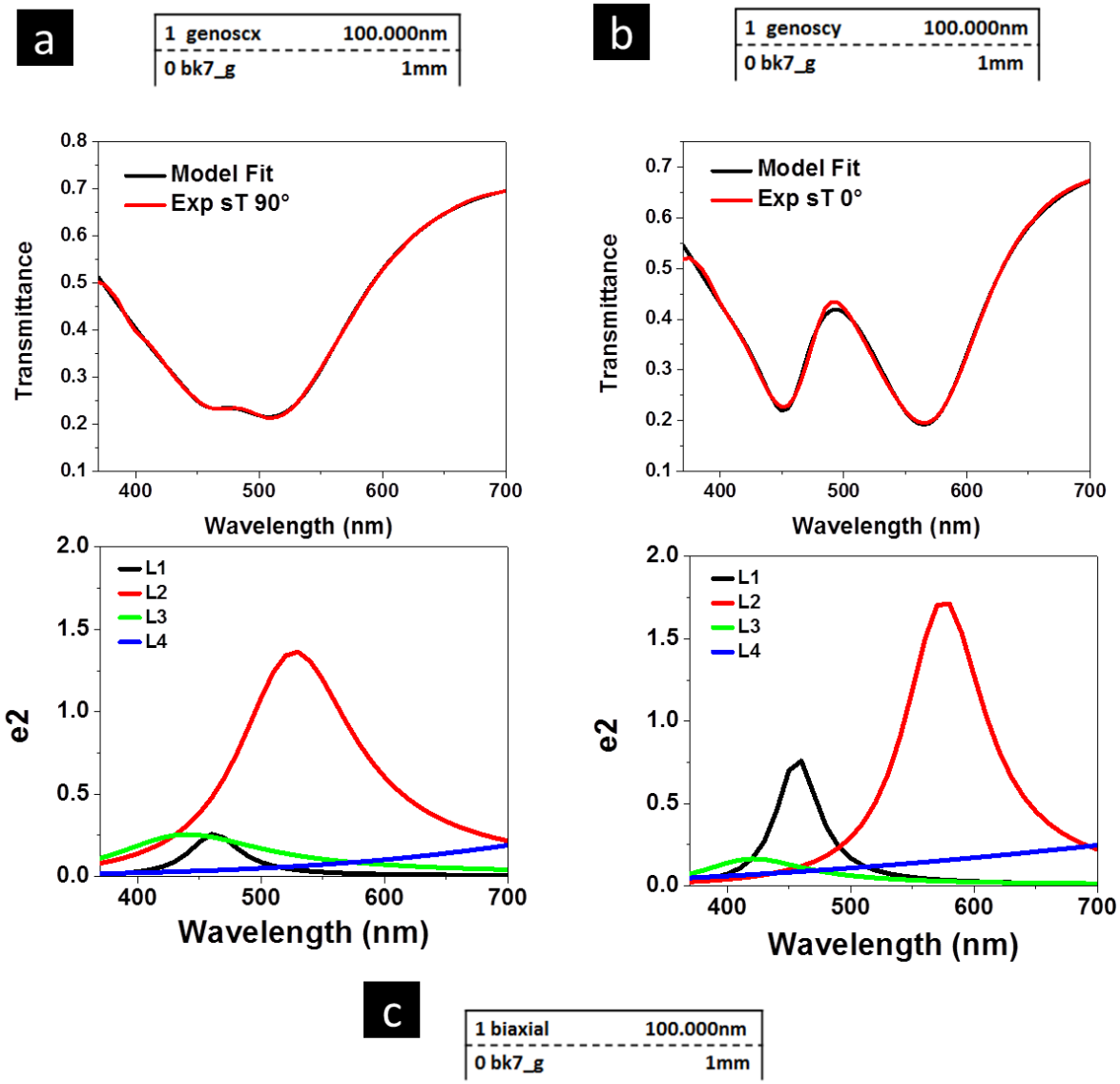

Figure 4. 59: Modeled and measured T_{ss} at normal incidence together with oscillators plots along (a) α=90° and (b) 0°. (c) Biaxial layer model with genoscx in X direction, genoscy in Y direction and Cauchy in Z direction.

4.4.6 Mueller Matrix in transmission

To gain deeper insight in the anisotropy and polarization mixing of this complex sample, pure intensity measurements are not sufficient, and MM measurements should be performed. Figure 4. 60(a) shows the normalized MM measured at normal incidence. The MMs at oblique incidence 10° and 20° are shown in Figure 4. 61(a) and Figure 4. 62(a). All the MM elements are normalized to the element M11 and are presented as polar contour plots, where the azimuthal angle α is the polar angle and the radial axis represents the wavelength, to visualize the large amount of available data. First of all, we notice the symmetry in the MM contour plots. As expected from a MM measured in transmission, we have identical pairs M12/M21, M13/M31

and inverted pairs M24/M42, M34/M43. The identical pairs M12/M21 and M13/M31 are a first hint that depolarization effects can be neglected in our sample [33]. This means that the MM can be considered as a Mueller-Jones matrix and therefore only describes polarization conversion [104]. Besides, the symmetry of the patterns in each single MM element (MME) reflects the sample optical axes at α=0° and 90°. An interesting signal is observed in the elements M14, M41 and M44, related to the circular polarization. The question is here to identify the origin of this signal: is the signal a trivial signature of the combination of the linear effects, or is it intrinsically created by the nanostructure of the sample? In other words, what is the origin of the symmetry breaking? And what is the role of interparticle interactions? In transmission geometry, the general MM for a homogeneous non-depolarizing optical media can be written in the following matrix [42]:

$$M = \begin{pmatrix} 1+\frac{1}{2}(\mathrm{LD'^2}+\mathrm{LD^2}) & -\mathrm{LD} & -\mathrm{LD'} & \mathrm{CD}+\frac{1}{2}(\mathrm{LB}\cdot\mathrm{LD'}-\mathrm{LB'}\cdot\mathrm{LD}) \\ -\mathrm{LD} & 1+\frac{1}{2}(\mathrm{LD^2}-\mathrm{LB'^2}) & \mathrm{CB}+\frac{1}{2}(\mathrm{LB}\cdot\mathrm{LB'}+\mathrm{LD}\cdot\mathrm{LD'}) & \mathrm{LB'} \\ -\mathrm{LD'} & -\mathrm{CB}+\frac{1}{2}(\mathrm{LB}\cdot\mathrm{LB'}+\mathrm{LD}\cdot\mathrm{LD'}) & 1+\frac{1}{2}(\mathrm{LD'^2}-\mathrm{LB^2}) & -\mathrm{LB} \\ \mathrm{CD}-\frac{1}{2}(\mathrm{LB}\cdot\mathrm{LD'}-\mathrm{LB'}\cdot\mathrm{LD}) & -\mathrm{LB'} & \mathrm{LB} & 1+\frac{1}{2}(\mathrm{LB^2}+\mathrm{LB'^2}) \end{pmatrix} \quad (4.12)$$

where LB and LB´ are linear birefringence along the x/y and ±45° axes, LD and LD´ are linear dichroism along the x/y and ±45° axes. CD is the true circular dichroism corresponding to the intrinsic CD (CD_{int}), and CB is the true circular birefringence corresponding to the intrinsic CB (CB_{int}). This MM representation illustrates clearly that each MME can be described by combinations of the 6 basic optical properties. In particular, it is worth to mention that $\mathrm{M14} = \mathrm{CD_{int}} + \frac{1}{2}(\mathrm{LB}\cdot\mathrm{LD'} - \mathrm{LB'}\cdot\mathrm{LD}) = \mathrm{CD_{app}}$ is the apparent circular dichroism with $\frac{1}{2}(\mathrm{LB}\cdot\mathrm{LD'} - \mathrm{LB'}\cdot\mathrm{LD}) = \mathrm{CD_{lin}}$ the linear part of the circular dichroism originating from the combination of the linear optical properties. Similarly, $\mathrm{M23} = \mathrm{CB_{app}}$ and $\frac{1}{2}(\mathrm{LB}\cdot\mathrm{LB'} - \mathrm{LD}\cdot\mathrm{LD'}) = \mathrm{CB_{lin}}$. Moreover, we can see from the formula (2) that, if $CB_{int} << CB_{lin}$ and $CD_{int} << CD_{lin}$, then $\mathrm{M14} \approx -\mathrm{M41}$ and $\mathrm{M23} \approx \mathrm{M32}$, which is not the case in the as-measured MM. In order to separate the effects, a decomposition of the MM needs to be applied.

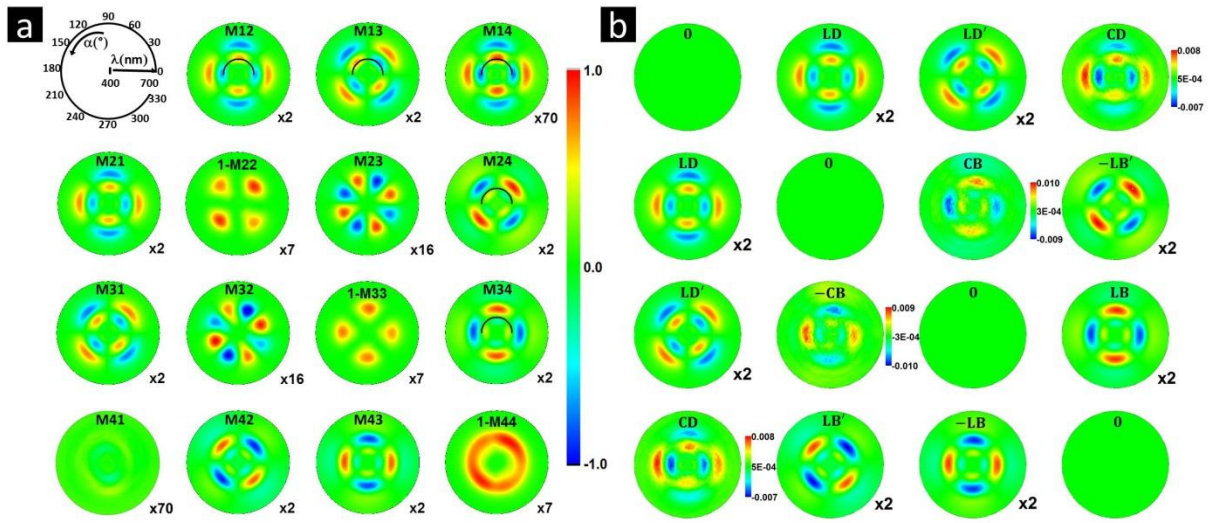

Figure 4. 60: (a) Mueller matrix elements measured in transmission at normal incidence with full azimuthal rotation in the spectral range between 400 nm and 700 nm. All the MM elements are normalized to M11. M22, M33, M44, M14 and M41 elements have original scale, while the rest elements have multiplication factors to have the same scale bar (-1.1) which is placed on the right. The diagonal elements are shown as 1-M22, 1-M33 and 1-M44 in order to enhance the color contrast because M22, M33 and M44 have values close to 1. M12, M13, M14, M24 and M34 elements are shown together with RWAs (±1) lines only in the half space to enable the visualization of the raw data in the other half space. (b) Differential decomposition matrix L_m of the MM. L_m14, L_m23, L_m32 and L_m41 have their original scale, while all the rest elements have the same scale bar [-1:1].

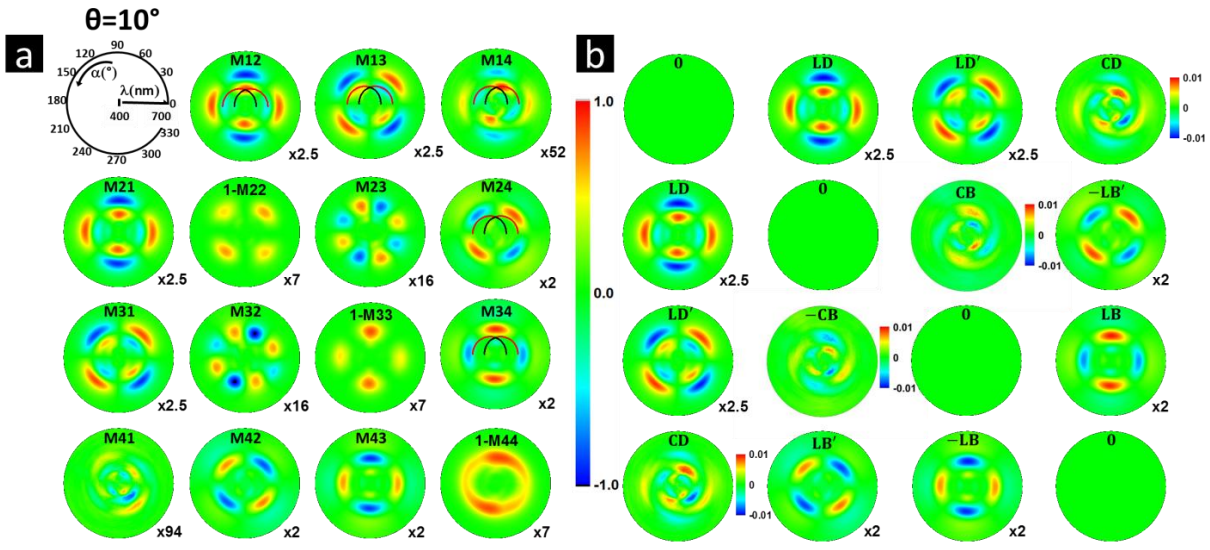

Figure 4. 61: (a) MM elements measured in transmission at AOI 10° with full azimuthal rotation in the spectral range between 400 nm and 700 nm (b) The differential decomposition matrix L_m at AOI 10°.

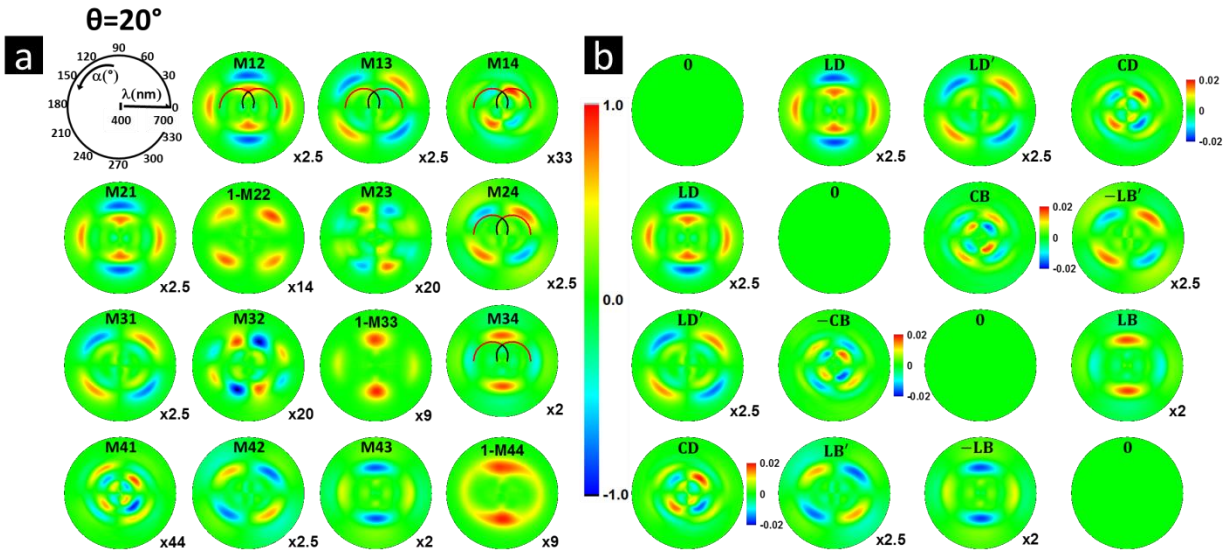

Figure 4. 62: (a) MM elements measured in transmission at AOI 20° with full azimuthal rotation in the spectral range between 400 nm and 700 nm (b) The differential decomposition matrix L_m at AOI 20°.

First of all, we applied cloude decomposition of the MM at normal incidence. The coefficients λ_i at different azimuthal angles α=0°, 45° and 90° are shown in Figure 4. 63(a), (b) and (c), respectively. We can see λ_1 is 1 and λ_2 to λ_4 are zero. The physical image for the Cloude decomposition is that the medium is not homogeneous in the direction perpendicular to the light propagation and the sample can be regarded as separated areas with different M which are pure Mueller-Jones matrices [35]. So again, Cloude decomposition also shows our sample has negligible depolarization effects.

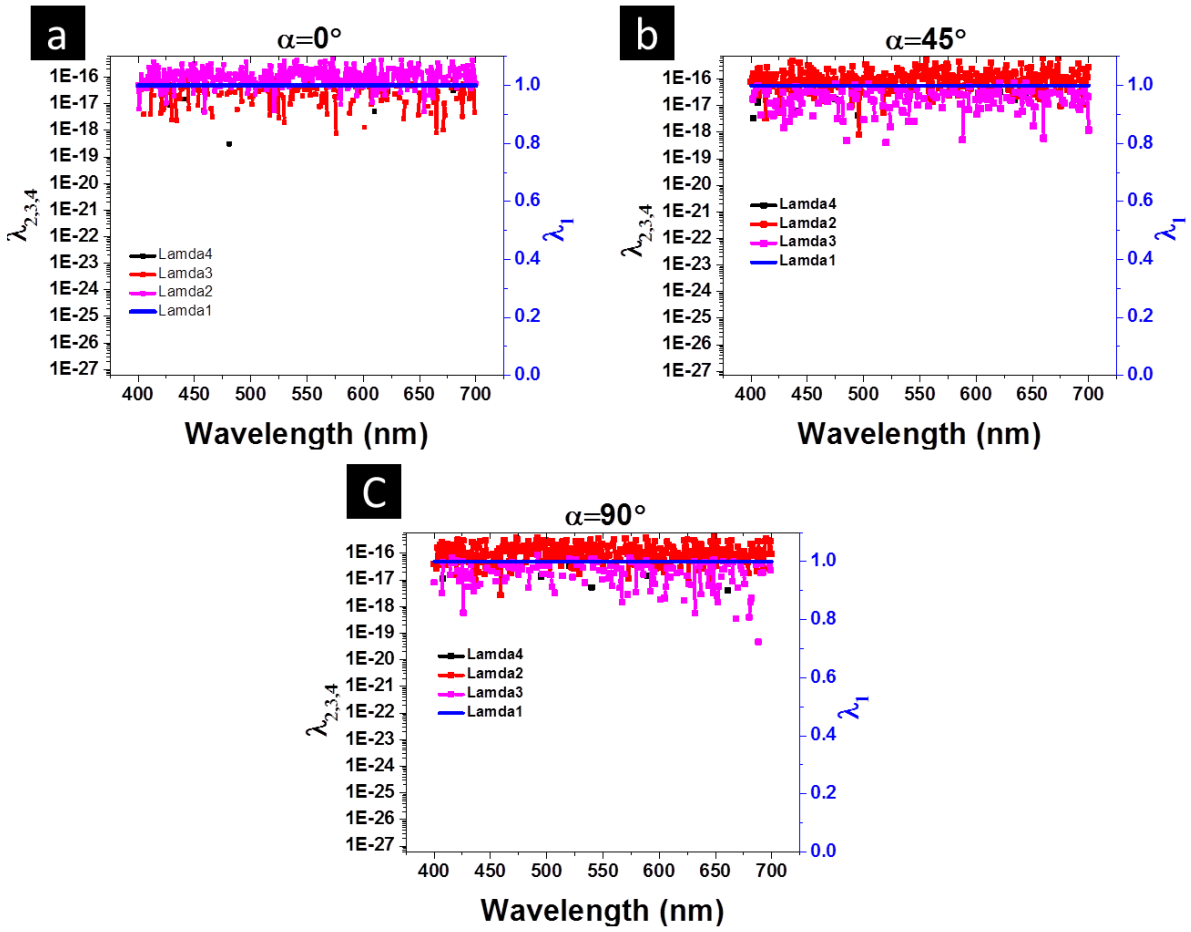

Figure 4. 63: Coefficients λ_i from Cloude decomposition of MM measured at normal incidence at (a) α=0°, (b) α=45°, and (c) α=90°.

Then, we explicitly extract all birefringent and dichroic properties, as well as the depolarization characteristics of the sample by using the differential decomposition formalism described in Eq. (2.63) and (2.64). From the ellipsometric model created in the previous section, which reproduces very well the intensity data, we now calculate the MM in transmission at normal incidence as shown in Figure 4. 64(a). In general, one can see that 14 elements of the simulated MM look very similar to the measured MM (Figure 4. 60(a)) in terms of not only the positions but also the intensity of the features. Only M14 and M41 differ from measured MM. However, a detailed comparison between the measured and simulated MM show other differences. Our anisotropic layer model includes only linear properties based on two orthogonal optical axes; therefore, there should be no difference for the optical response of left and right circular polarized light and, hence, no circular dichroism and circular birefringence can be generated. As a consequence, the simulated M23 and M32 can be described by a combination of linear birefringence and linear dichroism as 1/2(LB·LB´-LD·LD´) while M14 and M41 can be described as the equations with opposite values 1/2(LB·LD´-LB´·LD) and -1/2(LB·LD´-LB´·LD), respectively. Overall, our simple anisotropic model can reproduce the majority of the MM elements, so we can say that most of the optical response of Ag nanoparticle ensemble at normal incidence can be explained by the effects related to linear polarization. When the differential decomposition is applied to the simulated MM data, L_m and L_u matrices are obtained. In L_m matrix (Figure 4. 64(b)), the difference along the second diagonal where CB

and CD data are represented between measured and simulated MM is striking. As expected, these MME are equal to zero in the simulation, while the measured data indicates that the sample creates the conditions for the appearance of pure circular dichroism and birefringence. The next section will investigate the origin of this surprising signal in more details. Figure 4. 65 shows the differential matrix L_u of measured MM at normal incidence. We can see the diagonal elements in the Lu matrix which are A, A-LDP, A-LDP' and A-CDP have similar values. In order to analyze the linear and circular polarization effects, A, LDP, LDP' and CDP were extracted and shown in Figure 4. 66. The very small values of LDP, LDP' and CDP confirms that the depolarization effect of the sample is very small and the measured MM at normal incidence is a non-depolarizing MM.

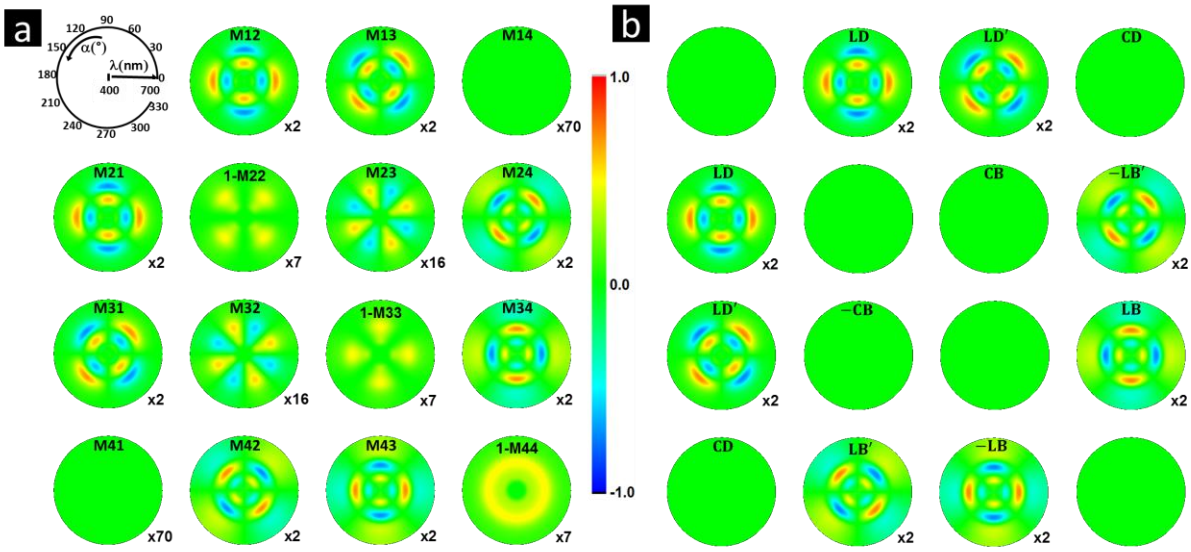

Figure 4. 64: (a) Simulated transmission MM at normal incidence in the spectral range between 400 nm and 700 nm with full azimuthal rotation. All the MM elements are normalized to M11 which is set to 1. The diagonal elements are 1-M22, 1-M33 and 1-M44 to enhance the contrast due to the values of M22, (b) Differential decomposed matrix L_m obtained from the simulated MM.

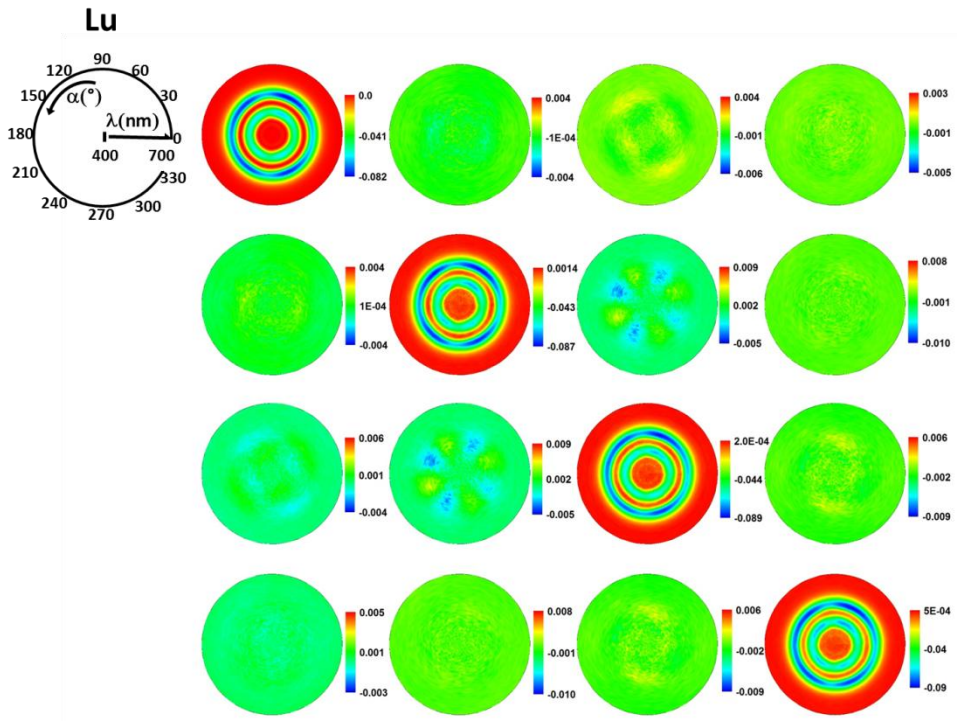

Figure 4. 65: Differential decomposition matrix L_u of measured MM elements in transmission at normal incidence with full azimuthal rotation in the spectral range between 400 nm and 700 nm.

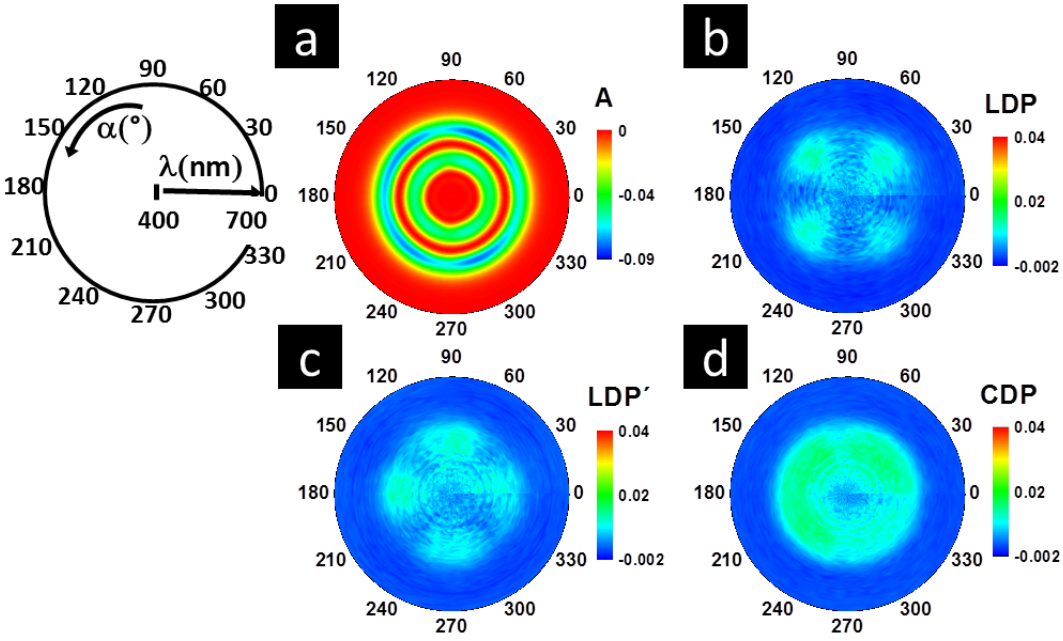

Figure 4. 66: (a) Absorption A, (b) depolarization of linear horizontal polarized light LDP, (c) depolarization of linear 45° polarized light LDP' and (d) depolarization of circular polarized light CDP extracted from differential decomposition matrix L_u of measured MM at normal incidence with full azimuthal rotation in the spectral range between 400 nm and 700 nm.

4.4.7 Circular dichroism

After speculating our sample has CD feature from the MM measurement in the previous section, we will discuss the CD in detail in this section.

From Equation 2.66, we already know that in transmission geometry, the general MM elements for a homogeneous non-depolarizing optical media can be extracted as the combinations of basic optical properties LD, LD', LB, LB', CD and CB. Figure 4. 67 shows comparison between either measured or extracted MM elements M14, M23, M32 and M41. The extracted MM elements are calculated from differential decomposition matrix L_m. We can see the measured MM and extracted MM elements are identical. This confirms that the optical response of our sample can be discussed by the combinations of six basic optical properties LD, LD', LB, LB', CD and CB.

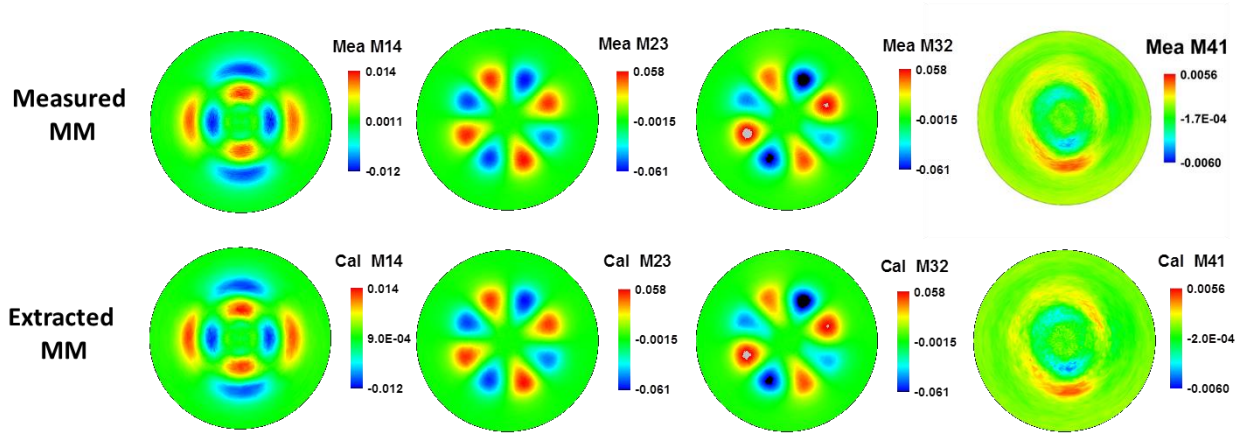

Figure 4. 67: Comparison between either measured or simulated MM elements M14, M23, M32 and M41 with calculated MM elements from differential decomposition matrix L_m. Elements are plotted with full azimuthal rotation in the spectral range between 400 nm and 700 nm.

We turn our attention to the different representations of the circular dichroism effects in more details. CD_{int} and CB_{int} are directly obtained from differential matrix as L_{m14} and L_{m23}. Alternatively, CD_{int} and CB_{int} can also be easily calculated directly from the measured MM from Equation 2.66 as:

$$\mathrm{CD_{int}} = \mathrm{M_{14}} - \frac{1}{2}(\mathrm{LB{\cdot}LD' - LB'{\cdot}LD}) = \mathrm{M_{14}} - \frac{1}{2}(\mathrm{Lm_{13}{\cdot}Lm_{34} - Lm_{12}{\cdot}Lm_{24}}) \qquad (4.16)$$

and

$$\mathrm{CB_{int}} = \mathrm{M_{23}} - \frac{1}{2}(\mathrm{LB{\cdot}LB' + LD{\cdot}LD'}) = \mathrm{M_{23}} - \frac{1}{2}(\mathrm{-Lm_{24}{\cdot}Lm_{34} + Lm_{12}{\cdot}Lm_{13}}) \qquad (4.17)$$

Figure 4. 68 compares the different ways to represent the circular dichroism. While Figure 4. 68(a) shows CD_{app} (i.e., the sum of CD_{int} and CD_{lin}) of the measured sample, we find that CD_{int} obtained as equal to L_{m14} from the differential decomposition (Figure 4. 68(b)) or by applying the Equation 2.66 (Figure 4. 68(d)) are identical. Figure 4. 68(c) shows CD_{lin} which is calculated from L_m as 1/2(LB·LD´-LB´·LD). All CD_{app}, CD_{int} and CD_{lin} have similar shape and CD_{app} is indeed the sum of CD_{lin} and CD_{int}, as it can be confirmed by the comparison of the linecuts in Figure 4. 68(e) and (f). We recall that, at the

molecular level, intrinsic circular dichroism comes from the geometrical arrangement of the molecule itself. In this case, the optical response is determined by locality and causality, and Kramers-Kronig relationships are directly applicable. In the present case, of course none of the materials is optically active, there is no circular dichroism at the molecular level; instead the observed effect is created at the mesoscopic level, arising from the geometrical arrangement of the dipoles. In particular, the curvature of the nanoparticle lines plays here a crucial role: by breaking the symmetry of the one-dimensional particle grating, the possibility for a different response when the electromagnetic field rotates clock-wise or counter-clockwise is opened. In particular, the interactions of the nanoparticles in the nearest-neighbor range are suspected to play a crucial role that can be tailored by the precise arrangement of the metallic nanoparticles. Although we are not dealing with a local optical response here, we can observe a "Kramers-Kronig"-like relation between the CB_{int} and the CD_{int} spectra, similarly to the ideal case of active molecules, as illustrated in Figure 4. 68(f) where the maxima/minima of one corresponds to the inflection points of the other.

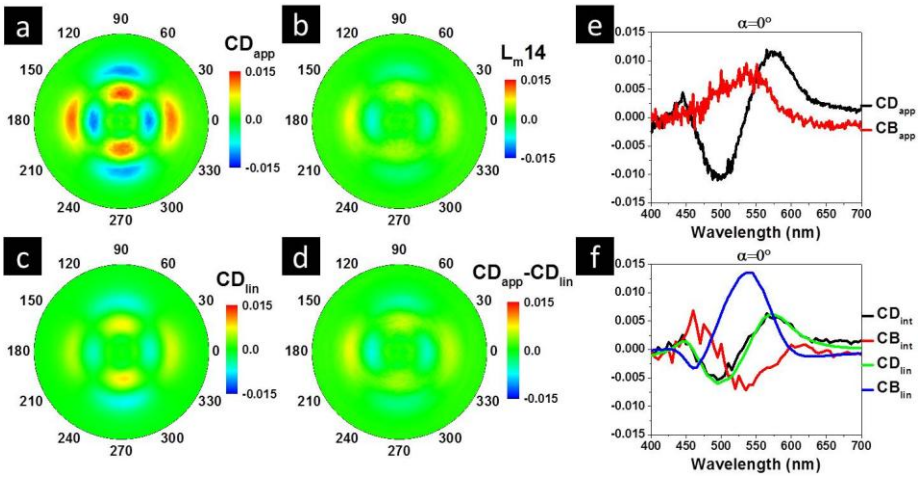

Figure 4. 68: Azimuthal dependent spectra (400-700 nm) obtained from the measured MM in transmission at normal incidence (a) CD_{app}=M14 (b) $CD_{int1}=L_{m14}$ (c) CD_{lin} =1/2(LBLD´-LB´LD) from L_m (d) CD_{int2}= CD_{app}-CD_{lin}=M14-1/2(M13M34+M12M24) calculated from Equation 2.66 (e) CD_{app} (M14) and CB_{app}(M23) along α=0°. (f) CD_{int} and CB_{int}, CD_{lin} and CB_{lin} along α=0°. The contour plots (a), (b), (c) and (d) are shown with full azimuthal rotation.

We will now detail the characteristics of the CD signal and evaluate the role of the DIM lines. To this purpose, we plot the comparison of the transmittance intensities T_{pp} and T_{ss} next to the above-discussed CD_{app}, CD_{int} and CD_{lin} in a cartesian frame (α, λ). The calculated position of the DIM is superposed onto the data at normal incidence in the first row of Figure 4. 69- the black dashed line is the DIM (±1) line at 492 nm -, and at θ=20° in the second row of Figure 4. 69. While the splitting of the plasmonic mode by the DIM is clearly visible in the transmittance plots, the CD signals are also strongly linked to the DIM. At first glance, all three CD representations show similarly alternating signal, mostly around lines at 490 nm and 570 nm. At wavelengths higher than the DIM wavelengths (dashed black line), the position of the maxima of CD correspond to the lowest transmittance points for T_{ss} while the minima of CD correspond to the lowest transmittance points of T_{pp}. This description gets confirmed with the data at θ=20°. In this case, the CD signal does not only concentrate around two main azimuth independent spectral lines, but rather spread over a larger spectral range with strong azimuth dependence, as determined by the position of the DIM lines. Specifically, the CD signal is linked to the intensity

modifications due to the presence of the DIMs. Independently on the angle of incidence, the intrinsic part of CD is at least as strong as the result of the linear combinations, and becomes stronger than CD_{lin} as the incidence angle increases. Indeed at higher θ, the intrinsic part becomes stronger and the azimuthal as well as spectral symmetry is broken: the complexity of the CD signal increases. In particular, CD_{int} is zero at the degeneracy point of the DIM lines (see Figure 4. 69(i)), and there is a phase change across the DIM lines. In opposition, CD_{lin} is less influenced by the DIM lines and the signal keeps its value at the degeneracy point while being elongated along the DIM line (see Figure 4. 69(j)). These observations underline the fact that the studied structures do present mesoscopic circular dichroism and that its origin is strongly linked to the interplay between the DIM and the plasmonic resonances.

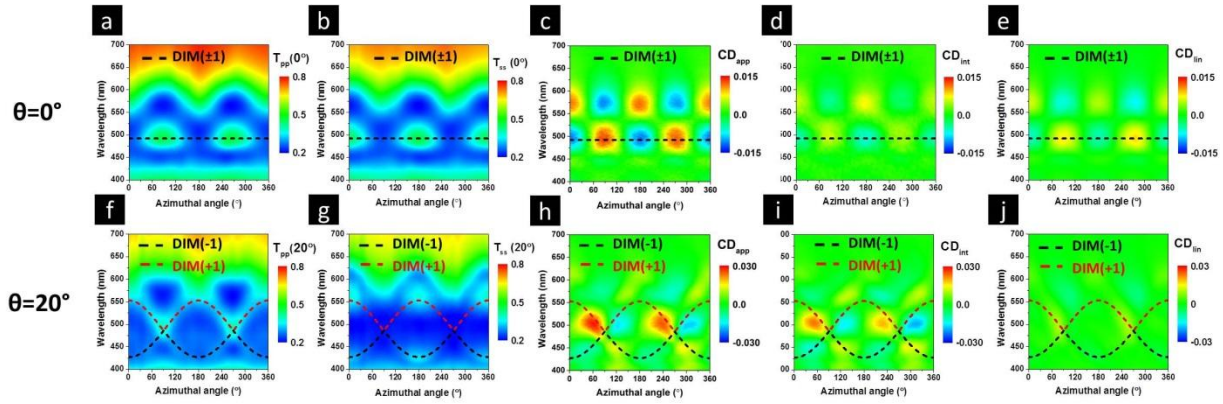

Figure 4. 69: (a) T_{pp} (b) T_{ss} (c) CD_{app} (d) CD_{int} and (e) CD_{lin} at normal incidence; (f) T_{pp} (g) T_{ss} (h) CD_{app} (i) CD_{int} and (j) CD_{lin} at θ=20°. All contour plots are shown together with RWAs lines in the spectral range between 400 nm and 700 nm with full azimuthal rotation.

A second check can be performed with the investigation of the wavelength dependence of the angularly dependent patterns. In order to compare the azimuthal width of the CD signal as well as its shift when the AOI varies, we plot CD_{int} and CD_{lin} in Cartesian coordinates in the α/θ plane at five relevant wavelengths in Figure 4. 70: 492 nm the position of the DIM at normal incidence, which is also the minimum of CD_{int} at α=0° and θ=0°, 510 nm and 530 nm in the region of the minimum of CB_{int} strongly influenced by the DIM, 575 nm around the maximum of CD_{int} and 630 nm outside the CD relevant spectral area as shown in Figure 4. 68(f). Several observations can be made: as it was already observed in Figure 4. 69, CD_{int} is always of similar or larger intensity than CD_{lin} in such a way that the apparent CD is dominated by the variations of CD_{int}. CD_{int} is already non-zero at normal incidence and another contribution is superposed to it at larger θ. The azimuthal width of the CD_{lin} keeps mostly constant, whereas it gets wider for CD_{int}. Finally, even though CD_{int} keeps the same 4-fold symmetry as CD_{lin} at θ constant, the signal of CD_{int} is always azimuthally shifted at large angles of incidence, except at λ=630 nm outside the influence of the main modes (plasmonic and DIM).

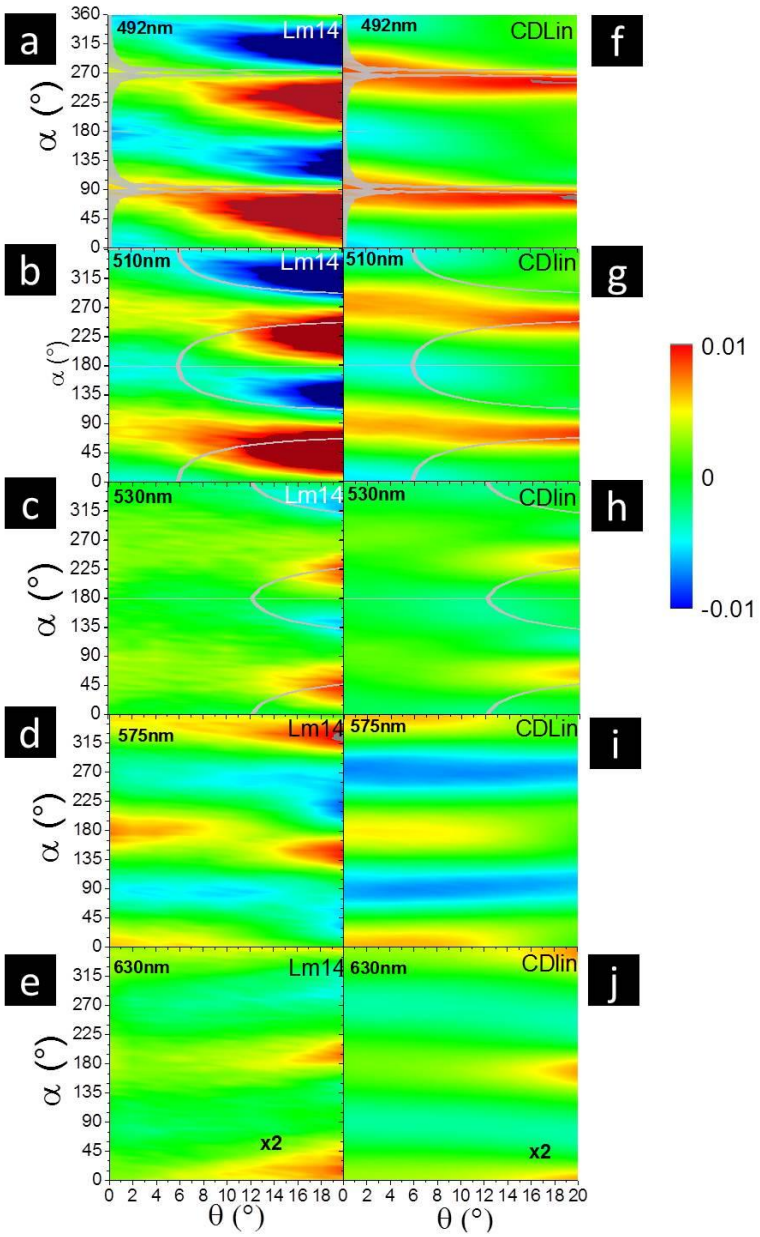

Figure 4. 70: Comparison of CD_{int} (L_{m14}) and CD_{lin} in the α/θ plane for five different wavelengths: L_{m14} in the left-handside column (a) 492 nm; (b) 510 nm; (c) 530 nm; (d) 575 nm ; (e) 630 nm ; and CD_{lin} in the right-handside column (f) 492 nm; (g) 510 nm; (h) 530 nm; (i)575 nm and (j) 630 nm. The light gray lines at 492 nm, 510 nm and 530 nm correspond to the calculated DIM(+1) line.

While searching for the origin of the CD_{int} signal, several hypotheses need to be evaluated. A first hypothesis could be that the optical axes are not perfectly normal to each other. Non-perpendicular optical axes can break the symmetry of left and right circular polarized light and therefore generate some CD_{int}. Two 50 nm thick biaxial layers shown in Figure 4. 71(c), is placed on top of the glass substrate named bk7_g in ellipsometric software. Here we define two main optical axes along α=0° and 88°. So as shown in Figure 4. 71(d), biaxial layer has euler angles (0°, 0°, 0°) and biaxial2 layer has euler angles (88°, 0°,

0°). Along the Z direction which is perpendicular to the layer interface, a Cauchy oscillator representing the TiO_2 matrix is used. As shown in Figure 4. 71(a) and (b), we create the model by fitting the experimental transmittance measured at normal incidence along α=0° and 90° using two different general oscillator (Genosc) layer models [18].

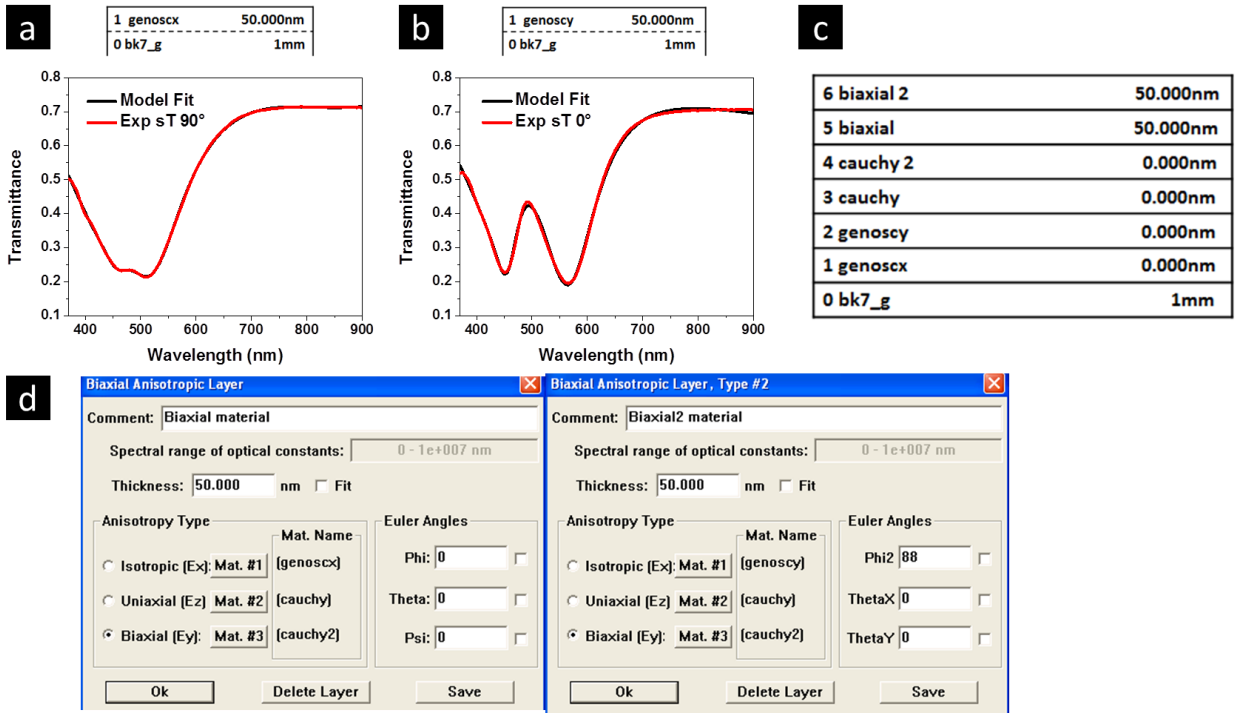

Figure 4. 71: Modeled and measured T_{ss} at normal incidence along (a) α=90° and (b) 0°. (c) Biaxial layer model with genoscx in X direction, genoscy in Y direction and Cauchy in Z direction.

As shown in Figure 4. 72 (a) and (b), T_{pp} and T_{ss} over the whole azimuthal range at θ=0° were calculated by using this model with non-perpendicular optical axes. As expected, we see a tilt of the optical features towards α=88°.

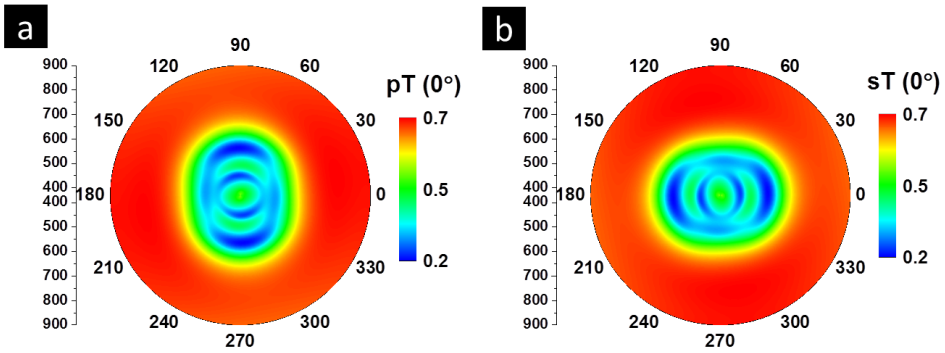

Figure 4. 72: Calculated (a)T_{pp} and (b)T_{ss} over the whole azimuthal range at normal incidence by non-perpendicular optical axes model.

In the next step, MM was calculated from this model and differential decomposition was performed. CD_{lin} and CD_{int} were extracted and shown in Figure 4. 73. We can see, the deviation of the direction of the optical axis by a few degrees away from the normal direction would result in a non-zero CD signal but this signal would be azimuthal independent, which is in contradiction with the measured data shown in Figure 4. 73(a)-(c). Therefore, the hypothesis of non-orthogonal axes is not valid here.

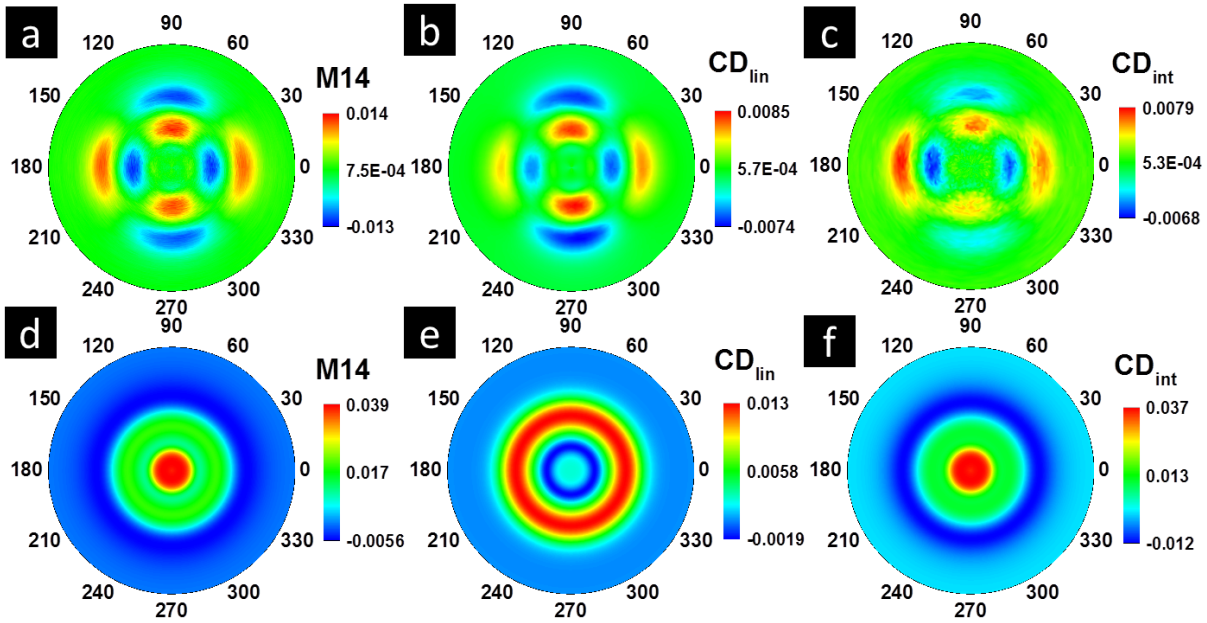

Figure 4. 73: Comparison between measured M14, CD_{lin} and CD_{int} and calculated ones by non-perpendicular optical axes model.

The second hypothesis concerns the nanoparticle arrangement itself. As already mentioned earlier, the Ag nanoparticles are not periodically arranged as straight lines but are curved with radius of curvature around 15µm. These arc-shaped nanoparticle chains can, not only break the symmetry of left and right circular polarized light as the non-orthogonal optical axes does, but also generate an azimuth dependent optical response due to the varying environment that neighboring particles see as a function of the rotation of the electric field along the arc. In other words, a part of the true (intrinsic) CD originates from a broken symmetry on a mesoscopic level (here: curvature of the lines). We are now in state of fully determining the origin of the apparent CD signal, composed of three parts. The first part, CD_{lin} comes from the anisotropy of the sample and the presence of a nanoparticle grating. The "intrinsic" part of the CD is itself composed of two parts: the first part originate from the curvature of the grating lines (mediated by the interparticle interactions) and it is present already at normal incidence, and the second part of CD_{int} originates from the DIM lines, and in particular the lift of degeneracy of the DIM (+1) and DIM (-1) modes. This second part of CD_{int} follows the DIM lines and appears at non-zero angles of incidence. It is seen in Figure 4. 70 that the intrinsic signal is indeed composed of two parts which slowly "diffuse" into each other, the part linked to the curvature of the grating lines and that due to the degeneracy of the DIMs, as θ increases. It is interesting to see that at all wavelengths both CD_{lin} and CD_{int} are shaped by the presence of the DIM line. At 492, 510 and 530 nm, the DIM lines are visible inside the plotted area, and CD_{lin} deviates azimuthally in the vicinity of the DIM line. The intrinsic part is strongly reshaped by the DIM mode: a stronger contribution appears at larger θ and as the wavelength varies it follows the θ

dependence of the DIM line. Therefore we conclude that not only the plasmonic modes play an important role but also the DIM mode is a crucial tailoring parameter for the CD_{int} signal of the sample. Finally we conclude that the nature and size of the particles, their density, their periodic arrangement (grating periodicity as well as curvature of the lines) as well as the thickness of the waveguide are important design parameters that will act upon the intrinsic part of the CD of the nanoplasmonic structure. Therefore we can conclude that the strength and position of the intrinsic circular dichroism signal can be actively tailored to specific needs by design of the plasmonic arrangement.

4.4.8 Conclusion

We have in full detail and completeness investigated the optical properties of a complex plasmonic sample where an interplay is found of the contributions from plasmonic resonances, periodicity, interference with waveguide modes and nearest-neighbor coupling between adjacent particles. To fully characterize this sample, we have used the powerful framework of Mueller matrices advanced by the differential decomposition formalism. We show that even in the presence of large complexity, the optical response can be easily disentangled by the presented method. The investigated sample is easily manufactured in a self-assembly process stirred by the properties of the illuminating laser light during fabrication. It consists of silver nanoparticles periodically arranged along curved lines, which are embedded in a TiO_2 waveguide. When light is impinging on the sample surface and reaches the nanoparticle layer, several phenomena occur. First the plasmonic resonance of the individual nanoparticles is excited, and part of the transmitted light is hence absorbed. The nanoparticles also serve as scattering elements for the incident light: part of the light is coupled to the waveguide modes via interaction with nanoparticles. On its turn, the waveguide modes are leaky modes and can be scattered by the presence of nanoparticles: this diffracted part of the leaky mode will interfere with the directly transmitted light. The result of this interference is the so-called "destructive interference mode". The destructive interference mode has a large influence on the optical response of the sample. Its signature is found both in intensity plots as well as in the phase, as attested by MM measurements. Moreover, it was discovered that such structures are characterized by a particular circular dichroism behavior, which cannot be explained by the sole superposition of the linear optical properties. Whereas the linear circular dichroism is coming from the anisotropy of the sample, the true circular dichroism is due to the coupling between destructive interference mode and plasmonic modes as well as the nearest-neighbor coupling between plasmonic nanoparticles.

Bibliography

[1] D. Sarid and W. Challener, *Modern Introduction to Surface Plasmons: Theory, Mathematica Modeling, and Applications*. Cambridge University Press, 2010.

[2] R. Charbonneau, N. Lahoud, G. Mattiussi, and P. Berini, "Demonstration of integrated optics elements based on long-ranging surface plasmon polaritons," *Opt. Express*, vol. 13, no. 3, pp. 977–984, 2005.

[3] S. A. Maier, "Plasmonic field enhancement and SERS in the effective mode volume picture," *Opt. Express*, vol. 14, no. 5, pp. 1957–1964, 2006.

[4] M. Albooyeh and C. R. Simovski, "Huge local field enhancement in perfect plasmonic absorbers," *Opt. Express*, vol. 20, no. 20, pp. 1–4, 2012.

[5] J. Homola, S. S. Yee, and G. Gauglitz, "Surface plasmon resonance sensors: review," *Sensors Actuators B Chem.*, vol. 54, no. 1, pp. 3–15, 1999.

[6] M. Perino, E. Pasqualotto, M. Scaramuzza, A. De Toni, and A. Paccagnella, "Enhancement and control of surface plasmon resonance sensitivity using grating in conical mounting configuration," *Opt. Lett.*, vol. 40, no. 2, pp. 221–224, 2015.

[7] A. Brolo, "Plasmonics for future biosensors," *Nat. Photonics*, vol. 6, pp. 709–713, 2012.

[8] D. K. Gramotnev and S. I. Bozhevolnyi, "Plasmonics beyond the diffraction limit," *Nat. Photonics*, vol. 4, no. 2, pp. 83–91, 2010.

[9] K. L. Kelly, E. Coronado, L. L. Zhao, and G. C. Schatz, "The optical properties of metal nanoparticles: The influence of size, shape, and dielectric environment," *J. Phys. Chem. B*, vol. 107, no. 3, pp. 668–677, 2003.

[10] G. Armelles, A. Cebollada, A. García-Martín, and M. U. González, "Magnetoplasmonics: Combining Magnetic and Plasmonic Functionalities," *Adv. Opt. Mater.*, vol. 1, no. 1, pp. 2–2, 2013.

[11] Lord Rayleigh, "On the Dynamical Theory of Gratings," *Proc. R. Soc. London. Ser. A*, vol. 79, no. 532, pp. 399–416, 1907.

[12] M. James Clerk, "A Dynamical Theory of the Electromagnetic Field," *Philos. Trans. R. Soc. London*, vol. 155, no. January, pp. 459–512, 1865.

[13] H. Fujiwara, *Spectroscopic Ellipsometry*. John Wiley & Sons, Ltd, 2007.

[14] S. De Zuani, "Spectroscopic Investigation of Metallic Nanostructures towards Percolation," *PhD Thesis*, 2016.

[15] J. A. Woollam Co, *CompleteEase Software Manual*. 2014.

[16] J. A. Woollam Co, *Guide to Using WVASE32*. 2010.

[17] A. March, "Zur Elektronentheorie der Metalle," *Ann. Phys.*, vol. 354, no. 6, pp. 710–724, 1916.

[18] H. G. Tompkins and E. A. Irene, *Handbook of Ellipsometry*. William Andrew Publishing, 2005.

[19] P. S. Hauge, R. H. Muller, and C. G. Smith, "Conventions and formulas for using the Mueller-Stokes calculus in ellipsometry," *Surf. Sci.*, vol. 96, no. 1–3, pp. 81–107, 1980.

[20] F. Le Roy-Brehonnet and B. Le Jeune, "Utilization of Mueller matrix formalism to obtain optical targets depolarization and polarization properties," *Prog. Quant. Electr.*, vol. 21, no. 2, pp. 109–151, 1997.

[21] N. Agarwal *et al.*, "Spatial evolution of depolarization in homogeneous turbid media within the differential Mueller matrix formalism," *Opt. Lett.*, vol. 40, no. 23, pp. 5634–5637, 2015.

[22] S. Liu, X. Chen, and C. Zhang, “Development of a broadband Mueller matrix ellipsometer as a powerful tool for nanostructure metrology,” *Thin Solid Films*, vol. 584, pp. 176–185, 2015.
[23] X. Chen, Y. Shi, H. Jiang, C. Zhang, and S. Liu, “Nondestructive analysis of lithographic patterns with natural line edge roughness from Mueller matrix ellipsometric data,” *Appl. Surf. Sci.*, vol. 388, pp. 524–530, 2016.
[24] T. W. H. Oates, T. Shaykhutdinov, T. Wagner, A. Furchner, and K. Hinrichs, “Mid-infrared gyrotropy in split-ring resonators measured by Mueller matrix ellipsometry,” *Opt. Mater. Express*, vol. 4, no. 12, p. 2646, 2014.
[25] B. Gompf, J. Braun, T. Weiss, H. Giessen, M. Dressel, and U. Hübner, “Periodic nanostructures: Spatial dispersion mimics chirality,” *Phys. Rev. Lett.*, vol. 106, no. 18, p. 185501, 2011.
[26] O. Arteaga, B. M. Maoz, S. Nichols, G. Markovich, and B. Kahr, “Complete polarimetry on the asymmetric transmission through subwavelength hole arrays,” *Opt. Express*, vol. 22, no. 11, p. 13719, 2014.
[27] A. Berrier, B. Gompf, L. Fu, T. Weiss, and H. Schweizer, “Optical anisotropies of single-meander plasmonic metasurfaces analyzed by Mueller matrix spectroscopy,” *Phys. Rev. B*, vol. 89, no. 19, p. 195434, 2014.
[28] T. Brakstad, M. Kildemo, Z. Ghadyani, and I. Simonsen, “Dispersion of polarization coupling, localized and collective plasmon modes in a metallic photonic crystal mapped by Mueller Matrix Ellipsometry,” *Opt. Express*, vol. 23, no. 17, p. 22800, 2015.
[29] L. Fu *et al.*, “Depolarization of a randomly distributed plasmonic meander metasurface characterized by Mueller matrix spectroscopic ellipsometry,” *Opt. Express*, vol. 24, no. 24, pp. 28056–28064, 2016.
[30] D. Schmidt, C. Briley, E. Schubert, and M. Schubert, “Vector magneto-optical generalized ellipsometry for sculptured thin films,” *Appl. Phys. Lett.*, vol. 102, no. 12, p. 123109, 2013.
[31] H. Arwin, “Application of ellipsometry techniques to biological materials,” *Thin Solid Films*, vol. 519, no. 9, pp. 2589–2592, 2011.
[32] C. Chen, I. An, G. M. Ferreira, N. J. Podraza, J. A. Zapien, and R. W. Collins, “Multichannel Mueller matrix ellipsometer based on the dual rotating compensator principle,” *Thin Solid Films*, vol. 455–456, pp. 14–23, 2004.
[33] S.-Y. Lu and R. A. Chipman, “Interpretation of Mueller matrices based on polar decomposition,” *J. Opt. Soc. Am. A*, vol. 13, no. 5, pp. 1106–1113, 1996.
[34] S.R.Cloude, “Group theory and polarization algebra,” *Optik (Stuttg).*, vol. 75, pp. 26–36, 1986.
[35] J. J. Gil, “Review on Mueller matrix algebra for the analysis of polarimetric measurements,” *J. Appl. Remote Sens.*, vol. 8, no. 1, p. 81599, 2014.
[36] O. Arteaga and A. Canillas, “Analytic inversion of the Mueller–Jones polarization matrices for homogeneous media,” *Opt. Lett.*, vol. 35, no. 4, pp. 559–561, 2010.
[37] O. Arteaga and B. Kahr, “Characterization of homogenous depolarizing media based on Mueller matrix differential decomposition.,” *Opt. Lett.*, vol. 38, no. 7, pp. 1134–6, 2013.
[38] H. A. Rwin *et al.*, “Structural circular birefringence and dichroism quantified by differential decomposition of spectroscopic transmission Mueller matrices from Cetonia aurata,” *Opt. Lett.*, vol. 41, no. 14, pp. 3293–3296, 2016.
[39] Y. Kim *et al.*, “Reconfigurable chiroptical nanocomposites with chirality transfer from the macro- to the nanoscale,” *Nat. Mater.*, vol. 15, no. 4, pp. 461–468, 2016.

[40] O. Arteaga, “Circular dichroism | Mueller Matrix Polarimetry.” [Online]. Available: http://www.mmpolarimetry.com/circular-dichroism/.
[41] O. A. Barriel, “Mueller matrix polarimetry of anisotropic chiral media,” *PhD thesis*, 2010.
[42] O. Arteaga and A. Canillas, “Pseudopolar decomposition of the Jones and Mueller-Jones exponential polarization matrices.,” *J. Opt. Soc. Am. A*, vol. 26, no. 4, pp. 783–793, 2009.
[43] S. A. Maier, *Plasmonics : Fundamentals and Applications*. Springer US, Boston, MA, 2007.
[44] H. Raether, *Surface Plasmoncs on Smooth and Rough Surfaces and on Gratings*. Springer-Verlag, 1986.
[45] A. Otto, “Excitation of nonradiative surface plasma waves in silver by the method of frustrated total reflection,” *Zeitschrift für Phys.*, vol. 216, no. 4, pp. 398–410, 1968.
[46] E. Kretschmann and H. Raether, “Radiative decay of non-radiative surface plasmons excited by light,” *Z. Naturforsch.*, vol. 23, no. November 1968, pp. 2135–2136, 1968.
[47] L. Novotny and B. Hecht, *Principles of Nano-Optics*. Cambridge University Press, 2012.
[48] G. Ruffato and F. Romanato, “Grating-coupled surface plasmon resonance in conical mounting with polarization modulation.,” *Opt. Lett.*, vol. 37, no. 13, pp. 2718–2720, 2012.
[49] U. Kreibig and M. Vollmer, *Optical Properties of Metal Clusters*. Springer Berlin Heidelberg, Berlin, Heidelberg, 1995.
[50] “MiePlot.” [Online]. Available: http://www.philiplaven.com/mieplot.htm.
[51] G. Mie, “Beiträge zur Optik trüber Medien, speziell kolloidaler Metallösungen,” *Ann. Phys.*, vol. 330, no. 3, pp. 377–445, 1908.
[52] T. W. H. Oates, H. Wormeester, and H. Arwin, “Characterization of plasmonic effects in thin films and metamaterials using spectroscopic ellipsometry,” *Prog. Surf. Sci.*, vol. 86, no. 11–12, pp. 328–376, 2011.
[53] R. W. Wood, “On a Remarkable Case of Uneven Distribution of Light in a Diffraction Grating Spectrum,” *Proc. Phys. Soc. London*, vol. 18, no. 1, pp. 269–275, 1902.
[54] A. Yariv and P. Yeh, *Photonics: optical electronics in modern communications*, 6th ed. Oxford University Press, 2007.
[55] R. M. A. Azzam, “Phase shifts that accompany total internal reflection at a dielectric-dielectric interface,” *J. Opt. Soc. Am. A*, vol. 21, no. 8, pp. 1559–1563, 2004.
[56] S. Feng, X. Zhang, J. Song, H. Liu, and Y. Song, “Theoretical analysis on the tuning dynamics of the waveguide-grating structures.,” *Opt. Express*, vol. 17, no. 2, pp. 426–436, 2009.
[57] G. Binnig and C. F. Quate, “Atomic Force Microscope,” *Phys. Rev. Lett.*, vol. 56, no. 9, pp. 930–933, 1986.
[58] D. Y. Abramovitch, S. B. Andersson, L. Y. Pao, and G. Schitter, “A tutorial on the mechanisms, dynamics, and control of atomic force microscopes,” *Proc. Am. Control Conf.*, pp. 3488–3502, 2007.
[59] “Gwyddion.” [Online]. Available: http://gwyddion.net/download.php.
[60] “TT-AFM - AFM Workshop.” [Online]. Available: http://www.afmworkshop.com/tt-2-afm.html.
[61] P. Gaiser, “Optische Eigenschaften durchstimmbarer metall-dielektrischer Komposits auf der Basis von metallischen Nanopartikeln und Dünnfilmen,” *Master Thesis*, pp. 1–115, 2013.
[62] “VASE Ellipsometer - J.A. Woollam Co.” [Online]. Available: https://www.jawoollam.com/products/vase-ellipsometer.

[63] R. W. Collins and J. Koh, “Dual rotating-compensator multichannel ellipsometer: instrument design for real-time Mueller matrix spectroscopy of surfaces and films,” *J. Opt. Soc. Am. A*, vol. 16, no. 8, pp. 1997–2006, 1999.
[64] “RC2 Ellipsometer - J.A. Woollam Co.” [Online]. Available: https://www.jawoollam.com/products/rc2-ellipsometer.
[65] K. Efimenko, W. E. Wallace, and J. Genzer, “Surface Modification of Sylgard-184 Poly(dimethyl siloxane) Networks by Ultraviolet and Ultraviolet/Ozone Treatment,” *J. Colloid Interface Sci.*, vol. 254, no. 2, pp. 306–315, 2002.
[66] “Production information on Sylgard-184 obtained from Dow Corning.” [Online]. Available: http://www.dowcorning.com/.
[67] S. Lynn, “Virtual Metrology for Plasma Etch Processes Declaration of Authorship,” *PhD Thesis*, 2011.
[68] C. Yu, K. O’Brien, Y. H. Zhang, H. Yu, and H. Jiang, “Tunable optical gratings based on buckled nanoscale thin films on transparent elastomeric substrates,” *Appl. Phys. Lett.*, vol. 96, no. 4, p. 41111, 2010.
[69] C. Yu and H. Jiang, “Forming wrinkled stiff films on polymeric substrates at room temperature for stretchable interconnects applications,” *Thin Solid Films*, vol. 519, no. 2, pp. 818–822, 2010.
[70] P. C. Lin and S. Yang, “Spontaneous formation of one-dimensional ripples in transit to highly ordered two-dimensional herringbone structures through sequential and unequal biaxial mechanical stretching,” *Appl. Phys. Lett.*, vol. 90, no. 24, p. 241903, 2007.
[71] R. W. Cohen, G. D. Cody, M. D. Coutts, and B. Abeles, “Optical properties of granular silver and gold films,” *Phys. Rev. B*, vol. 8, no. 8, pp. 3689–3701, 1973.
[72] S. B. Jones and S. P. Friedman, “Particle shape effects on the effective permittivity of anisotropic or isotropic media consisting of aligned or randomly oriented ellipsoidal particles,” *Water Resour. Res.*, vol. 36, no. 10, pp. 2821–2833, 2000.
[73] A. P. Hibbins, “Grating coupling of surface plasmon polaritons at visible and microwave frequencies,” University of Exeter, 1999.
[74] F. Romanato, K. H. Lee, G. Ruffato, and C. C. Wong, “The role of polarization on surface plasmon polariton excitation on metallic gratings in the conical mounting,” *Appl. Phys. Lett.*, vol. 96, no. 11, 2010.
[75] B. Auguié and W. L. Barnes, “Collective resonances in gold nanoparticle arrays,” *Phys. Rev. Lett.*, vol. 101, no. 14, p. 143902, 2008.
[76] V. G. Kravets, F. Schedin, and A. N. Grigorenko, “Extremely narrow plasmon resonances based on diffraction coupling of localized plasmons in arrays of metallic nanoparticles,” *Phys. Rev. Lett.*, vol. 101, no. 8, p. 87403, 2008.
[77] Y. Chu, E. Schonbrun, T. Yang, and K. B. Crozier, “Experimental observation of narrow surface plasmon resonances in gold nanoparticle arrays,” *Appl. Phys. Lett.*, vol. 93, no. 18, p. 181108, 2008.
[78] G. Vecchi, V. Giannini, and J. Gómez Rivas, “Surface modes in plasmonic crystals induced by diffractive coupling of nanoantennas,” *Phys. Rev. B*, vol. 80, no. 20, p. 201401(R), 2009.
[79] A. I. Väkeväinen *et al.*, “Plasmonic surface lattice resonances at the strong coupling regime,” *Nano Lett.*, vol. 14, no. 4, pp. 1721–1727, 2014.
[80] S. De Zuani, M. Rommel, B. Gompf, A. Berrier, J. Weis, and M. Dressel, “Suppressed Percolation in Nearly Closed Gold Films,” *ACS Photonics*, vol. 3, no. 6, pp. 1109–1115,

2016.
[81] G. P. Bryan-Brown, J. R. Sambles, and M. C. Hutley, “Polarisation Conversion through the Excitation of Surface Plasmons on a Metallic Grating,” *J. Mod. Opt.*, vol. 37, no. 7, pp. 1227–1232, 1990.
[82] S. J. Elston, G. P. Bryan-Brown, and J. R. Sambles, “Polarization conversion from diffraction gratings,” *Phys. Rev. B*, vol. 44, no. 12, pp. 6393–6400, 1991.
[83] A. V. Kats, I. S. Spevak, and N. A. Balakhonova, “Energy redistribution and polarization transformation in conical mount diffraction under resonance excitation of surface waves,” *Phys. Rev. B*, vol. 76, no. 7, p. 75407, 2007.
[84] T. Inagaki, J. P. Goudonnet, and E. T. Arakawa, “Plasma resonance absorption in conical diffraction: effects of groove depth,” *J. Opt. Soc. Am. B*, vol. 3, no. 7, p. 992, 1986.
[85] A. Heinrich, J. Bischoff, K. Meiner, U. Richter, T. Mikolajick, and I. Dirnstorfer, “Interpretation of azimuthal angle dependence of periodic gratings in Mueller matrix spectroscopic ellipsometry,” *J. Opt. Soc. Am. A*, vol. 32, no. 4, p. 604, 2015.
[86] E. D. Palik, *Handbook of Optical Constants of Solids*, vol. 1. 1985.
[87] P. B. Johnson and R. W. Christy, “Optical constants of the noble metals,” *Phys. Rev. B*, vol. 6, no. 12, pp. 4370–4379, 1972.
[88] J. C. Hulteen, D. A. Treichel, M. T. Smith, M. L. Duval, T. R. Jensen, and R. P. Van Duyne, “Nanosphere lithography: Size-tunable silver nanoparticle and surface cluster arrays,” *J. Phys. Chem. B*, vol. 103, no. 19, pp. 3854–3863, 1999.
[89] A. N. Shipway, E. Katz, and I. Willner, “Nanoparticle Arrays on Surfaces for Electronic, Optical, and Sensor Applications,” *ChemPhysChem*, vol. 1, no. 1, pp. 18–52, 2000.
[90] S. A. Maier, P. G. Kik, and H. A. Atwater, “Observation of coupled plasmon-polariton modes in Au nanoparticle chain waveguides of different lengths: Estimation of waveguide loss,” *Appl. Phys. Lett.*, vol. 81, no. 9, pp. 1714–1716, 2002.
[91] C. R. Raj, T. Okajima, and T. Ohsaka, “Gold nanoparticle arrays for the voltammetric sensing of dopamine,” *J. Electroanal. Chem.*, vol. 543, no. 2, pp. 127–133, 2003.
[92] D. A. Genov, A. K. Sarychev, V. M. Shalaev, and A. Wei, “Resonant Field Enhancements from Metal Nanoparticle Arrays,” *Nano Lett.*, vol. 4, no. 1, pp. 153–158, 2004.
[93] H. H. Wang *et al.*, “Highly raman-enhancing substrates based on silver nanoparticle arrays with tunable sub-10nm gaps,” *Adv. Mater.*, vol. 18, no. 4, pp. 491–495, 2006.
[94] C. Noguez, “Surface Plasmons on Metal Nanoparticles: The Influence of Shape and Physical Environment,” *J. Phys. Chem. C*, vol. 111, no. 10, pp. 3806–3819, 2007.
[95] C. L. Haynes *et al.*, “Nanoparticle Optics: The Importance of Radiative Dipole Coupling in Two-Dimensional Nanoparticle Arrays,” *J. Phys. Chem. B*, vol. 107, no. 30, pp. 7337–7342, 2003.
[96] G. Nair, H. J. Singh, D. Paria, M. Venkatapathi, and A. Ghosh, “Plasmonic interactions at close proximity in chiral geometries: Route toward broadband chiroptical response and giant enantiomeric sensitivity,” *J. Phys. Chem. C*, vol. 118, no. 9, pp. 4991–4997, 2014.
[97] S. Bakhti, N. Destouches, and A. V. Tishchenko, “Coupled mode modeling to interpret hybrid modes and Fano resonances in plasmonic systems,” *ACS Photonics*, vol. 2, no. 2, pp. 246–255, 2015.
[98] N. Destouches *et al.*, “Self-organized growth of metallic nanoparticles in a thin film under homogeneous and continuous-wave light excitation,” *J. Mater. Chem. C*, vol. 2, no. 31, pp. 6256–6263, 2014.
[99] N. Destouches *et al.*, “Dichroic colored luster of laser-induced silver nanoparticle gratings

buried in dense inorganic films," *J. Opt. Soc. Am. B*, vol. 31, no. 11, pp. C1–C7, 2014.
[100] Z. Liu *et al.*, "Three-Dimensional Self-Organization in Nanocomposite Layered Systems by Ultrafast Laser Pulses," *ACS Nano*, vol. 11, no. 5, pp. 5031–5040, 2017.
[101] M. Wang, A. Löhle, B. Gompf, M. Dressel, and A. Berrier, "Physical interpretation of Mueller matrix spectra: a versatile method applied to gold gratings," *Opt. Express*, vol. 25, no. 6, pp. 6983–6996, 2017.
[102] M. Born and E. Wolf, *Principles of Optics*. New York Pergamon Press, 1999.
[103] S. De Zuani *et al.*, "Large-Area Two-Dimensional Plasmonic Meta-Glasses and Meta-Crystals: a Comparative Study," *Plasmonics*, pp. 1–10, 2016.
[104] D. H. Goldstein, *Polarized Light*, no. April 2000. Taylor & Fransis Group, 2011.

Chapter 5

Conclusions and Outlook

5.1 Conclusions

On the example of two simple prepared plasmonic nanostructures, we have demonstrated in the thesis, how the optical response of complex plasmonic nanstructures can be understood in the framework of a full MM analysis. The developed procedure is very general and can in principle be applied to all complex samples exhibiting anisotropy, circular dichroism and dispersion. The procedure especially links the optical properties to their physical origin. This on the other hand opens up the possibility to tailor the optical response of plasmonic nanostructures in a desired way.

Mueller matrix (MM) describes the interaction of polarized light and matter in either reflection or transmission configurations, which connects the incoming to the outgoing Stokes vectors, independently from any assumed model. Since Stokes vectors are able to represent any polarization state of light, Mueller matrix spectroscopic ellipsometry (MMSE) gives complete optical response about polarization properties even in the case of complex samples under study, which cannot be achieved by simple intensity measurements. However, MMSE results in complex data hiding the underlying physics making the physical interpretation of a measured MM a big challenge.

We have shown in the thesis, by applying the simple analytical model we made to the MM, we can fully characterize all the physical origins hidden in the measured MM of our two examples: one-dimensional plasmonic gratings and Ag nanoparticle array.

One-dimensional plasmonic grating

For convenience of comparison, we first demonstrated how the complex optical response of a pure PDMS grating can be decomposed into its physical ingredients. First, we measure the MM in refection at different AOI over a complete azimuthal rotation. The MM is then modeled by a simple anisotropic effective medium approach called Biaxial Bruggeman effective approximation. From this simple anisotropic model, MM plots over the whole spectral and angular range are generated. On top of this modeled MME we superimpose the expected dispersive RWA modes, calculated from the known periodicity of the grating. Comparing this composed result with measured MMs gives a deep insight on how the different physical contributions originating from periodicity and geometry influence the complex polarization mixing.

Then, we have demonstrated how the complex optical response of a simple Au grating can be decomposed into its physical ingredients. First, we measure the reflectance along the two optic axes of the grating, along and perpendicular to the grooves under s- and p-polarization. The reflectance is then modeled by a simple anisotropic effective medium approach using Drude-Lorentz oscillators. From this anisotropic model, reflectance plots over the whole spectral and angular range are generated. Once the agreement between the generated and measured plots is

insured, the Mueller-matrix plots can be calculated. On top of this calculated MME we superimpose the expected dispersive SPP and RWA modes, calculated from the known periodicity of the grating. Comparing this composed result with measured MMs gives a deep insight on how the different physical contributions originating from periodicity, anisotropy and material properties influence the complex polarization mixing. We have seen that SPPs can be excited by both p- or s-polarized light when the incident plane is perpendicular or parallel to the grating grooves. Both SPP modes are dispersive with the AOI and follow the same phase matching condition. P- or s-polarized light can be converted to s- or p- polarized light via SPP excitation, and maximum polarization conversion occurs when the angle between incident plane and grooves is 45°. Additionally to the excitation of SPPs, the optical properties are influenced by geometric anisotropy, by the RWAs related to the periodic grating structure and, to a lesser extent, by the Au interband transition. The anisotropy, the interband transition and the non-dispersive approximation of the SPPs are understood in terms of an effective medium approach, obtained from fitting the measured reflectance. However, the dispersion of the SPP modes and the RWAs effects should be added on top of this model.

In order to tailor the plasmonic property with external magnetic field, Au/Ni/Au grating is fabricated with Ni layer placed in between two Au layers by the same fabrication method as the Au grating. The optical properties of Au/Ni/Au grating are influenced by the excitation of SPPs, geometric anisotropy and to a lesser extent, the Au/Ni/Au interband transition. There is no influence of RWAs which comes from periodicity. The anisotropy, the interband transition and the non-dispersive approximation of the SPPs are understood in terms of the effective medium approach similar to the Au grating section. We attribute the broad plasmonic resonance and no RWA effects to the large absorption of the Ni layer. Finally, we introduced an active way for tuning SPP via mechanical stretching. By actively stretching the PDMS grating template, the periodicity of the grating increases and SPP peak position red shifts. This method has very good reversibility. The plasmonic peak position is reversed by releasing the whole original strain.

Ag nanoparticle array

The optical properties of a complex plasmonic Ag nanoparticle array, where an interplay is found between contributions from plasmonic resonances, periodicity, interference with waveguide modes and nearest-neighbor coupling between adjacent particles was also fully characterized in this thesis. We have used the powerful framework of Mueller matrices advanced by the differential decomposition formalism. We show that even in the presence of large complexity, the optical response can be easily disentangled by the presented method. The investigated sample is easily manufactured in a self-assembly process stirred by the properties of the illuminating laser light during fabrication. It consists of silver nanoparticles periodically arranged along curved lines, which are embedded in a TiO2 waveguide. When light is impinging on the sample surface and reaches the nanoparticle layer, several phenomena occur. First the plasmonic resonance of the individual nanoparticles is excited, and part of the transmitted light is hence absorbed. The nanoparticles also serve as scattering elements for the incident light: part of the light is coupled to the waveguide modes via interaction with nanoparticles. On its turn, the waveguide modes are leaky modes and can be scattered by the presence of nanoparticles: this diffracted part of the leaky mode will interfere with the directly transmitted light. The result of this interference is the so-called “destructive interference mode”. The destructive interference mode has a large influence on the optical response of the sample. Its signature is found both in intensity plots as well as in the phase, as tested by Mueller matrix measurements. Moreover, it was discovered that such structures are characterized by a particular circular dichroism behavior,

which cannot be explained by the sole superposition of the linear optical properties. Whereas the linear circular dichroism is coming from the anisotropy of the sample, the true circular dichroism is due to some curvature in the aligned nanoparticles, which in the end breaks the symmetry.

5.2 Outlook

New Experiments

- Since the limit of time, investigation of the influence of external magnetic fields on the SPPs of Au/Ni/Au grating with the MM approach were not finished and needed to be done in the future.

- The mechanical stretching of metallic layers on PDMS polymer could easily tune the periodicity and amplitude of the grating and induce cracks after certain percentage of stretching. The cracks become more and more when stretching into a higher and higher percentage. This gives the possibility and freedom to tune the SPP resonance position and intensity and also decrease the propagating length between the cracks in proximity. It is interesting to perform the measurement on the fine tuning of SPPs with mechanical stretching, in particular with the MM approach.

- By releasing the stretched metallic grating further, the size of cracks decrease by keeping the shape unchanged. Besides, the plasmonic effect completely reverses to the stage without stretching when all the original strain is released. So it will be very interesting to investigate the dependence of plasmonic effect on the crack size with releasing with MM.

New photonic materials

Our MM based approach is a more powerful and straightforward method than the use of full Maxwell solvers: it needs much less computer power, it is very fast and it is directly linked to the physical interpretation. It is very general and can be applied to various nanostructures in order to predict and interpret the Mueller matrix contour plots. The separate role of anisotropies and photonic/plasmonic modes is at first distinguished: once the isotropic or anisotropic optical model is made, it is extended with the analytical expressions of the identified additional modes. These could be, for instance, localized plasmonic modes, photonic passive modes originating from waveguides or scattering, active modes related to emissive nanostructures, etc, under the condition that an analytical dependence of the optical dispersion can be given as a function of λ, θ and α. Beyond the simple interpretation, the exact attribution of every spectral feature (both in amplitude and in phase) together with its azimuthal dependence opens up the path to a possible tailoring of specific functionalities of nanostructures and therefore paves the way for a very precise control of the design and metrology of plasmonic nanostructures. Therefore the presented method is not only powerful in identifying the optical features of a given sample, but also for optimization of the design of novel structures and for characterization or metrology. The optimization of the structure design will be facilitated by the decomposition of complex patterns into its basic modes, which can be tailored individually.

Declaration of Originality

I hereby declare that this thesis and the work reported herein was composed by and originated entirely from me. Information derived from the published and unpublished work of others has been acknowledged in the text and references.

Hiermit erkläre ich, dass diese Arbeit eigenständig von mir verfasst wurde und die darin enthaltenen Inhalte auf Resultaten von mir durchgeführten Messungen beruhen. Alle Referenzen auf veröffentlichte oder bislang unveröffentliche Arbeiten anderer Personen sind eindeutig als solche im Text gekennzeichnet.

Meng Wang

Acknowledgements

First of all, I would like to thank Prof. Dr. Martin Dressel for giving me the opportunity to work on my PhD project at his institute. I am especially thankful to my supervisors Dr. Audrey Berrier and Dr. Bruno Gompf. My research would not be able to finish without their patient guidance, support and encouragement. Under their guidance I overcame many difficulties and learned a lot in experimental skills, data analysis, presentation and scientific writing, which will lay the groundwork for my future work. I would also like to thank all the people of the 1. Physikalisches Institut, in particular Stefano De Zuani and all the people of the ellipsometry group. I thank their help for my work and I enjoyed the time here in Stuttgart. Thanks also to Gabi Untereiner for evaporating my samples. Thanks to Agni Schmidt for the great help in many different occasions, especially for solving the health insurance problem for my family at the end of my PhD. Thanks to Prof. Nathalie Destouches of University of Saint-Etienne for fabricating the Ag nanoparticle arrays investigated in this work.

I would like to acknowledge the China Scholarship Council (CSC) that offer generous scholarship for my study in Germany. I would like to thank my parents for their continuous support and encouragement through these years. Finally, I would like to express my gratitude to my wife Fang Liu who has been always supporting me through the difficult time. I also thank to her help and company.

List of Figures